GDAŃSK UNIVERSITY
OF TECHNOLOGY
FACULTY OF CHEMISTRY

The author of the PhD dissertation: **Ahmet Kertmen**
Scientific discipline: **Chemistry**

DOCTORAL DISSERTATION

Title of PhD dissertation: Development of Biocompatible Fe_3O_4@SiO_2 Nanoparticles as Subcellular Delivery Platform for Glucosamine-6-Phosphate Synthase Inhibitors

Title of PhD dissertation (in Polish): Rozwój biokompatybilnych nanocząsteczek Fe_3O_4@SiO_2 typu rdzeń-powłoka jako subkomórkowa platforma dla inhibitorów syntazy glukozamino-6-fosfatazy

Supervisor	**Auxiliary supervisor**
Prof. dr. hab. eng. Ryszard Andruszkiewicz	Dr. eng. Błazej Scheibe

Gdańsk, 2018

GDAŃSK UNIVERSITY OF TECHNOLOGY
FACULTY OF CHEMISTRY

STATEMENT
The author of the PhD dissertation: *Ahmet Kertmen*

I, the undersigned, agree that my PhD dissertation entitled:

Development of Biocompatible Iron Oxide-Silicon oxide Core-Shell Nanoparticles as Subcellular Delivery Platform for Glucosamine-6-Phosphate Synthase Inhibitors

may be used for scientific or didactic purposes.[1]

Gdańsk, ...
signature of the PhD student

Aware of criminal liability for violations of the Act of 4th February 1994 on Copyright and Related Rights (Journal of Laws 2006, No. 90, item 631) and disciplinary actions set out in the Law on Higher Education (Journal of Laws 2012, item 572 with later amendments),[2] as well as civil liability, I declare, that the submitted PhD dissertation is my own work.
I declare, that the submitted PhD dissertation is my own work performed under and in cooperation with the supervision of Prof. dr. hab. eng. Ryszard Andruszkiewicz, the auxiliary supervision of dr eng. Błażej Scheibe.

This submitted PhD dissertation has never before been the basis of an official procedure associated with the awarding of a PhD degree.
All the information contained in the above thesis which is derived from written and electronic sources is documented in a list of relevant literature in accordance with art. 34 of the Copyright and Related Rights Act.
I confirm that this PhD dissertation is identical to the attached electronic version.

Gdańsk, ...
signature of the PhD student

I, the undersigned, agree to include an electronic version of the above PhD dissertation in the open, institutional, digital repository of Gdańsk University of Technology, Pomeranian Digital Library, and for it to be submitted to the processes of verification and protection against misappropriation of authorship.

Gdańsk, ...
signature of the PhD student

DESCRIPTION OF DOCTORAL DISSERTATION

1 Decree of Rector of Gdansk University of Technology No. 34/2009 of 9th November 2009, TUG archive instruction addendum No. 8.

2 Act of 27th July 2005, Law on Higher Education: Chapter 7, Criminal responsibility of PhD students, Article 226.

GDAŃSK UNIVERSITY OF TECHNOLOGY
FACULTY OF CHEMISTRY

The Author of the PhD dissertation: Ahmet Kertmen
Title of PhD dissertation: Development of Biocompatible Iron Oxide-Silicon oxide Core-Shell Nanoparticles as Subcellular Delivery Platform for Glucosamine-6-Phosphate Synthase Inhibitors
Title of PhD dissertation in Polish: Rozwój biokompatybilnych nanocząsteczek Fe_3O_4@SiO_2 typu rdzeń-powłoka jako subkomórkowa platforma dla inhibitorów syntazy glukozamino-6-fosfatazy
Language of PhD dissertation: English
Supervision: Prof. dr. hab. eng. Ryszard Andruszkiewicz
Auxiliary supervision: dr. eng. Błażej Scheibe
Date of doctoral defense:
Keywords of PhD dissertation in Polish: nanocząsteczki typu rdzeń-powłoka, klastry nanocząsteczek, koloidosomy, syntaza glukozamino-6-fosfatazy, dostarczanie leków
Keywords of PhD dissertation in English: core-shell nanoparticles, nanoparticle clusters, colloidosomes, Glucosamine-6-phosphate synthase, drug delivery
Summary of PhD dissertation in Polish: Wiele inhibitorów syntazy glukozamino-6-fosforanu (GlcN-6-P), enzymu odpowiedzialnego za katalizę pierwszego etapu szlaku metabolicznego prowadzącego do metabolizowania 5'-difosfo-N-acetylo-D-glukozaminy, wykazuje zdolność do efektywnej inhibicji wzrostu licznych patogenów grzybiczych. Pośród nich kwas N^3-(4-metoksyfumarolo)-L-2,3-diaminopropionowy (FMDP) jest określany jako najskuteczniejszy inhibitor GlcN-6-P. Jednocześnie słabe stężenia hamujące *in vitro* wyznaczone dla FMDP w postaci wolnych cząsteczek wymusiły zaistnienie dalszych badań nad bardziej efektywnymi pochodnymi tego cennego inhibitora. Pomimo 35 lat intensywnych badań na ten temat oraz licznych doniesień o nowych peptydach i prolekach na bazie FMDP, słabe właściwości hamujące proleków oraz szybko wykształcana oporność komórkowa przeciwko peptydom z FMDP wymusiły poszukiwania innych kierunków rozwoju leków przeciwgrzybiczych. Pośród nich znalazło się dostarczanie FMDP z wykorzystaniem nanocząstek, co stanowi podmiot tej rozprawy. Zgodnie z tą ideą, nanocząstki tlenku żelaza opłaszczonego krzemionką (ang. *core-shell nanoparticles*; CSNPs), dotychczas jedyne zatwierdzone przez Agencję do spraw Żywności i Leków (ang. *Food and Drug Administration*; FDA), wybrano jako biokompatybilne nośniki leków hamujących działanie syntazy GlcN-6-P.
W celu rozwoju metody przygotowywania CSNPs rozprawa dogłębnie opisuje powlekanie krzemionką nanocząstek tlenku żelaza funkcjonowanych kwasem oleinowym (ang. *oleic-acid capped iron oxide nanoparticles*; *OA-IONPs*) z wykorzystaniem cetylotriamonu (CTA^+) w warunkach niemal neutralnego pH. W pracy wykazano, iż wstępna alkaliczna hydroliza octanu etylu w obecności CTA^+ oraz OA-IONPs indukuje unikatowy mechanizm wymiany ligandów między kwasem oleinowym oraz formułującymi się *in situ* jonami octanu. Indukowany przez octan mechanizm powoduje formowanie się amorficznej powłoki o grubości ok. 20 – 25 nm wokół pojedynczych nanocząstek tlenku żelaza tworząc silnie monodyspersyjne CSNPs. Wykazano również synergiczne działanie klasterów nanocząstek tlenku żelaza (ang. *iron oxide nanoparticle* clusters; IONPCs) i utworzonych *in situ* pęcherzyków CTAB zamykających prekursory krzemionki utworzone w warunkach wysokiego stosunku [CTAB]/[IONP]. Czasowo-rozdzielcza transmisyjna mikroskopia elektronowa wysokiej rozdzielczości (HR-TEM) oraz obserwacje cryo-TEM przedstawiają unikatowy mechanizm fuzji micelarnej prowadzący do formułowania się monodyspersyjnego układu nanocząstek. Dokładna analiza spektroskopowa strat energii elektronów (ang. *electron energy-loss spectroscopy*; EELS), spektroskopii fourierowskiej w podczerwieni (ang. *Fourier transform infrared*; FTIR), spektroskopii Ramanowskiej oraz NMR (ang. *nuclear magnetic resonance*) potwierdzają mechanizm micelarnej fuzji prowadzącej do formacji CSNPs. Następnie przedstawiono superparamagnetyczne właściwości wodnych roztworów CSNPs przygotowanych za pomocą techniki

nanoemulsyjnej. Pomiary właściwości magnetycznych zostały dokładnie opisane. Za pomocą magnetometrii stałoprądowej (ang. *DC magnetometry*) potwierdzono superparamagnetyczny charakter CSNPs, a przy użyciu magnetometrii zmiennoprądowej ich właściwości paramagnetyczne (ang. *AC magnetometry*).

Badania biologiczne *in vitro* zdolności inhibitorowych układów CSNP-GlcN-6-P przeprowadzone na komórkach ludzkich raka szyjki macicy (HeLa), raka gruczłowo-gardłowego (FaDu), fibroblastach (MSU1.1) oraz na komórkach drożdżaka *Candida albicans* wykazały, że komórki ludzkie niemal całkowicie tracą swoją żywotność w obecności koniugatów CSNP-GlcN-6-P, podczas gdy wzrost komórek grzybicznych został zahamowany jedynie o 30%. Niemniej jednak, badania internalizacji komórkowej wykonane za pomocą obrazowania TEM dla nanocząstek (OH-PEG-CSNPs) funkcjonalizowanych polietylenoglikolem (ang. *polyethyleneglycol*, PEG) bez inhibitora GlcN-6-P wykazały znakomitą biokompatybilność OH-PEG-CSNPs. Obrazowanie TEM sugeruje iż zwiększona internalizacja OH-PEG-CSNPs przez komórki ludzkie, w przeciwieństwie do niewystarczającej internalizacji przez komórki *Candida albicans,* może być wyjaśnieniem słabej inhibicji wzrostu komórek grzybiczych. Ogólnie rzecz biorąc, praca kwestionuje zasadność i znaczenie "biokompatybilności" w nanocząsteczkowych preparatach środków przeciwgrzybiczych.

Summary of PhD dissertation in English: Numerous inhibitors of glucoseamine-6-phophate synthase (GlcN-6-P), the enzyme responsible from catalysis of the first step of metabolic pathway leading to metabolism 5'-diphospho-N-acetyl-D-glucosamine, were reported as effective agents for inhibiting the growth of various fungal pathogens. Among the reported inhibitors, N^3-4-(methoxyfumaroyl)-L-2,3-diaminopropanoic acid (FMDP) was reported to be the most effective inhibitor of GlcN-6-P. However, poor *in vitro* inhibitory concentrations recorded for FMDP in free molecular form required further research on development of more effective derivatives of this valuable inhibitor. Despite the 35-years of intensive research on the topic and numerous reports on new peptide and prodrug forms of FMDP, poor inhibitory effects of prodrugs and the rapid cellular resistance acquired against FMDP-peptides required the other areas of the antifungal development to be discovered. Among these areas, nanoparticle mediated delivery of FMDP constitutes the topic of this thesis. Within this concept, iron oxide-silica core-shell nanoparticles (CSNPs) as the only Food and Drug Administration (FDA) approved nanomaterials to the date has been further developed to function as biocompatible drug delivery platforms for GlcN-6-P enzyme.

In order to develop the preparation of CSNPs, thesis deeply explores the cetyltrimethylammonium (CTA^+) directed silica coating methods of the oleic-acid capped iron oxide nanoparticles (OA-IONPs) initialized under near-neutral pH conditions. It is demonstrated that the initial alkaline hydrolysis of ethyl acetate in the presence of CTA^+ and OA-IONPs induces an unusual ligand exchange mechanism between oleic acid and *in situ* formed acetate ions. The acetate induced mechanism is shown to be catalysing the formation of ~20-25 nm thick amorphous silica shells around the individual iron oxide nanoparticles resulting in highly mono-dispersed CSNPs. Synergetic effects of the iron oxide nanoparticle clusters (IONPCs) and the *in situ* formed CTAB vesicles encapsulating the silica precursors formed in high [CTAB]/[IONP] ratio conditions are demonstrated. Time-resolved HR-TEM and cryo-TEM observations demonstrates a unique micellar fusion mechanism inducing the formation of mono-dispersed core-shell nanoparticles. Detailed electron energy-loss spectroscopy (EELS), Fourier transform-infrared (FT-IR), Raman and NMR spectroscopy further supports the micellar fusion mechanism behind the formation of CSNPs. Thesis further presents the superparamagnetic properties of aqueously well dispersible CSNPs prepared by

reported nanoemulsion procedure. Measurement of the magnetic properties, confirming the superparamagnetic nature of CSNPs by DC magnetometry and paramagnetic nature of the particles confirmed by AC magnetometry, are discussed in detail.

In vitro biological activities of CSNP-GlcN-6-P inhibitor conjugates against human cervical cancer (HeLa), hypopharyngeal carcinoma (FaDu), human fibroblast (MSU1.1) cell lines and *Candida albicans* demonstrates that the human cells almost completely loose their viability in the presence of CSNP-GlcN-6-P inhibitor conjugates, whereas, the growth of *Candida albicans* is reduced by only 30%. Nevertheless, cellular internalization studies performed with polyethyleneglycol functionalized core-shell nanoparticles (OH-PEG-CSNPs) in the absence of GlcN-6-P inhibitors by TEM imaging evidences the excellent biocompatibility of OH-PEG-CSNPs. Biological TEM studies suggest that, elevated internalization of OH-PEG-CSNPs by human cells in contrast to inefficient internalization by *Candida albicans* could be the explanation for ineffective inhibition of fungal cells. Overall, the thesis questions the validity and meaning of “biocompatibility” approach in nanoparticle formulations of antifungal agent.

Table of Contents

List of Tables

Abbreviations

Outline of the thesis

CHAPTER 1: Introduction 1

1.1 Motivation 1

1.2 Biological background 4
1.2.1 Antimicrobial Resistance (AMR) – an outlook 4
1.2.2 Infections caused by *Candida* species: Candidiasis 6
1.2.2.1 Clinically used anti-*Candida* drugs and their cellular targets 7
1.2.2.2 Emerging multi-drug resistance (MDR) problem in Candidiasis 9
1.2.2.3 State of fungal infection treatment in the MDR era – call for action 11
1.2.3 Glucosamine-6-phosphate synthase — a potential new target in antimicrobial chemotherapy 13
1.2.3.1 Inhibitors of GlcN-6-P synthase from *Candida albicans* – 35 years of a systematic study 15
1.2.3.2 Summary 36

1.3 Chemical and physical background 39
1.3.1 Preparation Iron oxide nanoparticles (IONPs) and core-shell nanoparticles 39
1.3.2 Magnetic properties of iron oxide nanoparticles 42
1.3.3 Synthesis of antifungal agents their nanoparticle conjugates 44

1.4 Objectives of the thesis 46

CHAPTER 2: Experimental Section 48

2.1 Chemicals and Materials 48

2.2 Methods 48
2.2.1 TEM imaging and structural HRTEM analysis 48
2.2.2 FTIR and Raman spectroscopy 49
2.2.3 Dynamic light scattering (DLS) nanoparticle tracking analysis (NTA) 50
2.2.4 X-Ray Photoelectron Spectroscopy 50
2.2.5 Vibrating sample magnetometry measurements 50
2.2.6 NMR analysis 51
2.2.7 ICP-MS analysis of functionalized CSNPs 51
2.2.8 UV-Vis spectroscopy analysis 51

2.3 Synthesis of nanoparticles 52
2.3.1 Iron oxide nanoparticles 52
2.3.1.1 IONPs prepared by thermal decomposition method (OA-IONPs) 52
2.3.1.2 Iron oxide nanoparticle clusters (IONPCs) 52
2.3.1.3 IONPCs after saponification reaction (Ac-IONPs) and dried oleic acid-capped iron oxide nanoparticles (dOA-IONPs) 53
2.3.2 Core – shell nanoparticles (CSNPs) 54
2.3.2.1 CSNPs prepared by microemulsion (low concentration) method 54
2.3.2.2 CSNPs prepared by nanoemulsion (high concentration) method 54
2.3.2.3 Purification of CSNPs prepared by Nanoemulsion method 55
2.3.2.3.1 Purification by dialysis in concentrated acetic acid solution 55
2.3.2.3.2 Purification by dialysis in acetate buffer 55

2.4 Synthesis of antifungals and their intermediates....56
2.4.1 *N*-succinimidyl, methyl fumarate....56
2.4.2 *N*-succinimidyl, *trans*-4-oxo-4-phenyl-2-butenoate....57
2.4.3 N^2-(Fmoc), N^3-(4-methoxyfumaroyl)-L-2,3-diaminopropanoic acid (Fmoc-FMDP)....57
2.4.4 N^2-(Fmoc), N^3-*trans*-4-oxo-4-phenyl-2-butenoyl-L-2,3-diaminopropanoic acid (Fmoc-BADP)....58
2.4.5 *cis*-2-(9-Fluorenylmethyloxycarbonyl)amino-cyclopentanecarboxylic acid (Fmoc-cispentacin)....58

2.5 Synthesis of nanoparticle – antifungal conjugates....59
2.5.1 Functionalization of CSNPs by Fluorenylmethyloxycarbonyl (Fmoc)....59
2.5.2 Preparation of OH-PEG functionalized CSNPs (OH-PEG-CSNPs)....61
2.5.3 Preparation of Fmoc-FMDP-PEG-CSNPs and Fmoc-BADP-PEG-CSNPs....61
2.5.4 Preparation of FMDP-PEG-CSNPs and BADP-PEG-CSNPs....62

2.6 *In vitro* Biological experiments....62
2.6.1 Cell lines and cell culture conditions....62
2.6.2 Cytotoxicity and viability assays of human cells....63
2.6.3 Growth kinetics and viability of *Candida albicans.*....63
2.6.4 Cellular internalization studies....64

CHAPTER 3: Preparation of Nanoparticles....65

3.1 Morphological analysis of nanoparticles by TEM imaging....65
3.1.1 IONPs prepared by thermal decomposition method (OA-IONPs)....65
3.1.2 Iron oxide nanoparticle clusters (IONPCs)....66
3.1.3 Core – shell nanoparticles by microemulsion versus nanoemulsion method....67

3.2 Time-resolved TEM and cryo-TEM observations of CSNP formation....73

3.3 FT-IR and Raman spectroscopy analysis of IONPs and CSNPs....79

3.4 Structural TEM analysis of IONPs and CSNPs of nanoemulsion process....88
3.4.1 Crystallographic properties....88
3.4.2 Surface coating analysis....90
3.4.3 Elemental analysis of CSNPs....96

3.5 Dynamic Light Scattering / Nanoparticle Tracking Analyses....99
3.5.1 DLS analysis of nanovesicle–IONPC hybrids....99
3.5.2 NTA of CSNPs synthesized by nanoemulsion method....101

3.6 X-ray Photoelectron Spectroscopy Analysis....101

3.7 Conclusion of the Chapter....103

CHAPTER 4: Magnetic properties of CSNPs....109

4.1 Vibrating sample magnetometry (VSM)....109

4.2 Alternating Current Magnetic Susceptibility (ACMS)....111

CHAPTER 5: Organic Synthesis and Nanoparticle Functionalization....114

5.1 Surface purification of CSNPs by dialysis....114

5.2 Determination of free amino groups on CSNP surfaces by UV-vis spectroscopy....115

5.3 Determination of OH-PEG attachment to the CSNPs by FT-IR analysis....117

5.4 ICP-MS analysis of OH-PEG-CSNPs....118

5.5 NMR analysis of Fmoc-FMDP, Fmoc-BADP and their intermediates....118
5.5.1 N-succinimidyl, methyl fumarate....118
5.5.2 N-succinimidyl, trans-4-oxo-4-phenyl-2-butenoate....118
5.5.3 N^2-(Fmoc), N^3-(4-methoxyfumaroyl)-L-2,3-diaminopropanoic acid (Fmoc-FMDP)....119

5.5.4 N^2-(Fmoc), N^3-trans-4-oxo-4-phenyl-2-butenoyl-L-2,3-diaminopropanoic acid (Fmoc-BADP) 119
5.5.5 *cis*-2-(9-Fluorenylmethyloxycarbonyl)amino-cyclopentanecarboxylic acid 119
5.6 Determination of Fmoc-FMDP and Fmoc-BADP attachment to the OH-PEG-CSNPs by FT-IR 120
5.7 Determination of the amount of FMDP and BADP attachment to CSNPs by UV-Vis spectroscopy 121
5.8 X-ray Photoelectron analysis of Fmoc-FMDP-PEG-CSNPs, Fmoc -BADP-PEG-CSNPs and OH-PEG-CSNPs....123
5.9 ICP-MS analysis of BADP-PEG-CSNPs and FMDP-PEG-CSNPs....128
5.10 Conclusion of the chapter....128

CHAPTER 6: *In vitro* Biological Studies....130

6.1 Cytotoxicity and viability assays of human cells....130
6.2 Growth kinetics and viability of *Candida albicans*....132
6.3 Determination of CSNP internalization by TEM imaging 134
6.3.1 TEM imaging of HeLa cells....134
6.3.2 TEM imaging of FaDu cells 136
6.3.3 TEM imaging of Candida albicans....139

CONCLUSIONS....142

Bibliography....147

APPENDIXES

1 N-succinimidyl, methyl fumarate ^{1}H-NMR 1
2 N-succinimidyl, methyl fumarate ^{13}C-NMR 2
3 N-succinimidyl, methyl fumarate HSQC 3
4 N-succinimidyl, trans-4-oxo-4-phenyl-2-butenoate ^{1}H-NMR 4
5 N-succinimidyl, trans-4-oxo-4-phenyl-2-butenoate ^{13}C-NMR 5
6 N-succinimidyl, trans-4-oxo-4-phenyl-2-butenoate HSQC....6
7 N-succinimidyl, trans-4-oxo-4-phenyl-2-butenoate HMBC....7
8 N^2-(Fmoc), N^3-trans-4-oxo-4-phenyl-2-butenoyl-L-2,3-diaminopropanoic acid (Fmoc-BADP) ^{1}H-NMR 8
9 N^2-(Fmoc), N^3-trans-4-oxo-4-phenyl-2-butenoyl-L-2,3-diaminopropanoic acid (Fmoc-BADP) ^{13}C -NMR 9
10 N^2-(Fmoc), N^3-trans-4-oxo-4-phenyl-2-butenoyl-L-2,3-diaminopropanoic acid (Fmoc-BADP) HSQC 10
11 N^2-(Fmoc), N^3-trans-4-oxo-4-phenyl-2-butenoyl-L-2,3-diaminopropanoic acid (Fmoc-BADP) HMBC 11
12 N^2-(Fmoc), N3-(4-methoxyfumaroyl)-L-2,3-diaminopropanoic acid acid (Fmoc-FMDP) ^{1}H-NMR .12
13 N^2-(Fmoc), N3-(4-methoxyfumaroyl)-L-2,3-diaminopropanoic acid acid (Fmoc-FMDP) ^{13}C-NMR13
14 N^2-(Fmoc), N3-(4-methoxyfumaroyl)-L-2,3-diaminopropanoic acid acid (Fmoc-FMDP) HSQC 14

15 N^2-(Fmoc), N3-(4-methoxyfumaroyl)-L-2,3-diaminopropanoic acid acid (Fmoc-FMDP) HMBC 15
16 cis-2-(9-Fluorenylmethyloxycarbonyl)amino-cyclopentanecarboxylic acid (Fmoc-cispentacin) ^{1}H-NMR 16
17 cis-2-(9-Fluorenylmethyloxycarbonyl)amino-cyclopentanecarboxylic acid (Fmoc-cispentacin) ^{13}C-NMR 17
18 cis-2-(9-Fluorenylmethyloxycarbonyl)amino-cyclopentanecarboxylic acid (Fmoc-cispentacin) HSQC 18
19 cis-2-(9-Fluorenylmethyloxycarbonyl)amino-cyclopentanecarboxylic acid (Fmoc-cispentacin) HMBC 19

List of Figures

Figure 1. Infographic for deaths attributable to AMR every year (O 'neill, 2016).....4
Figure 2. Graphical presentation of resistance surveillance data on *Candida* and non-*Candida* infections (WHO, 2014).....5
Figure 3. Metabolic pathway leading to UDP-GlcNAc (image acquired from IUBMB website).....13
Figure 4. Fumarylcarboxyamido-L-2,3-diaminopropionyl-L-alanine (FCDP-Ala) and fumaryl-D,L-alanine (left); N^3-fumarylcarboxyamido-L-2,3-diaminopropionic acid (FCDP) and FCDP-Ala (right). 15
Figure 5. The structures of glutamine, FMDP and synthesized derivatives (Zgódka et al., 2001b). ...26
Figure 6. Inhibition of GlcN-6-P synthase activity *in situ* in *Candida albicans* cells: a) effect of ADGP, AMB and their combination; b) effect of FMDP, AMB or their combination (Janiak et al., 2002). 27
Figure 7. Explanation of a magnetic hysteresis curve (Soler and Paterno, 2017). 43
Figure 8. Original synthesis pathway of FMDP and BADP.....45
Figure 9. Scheme for synthesis of Fmoc-FMDP, Fmoc-BADP and their intermediates.....56
Figure 10. General functionalization scheme of CSNPs via amino groups 59
Figure 11. Functionalization of CSNPs by fluorenylmethyloxycarbonyl.....59
Figure 12. Functionalization of CSNPs by OH-PEG.....60
Figure 13. Functionalization of CSNPs by Fmoc-FMDP or Fmoc-BADP via ester and amide bonds. R: -OCH_3 or -Ph.....62
Figure 14. (A) Low-magnification TEM image of 30 min synthesized OA–IONPs and, (B) high-magnification TEM image of OA–IONPs where the overlapping graph shows their size distribution. 65
Figure 15. (A) Low-magnification TEM image of 25 min synthesized monodispersed OA–IONPs and, (B) high-magnification TEM image of OA–IONPs.....66

Figure 16. (A) Low-magnification TEM image and, (B) high-magnification TEM image of 45 min synthesized OA–IONPs OA–IONPs. 66

Figure 17. A-D) cryo-TEM images of IONPCs (grids were prepared using highly diluted dispersions of IONPCs). 67

Figure 18. A,B) low-magnification and, C-F) high magnification HR-TEM images of CSNPs prepared by microemulsion method.....68

Figure 19. A,B) CSNPs shown in different levels of low-magnification, (C) high magnification TEM image of CSNPs prepared by nanoemulsion method. Overlapping graph shows their size distribution, and (D-F) High magnification HR-TEM images of the individual CSNPs prepared by nanoemulsion method.....69

Figure 20. A,B) Nanoemulsion reaction performed with OA-IONPs having very wide size distribution (polydisperse). Red arrows indicates the silica shells with the tiniest iron oxide cores. 70

Figure 21. A,B) CSNPs synthesized by nanoemulsion method in the presence of elevated amounts of CTAB (6x CTAB than typical microemulsion method and 2xCTAB than typical nanoemulsion method).....70

Figure 22. Time-resolved TEM observation of the silica-coating reaction progress: (A–C) 180 min after the silica precursor addition; (D–F) 195 min after the silica precursor addition; (G–I) 210 min after the silica precursor addition; and (J–L) 225 min after the silica precursor addition. 72

Figure 23. A–C) Hemispheres of IONPCs partially coated with silica formed after 180 min of the nanoemulsion process. Red circles in image "C" indicate the positions of two hemispheres overlapping, D) Hemi- sphere of IONPCs with almost full silica coating on every single IONP building block formed around 225 min of the nanoemulsion process. Hollow opening of the hemisphere positioned perpendicularly to the viewing angle. If "image A" was observed from the angle shown with the red arrow, the hemisphere would be positioned like the one in "image D" 74

Figure 24. A–C) Cryo-TEM images of the nanoemulsion process collected at 120 min of the reaction show the fusion of IONP clusters and silica nanovesicles (nanoemulsions) and, D) independently coexisting nanovesicles found in the same sample before coalescence to IONPCs. 75

Figure 25. FT-IR spectroscopy analyses of OA-IONPs, dried OA-IONPS and Ac-IONPs. 79

Figure 26. FT-IR spectroscopy comparison of OA- and Ac-IONPs with oleic acid, sodium oleate and iron(II) acetate.....80

Figure 27. A) Demonstration of the phase separation between the upper aqueous phase containing Ac-IONPs and lower chloroform phase. Images from left to right shows the rapid phase separation after vigorous shaking, B) Demonstration of the phase separation between the lower chloroform phase containing OA-IONPs and upper aqueous phase. Images from left to right shows the rapid phase separation after vigorous shaking.....83

Figure 28. A) Raman spectroscopy analysis of dOA–IONPs in comparison to oleic acid, sodium oleate, iron oleate, and iron(II) acetate and the list of the peaks found in spectra (Kertmen et al., 2017). 84

Figure 29. A) Raman spectroscopy analysis of dOA–IONPs and Ac–IONPs at the iron oxide fingerprint region, B) comparison of the dOA–IONPs and Ac– IONPs under different laser excitations. Raman spectroscopy analysis of Ac- and OA-IONPs (Kertmen et al., 2017) 85

Figure 30. Raman spectroscopy comparison of OA-IONPs, Ac-IONPs and CSNPs of the nanoemulsion process (Kertmen et al., 2017). 87

Figure 31. A,B) HR-TEM and corresponding FFT of the Ac-IONPs showing that the iron oxide structures is magnetite; C,D) HR-TEM and corresponding FFT of the OA-IONPs showing that the iron oxide structures is magnetite; E) Oxygen and Iron content analysis of Ac- and OA-IONPs shows that the composition of the structures are identical and ligand exchange did not result in any significant modification in magnetite structure. 88

Figure 32. Oxygen and Iron content analysis of Ac- and OA-IONPs shows that the composition of the structures is identical and ligand exchange did not result in any modification in magnetite structure. 89

Figure 33. A, D) HRTEM images of CSNPS structures of nanoemulsion process; B,E) magnified views of the regions highlighted by red squares thereof and corresponding FFT images; C,F) images unambiguously show that the core of the nanoparticles are perfectly crystalline and observed crystal lattice is consistent with magnetite (Fe_3O_4) and the silica shells are found to be amorphous. In "images D" and "E" the cavity in silica shell is facing up.....90

Figure 34. EELS analyses of carbon content: A,B) acetate-coated IONPs and, C,D) oleic acid-coated IONPs. 91

Figure 35. PCA decomposition maps. This demonstrates uniform composition of SiO_2 (upper left and right) shells and Fe_3O_4 cores (lower left and right). 92

Figure 36. A) HAADF image of CSNPs of nanoemulsion process. Inset is the Fe $_{L2,3}$ edge spectra obtained from the core shell particles and from the seeds. The spectra where calibrated with the oxygen K edge and normalized. It confirms that no detectable chemical change happened to iron oxide cores after silica coating.; B,C) EELS fine structure parameter maps. Shifts in the Fe L_3 position of 1-2eV are known to be related to changes in the oxidation state of iron. Also the presence of a pre-peak in the oxygen edge in FeOx consistent with the iron core being Fe_3O_4. The homogeneity in these parameters maps indicates that oxidation state of the iron oxide cores is homogenous; D) Carbon EELS signal map after PCA de-noising. Note that the bright region at the top of the image corresponds to the surface of the hole in the silica populated with high concentration of carbon. However, carbon signal can be still seen surrounding the iron oxide core; E) co-acquired HAADF image showing the region where EELS SI was taken from.....93

Figure 37. A) HAADF image with a highlighted region where an EELS spectrum image was taken; B) oxygen signal coming from silica; (C) carbon relative composition from the EELS SI; D) carbon signal; and E) coloured map of carbon relative composition (green) with iron oxide core (red)..94

Figure 38. EELS analysis showing A) oxygen signal, B) iron signal, C) carbon signal, and D) colored map of oxygen (blue), iron (green), and carbon (red).....95

Figure 39. A) a HAADF image of the adjacent CSNPs of nanoemulsion process, B) EELS carbon analysis of two adjacent CSNPs shown in "image A", C) EELS oxygen analysis of two adjacent CSNPs shown in "image A", D) EELS iron analysis of two adjacent CSNPs shown in "image A" ...95

Figure 40. A) HAADF image taken from the ring formations in 3.30 h of nanoemulsion process; B) a magnified view of the "image A"; C) EDX analysis of silicon content in the area shown in red frame in image B; D) EDX analysis of iron content within the area shown in red frame in image B; E) Overlapped view of the image C and D; F) Elemental composition of the sample.....96

Figure 41. TEM image taken at 180 min of nanoemulsion process, B) magnified view of the region highlighted with red square in image A, C) cryo-TEM image of an CTAB-OA-IONPC at 120 min of nanoemulsion process, D) (C) magnified view of the region highlighted with red square in image C. Red arrows indicates the thin shells created around individual IONPs, E) The same CTAB-OA-IONPC shown in image D was destructed by melting the cryogenic medium with electron beam. Blue arrows indicates the direction of melting medium, F) magnified view of the region highlighted with red square in image C demonstrates the existence of tiny iron oxide particles within shells similar to those seen in image B.....98

Figure 42. A) typical correlation function with a fit performer using the CONTIN algorithm, B) size distribution obtained from the CONTIN analysis for diluted (black) and concentrated (red) sample. The dashed lines refer to weakly regularized CONTIN solutions. 99

Figure 43. NTA analysis graph of CSNPs from nanoemulsion process. 100

Figure 44. XPS analysis of CSNPs of the nanoemulsion process: A) nitrogen; B) carbon; C,D) General XPS survey. Red line indicates the 1073.38 eV sodium peaks.....102

Figure 45. Micellar fusion mechanism leading to the formation of CSNPs of nanoemulsion process (IONPs@acetate@SiO_2 structures): (A initial mixtures of aqueous CTAB solution and OA–IONPs dispersion in chloroform showing the phase separation between the aqueous (blue) and hydrophobic (yellow) phase oil. CTAB molecules create a monolayer at the liquid–liquid interface; B) after the evaporation of the organic phase, OA–IONPs are stabilized at the liquid– liquid interfaces, which results in the formation of IONPCs encapsulating the hydrophobic phase; C) IONP building blocks of IONPCs at the liquid–liquid interface and some micellar structures of CTA^+ in the aqueous phase; D) upon ethyl acetate addition into the solution, it is dispersed within the CTA^+–oleate bilayer on the surface of the clusters; E) after ethyl acetate saponification, the resulting acetate ions interact with the iron oxide surface and break the iron oxide structure. The breakage results in thin iron oxide shell formations stabilized by the CTA^+–oleate bilayer; F) later, the acetate layer penetrates the hydrophobic phase and removes the oleate-only coated surface

of the IONPs. This results in fully dynamic IONP formations as seen for the fourth IONP from the left; G) after addition of silica precursors, they form nanovesicles with excess CTAB molecules/micelles in solution. They eventually attack the dynamic sites of the IONPCs (fourth IONP from the left), which they use as tiny gates to fuse with the hydrophobic core of the clusters. The fusion process takes place by the coalescence of CTA^+ monolayers of nanovesicles to the CTA^+–oleate bilayers; (H) encapsulated silica precursors start to accumulate to space between the dynamic CTA^+–oleate bilayer and acetate-coated IONPs. Silica eventually starts to form, initially in the agglomerated form as observed in Figure 22A-C I) as time progresses, silica shell continues to grow, which will eventually lead to the formation of monodispersed IONPs@acetate@SiO_2 (Kertmen et al., 2017). 106

Figure 46. Hysteresis loop measured at different temperatures from 300 K - 4 K range, inset shows the coercive field for 300 K and 4 K measurement. 109

Figure 47. a,b) shows zero field cooling (ZFC open symbol) and field cooling (FC solid symbol) magnetization curves exhibit characteristic superparamagnetic behaviour, with the magnetic field increase (from 0.01 to 1 T) T_B shifts into the lower temperatures. 112

Figure 48. a) Real part χ' of AC susceptibility as a function of temperature for 10-10 000 Hz frequencies, b) T_{max} as a function of frequency. 113

Figure 49. A) Low magnification and, B) high magnification dark-field HR-TEM image of CSNPs after dialysis in acetic acid solution 114

Figure 50. A) Low magnification TEM image and, B) higher magnification TEM image of CSNPs of nanoemulsion process dialyzed in acetate buffer. 115

Figure 51. Absorbance spectra and its calibration curve obtained for Fmoc-piperidine adduct from Fmoc-cispentacin, fitted to absorption spectrum of Fmoc-piperidine adduct released from CSNPs. CSNPs-Fmoc-piperidine stands for Fmoc released from CSNPs 116

Figure 52. FTIR analysis of as-synthesized, dialyzed and OH-PEG functionalized CSNPs of the nanoemulsion process. 117

Figure 53. FTIR analysis of Fmoc-FMDP-PEG-CSNPs and Fmoc-BADP-PEG-CSNPs 120

Figure 54. Absorbance spectra of Fmoc-piperidine adducts obtained from Fmoc-BADP-PEG-CSNPs and Fmoc-FMDP-PEG-CSNPs. 121

Figure 55. Absorbance spectra and calibrations curves obtained for Fmoc-piperidine adduct from pure Fmoc-BADP and Fmoc-FMDP, fitted absorption spectrum of Fmoc-piperidine adducts released from Fmoc-BADP-PEG-CSNPs and Fmoc-FMDP-PEG-CSNPs. “BADP-20% piperidine” and “FMDP-20% piperidine” stand for absorbance curves of Fmoc-piperidine released from Fmoc-BADP-PEG-CSNPs and Fmoc-FMDP-PEG-CSNPs. 122

Figure 56. C1s analysis of as-synthesized CSNPs from nanoemulsion process (A), purified CSNPs by dialysis against acetic acid buffer (B), OH-PEG-CSNPs (C), Fmoc-FMDP-PEG-CSNPs (D), and Fmoc-BADP-PEG-CSNPs (E) 123

Figure 57. N1s analysis of as-synthesized CSNPs from nanoemulsion process (A), purified CSNPs by dialysis against acetic acid buffer (B), OH-PEG-CSNPs (C), Fmoc-FMDP-PEG-CSNPs (D), and Fmoc-BADP-PEG-CSNPs (E). 125

Figure 58. O1s analysis of as-synthesized CSNPs from nanoemulsion process (A), purified CSNPs by dialysis against acetic acid buffer (B), OH-PEG-CSNPs (C), Fmoc-FMDP-PEG-CSNPs (D), and Fmoc-BADP-PEG-CSNPs (E). 127

Figure 59. FaDu viability: FMDP-PEG-CSNPs tested for 2.5-25 µg/ml and BADP-PEG-CSNPs tested for 2.5-50 µg/ml in comparison to 2.5-50 µg/ml OH-PEG-CSNPs. 130

Figure 60. MSU-1.1 viability: FMDP-PEG-CSNPs tested for 2.5-25 µg/ml and BADP-PEG-CSNPs tested for 2.5-50 µg/ml in comparison to 2.5-50 µg/ml OH-PEG-CSNPs. 131

Figure 61. HeLa viability: FMDP-PEG-CSNPs tested for 2.5-25 µg/ml and BADP-PEG-CSNPs tested for 2.5-50 µg/ml in comparison to 2.5-50 µg/ml OH-PEG-CSNPs. 131

Figure 62. *Candida albicans* growth kinetics in the presence of 1-50 µg/ml concentration of CSNPs. The results are expressed as the mean of three independent experiments and the error bars show the standard deviation. 132

Figure 63. Viability of *Candida albicans* in the presence of 0.4-25 µg/ml OH-PEG-CSNPs and 0.4 -50 µg/ml FMDP-PEG-CSNPs and 50 µg/ml BADP-PEG-CSNPs. 133

Figure 64. Growth inhibitory activity of 25 µg/ml FMDP-PEG-CSNPs and 50 µg/ml BADP-PEG-CSNPs against *Candida albicans* in comparison to 25 ul OH-PEG-CSNPs. 133

Figure 65. TEM images of HeLa cells after 3-24h incubation with 25 µg/ml OH-PEG-CSNPs. X' and X'' represents the different levels of magnification of one selected area in image X. X' represents the magnified view of the second selected area in image X. 134

Figure 66. TEM images of HeLa cells after 3-24h incubation with 25 µg/ml OH-PEG-CSNPs. X' and X'' represents the different levels of magnification of one selected area in image X. 135

Figure 67. TEM images of FaDu cells in the absence of nanoparticles, presented as control sample. X' and X'' represents the different levels of magnification of one selected area in image X. Magnified view if the second selected area in image X is represented by X' 136

Figure 68. TEM images of FaDu cells after 3h (A-C) and 24h incubation with 25 µg/ml OH-PEG-CSNPs (B-I). X' and X'' represents the different levels of magnification of one selected area in image X. Magnified view if the second selected area in image X is represented by X' 137

Figure 69. TEM images of FaDu cells after 24h incubation with 25 µg/ml OH-PEG-CSNPs. X' and X'' represents the different levels of magnification of one selected area in image X. Magnified view if the second selected area in image X is represented by X' 138

Figure 70. TEM images of *Candida albicans* after 24h incubation with 25 µg/ml OH-PEG-CSNPs showing the particles passing through to cell-wall to cell membrane 139

Figure 71. TEM images of *Candida albicans* after 24h incubation with 25 µg/ml OH-PEG-CSNPs showing internalization of particles by shifted cytoplasm. 140

Figure 72. TEM images of *Candida albicans* after 24h incubation with 25 µg/ml OH-PEG-CSNPs showing the particles passed through cell membrane and reached to cytoplasm.....141

List of Tables

Table 1. Molecular scheme showing the general structure of GlcN-6-P synthase inhibitors and the table showing the derivatives.....16

Table 2. IC_{50} values of compounds against *Salmonella typhimurium* and *Saccharomyces cerevisiae.* 17

Table 3. Activity of dipeptides against selected microorganisms.....18

Table 4. Activity of selected antifungal agents and FMDP dipeptides against *Candida albicans* (ATCC 26278) by inhibition zone tests.....18

Table 5. Rates of peptide transport in yeast and mycelial forms of *Candida albicans* ATCC 26278. Initial peptide concentration was 100 uM. The residual peptide concentration in filtrates was assayed by the TNBS method.....19

Table 6. Antifungal *in vitro* activities (left); rate of transport and intracellular cleavage of FMDP peptides in *Candida albicans* ATCC 26278 (right) 19

Table 7. Number of resistant colonies obtained from 10^5 inoculum cells of *Candida albicans* ATCC 26278.....20

Table 8. Antimicrobial in vitro activity of some peptides containing A_2pr(IAc) to bacterial and fungal strains.....21

Table 9. Rate of Transport and Intracellular Cleavage of Peptides in *Candida albicans* ATCC 2627822

Table 10. Anticandidal activity and initial rates of transport and intracellular cleavage of FMDP dipeptides.....23

Table 11. Cleavage rate of FMDP-peptides in crude cell-free extract from L1210 cells and their comparison to previous results with *Candida albicans* (Milewski et al., 1991).....24

Table 12. Inhibitory and inactivation data for AADP, AEDP, BADP and FEDP in respect to *Candida albicans* GlcN-6-P synthase and dipeptide MIC values. 25

Table 13. Inhibition of glucosamine-6-phosphate synthase from *Candida albicans* by FMDP and derivatives 1-8 compounds (Zgódka et al., 2001b). 26

Table 14. FIC indexes found for combinations of antifungal agents (Janiak et al., 2002).....27

Table 15. Structures of BADP and AADP derivatives and their antifungal activities (Walkowiak et al., 2005).....28

Table 16. Activity of tested peptides against HL-60 human promyelocytic leukaemia cells and fungi. 29

Table 17. Anti-Candidal activity of *N*-acylated lipophilic dipeptides of FMDP (Andruszkiewicz et al., 2005).....29

Table 18. ***In vitro*** **cytotoxic activity of examined compounds against HL-60 human promyelocytic leukemia cells. 30**

Table 19. In vitro susceptibilities of *Candida albicans* reference strain and clinical isolates to oligopeptide and amino acid antifungals and fluconazole (Wakieć et al., 2008). 31

Table 20. Antifungal activity of NvaFMDP, Lys-NvaFMDP, Nva-Ψ[CSN^{2}H]-FMDP and Lys[CSNH]-Nva-Ψ[CSN^{2}H]-FMDP (Nowak-Jary and Andruszkiewicz, 2009).....32

Table 21. Antifungal activity of *bis-N,N*-(2-hydroxyethyl)glycine (bicine) derivatives 8a-i of FMDP (Koszel et al., 2012).....33

Table 22. Antimicrobial activity of amide derivatives of FMDP (Pawlak et al., 2015).....33

Table 23. Antimicrobial activity of A) keto-ester 11-13; B) amide-ester 14-19 derivatives of FMDP (Pawlak et al., 2016). 34

Table 24. Parameter *Φ* determined based on the Eq. (1) for 36–10 000 Hz frequencies. 112

Table 25. Relative C-C and C-O-C binding energy ratios of samples and their graphical presentation (O-C=O included in C-O-C).....124

Abbreviations

AADP	N^3-β-acetyl-acroyl-L-2,3-diaminopropanoic acid
AC	alternating current
Ac-	acetate-
Ac-IONPs	acetate-capped iron oxide nanoparticles
ACMS	alternating current magnetic susceptibility
AEDP	N^3-*DL*-trans-3-(1 -oxoethyl)oxirane-2-carbonyl-L-2,3- diaminopropanoic acid
AIDS	acquired immune deficiency syndrome
Ala	alanine
AMR	antimicrobial resistance
APTES	(3-Aminopropyl) triethoxysilane
Asp	aspartate
ATCC	American Type Culture Collection
ATP	adenosine triphosphate
BADP	N^3-trans-4-oxo-4-phenyl-2-butenoyl-L-2,3-diaminopropanoic acid
BADP-PEG-CSNP	(N^3-trans-4-oxo-4-phenyl-2-butenoyl-L-2,3-diaminopropanoic acid)-(polyethylene glycol)-iron oxide-silica core-shell nanoparticles
BSI	bloodstream infections
CDR1	multidrug resistance protein CDR1
Cdr1p	multidrug resistance protein CDR1
CDR2	multidrug resistance protein CDR2
Cdr2p	multidrug resistance protein CDR2
CRDP	N^3-crotonoyl-L-2,3-diaminopropanoic acid
cryo-TEM	cryogenic transmission electron microscopy
CSNPs	iron oxide-silica core-shell nanoparticles prepared by nanoemulsion method
CTA^+	cetyltrimethylammonium
CTAB	cetyltrimethylammonium bromide
DCC	*N,N'*-Dicyclohexylcarbodiimide
Dec	decanoyl
DLS	dynamic light scattering
dOA-IONPs	dried oleate-capped iron oxide nanoparticles
DON	6-diazo-5-oxo-L-norleucine
DSM	Deutsche Sammlung von Mikroorganismen (eng. German collection of microorganisms)
EADP	N^3-D-trqns-epoxysuccinamoyl-L-2,3-diaminopropanoic acid
EDX	energy-dispersive X-ray spectroscopy
FaDu	hypopharyngeal carcinoma cancer cells
FC	field cooled

FCDP	N^3-fumaramoyl-L-2,3-diaminopropanoic acid
FDP	N^3-Fumaroyl-L-2,3-diaminopropanoic acid
FMDP	N^3-4- Methoxyfumaroyl-L-2,3-diamino-propanoic acid
FMDP-PEG-CSNP	(N^3-trans-4-methoxyfumaroyl-L-2,3-diaminopropanoic acid)- (polyethylene glycol)-iron oxide-silica core-shell nanoparticles
Fmoc	fluorenylmethyloxycarbonyl
Fmoc-Osu	9-fluorenylmethyl *N*-succinimidyl carbonate
FPhe	*m*-fluorophenylalanin
Fru-6-P	fructose 6-phosphate
GlcN-6-P	glucosamine-6-phosphate
Gln	glutamine
Gly	glycine
H_c	coercive force
HeLa	human cervical cancer
Hex	hexanoyl
HIV+	human immunodeficiency virus positive
HMG-CoA	3-hydroxy-3-methylglutaryl coenzyme A
HRTEM	high-resolution transmission electron microscopy
IC50	half maximal inhibitory concentration
ICP-MS	inductively-coupled mass spectroscopy
IDSA	Infectious Diseases Society of America
IONPs	iron oxide nanoparticles
IONPs@SiO2	iron oxide-silica core-shell nanoparticles
k_2	dissociation rate constant
k_{intact}	maximal inactivation rate constant
Leu	leucine
Lys	lysine
FMDB	N^3-4-methoxyfumaroyl-L-2,4-diaminobutanoic acid
MDR	multidrug resistance
Met	methionine
MF-AME	N-methyl-N-fructosyl-amphotericin B methyl ester
MMDP	N^3-4-α-methoxymesaconoyl-L-2,3-diaminopropanoic acid
M_r	remanent magnetization
M_s	saturation magnetization
MSU1.1	human fibroblast line
NAC	non-albican *Candida*
NHS	*N*-hydroxysuccinimde

Nle	norleucine
NMR	nuclear magnetic resonance
NTA	nanoparticle tracking analysis
Nva	norvaline
OA-IONPs	oleate-capped iron oxide nanoparticles
OH-PEG-CSNPs	hydroxyl-polyethylene glycol-iron oxide-silica core-shell nanoparticles
OLys	oxalysine
OPT	oligopeptide permeases
PBS	phosphate buffered saline
Phe	Phenylalanine
PTR	tri-peptides transported
RPMI-1640	Roswell Park Memorial Institute 1640 Medium
SPIONs	superparamagnetic iron oxide nanoparticles
spp.	species
STEM-HAADF	scanning TEM high-angle annular dark field
T_B	blocking temperature
T_c	Curie temperature
TEM	transmission electron microscopy
TEOS	tetraethyl orthosilicate
TFA	trifluoroacetic acid
FTIR	Fourier-transform infrared
Tyr	tyrosine
UDP-GlcNAc	uridine-5'-N-acetylglucosamine
UK	United Kingdom
UN	United Nations
US	United States
UV-vis	ultraviolet-visible
Val	valine
VSM	vibrating sample magnetometry
WHO	World Health Organization
XPS	X-ray photoelectron spectroscopy
YNB-AS	yeast nitrogen base w/o amino acids
YNB-SG	yeast nitrogen base w/o amino acids and ammonium sulfate + 2% glucose + 0.2 g L^{-1} sodium glutamate
YPD	yeast-peptone-dextrose
ZFC	zero-field cooled
χAC	magnetic susceptibility

Outline of the thesis

Thesis consists of six (6) chapters covering the following issues:

CHAPTER 1 presents a detailed introduction of multi-drug resistance (MDR) and anti-microbial resistance (AMR). The chapter specifies the importance of emerging drug resistance to antifungal agents, with special emphasis given on fungal infections caused by *Candida spp.* (Candidiasis) within broad AMR context. After a detailed outlook of the species causing Candidiasis and introduction to targets (mechanism of action) of antifungal drugs currently in use, a roadmap to fight resistance to antifungals is presented. Relatedly, glucosamine-6-phosphate synthase (GlcN-6-P) enzyme as a new anti-candidal target and 35-years of research carried out to develop GlcN-6-P inhibitors as anti-candidal agents are presented in detail, as potential solution to MDR problem in Candidiasis. At last, preparation methods of iron oxide nanoparticles, their silica coated core-shell forms and magnetic properties of these particles are presented for nanoparticle-mediated drug delivery approach to be used to target GlcN-6-P enzyme; which constitutes the main task of the thesis. In the end of the chapter, objectives of the thesis are listed.

CHAPTER 2 presents the characterization and analysis techniques used throughout the thesis. These includes TEM imaging techniques to reveal nanoparticle morphology and elemental analysis by HRTEM; FTIR and Raman spectroscopy for nanoparticle surface functionalization as well as nanoparticle crystallographic analysis; X-ray photoelectron spectroscopy analysis for nanoparticle component and surface functionalization analysis; vibrating sample magnetometry (VSM), alternating current magnetic susceptibility (ACMS) spectroscopy analysis to reveal magnetic properties of core-shell nanoparticles; NMR analysis of Fmoc protected derivatives of the anticandidal agents (FMDP and BADP), ICP-MS analysis for determination of core-shell nanoparticle concentrations and UV-vis spectroscopy analysis for determination for quantitative analysis of nanoparticle functionalities. Chapter also gives detailed information of nanoparticle and antifungal synthesis procedures, nanoparticle-drug conjugation procedures and methods/conditions used for *in vitro* biological studies.

CHAPTER 3 presents the results of nanoparticle preparation procedures. Therein, time-dependent formation properties of IONPs and preparation of CSNPs by nanoemulsion process that constitutes the primary finding of the thesis are shown. The

morphological differences between CSNPs produced by well-known microemulsion and nanoemulsion method that proposed in the concept of this thesis for the first time are shown. Detailed time-resolved TEM and cryo-TEM imaging results to reveal the mechanism of CSNP formation by nanoemulsion method are demonstrated. FTIR and Raman spectroscopic analysis on surface functionality of IONPs and surface functionality analysis of CSNPs by HRTEM (EELS) techniques are shown. Chapter also includes structural and elemental analysis by HRTEM and XPS; as well as DLS and NTA analysis of CSNPs and IONPs to support the discussion. The conclusion included in the end of chapter includes a schematic presentation of CSNP formation mechanism in nanoemulsion process.

CHAPTER 4 discusses the magnetic properties of the CSNPs determined by vibrating sample magnetometry (VSM) and alternating current magnetic susceptibility (ACMS) measurements. Results shown in chapter include the hysteresis loop measured at 300 K - 4 K temperature range and determination of blocking temperature T_B obtained from zero-field cooling (ZFC) and field cooling (FC) magnetization curves; and determination of χ' of AC susceptibility as a function of temperature at 10-10 000 Hz frequencies.

CHAPTER 5 presents the results of all of the chemical synthesis procedures followed in the concept of thesis. It includes the quantification of functional groups and calculation of drug loading capacity of CSNPs, which were determined by UV-vis spectroscopy. FTIR and XPS spectroscopy results presents the confirmation of drug attachment to the nanoparticles. NMR analysis of synthesized organic compounds are presented in this chapter.

CHAPTER 6, as the final chapter of the thesis, presents the results of *in vitro* biological studies carried out with CSNP-drug conjugates. Chapter includes cell viability tests for three different human cell lines (Human cervical cancer - HeLa, hypopharyngeal carcinoma- FaDu and human fibroblast - MSU1.1) and wild type *Candida albicans*. Cellular internalization analysis of OH-PEG-CSNPs carried out for HeLa, FaDu and *Candida albicans* by TEM imaging are presented here.

CHAPTER 1

Introduction

1.1 Motivation

Among different areas of antimicrobial chemotherapy, especially the difficult situation is observed in its anti-fungal branch. Fungal micro-organisms are etiological factors of many serious, often deadly infectious diseases, especially in immunocompromised patients. A number of these patients is growing rapidly, not only because of the AIDS but also as a consequence of a frequent use of therapies that affect the human immune defense system (e.g. anticancer therapy with cytostatics, steroid therapy, use of immunosuppressive agents in transplant patients). Systemic mycoses are caused in these patients mainly by filamentous fungi from the *Aspergillus* genus and by the yeast-like microorganisms from the *Candida* genus. On the other hand, a number of fungal microorganisms are known as one of the most frequent reasons of nosocomial infections. *Candida albicans* is considered the fourth most popular etiological agent of nosocomial blood stream infections (candidemia) worldwide (Patterson; Pfaller and Diekema, 2007; Richardson and Lass-Flörl, 2008; Miceli et al., 2011).

Treatment of systemic fungal mycoses is difficult, in part because of the diagnostic problems but first of all, because of the very limited repertoire of effective antifungal chemotherapeutics. Such a drug should possess several features, including the fungicidal mode of action, the broadest possible spectrum of antifungal activity, the lowest possible toxicity to the mammalian host and a minimal ability to induce specific and multidrug resistance. None of the clinically used antifungal chemotherapeutics fulfills all of the above criteria. In the recent years, only two new antifungal agents have been introduced to clinics: Voriconazole and Caspofungin. On the other hand, contemporary chemotherapy faces many challenges. As a method of therapy based on the use of the selectively toxic substances, i.e. agents able to inactivate invasive cells, has been dynamically developed for decades, including the so called “golden area of antibiotics” that started with the discovery of penicillin. In the recent years, a growing concern has emerged that the era is coming to its end. A massive, uncontrolled use of

antibiotics has become a reason for the development of resistance to the present drugs. Chemotherapeutics used in clinics have actually become factors stimulating selection of resistant cells.

Considering the above outlined situation, there is a generally accepted opinion on an urgent need for novel anti-fungal chemotherapeutics, especially these attacking new molecular targets. Among several promising fungal cytoplasmic enzymes targets, glucosamine-6-phosphate synthase was found to be inhibited by amino acids or amino acid analogues. Since glucosamine-6-phosphate synthase is of a crucial importance for the survival of fungal cells, inhibitors selectively targeting this enzyme are potential antimicrobials. These include glutamine analogues N^3-(4-methoxyfumaroyl)-L-2,3-diaminopropanoic acid (FMDP) and N^3-trans-4-oxo-4-phenyl-2-butenoyl-L-2,3-diaminopropanoic acid (BADP). Despite these inhibitors in their native form exhibit some antifungal activity, their activity is limited by their poor uptake efficiency. These low molecular weight compounds, sometimes containing charged functionalities, do not diffuse through the cell membrane and on the other hand, are poorly transported by fungal amino acid permeases. Most of them cannot reach their targets since the cell membrane is impermeable for such molecules. For access to their targets, they must also compete with proteinogenic amino acids present in synthetic growth media and in mammalian extracellular body fluids, including blood serum (Andruszkiewicz et al., 1986; Chmara et al., 1986; Borowski, 2000; Milewski, 2002).

To allow internalization of amino acid enzyme inhibitors and thus enhance their potential as antimicrobials, two strategies were developed in the past. One of them, called the “warhead delivery” or “smuggling” concept, was based on the idea of incorporation of an amino acid enzyme inhibitor into a small peptide (2-4 amino acid residues), an active transport of the inhibitor-containing oligopeptide by oligopeptide permeases demonstrating a broad range of substrate specificity and the release of an active inhibitor upon the intracellular enzymatic hydrolysis (Ames et al., 1973; Lichliter et al., 1976). Several compounds exhibiting good antifungal *in vitro* activity were designed, synthesized and characterized (Andruszkiewicz et al., 1987), unfortunately, their properties under *in vivo* conditions were substantially limited by poor serum stability and a fast development of fungal specific resistance resulting from the phenotypic repression of fungal oligopeptide transport systems (Milewski et al., 1988;

Shallow et al., 1991). Another possibility is the construction of the latent esters of amino acid enzyme inhibitors, to facilitate their free diffusion through the membrane, followed by an intracellular enzymatic hydrolysis of the ester bond. Unfortunately, the antifungal activity of such constructs are not always satisfactory (Aoki et al., 1995; Zgódka et al., 2001a).

The plasma membrane enveloping cells is highly effective in its role as a selectively permeable barrier. While this phospholipid bilayer is essential to the cell survival and function, it also presents a major challenge for intracellular delivery of fungicidal cargo. Since chemotherapeutics often require intracellular access to function, identifying strategies for membrane translocation is essential. While compounds can sometimes be chemically modified to improve permeability, this often requires many interactions before translocation is achieved without sacrificing activity. Alternatively, **a synthetic transporter** can be utilized to promote cellular uptake, an approach that can be employed for a wide range of applications. Correspondingly, construction of the antifungal pro-drugs by linkage of the amino acid enzyme inhibitor as the cell membrane penetrating nano-carriers is considered as a promising approach. Pro-drugs composed of the amino acid or cyclic enzyme inhibitor linked to a nano-carrier, which would be able to cross the membrane by free diffusion or by endocytosis, may provide an entirely novel rationale for antifungal chemotherapy. Such an antifungal pro-drug construction may exhibit a broad spectrum of antimicrobial activity, due to the nonspecific mechanism of internalization of the nano-carrier and on the other hand, be active against the multiple drug resistant (MDR) microbial cells as the intracellularly released amino acid enzyme inhibitor should not be effluxed from the cells by the MDR drug exporters. **Nanomedical** approach is considered as a vital step towards discovery of novel antifungal chemotherapy methods, where a relatively small number of effective chemotherapeutics used in clinical practice is becoming further limited by the emerging fungal resistance (Perfect, 2017).

1.2 Biological background

1.2.1 Antimicrobial Resistance (AMR) – an outlook

According to European Commission, AMR is defined as the ability of microorganisms (such as bacteria, fungi, viruses, and parasites), to become increasingly resistant to an antimicrobial (such as antibiotics, antifungals, antivirals, antimalarials, and anthelmintics) to which they were previously susceptible. Natural selection and genetic mutations are the primary cause of AMR. Inappropriate use of antimicrobial agents in human/veterinary medicine and practices in healthcare/food chain are listed as the exacerbating reasons of the natural selection process leading to AMR (European Commission, 2017).

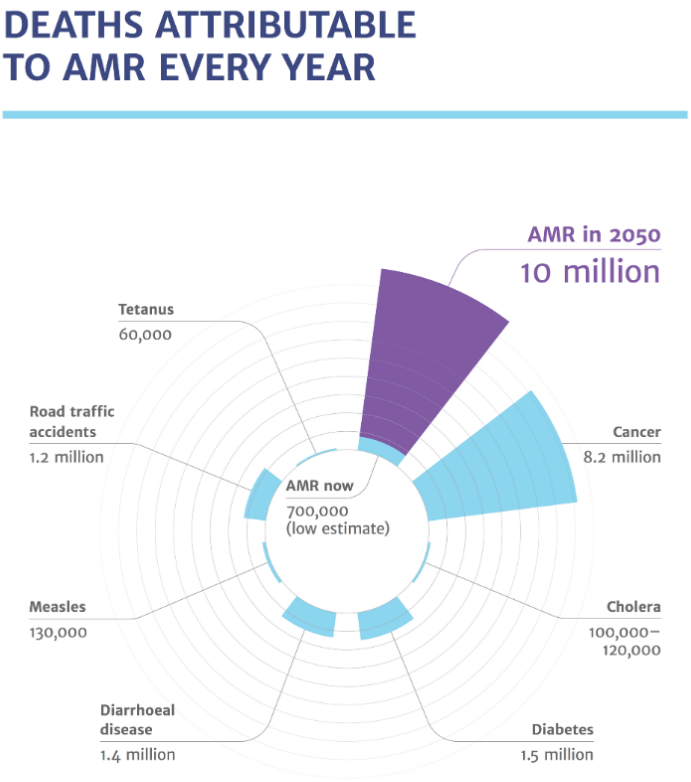

Figure 1. Infographic for deaths attributable to AMR every year (O 'neill, 2016)

On September 2016, General Assembly of the United Nations convened a **high-level** meeting on AMR in order to achieve a global consensus on the significant public health challenge possessed by the emerging AMR threat. In this high-level meeting, it was highlighted that; unlike the other medicines against other diseases, resistance to

antibiotics is the greatest and most urgent global risk that requires increased attention of all nations at regional and international levels. In the meeting, UN acknowledged that many achievements of the 20th century, such as reductions in death from infectious diseases and illnesses achieved through social/economic development are particularly challenged because of AMR. It was underlined that people, such as women giving birth, new-borns, patients with certain chronic diseases and people undergoing chemotherapy or surgery, are going to have fewer options of treatment and be vulnerable to serious life-threatening infections in the absence of effective antibiotics (UN, 2016).

"The Review on Antimicrobial Resistance" that was commissioned in July 2014 by the UK government and published in 2016, AMR each year causes 50,000 deaths in Europe and US, and 700000 deaths globally (Figure 1) (O 'neill, 2016). The report estimated that AMR will cause more deaths than cancer until 2050; in other words, 300 million premature deaths within 30 years (King, 2014).

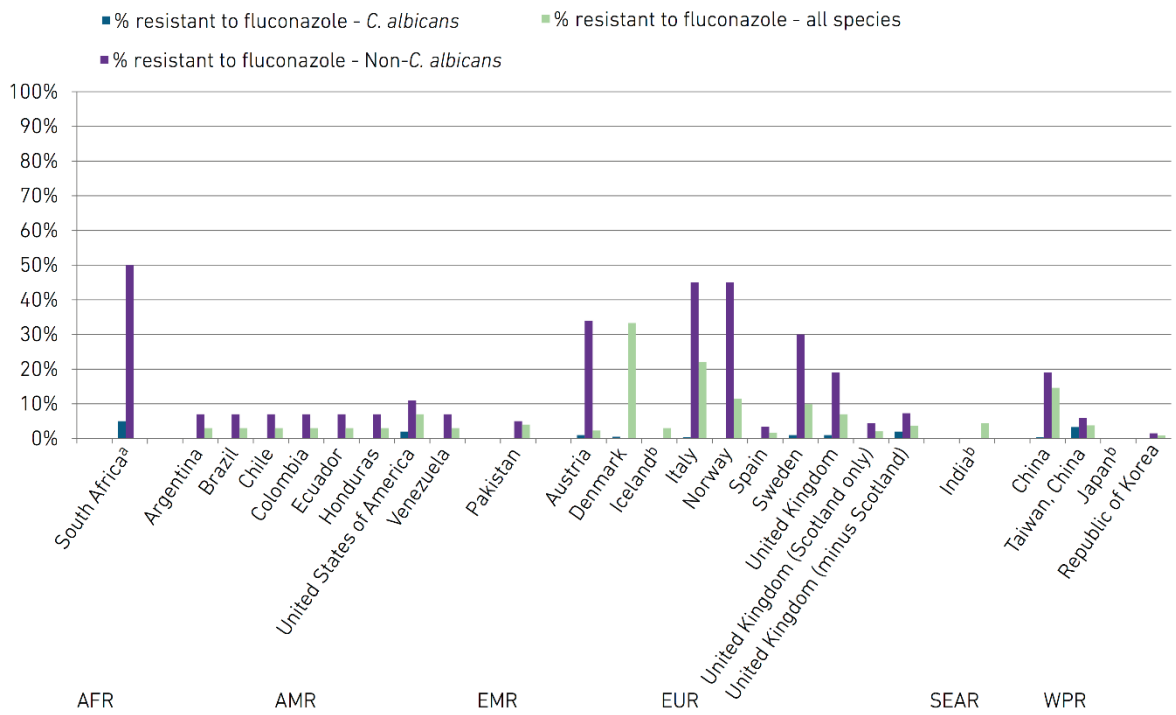

AFR, African Region; AMR/PAHO, Region of the Americas/Pan American Health Organization; EMR, Eastern Mediterranean Region; EUR, European Region; SEAR, South-East Asia Region; WPR; Western Pacific Region.

a. No data on overall resistance to fluconazole.
b. No data on per cent resistant by species.

Figure 2. Graphical presentation of resistance surveillance data on *Candida* and non-*Candida* infections (WHO, 2014).

WHO's global report on antimicrobial resistance surveillance published in 2014 covers various kind of vital AMR cases such as tuberculosis, malaria, HIV, influenza. Additionally, an equally important chapter of the report highlights the AMR of the antifungal drugs in Candidiasis (WHO, 2014). Report highlights the current AMR surveillance data from around the world that raises concerns with the current resistance trends of microbes to fluconazole where elevated incidents in developed countries (Figure 2).

1.2.2 Infections caused by *Candida* species: Candidiasis

Candidiasis is a generic term that is used to describe fungal human infection caused by opportunistic *Candida* genus. "Systemic" or "invasive" candidiasis (disseminated candidiasis) having an acute or chronic course can cause infections to multiple organs. Prolonged superficial candidiasis morbidity is the leading cause of invasive candidiasis (Sychrová, 2016).

Among 154 species of *Candida* genus, *Candida albicans* is known as the most pathogenic type. Its pathogenicity arises from the impairment of patients' immune functions that lead to reproduction of fungus by colonization in internal organs. *Candida albicans* is the primary cause of "superficial Candidiasis" involving skin/oral infections (oropharyngeal candidiasis. 100% of cases) and female genital infection (*Candida* vulvovaginitis. 90% of cases) (Zierhut et al., 2016; Kumar and Jha, 2017). On the other hand, nosocomical blood stream infections caused by *Candida* genus is called Candidemia.

Although *Candida albicans* is the predominant cause of disseminated candidiasis in 50-70% of the cases in clinical settings, longitudinal studies shows that the epidemiology of the *Candida* infections has changed and the non-Albican species were also involved in candidiasis (Edwards, 2015; Zierhut et al., 2016). HIV+ and intensive care unit patients, together with the patients undergoing cancer chemotherapy and organ transplantations are especially prone to morbidity by systematic candidiasis; which eventually results in 50-100% mortality (Kumar and Jha, 2017).

A comprehensive surveillance study carried out in 2004 on 24,179 nosocomial bloodstream infections (BSI) occurred in US hospitals revealed that BSI were the 10th leading cause of mortality. The study pointed out 78% increase in age-adjusted mortality rate caused by BSI in previous 2 decades from the date of study. Among the 1890 *Candida* isolates causing nosocomial BSI, 54% of the cases were caused by *Candida albicans*; which was followed by *Candida glabrata* (19%), *Candida parapsilosis* (11%), and *Candida tropicalis* (11%). Strikingly, the mortality caused by *Candida krusei* infections was highest (59%) and lowest for *Candida albicans* (37%) (Wisplinghoff et al., 2004). Most recent data acquired from multiple reports also confirms that, in the current epidemiological state, *Candida albicans* were the leading cause of in US; but also in Europe and Middle East. However, among the most common non-albican *Candida* (NAC) species causing invasive candidiasis and candidemia in US, *Candida krusei* was the 4th most common (accounting approximately 2.7% of NAC species isolated across the US) (Whaley et al., 2017). On the other hand, a European based prospective study (AmarCand) revealed that *Candida glabrata* was the most predominant NAC species after *Candida albicans* (Montravers et al., 2011), which was also concluded by Zavrel *et al.* (Zavrel and White, 2015). Number of reports confirms the steady emergence of NAC species (*Candida parapsilosis*, *Candida tropicalis*, *Candida glabrata* and *Candida krusei*) in last decade as the leading cause of the >50% of the candidemia (Pappas et al., 2015; Kaaniche et al., 2016; Arendrup and Patterson, 2017; Berkow and Lockhart, 2017) and ~95% of the all candidemia infections along with *Candida albicans* (Zavrel and White, 2015). Similarly, clinical guideline for the management of Candidiasis published by Infectious Disease Society of America (IDSA) in 2016 pointed out that >90% of the invasive candidiasis incidents were caused by *Candida albicans*, *Candida parapsilosis, Candida tropicalis, Canida glabrata* and *Candida krusei* (Pappas et al., 2015).

1.2.2.1 Clinically used anti-*Candida* drugs and their cellular targets

Antifungal drugs used to cure fungal infections can be generally classified under two groups by their general mode of action: “fungicidal” that aim to kill fungi or “fungistatic” that are used to inhibit the growth of fungi. Antifungal drug development

is usually based on targeting essential fungal cell viability functions, which are specific to fungal cells and not present in the host or significantly different than the host.

Antifungal drugs currently in use at clinics are categorized by their cellular target under two main classes: **echinocandins that target the fungal-cell wall;** and **azoles, polyenes and allylamines that target the fungal-specific sterol cell membrane components**. Additionally, **fungal drug 5-flucytosine alone represents a third class by specifically targeting the metabolism of fungal-specific pyrimidines in DNA and RNA synthesis**. On the other hand, cell-membrane targeting antifungals are categorized under three subgroups by the enzyme that they inhibit in the sterol biosynthetic pathway: i) HMG-CoA reductase targeted by statins that belongs to polyene class; ii) squalene epoxidase targeted by allylamines and; iii) anosterol 14α-demethylase targeted by azoles. Non-statin polyenes, such as Amphotericin-B, directly target ergosterol component in fungal membranes and alter the membrane structure. Echinocandins as the only cell-wall targeting class of antifungals, inhibit β(1→3) glucan synthase, an enzyme involved in biosynthesis of the main component of the cell wall (β-1, 3-glycan) in many (but not all) human pathogenic fungi (Zavrel and White, 2015; Sychrová, 2016).

Targeting sterols as membrane components or sterol biosynthetic pathways directly influence the membrane rigidity, stability and integrity by destabilization of the membrane to increase permeability and susceptibility of antifungal agents. Targeting sterols either induce cell death or the cell growth. On the other hand, inhibition of cell-wall enzyme β(1→3) glucan synthase makes the cells prone to osmotic forces that results in cell lysis (Sychrová, 2016).

Azoles are used as the primary agents in treatment of fungal infections because other classes of antifungals (polyenes, allylamines, echinocandins and 5-flucytosine) are costly and cause increased side-effects. Since azoles exhibit only fungistatic effects, well-functioning host immune system is essential to eliminate the pathogen. Thus, fungal pathogens are refractory to azole treatment in immunocompromised patients because of the malfunctioning immune defense mechanisms (Zavrel and White, 2015).

According to recommendations of IDSA, despite the number of randomized drug trials have been carried out to find the most effective antifungal treatment, there is no single trial demonstrating advantage of one therapeutic agent over another to cure

candidemia or invasive candidiasis. Geographic -"center-to-center" and "unit-to-unit"-variability and distribution of *Candida* species plays an important role in making critical therapeutic decisions specific to local epidemiology knowledge and drug resistance rates. IDSA-recommends pharmacologic considerations for treatment of invasive Candidiasis compromise four *(4)* categories: i) four *(4)* different formulation of amphotericin B from polyenes class (amphotericin B deoxycholate, liposomal amphotericin B, Amphotericin B lipid complex and Amphotericin colloidal dispersion); ii) azoles (fluconazole, itraconazole, voriconazole, posaconazole, isavuconazole); iii) echinocandins (caspofungin, anidulafungin, micafungin) and iv) flucytosine (Pappas et al., 2015). Notably, Fluconazole, Voriconazole, itraconazole, flucytosine and Amphotericin B were listed in the 20th WHO Model List of Essential Medicines to cure fungal infections (WHO, 2017). Among the above listed drugs by IDSA, azole group found to be active against most of the *Candida* species however each of the listed drugs were less active against *Candida glabrata* and *Candida krusei*. Voriconazole was reported to be effective against both invasive and mucosal Candidiasis and especially used for patients infected by *C. krusei* and fluconazole-resistant, Voriconazole-susceptible *Candida glabrata*. It was pointed out that echinocandins are available only as parenteral preparations however effective against most *Candida* species including *Candida glabrata* and *Candida krusie* with low MICs, except *Candida parapsilosis*. Nevertheless, some resistant strains of *Candida glabrata* were the cause of treatment failure in recent case series. At last, flucytosine was reportedly effective against most *Candida* species except *C. krusei* (Pappas et al., 2015).

1.2.2.2 Emerging multi-drug resistance (MDR) problem in Candidiasis

Since the clinically available antifungals, including the largest and most widely used azole class, are mostly fungistatic, pathogenic fungal species develop tolerance (acquired resistance) to these drugs. Acquired resistance may be consequence of the cell transformation to more resistant species/strain of *Candida* by random mutations. Such mutations alter the phenotype of cells to become resistant in the presence of the drug. For instance, genetic changes caused by mutations may result in over expressions of protein efflux pump proteins or mitotic recombination in enzyme targets of antifungal

agents (Kumar and Jha, 2017). On the other hand, intrinsic (primary, not acquired) resistance is an inherent characteristic of almost all representative of species that leads to clinical failure. Examples of intrinsically resistant species are *Candida krusei* being unsusceptible to fluconazole; or *Candida auris* being susceptible to several antifungal drugs (echinocandins, azoles, polyenes) with elevated minimum inhibitory concentration (MIC) requirements (Arendrup and Patterson, 2017). Resistance mechanisms are not genetically exchanged between *Candida* species. Emergence of acquired resistance is therefore a consequence of the decision on which antifungal will be used to treat an individual patience. Additionally, although more rarely occurs, resistance may also be a consequence of horizontal transmission of resistant strains between patients (Arendrup and Patterson, 2017).

The rates of systematic fungal infections are increasing primarily due to a rise in immune suppressive disorders that leads to growing population of immune compromised patients. However, there are only limited number of antifungals to treat systematic infections (Butts et al., 2017). Among the all clinically available antifungals, only fluconazole and echinocandins are recommended as first-line agents for invasive candidiasis. However, shift of fungal infection epidemiology toward intrinsically fluconazole resistant species makes fungal infections difficult to treat (Arendrup and Patterson, 2017; Berkow and Lockhart, 2017).

Due to fact that the different drugs have different targets and mode of actions on fungal cells, combinatory therapy by administering multiple drugs simultaneously is a widely adopted approach. Drug combinations are usually used to achieve synergetic effects between the drugs, where both cell wall and cell membrane are targeted in the same time. The idea behind the combinatory therapy is damaging cell wall to increase the efficacy of cell membrane targeting drugs or allowing the other inhibiting agents to reach their intracellular targets (Prasad et al., 2016). Development of simultaneous tolerance to multiple mechanisms over time is the primary cause of the emerging "multi-drug resistance (MDR)" in clinics. Taking into consideration that multi-drug resistance is developing faster than the discovery of new antifungals, emergence of MDR require continues development of novel antifungal drugs with broad spectrum and/or specific mode of action (Prasad et al., 2016; Kumar and Jha, 2017).

1.2.2.3 State of fungal infection treatment in the MDR era – call for action

It is almost a consensus that currently available antifungal agents are no more capable of keeping fungal infections under control. As a result of the current antifungal-use regime, the very limited number of distinct targets of antifungals have been already exploited; which eventually lead the increase of cross-resistance. Fungal infection caused mortality rates are unacceptably high especially as a consequence of more frequent occurrence of the intrinsically resistant non-*Albican* strains. On the other hand, use of current antifungals in increasing dosages to meet the needs of fungal infection treatments often results in acute or/and chronic toxicity. Consequently, development of new drugs that either synergistically work along with the current fungistatic agents and transform them into fungicidal; or act solely on their own novel cellular targets is crucial (Zavrel and White, 2015; Butts et al., 2017; Campoy and Adrio, 2017).

According to most recent review on the current state of clinical fungal infection treatment decisions and antifungal pipeline, the current mortality rates are too high to be tackled with currently available antifungals (Perfect, 2017). According to review from Perfect, several issues must be addressed to meet the specific needs of fungal infection treatment and antifungal development: ***i)*** as the consequence of too long treatment courses currently followed using common antifungals, chances of reaching immediate-term fungicidal activity is poor, and thus the emphasis in future antifungal development must be put on achieving rapid fungicidal activity or ultimate fungistatic effects; ***ii)*** in the current repertoire of the antifungals, there are simply no agents that can adequately tackle with certain fungal strains. Highly-resistant fungi, such as *Candida auris,* especially requires **the development of broad-spectrum antifungals**; ***iii)*** resistance against especially azole and echinocandin class antifungal agents developing fast and thus combination therapies must be optimized to reduce the emergence of MDR; ***iv)*** immunosuppressed patients who are admitted to hospitals for severe diseases usually cannot tolerate additional organ toxicities caused by other treatments for additional underlying infections, so drug-drug interactions must be carefully taken into account during multiple treatments. This is especially important for azole treatment, which is

reported to be causing negative **side (toxic) effects** in many individuals through drug–drug interactions.

In comparison to development of antimicrobial drugs in general, antifungal development is challenging because eukaryotic fungi involve numerous cellular mechanisms in common with mammalian cells. Consequently, identification of fungal-specific cellular targets exhibiting minimal similarity to targets among human proteins has been the main focus in anti-fungal development (Campoy and Adrio, 2017). However, despite the fact that almost all non-*Albican* species exhibit similar resistance mechanisms with *Candida albicans*, unexpected differences between the species are plausible. Unknown fluconazole resistance mechanism in emerging *Candida spp*., especially *Candida auris* as a global threat along with *Candida krusei* or *Candida glabrata*, are alarming examples of this fact (Kaaniche et al., 2016; Berkow and Lockhart, 2017). Ineffectiveness or lower potency of the antifungals against non-*Albican* spp. is the consequence of the fact that the most antifungals were primarily developed to treat *Candida albican* infections (Zavrel and White, 2015). Relatedly, due to obvious challenges in developing **broad-spectrum** antifungals against multiple pathogens, development of **narrow-spectrum** drugs against specific targets in specific species is suggested to be more effective approach. Nevertheless, it is taken into consideration that the approval of a drug, from discovery to extensive clinical tests, is usually a decades-long process, there is simply no time left for such long development and approval processes to be initiated for individual pathogens in the era of MDR. However, "-omics" approach (Milewski, 2017), which focuses on the determination of unique gene-drug interactions in particular pathogens by genome-wide screening of potential targets in a particular pathogen, is a promising new field of research that may one day lead to more potent antifungals against invasive infections (Campoy and Adrio, 2017).

When the development of new antifungal agents are considered, selective toxicity (highest antimicrobial activity and lowest toxicity to mammalian host) is the most important feature that a good chemotherapeutic agent must have (Milewski, 2017). According to Milewski, five major scenarios that could be expected from an antimicrobial drug with a good selective toxicity in descending order are the ones: ***i)*** aiming a target which is essential for survival of pathogen however absent from the host; ***ii)*** aiming a target existing in both pathogen and the host however possessing substantial

structural differences that could give rise to the differential drug-target affinity; ***iii)*** being uptaken selectively only by the pathogen; ***iv)*** being in the form of a prodrug that is specifically activated in pathogen but not in the host cells; ***v)*** aiming qualitatively different inhibition of the target in pathogen and the host cells. Despite scenario "***i"*** is the most desirable one to be achieved, Milewski points that fungi are evolutionarily closer to humans than any other microbial pathogens. This situation limits the possible discovery of molecular targets constituting a proper basis for selective toxicity. Consequently, the scope of new targets molecular targets is left limited to exploitation of other four (4) scenarios.

1.2.3 Glucosamine-6-phosphate synthase — a potential new target in antimicrobial chemotherapy

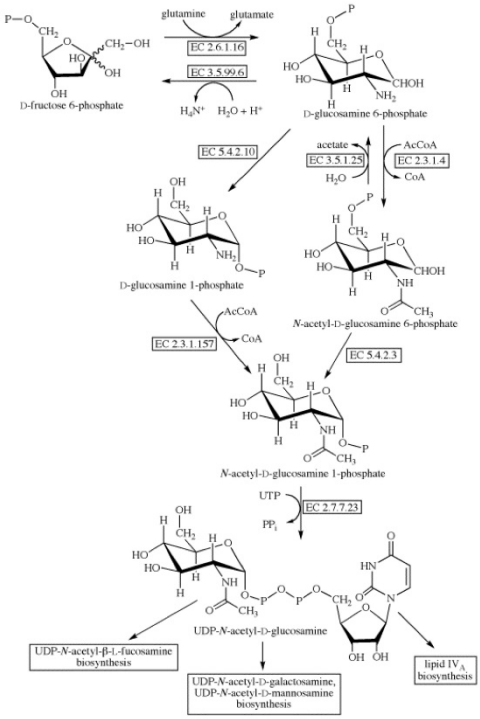

Figure 3. Metabolic pathway leading to UDP-GlcNAc (image acquired from IUBMB website).

Glucosamine-6-phosphate (GlcN-6-P) synthase, also known as L-Glutamine: D-fructose-6-phosphate amidotransferase, is classified by International Union of Biochemistry and Molecular Biology as EC 2.6.1.16 as the only member of the amidotransferase subfamily of enzymes. GlcN-6-P synthase is present in all known prokaryotic and eukaryotic organisms, which displays an amino-independent activity.

GlcN-6-P synthase plays an important role in biosynthesis of amino sugar-containing macromolecules (Figure 3) by catalyzing the first step in the metabolic pathway leading to formation of uridine 5'-diphospho-N-acetyl-D-glucosamine (UDP-GlcNAc) (Milewski, 2002).

L-glutamine has been previously identified as a substrate of GlcN-6-P synthase; and glucosamine-6-phosphate (GlcN-6-P) and glutamate as the products of this enzymatic reaction (Figure 3). GlcN-6-P synthase does not display any ammonia-dependent activity. The reaction it catalyzes is irreversible, and its catalytic activity does not require ATP or any cofactor. Among sixteen different glutamine-dependent enzymes identified in amidotransferase family of enzymes to date, GlcN-6-P synthase is unique, as the only enzyme accepting L- glutamine as the only amino-donating substrate. Unlike the other amidotransferases that utilize exogenous ammonia as an alternative to L-glutamine nitrogen donor, GlcN-6-P synthase excepts only L-glutamine as an amino donor. This fact is important to distinguish "GlcN-6-P synthase" from "GlcN-6-P isomerase" which can catalyze the formation of GlcN-6-P from Fru-6-P and ammonia. Despite the formation of glucosamine-6-P is the main activity of GlcN-6-P synthase, the enzyme catalyzes the hydrolysis of glutamine in the absence of Fru-6-P, however in the absence of glutamine, it demonstrates phosphoglucose isomerase-like activity. When both substrates are present, these ''side'' activities are not detectable. Formation of GlcN-6-P has been described as a three-step reaction that involves hydrolysis of glutamine, transfer of the released ammonia to fructose-6-phosphate and isomerisation of fructosimine-6-phosphate. Although the isomerazation step of Fru-6-P has reached to a consensus, details of glutamine hydrolysis and ammonia transfer have not been well-established yet (Milewski, 2002).

UDP-GlcNAc serves as an activated form of N-acetylglucosamine. It is responsible from chitin formation in fungi; and glycoproteins, glycosaminoglycans and mucopolysaccharides formation in mammals by incorporating nucleotide sugar (UDP-GlcNAc) into these macromolecules. As an enzyme responsible from the biosynthesis of important cell wall component, chitin, GlcN-6-P synthase inhibition is lethal for fungal cells. This especially important when it is considered that, chitin content of the dimorphic fungi (such as *Candida albicans*) gets five-folds higher during its morphological transition from mycelial form to blastospore form (Milewski, 2002).

In comparison to fungi, activity of GlcN-6-P synthase in mammals is more complex. Tests carried out on different organ tissues obtained from rats revealed that GlcN-6-P synthase activity was the highest in submaxillary and sublingual glands, colon, thymus, testis, and liver; while it was the lowest in muscle, erythrocytes and kidney. Despite its importance as an essential enzyme, its short-term inhibition is not necessarily lethal for the whole organism (Milewski, 2002).

1.2.3.1 Inhibitors of GlcN-6-P synthase from *Candida albicans* – 35 years of a systematic study

It was long known that number of glutamine analogues were powerful inhibitors of GlcN-6-P synthase (Ghosh et al., 1960; Anderson et al., 1964; Winterburn and Phelps, 1971).

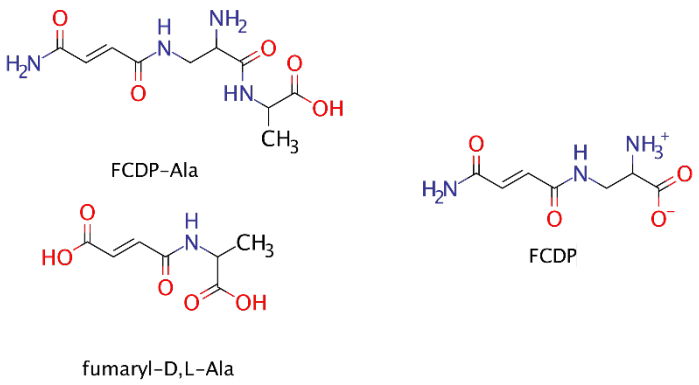

Figure 4. Fumarylcarboxyamido-L-2,3-diaminopropionyl-L-alanine (FCDP-Ala) and fumaryl-D,L-alanine (left); N^3-fumarylcarboxyamido-L-2,3-diaminopropionic acid (FCDP) and FCDP-Ala (right).

Fumarylcarboxyamido-L-2,3-diaminopropionyl-L-alanine (FCDP-Ala), a dipeptide antibiotic and fumaryl-D,L-alanine, an analogue of glutamine, isolated from *Streptomyces collinus* (Figure 4), has been well-known to be exhibiting reversible activity against *Salmonella gallinarum* in the presence of glucoseamine and N-acetylglucosemine (Molloy et al., 1972). Based on these preliminary researches, Chmara et al. further postulated the findings of Molloy *et al.* that fumarylcarboxyamido-L-2,3-diaminopropionic acid (FCDP) as a N-terminal amino acid (Figure 4) might have been

formed by cleavage of FCDP-Ala upon the activity of intracellular peptidases; and could have eventually inactivated GlcN-6-P synthase as a glutamine analogue (Chmara et al., 1984). Using cell-free extracts of GlcN-6-P synthase from Salmonella Typhimurium, Chmara et al. proved that the FCDP had higher binding activity to the enzyme active site than glutamine, in an irreversible manner. Additionally, they showed that FCDP activity was ~8-folds lower in the absence of fructose-6-phosphate and it was diminished when the high amounts of glutamine (1 mM) or L-glutamic acid-monohydroxamate (5 mM) were present.

Several synthetic analogues of FCDP were later reported in search for more active analogues (Table 1), where cell-free extracts of GlcN-6-P synthase from *Salmonella typhimurium*, *Saccharomyces cerevisiae* and *Candida albicans* were used (Milewski et al., 1985; Andruszkiewicz et al., 1986). In these studies, N^3-(4-methoxyfumaroyl)-L-2,3-diaminopropanoic acid hydrochloride (FMDP) was found to be the most active analogue with IC_{50} values of 15 μM against *Salmonella typhimurium*, 21 μM against *Saccharomyces cerevisiae*, where FCDP exhibited IC_{50} values of 100 μM, 82 μM, respectively (IC values for other analogues from same studies are shown Table 2).

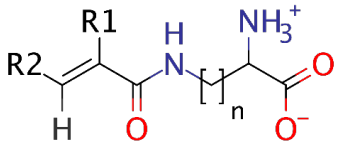

Abbreviation	n	R_1	R_2
FCDP	1	H	-C=O(NH_2)
FMDP	1	H	-C=O(OCH_3)
FDP	1	H	-C=O(H)
FMDB	2	H	-C=O(OCH_3)
AADP	1	H	-C=O(CH_3)
MMDP	1	CH_3	-C=O(OCH_3)
CRDP	1	H	-CH_3

Table 1. Molecular scheme showing the general structure of GlcN-6-P synthase inhibitors and the table showing the derivatives.

	IC_{50} (μM)	
compounds	*Salmonella typhimurium*	*Saccharomyces cerevisiae*
FCDP	100	82
FMDP	15	21
FDP	22	Not measured
FMDB	56	100
AADP	inactive	500
MMDP	inactive	inactive
CRDP	inactive	inactive

Table 2. IC_{50} values of compounds against *Salmonella typhimurium* and *Saccharomyces cerevisiae.*

After the identification of FMDP as the most effective glutamine analogue, Andruszkiewicz *et al.* studied the effectiveness of the FMDP-dipeptide structures (Table 3) against *Candida albicans, Escherichia Coli, Staphylococcus aureus, Bacillus pumilus* and *Shigella sonnei* (Andruszkiewicz et al., 1987). The idea behind incorporating FMDP into peptidic forms was using toxic FMDP (which would be impermeable to cells due to its toxicity) as a "warhead" component and facilitating its delivery upon the hydrolysis of peptide chains by intracellular peptidase activity; which has been also known as "smuggling", "portage", or "illicit" delivery/transport systems (Ames et al., 1973; Fickel and Gilvarg, 1973; Cheung et al., 1983; Kingsbury et al., 1983, 1984). In this study, it was shown that MIC values for the peptides containing aliphatic side-chains (Leu, Nva, Nle, Ala, Met) and the ones containing FMDP warhead at the C-terminal positions were substantially lower, although existence of aliphatic amino acids are generally known to be active against the bacteria or fungi (Table 3). When FMDP was at N-terminal position (such as FMDP-Met), anti-Candidal activity was 2-fold lower than its C-terminal isomer (Met-FMDP). On the other hand, Nva-FMDP was found to be the most active peptide with MIC values of 0,4 μg/ml against *Candida albicans* and *Bacillus pumilus,* whereas Lys-FMDP exhibited no anti-Candidal activity below 200 μg/ml. However, when Leu-FMDP and Nva-FMDP and FMDP-Met were compared to commonly used antifungal agents (nikkomycin, 5-fluorocytosine, clotrimazole and miconazole) against *Candida albicans* by disk diffusion method, Leu-FMDP and Nva-FMDP exhibited higher activity than the known drugs (Table 4). More importantly, by using an antagonistic experiment

using an inhibitory peptide, a non-inhibitory peptide or *N*-acetylglucosamine, Andruszkiewicz *et al.* concluded that transport of the peptides into cells were mediated peptide permeases and delivery of FMDP by peptidase mediated hydrolysis of peptides.

	MIC, µg/ml				
compounds	*Candida albicans*	*Staphylococcus aureus*	*Bacillus pumilus*	*Shigella sonnei*	*Escherichia Coli*
Ala-FMDP	0.8	50	1.56	3.12	100
Met-FMDP	0.8	50	3.12	3.12	100
Gly-FMDP	12.5	>200	25	50	>100
Val-FMDP	1.56	12.5	0.8	1.56	100
Leu-FMDP	0.8	12.5	1.56	1.56	100
Phe-FMDP	12.5	100	6.25	12.5	>200
Tyr-FMDP	50	100	12.5	25	>200
Nva-FMDP	0.4	12.5	0.4	3.12	100
Nle-FMDP	0.8	25	0.4	3.12	100
Abu-FMDP	1.56	25	0.8	6.25	100
Lys-FMDP	>200	>200	100	>200	>200
FMDP-Gly	>200	>200	>200	>200	>200
FMDP-Val	6.25	100	>200	>200	>200
FMDP-Leu	3.12	100	>200	>200	>200
FMDP-Phe	.156	>200	>200	>200	>200
FMDP-Tyr	25	>200	>200	>200	>200
FMDP-Nva	6.25	100	>200	>200	>200
FMDP-FMDP	>200	>200	>200	>200	>200
FMDP-Ala	3.12	>200	>200	>200	>200
FMDP-Met	1.56	>200	>200	>200	>200
FMDP	>200	>200	>200	>200	>200

Table 3. Activity of dipeptides against selected microorganisms.

	Zone size	
compounds	20 µg/disk	10 µg/disk
Leu-FMDP	41	39
Nva-FMDP	42	40
FMDP-Met	35	31
Nikkomycin X/Z	28	25
5-fluorocytosine	39	35
clotrimazole	21	17
miconazole	32	27

Table 4. Activity of selected antifungal agents and FMDP dipeptides against *Candida albicans* (ATCC 26278) by inhibition zone tests

Peptide	Rates of transport (nmol/min per mg dry weight)			
	Y forms[a]		M forms[b]	
$(Ala)_2$	7.5	5.7	2.0	2.4
Met-Leu	3.15	-	1.7	-
Leu-Gly	1.85	-	1.5	-
Leu-Val	2.9	3.2	1.5	1.8
$(Ala)_3$	6.0	4.6	13.0	11.7
Gly-Leu-Tyr	5.9	4.4	8.9	8.7
Leu-Gly-Gly	5.05	4.7	3.2	2.8
$(Met)_3$	5.4	-	7.2	-
$(Ala)_4$	4.3	5.4	9.5	9.2
Gly-Phe-Ala-Ala	4.8	-	7.2	-
$(Ala)_5$	2.9	-	4.5	-
$(Met)_6$	2.0	-	2.9	-
$(Ala)_3$-Tyr-$(Ala)_3$	<0.1	-	<0.1	-

[a]pH=4.5, 30°C, pH 6.5 37°C; [b]pH= 6.8, 37°C, pH 4.5 30°C

Table 5. Rates of peptide transport in yeast and mycelial forms of *Candida albicans* ATCC 26278. Initial peptide concentration was 100 uM. The residual peptide concentration in filtrates was assayed by the TNBS method

Peptide [a]	MIC, µg/ml				Transport rate (nmol/min per mg)	cleavage rate (nmol/min per mg)
	Candida albicans (ATCC 262)	*Candida albicans* [b]	*C. epidermidis* (OBS 6023)	*S. cerevisiae* (ATCC 9763)		
Leu-FMDP	0.8	0.25	100	62.5	1.8	15.4
Nva-FMDP	0.4	0.1	75	-	2.0	35.3
Ala-FMDP-Ala	0.75	0.25	80	37.5	0.9	5.4
Met-FMDP-Met	0.3	0.15	110	50	2.0	4.8
Met-Ala-FMDP	0.75	0.25	125	7.5	1.2	15.2
Met-Met-FMDP	0.25	0.1	125	37.5	1.4	4.9
Met-Nva-FMDP	0.125	0.05	130	7.5	1.4	17.3
FMDP-Met-Ala	0.25	0.1	50	15	1.0	4.9
FMDP-Met-FMDP	0.75	0.25	75	150	1.4	3.0
Sar-Nva-FMDP	1.0	0.5	130	150	-	-
Nva-Nva-FMDP	0.1	0.05	125	12.5	1.7	20.9
Nva-FMDP-Nva	0.05	0.01	125	50	2.9	8.9
Lys-Nva-FMDP	0.025	0.01	125	-	3.6	51.0
Met_3-FMDP	0.75	0.25	75	100	0.9	23.7
Met-$FMDP_2$	0.75	0.25	125	150	1.9	10.0
FMDP-Met_2-FMDP	0.25	0.25	75	75	1.2	5.8
Met_4-FMDP	0.5	0.25	75	37.5	1.3	18.8

[a] tested as hydrochlorides; [b] sixteen clinical strains

Table 6. Antifungal *in vitro* activities (left); rate of transport and intracellular cleavage of FMDP peptides in *Candida albicans* ATCC 26278 (right)

A significant work related to peptidic forms of FMDP was later carried out by Milewski *et al.,* where they identified two different peptide permeases in *Candida albicans,* playing important role on size-dependent uptake of FMDP peptides (Milewski et al., 1988). It was shown that, there are two different permeases; the one responsible

from the transport of di- and tri-peptides and the another one responsible from tri-, tetra-, penta- and hexa-peptides; whereas the transport rate for the latter type of permeases was 2-folds higher for mycelial form of *Candida albicans* than the yeast form (Table 5). Another significant finding of the same study was the identification of cross-resistance and peptide transport capabilities of the spontaneous mutants resistant to FMDP. Briefly, dipeptide transport defects were detected against transport of dipeptides in Nva-FMDP-resistant mutants while the uptake efficiency of tripeptides was reduced for these mutants. No susceptibility to potentially toxic peptides was observed for Met-Met-FMDP-resistant mutants. Tetra-peptides were no more taken by the Met-Met-Met-FMDP resistant mutants. While the di-peptide uptake was not affected, tripeptide transport was reduced. Nevertheless, the study demonstrated that the tripeptides would be the most appropriate delivery form for transport of FMDP since both permeases identified in *Candida albicans* were able to transport tripeptides.

Correspondingly, in the following study, Andruszkiewicz *et al.* studied a larger variety of tripeptides in comparison to tetra- and penta-peptides and tested them against the clinical isolates and the standard strains of *Candida albicans* (Andruszkiewicz et al., 1990a). The study demonstrated that the tested peptides, with MICs ranging from 0,025-1 µg/ml, showed excellent activity against the all tested strains of the *Candida albicans* (Table 6).

Peptides tested (10 µg/ml)	**Number of colonies**
Nva-FMDP	40
Leu-FMDP	30
Met-Met-FMDP	3
Nav-Nva-FMDP	2
Lys-Nva-FMDP	2
Met_3-FMDP	12

Table 7. Number of resistant colonies obtained from 10^5 inoculum cells of *Candida albicans* ATCC 26278

Among the tested peptides, Lys-Nva-FMDP tripeptide showed the highest activity with MICs= 0,025 µg/ml for standard *Candida albicans* strain ATCC 26278) and 0,01 µg/ml for clinical isolates. Such a high activity of Lys-Nva-FMDP was associated with the high rates

of uptake into the cells compared to other peptides tested (Table 6). More importantly, the study pointed out that the number of the resistant colonies were remarkably reduced in comparison to di- and tetra-peptides used as comparison (Table 7).

Andruszkiewicz *et al.* reinvestigated effectiveness of di- and tri-peptides in N^3-iodoacetyl derivative of L-2,3-diaminopropanoic acid [A_2pr(IAc)] derivatized form (Table 8), since A_2pr(IAc) itself was not active against whole microbial cells (Andruszkiewicz et al., 1990b). The study showed that the tri-peptides were more potent against the selected fungal strains, where the peptide with N-terminal Lysine residue was the most effective against *Candida albicans* with MIC value of 2,5 µg/ml. Substantiating the pervious study (Andruszkiewicz et al., 1990a), lysine and norvaline residues in peptide molecules was confirmed to be essential for efficient transport into fungal cells. Essentiality of norvaline residue was also proven by the structure-activity relationship studies, where the norvaline transport and cleavage rates outperformed the methionyl peptides (Table 9). Notably, study demonstrated that the MIC values obtained for A_2pr(IAc) peptides were higher than the values previously obtained for FMDP peptides and they exhibited lower antifungal activity. Despite the high enzyme inhibitory effects of the A_2pr(IAc), moderate antifungal activities obtained for A_2pr(IAc)-peptides were associated with the existence of highly reactive electrophilic group of A_2pr(IAc) that might have reacted with unspecific targets inside the cells.

	MIC, µg/ml			
Strain	**Nva-A_2pr(IAc)**	**A_2pr(IAc)-Nva**	**Nva-Nva-A_2pr(IAc)**	**Lys-Nva-A_2pr(IAc)**
Staphylococcus aureus 163 J	1	4	4	2
Staphylococcus epidermidis 154 J	4	16	8	8
Streptococcus faecalis CCM 1875	8	32	2	2
Streptococcus 8-haemolyticus A 800	4	16	2	2
Microsporum luteus NCTC 2665	16	32	4	32
Corynebacterium sp. 239	2	2	2	8
Bacillus purnilus CCM 1697	0.25	2	1	4
Geotrichum candidum	15	17.5	10	5
Candida albicans 4477	10	15	7.5	2.5
Candida tropicalis	12.5	15	8	3
Trychophyton nanum	7.5	10	5	2
Rhizopus arhizus	>50	>50	>50	>50
Aspergillus nidulans 590 Fungi	>50	>50	>50	>50

Table 8. Antimicrobial in vitro activity of some peptides containing A_2pr(IAc) to bacterial and fungal strains

Peptide	Transport rate (nmol/min per mg)	cleavage rate (nmol/min per mg)
Nva- **A_2pr(IAc)**	1.3	32.4
Met- **A_2pr(IAc)**	1.9	31-6.5
A_2pr(IAc) -Nva	0.4	27.0
Nva-Nva- **A_2pr(IAc)**	1.0	18.3
Met-Nva- **A_2pr(IAc)**	0.5	3.8
Lys-Nva- **A_2pr(IAc)**	4.4	17.1

Table 9. Rate of Transport and Intracellular Cleavage of Peptides in *Candida albicans* ATCC 26278

Because of the poor diversity of known anticandidal agents and thus, the lack of useful data on rational design of synthetic anticandidal agents at the time of study, Milewski *et al.* especially focused on the FMDP dipeptides in order to establish the factors determining their biological activity (Milewski et al., 1991). In this study, transport and the intracellular cleavage rates of twenty-one (21) different FMDP dipeptides were determined along with their MICs (Table 10). When the -log MIC data was expressed as a function of transport and intracellular cleavage velocities, a statistically significant correlation was found. The higher regression slopes obtained for transport velocity relations suggested that the transport velocity is a more important determinant of peptides' anticandidal activity than the intracellular cleavage velocity. Notably, Lys-FMDP was an exception by exhibiting low cleavage rates despite high transport velocity. However, in general, study pointed out that the X-FMDP peptides were more rapidly taken than the FMDP-X peptides, resulting in higher anticandidal activity for X-FMDPs. Relatedly, Nva-, Nle-, Leu- or Lys- peptides were more rapidly transported than the Gly-, Phe-, Tyr- peptides. Nva-FMDP and Nle-FMDP outperformed the other peptides with excellent transport and velocity rates and proved to be the best anticandidal candidates.

Peptide	Transport rate (nmol/min/mg)	Intracellular cleavage rate (nmol/min/mg)	MIC (μg/ml)
Gly-FMDP	1.0	0.5	50
Ala-FMDP	1.3	12.5	3.12
Abu-FMDP [a]	2.4	17.5	0.78
Nva-FMDP	2.0	25.3	0.20
Val-FMDP	1.8	9.1	0.78
Nle-FMDP [a]	2.0	17.8	0.20
Leu-FMDP	1.8	15.4	0.78
Met-FMDP	2.1	9.2	0.78
Phe-FMDP	0.8	14.2	3.12
Tyr-FMDP	0.4	6.7	12.5
Lys-FMDP	3.9	0.5	6.25
D-Ala-FMDP	0.6	14.2	>200
D-Ala-D-FMDP	0.7	0.5	>200
FMDP-Gly	0.2	0.8	100
FMDP-Ala	1.1	10.2	1.56
FMDP-Nva	1.3	15.5	3.12
FMDP-Val	1.2	16.7	3.12
FMDP-Leu	1.1	23.2	1.56
FMDP-Met	1.4	0.5	3.12
FMDP-Phe	1.0	7.5	3.12
FMDP-Tyr	0.2	0.5	12.50

[a] Abu: L-α-minobutyric acid; Nle:L-norleucine

Table 10. Anticandidal activity and initial rates of transport and intracellular cleavage of FMDP dipeptides

Experiments carried out in the presence of NaN_3, an inhibitor of mitochondrial activity, inhibited the uptake of peptides; which demonstrated that the peptides were taken by active transport. On the other hand, reduction of transport rates of peptides in the presence of *N*-ethylmaleimide was the indicative for the existence of cysteine sulfhydryl group in permease responsible from peptide transfer. By addition of strong enzyme inactivators, Zn^{2+} and 2,3-Dihydroxybenzoyl-L-alanyl-L-threonine; and in the presence of enzyme activators, Mn^{2+} and Co^{2+} were regarded as the indicators of aminopeptidase activity.

After the detailed investigations carried out on dipeptide-FMDP analogues, Nva-FMDP, the most effective dipeptide identified, was tested against human cancer cell lines (L1210 murine Leukemia, HeLa S_3 cervical carcinoma and LL2 murine Lewis carcinoma), in order demonstrate the impact of peptide on mammalian cells (Bontemps-Gracz et al., 1991). Up to 100 μg/ml concentration of Nva-FMDP used, no cytotoxic effects were observed against any of the cell lines. By using radioactively-labeled cellular macromolecule precursors (^{3}H- thymidine, ^{3}H-leucine, ^{3}H-uridine), it was shown that Nva-FMDP was not toxic to L1210 cell line up to 100 μg/ml. On the other

hand, IC_{50} value of FMDP for cell-free extract of GlcN-6 P synthase from L1210 cells with 0,05 activity unit was equal to 10 x 10^{-6} M for free FMDP, 241 x 10^{-6} M for Nva-FMDP, 690 x 10^{-6} M for FMDP-Nva and 44 x 10^{-6} M for Met-FMDP (whereas it was 4 x 10^{-6} M for *Candida albicans* exhibiting 0,04 unit activity (Milewski et al., 1985). However, competitive peptide uptake assay used in study demonstrated that the insensitivity of Nva-FMDP and FMDP-Nva were not related to peptide transport rates since these peptides were transported to as effectively as other proteinogenic peptides used as comparison. It was concluded that lack of cytotoxicity in L1210 cells, despite of the good drug uptake rates comparable activity towards target enzyme, could be the poor cleavage of rates (Table 11) of the peptides. Nevertheless, it was also considered that inhibition of glycoproteins in mammalian cells by inactivation of GlcN-6 P synthase was only a transient process and therefore it is not fatal for mammalian cells.

dipeptide	rate of cleavage (nmol/min .mg protein)	
	Leukemia L1210	*Candida albicans* ATCC 26278
Avl-FMDP	5	35.3
FMDP-Avl	0	15.5

Table 11. Cleavage rate of FMDP-peptides in crude cell-free extract from L1210 cells and their comparison to previous results with *Candida albicans* (Milewski et al., 1991).

Lys-Nva-FMDP, as the most effective tripeptide form of FMDP (Andruszkiewicz et al., 1990a), was later tested under *in vitro* conditions against *Histoplasma capsulatum* and *in vivo* conditions in a murine model of experimental histoplasmosis (fungal infection caused by *Histoplasma capsulatum*) (Milewski et al., 1998). *In vitro* tests showed that partial inhibition of fungal growth was achieved by 1.6 µg/ml of Lys-Nva-FMDP while complete inhibition was observed at 25 µg/ml. Importantly, when *N*-acetyl-D-glucosamine (2 mg/ml) was present in growth media, inhibitor activity of the Lys-Nva-FMDP was reversed; which confirmed that action of the FMDP peptide was the only process inhibited the biosynthesis of glucosamine. On the other hand, when Lys-Nva-FMDP was administered at a dose equivalent to concentration inhibiting the growth of fungi *in vitro,* 60% of the infected mice in one group of animals were completely

sterilized, while growth of fungi was remarkably reduced in 40% of the mice in another animal groups.

Andruszkiewicz *et al.* later designed acylated derivatives of L-2,3-diaminopropanoic acid at the N^3 amino groups by ketoacids, which would be more stable against hydrolysis in comparison to methyl ester bearing FMDP analogue that is prone to hydrolysis (Table 12) (Andruszkiewicz et al., 2000). Among the synthesized analogues, despite the lower IC_{50} values obtained in GlcN-6-P synthase inhibition experiments, N^3-trans-4-oxo-4-phenyl-2-butenoyl-L-2,3-diaminopropanoic acid (BADP) exhibited affinity and reactivity towards the enzyme, which was comparable to values obtained for FMDP. Inactivation potency of BADP (k_2/k_{inact}) was 30% lower in comparison to FMDP. Since it was known that all tested L-2,3-diaminopropanoic analogues exhibits poor anti-Candidal activity, norvaline dipeptides of the analogues were synthesized and tested against *Candida albicans.* Despite the good MIC values obtained for peptides, values were in direct contrast with their non-peptidic forms (Table 12) which was attributed to their potentially slow cleavage rates or the slow transport rates by peptidases. In conclusion, BADP was regarded as one of the most powerful inhibitors of GlcN-6-P synthase ever synthesized after FMDP.

	inhibition		Inactivation			
Compound	**MIC (μg/ml)**	**IC_{50} (μM)**	**k_{inact} (μM)**	**T (min)**	**K_2 (min^{-1})**	**K_2/k_{inact} ($M^{-1}.s^{-1}$)**
FMDP	-	4.0	2.1	2.97	0.233	1850
EADP	-	58	83	1.20	0.572	115
AADP	-	1400	7500	7.5	0.092	0.205
AEDP	-	2800	13100	1.20	0.573	0.730
BADP	-	200	8.3	1.15	0.597	1200
BADP (Gln)*	-	-	140	0.9	0.764	91
BADP(Fru-6-P)*	-	-	12.8	9.0	0.079	104
FEDP	-	380	2210	1.06	0.689	5.2
Nva-AEDP	2.5	-	-	-	-	-
Nva-BADP	7.5	-	-	-	-	-
Nva-FEDP	1.0	-	-	-	-	-

* inactivation performed in the presence of either L-Gln or 10 mM D-Fru-6-P

Table 12. Inhibitory and inactivation data for AADP, AEDP, BADP and FEDP in respect to *Candida albicans* GlcN-6-P synthase and dipeptide MIC values.

As a continuation of the prodrug approach, Zgódka *et al.* adopted derivatization of FMDP by esterification/amidation and increase its lipophilicity to enable free diffusion to cells (Zgódka et al., 2001b). Such approach was considered as a solution to fungal cells acquiring resistance to peptide conjugates of FMDP (Milewski et al., 1988). Among the synthesized derivatives (Figure 5), acetoxymethyl and pivaloyloxy-methyl ester derivatives (designated as 7 and 8) were most active after FMDP with lowest IC_{50} values (Table 13). However, in the buffer conditions used, acetoxymethyl was stable up to 24h and pivaloyloxy-methyl ester was unstable. While the amide derivatives were generally not good inhibitors, *N*-hexyl-*N*-methyl amide derivative (designated as 4) had the lowest IC_{50} values (125-fold higher than FMDP). These values suggested that the "portage transport" via peptides could be replaced by prodrug approach.

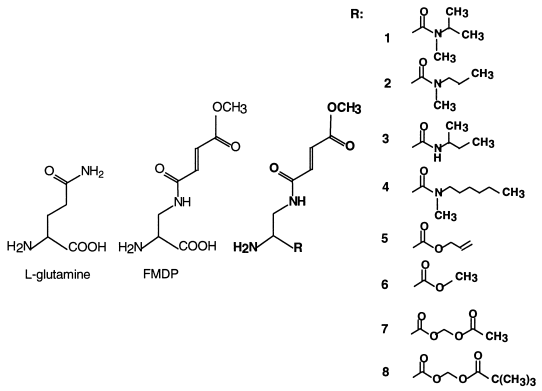

Figure 5. The structures of glutamine, FMDP and synthesized derivatives (Zgódka et al., 2001b).

Compounds	IC_{50}[a] (μM)
FMDP	4 ± 0.5
1	970 ± 80
2	1400 ± 120
3	2910 ± 95
4	500 ± 35
5	520 ± 48
6	300 ± 22
7	11.5 ± 1.5
8	15.6 ± 2.1

[a]IC_{50}, the 50% inhibitory concentrations of compounds that inhibit the enzyme activity by 50% of the control value. Values are the means of at least three independent estimations ± sd.

Table 13. Inhibition of glucosamine-6-phosphate synthase from *Candida albicans* by FMDP and derivatives 1-8 compounds (Zgódka et al., 2001b).

A study conducted by Janiak *et al.* (Janiak et al., 2002) one more time showed that FMDP was a poor antifungal agent *in vitro*. MIC values of FMDP were 0,625 mg/ml against *Candida albicans,* 1,25 mg/ml against *Candida glabrata* and 2,5 mg/ml against other *Candida spp*. Therefore, combination therapy by using synergistic effects between Amphotericin B (Amp B) [(or its structural derivative MF-AME (Grzybowska et al., 1997)] and FMDP was considered to increase the inhibitory effects of FMDP. Fractional inhibitory concentrations (FIC) calculated for combinations of FMDP and Amp B showed that interaction of combinatory drugs was either synergistic, additive or antagonistic depending on the fungal strain used in experiments (Table 14). On the other hand, *in situ* inhibition test of GlcN-6-P synthase from *Candida albicans* in the presence of FMDP and Amp B combination demonstrated that the combinatory therapy increased the inhibitory effect only less than 20%, which was regarded as too low to be of any practical value (Figure 6).

	AMB ADGP	MF-AME ADGP	AMB FMDP	MF-AME FMDP
C. albicans ATCC 26278	0.51	0.18	1.2	0.87
C. albicans ATCC 10261	0.33	0.42	0.78	0.82
S. cerevisiae ATCC 9763	0.29	0.48	1.0	0.98
C. glabrata	0.78	0.81	0.83	0.85
C. kruzei	0.69	0.58	1.0	0.78
C. parapsilosis	0.56	0.47	0.95	1.2
C. famata	0.73	0.58	0.96	1.0
C. humicola	0.72	0.64	0.81	0.90

Table 14. FIC indexes found for combinations of antifungal agents (Janiak et al., 2002).

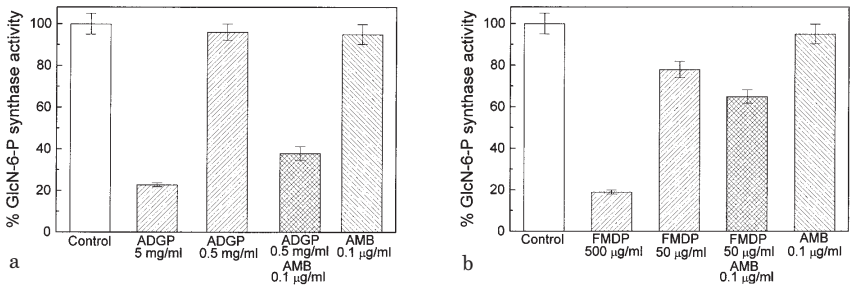

Figure 6. Inhibition of GlcN-6-P synthase activity *in situ* in *Candida albicans* cells: a) effect of ADGP, AMB and their combination; b) effect of FMDP, AMB or their combination (Janiak et al., 2002).

As a part of the continuing efforts for obtaining more lipophilic derivatives of GlcN-6-P synthase inhibitors, as series of compounds analogues to BADP and AADP containing keto functions and three different dipeptide derivatives from three selected analogues were prepared (Table 15) (Walkowiak et al., 2005). GlcN-6-P synthase inhibition studies in cell-free extracts demonstrated that the increasing K_{intact} values were correlated with the increasing substituent size in the aromatic rings (for BADP analogues). Only the compound showed inhibitory effect that was comparable to BADP was 4-ethylphenyl substituted analogue. Inactivation potencies (k_2/K_{inact}) were generally lower than BADP, suggesting that substitutions in phenyl ring does not provide better interaction with enzyme active site. On the other hand, MIC values of the analogues against three (3) different *Candida spp.* and *S. cerevisiae* proved that their activity were not correlated with their lipophilic derivatization and did not provide any improvement (Table 15). On the other hand, norvaline dipeptides prepared for 4-ethylphenyl, 2-pyrrolyl and ethyl derivatives exhibited high activity against *C. glabrata* however not against *Candida albicans* (Table 16). Notably, cytotoxicity tests carried on HL-60 human promyelocytic leukemia cells with dipeptides of 2-pyrrolyl and ethyl derivatives proved that they were non-toxic and thus, they were assumed to be non-toxic for normal human cells (Table 16).

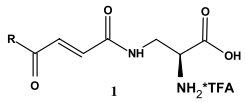

1

where R is:

phenyl (**BADP**)	2,4,6-trimethylphenyl (**1g**)	4-chloro-3-nitrophenyl (**1p**)
methyl (**AADP**)	2-chlorophenyl (**1h**)	naphthyl (**1q**)
methoxyl (**FMDP**)	3-chlorophenyl (**1i**)	2-furyl (**1r**)
4-methylphenyl (**1a**)	4-chlorophenyl (**1j**)	2-pyrrolyl (**1s**)
4-ethylphenyl (**1b**)	2-bromophenyl (**1k**)	*tert*-butyl (**1t**)
4-*n*-butylphenyl (**1c**)	3-bromophenyl (**1l**)	ethyl (**1u**)
4-*tert*-butylphenyl (**1d**)	4-bromophenyl (**1m**)	*iso*-propyl (**1w**)
4-decylphenyl (**1e**)	4-fluorophenyl (**1n**)	*n*-butyl (**1x**)
2,4-dimethylphenyl (**1f**)	3,4-dichlorophenyl (**1o**)	

Compound	MIC [μg/ml]			
	S. cerevisiae	*C. glabrata*	*C. albicans*	*C. crusei*
1a	125	250	250	250
1b	62.5	250	250	125
1c	62.5	250	125	125
1d	62.5	250	250	250
1e	> 500	> 500	> 500	> 500
1g	62.5	250	125	250
1f	125	250	125	250
1h	125	250	250	250
1i	62.5	250	250	250
1j	125	250	250	250
1k	62.5	250	125	250
1l	62.5	250	250	250
1m	62.5	250	250	125
1n	125	250	250	250
1o	62.5	250	250	250
1p	125	250	250	250
1q	62.5	250	250	250
1r	125	> 1000	> 1000	–
1s	> 250	> 250	> 250	–
1t	500	> 1000	> 1000	–
1u	125	> 1000	> 1000	–
1w	250	> 1000	> 1000	–
1x	> 250	> 250	> 250	–
BADP	–	250	125	250
AADP	15.64	> 1000	> 1000	–

Table 15. Structures of BADP and AADP derivatives and their antifungal activities (Walkowiak et al., 2005).

peptides	MIC (μg/ml)			HL-60 (IC_{50})
	S. cerevisiae	*C. glabrata*	*Candida albicans*	
Lys-Nva-FMDP	31.25	7.81	3.13	-
TFA.Nva-1b	>1000	31.25	>1000	-
TFA.Nva-1s	31.25	15.63	>1000	30%inhibtation at 250 **(μg/ml)**
TFA.Nva-1u	31.25	7.81	>1000	232 ± 2 **(μg/ml)**
Nva-FMDP	-	-	-	15% inhibition at 250 **(μg/ml)**

Table 16. Activity of tested peptides against HL-60 human promyelocytic leukaemia cells and fungi.

In order to overcome the resistance acquired by fungal cells and facilitate the free-diffusion of peptides, Andruszkiewicz *et al.* also studied more lipophilic *N*-acylated dipeptides of FMDP (Andruszkiewicz et al., 2005). In comparison to Nva-FMDP (a highly effective dipeptide form of FMDP) was compared to new *N*-acylated dipeptides in cell-free extract of GlcN-6-P synthase from *Candida albicans.* While some selected *N*-acylated dipeptides performed much better in pre-incubation studies than non-preincubation studies, results were quite similar for Nva-FMDP. From the IC_{50} results obtained from this experiment, it was concluded that the Nva-FMDP hydrolysis rate was much higher than the *N*-acylated dipeptides.

peptides	MIC (μg/ml)								
	Candida famata	*Candida glabrata*	*Candida humicola*	*Candida crusei*	*Candida parapsilosis*	*Candida tropcalisi*	*Candida albicans ATCC 10261*	*Candida albicans Gu4*	*Candida albicans Gu5*
AcFMDP	1500	1000	500	1000	500	1500	2000	3000	3000
AcNvaFMDP	250	750	500	250	125	500	250	250	1000
AcLys(Ac)NvaFMDP	250	500	250	250	125	500	250	500	>2000
HexFMDP	500	500	250	500	250	1000	1000	1000	1000
HexNvaFMDP	250	250	125	250	125	1000	500	31.25	1000
HexLys(Hex)NvaFMDP	125	125	62.5	125	62.5	500	250	250	1000
DecFMDP	125	500	500	125	62.5	250	62.5	62.5	250
DecNvaFMDP	125	250	250	125	62.5	250	125	15.6	125
DecLys(Dec)NvaFMDP	62.5	125	125	62.5	31.5	125	62.5	3.9 – 31.25	62.5

Table 17. Anti-Candidal activity of *N*-acylated lipophilic dipeptides of FMDP (Andruszkiewicz et al., 2005).

All the new *N*-acylated dipeptides were tested *in vitro* against variety of *Candida spp.* and also, fluconazole resistant (Gu4) and the drug efflux protein (Cdr1p and Cdr2p)

containing (Gu5) clinical strains of *Candida albicans.* MIC values obtained for peptides (Table 17) demonstrated that AcFMDP, AcNvaFMDP and AcLys(Ac)NvaFMDP exhibited poor antifungal activity. Much better results were obtained for decanoic acid bearing DecFMDP, DecNvaFMDP, DecLys(Dec)NvaFMDP, the last one being the most active against all species tested, including resistant *Candida albicans.* Notably, cytotoxicity tests performed with selected peptides on human promyelocytic leukemia cell line HL-60 demonstrated that the peptides were non-toxic even in very high concentrations (Table 18). Therefore, they were regarded as non-toxic for normal human cells.

Acylated peptides	HL-60 IC_{50} (mM)
AcNvaFMDP	10% inhibition at 500 mM
AcLys(Ac)NvaFMDP	20% inhibition at 500 mM
HexNvaFMDP	30% inhibition at 500 mM
HexLys(Hex)NvaFMDP	~600
DecFMDP 3	~230
DecNvaFMDP	250±65
DecLys(Dec)NvaFMDP	415±70

Table 18. *In vitro* cytotoxic activity of examined compounds against HL-60 human promyelocytic leukemia cells.

In the following study, Milewski *et al.* tested inhibitory effect of oligopeptides along with Nva-FMDP and Lys-Nva-FMDP against resistant strains of *Candida albicans* overexpressing drug efflux pumps encoded by CDR1 and/or CDR2 genes (G5 strain) and MDR1 gene (B4 strain); but also their respectively matched fluconazole-sensitive isolates Gu4 and B3, exhibiting basal expression of these resistance genes (Wakieć et al., 2008). The study was continuation of a previous findings on *Saccharomyces cerevisiae* (Milewski et al., 2001) where the yeast overexpressing Cdr1p drug efflux pump was paradoxically more susceptible to the action of oligopeptidic antifungal agents containing FMDP. The more recent study demonstrated that *Candida albicans* isolates overexpressing CDR1 and/or CDR2 genes were more susceptible to oligopetides, in comparison to their parent strains which are lacking the overexpressed genes (Table 19). It was suggested that that: “the enhanced susceptibility of MDR yeast strains to oligopeptide antifungals was due to enhanced oligopeptide antifungal uptake mediated

by oligopeptide permeases that are affected by an increased membrane potential induced by overexpression of the ABC drug efflux pumps Cdr1p and Cdr2p".

Compound	MIC (μg/ml) of[a]:				
	ATCC 10261	Gu4	Gu5 (*CDR1* and/or *CDR2*)	B3	B4 (*MDR1*)
OLys-Leu-Gly (2)	128	256	16	64	32
Leu-FPhe (5)	64	128	8	64	64
Met-Met-FPhe (6)	128	128	32	128	128
Nva-FMDP (7)	2	2	0.125	4	4
Lys-Nva-FMDP (8)	8	4	1	8	8
Nikkomycin (9)	32	16	4	8	8
Histatin 5	32	32	32	32	32
Asp-γ-hydroxamate (10)	256	256	128	256	256
OLys (11)	16	16	4	16	32
FPhe (12)	256	128	128	128	128
cis-pentacin (13)	1	1	4	2	8
DON (14)	4	4	1	4	4
Azaserine (15)	16	16	16	32	32
Fluconazole	4	8	256	4	64

[a] MICs were determined by using RPMI-1640 buffered medium, as described in Materials and Methods. No growth inhibition was observed for oligopeptides 1, 3, and 4 at a concentration of ≤1,024 μg/ml.

Table 19. In vitro susceptibilities of *Candida albicans* reference strain and clinical isolates to oligopeptide and amino acid antifungals and fluconazole (Wakieć et al., 2008).

Biologically active peptides are usually unstable in blood serum and thus, they are not good drug transporters. However, their thionated analogues more stable against hydrolyses and also transported via cell membranes with higher efficiencies. Correspondingly, thionated analogues of Nva-FMDP and Lys-Nva-FMDP were studied against *Candida albicans* Gu4 (fluconazole sensitive), *Candida albicans* Gu5 (fluconazole resistant), *Candida albicans* ATCC 10231, *Candida krusei* DSM 6128 and *Candida parapsilosis* DSM 5784 (Table 20) (Nowak-Jary and Andruszkiewicz, 2009). It was reported that thionated peptides with more than 100 μg/ml MIC values poorly performed against the *Candida spp.* tested. Therefore, the study focused on inhibitory growth effects at 500 μg/ml concentrations of the peptides. In this elevated concentration, it was demonstrated that Nva-FMDP and Lys-Nva-FMDP activities were significantly reduced after 48h of incubation in blood serum containing media. Consequently, formation of spontaneous resistant mutants against Nva-FMDP and Lys-Nva-FMDP were observed. On the other hand, thionated peptides remained their

activity up to 48h; which was attributed to their resistance to hydrolysis. Nevertheless, it was concluded that the thionated peptides were poor antifungals with insufficient transport and intracellular cleavage rates.

medium	YNB		YNB + 5% blood serum			YNB		YNB + 5% blood serum		MIC (μg/ml) or % of inhibition of growth at C = 500 μg/ml
time of incubation	24 h	48 h	24 h	48 h		24 h	48 h	24 h	48 h	
***Candida albicans* ATTC 10231**										
NvaFMDP	0.12–31.3	0.24– >100	0.24–>100	0.49–>100	Nva-Ψ[CSN^{2}H]--FMDP	24–35%	25–37%	23–25%	19–26%	
***Candida krusei* DSM 6128**										
NvaFMDP	0.98–1.95	3.9–>100	31.3–>100	>100	Nva-Ψ[CSN^{2}H]--FMDP	18–33%	16–35%	20–30%	23–40%	
***Candida parapsilosis* DSM 5784**										
NvaFMDP	0.98–>100	3.91–>100	31.3–>100	62.5–>100	Nva-Ψ[CSN^{2}H]--FMDP	7–40%	4–46%	8–30%	8–28%	
***Candida albicans* Gu4**										
NvaFMDP	0.03–0.12	0.24–0.49	0.03–0.24	0.24–0.98	Nva-Ψ[CSN^{2}H]--FMDP	14–35%	14–23%	25–31%	21–24%	
***Candida albicans* Gu5**										
NvaFMDP	0.06–0.12	0.12–0.49	0.06–0.24	0.24–0.98	Nva-Ψ[CSN^{2}H]--FMDP	27–50%	10–30%	31–45%	30–35%	

medium	YNB		YNB + 5% blood serum			YNB		YNB + 5% blood serum		MIC (μg/ml) or % of inhibition of growth at C = 500 μg/ml
time of incubation	24 h	48 h	24 h	48 h		24 h	48 h	24 h	48 h	
***Candida albicans* ATTC 10231**										
Lys--NvaFMDP	0.12–0.24	0.24–0.48	0.24–0.48	0.49–0.98	Lys-Ψ-[CSNH]--Nva-Ψ[CSN^{2}H]--FMDP	26–30%	25–28%	23–25%	21–24%	
***Candida krusei* DSM 6128**										
Lys--NvaFMDP	0.98	3.9	31.3	62.6	Lys-Ψ[CSNH]--Nva-Ψ[CSN^{2}H]--FMDP	30–36%	20–35%	27–32%	23–30%	
***Candida parapsilosis* DSM 5784**										
Lys--NvaFMDP	>100	>100	>100	>100	Lys-Ψ[CSNH]--Nva-Ψ[CSN^{2}H]--FMDP	4–23%	5–16%	4–21%	6–16%	
***Candida albicans* Gu4**										
Lys--NvaFMDP	0.03	0.24–0.49	0.03–0.24	0.48–0.98	Lys-Ψ[CSNH]--Nva-Ψ[CSN^{2}H]--FMDP	14–16%	16–23%	18–25%	15–19%	
***Candida albicans* Gu5**										
Lys--NvaFMDP	0.12	0.12	0.06	0.24	Lys-Ψ[CSNH]--Nva-Ψ[CSN^{2}H]--FMDP	22–27%	9–15%	12–17%	11–19%	

Table 20. Antifungal activity of NvaFMDP, Lys-NvaFMDP, Nva-**Ψ**[CSN^{2}H]-FMDP and Lys[CSNH]-Nva-**Ψ**[CSN^{2}H]-FMDP (Nowak-Jary and Andruszkiewicz, 2009).

More recent studies on derivatization of FMDP to obtain more lipophilic and thus more effective analogues of it. Number of lipophilic but efficiently water soluble bis-*N,N*-(2-hydroxyethyl)glycine (bicine) derivatized FMDP conjugates were shown to be more effective against *Candida albicans, Candida glabrata* and *Candida tropicalis* (Table 21) (Koszel et al., 2012). On the other hand, the amide derivatives of FMDP (Table 22), together with keto-ester and amide-ester derivatives of FMDP exhibited elevated inhibitory effects against *Candida albicans* (Table 23) (Pawlak et al., 2015, 2016).

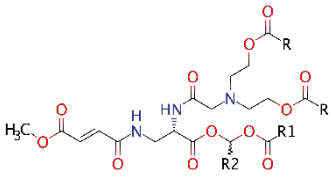

8a: R= CH_3; R_1= CH_3; R_2= H

8b: R= CH_3CH_2; R_1= CH_3; R_2= H

8c: R= $CH_3(CH_2)_2$; R_1= CH_3; R_2= H

8d: R= C_6H_5; R_1= CH_3; R_2= H

8e: R= CH_3; R_1= $CH(CH_3)_2$ R_2= H

8f: R= CH_3; R_1= $C_6H_5CH_2$; R_2= H

8g: R= CH_3; R_1= $CH(CH_2CH_3)_2$; R_2= H

8h: R= CH_3; R_1= CH_3; R_2= CH_3CH_2

8i: R= CH_3; R_1= OCH_2CH_3; R_2= CH_3

Compound	R	R_1	R_2	MIC (μg/mL) *C. albicans*	*C. glabrata*	*C. tropicalis*	*S. cerevisiae*	$\log k'_{IAM,0}$
8a	CH_3	CH_3	H	500	500	1000	1000	0.91
8b	CH_3CH_2	CH_3	H	1000	1000	500	1000	1.01
8c	$CH_3(CH_2)_2$	CH_3	H	1000	500	250	1000	1.36
8d	C_6H_5	CH_3	H	500	125	500	500	2.11
8e	CH_3	$CH(CH_3)_2$	H	125	125	62.5	31.3	1.34
8f	CH_3	$CH_2C_6H_5$	H	31.3	125	62.5	125	1.76
8g	CH_3	$CH(CH_2CH_3)_2$	H	31.3	250	125	500	1.72
8h	CH_3	CH_3	CH_3CH_2	62.5	125	125	250	1.55
8i	CH_3	OCH_2CH_3	CH_3	125	250	15.6	125	1.26
FMDP	—	—	—	>2000	>2000	>2000	>2000	−0.85

Table 21. Antifungal activity of *bis-N,N*-(2-hydroxyethyl)glycine (bicine) derivatives 8a-i of FMDP (Koszel et al., 2012).

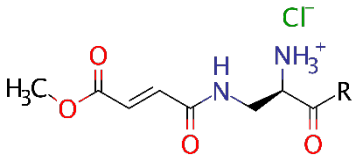

Co.	R=	*C. albicans* ATCC 10231	*C. glabra ta* DSM 11226	*C. parapsilosis* DSM 5784	*S. aureus* ATCC 29213	*S. epidermidis* PCM 2118	*E. coli* PCM 2560	*B. subtilis* ATCC9372	*P aeruginosa* ATCC 2756
4	NH_2	4	>1024	>1024	>1024	>1024	>1024	>1024	>1024
5	$NHCH_3$	32	>1024	>1024	>1024	>1024	>1024	>1024	>1024
6	$N(CH_3)_2$	512	>1024	>1024	>1024	>1024	>1024	>1024	>1024
FMDP	–	>2000	>2000	>2000	>2000	>2000	>2000	>2000	>2000
NvaFMDP	–	0.25	8	8	>1024	128	8	8	8

Table 22. Antimicrobial activity of amide derivatives of FMDP (Pawlak et al., 2015).

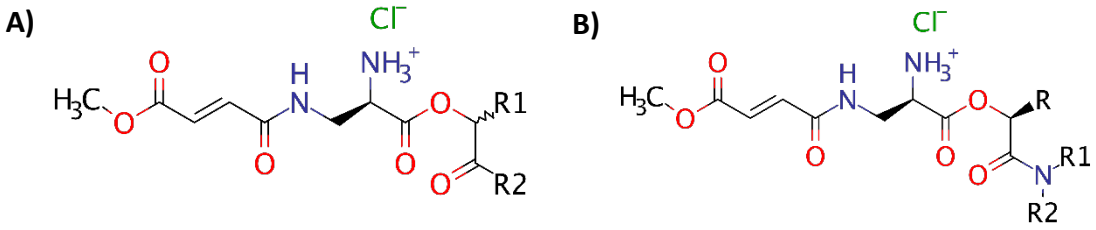

Compd				MIC (μg/mL)				IC_{50} (μM)
	R^1	R^2	R^3	*C. albicans* ATCC 10231	*C. glabrata* DSM 11226	*S. aureus* ATCC 29213	*E. coli* PCM 2560	
11	H	CH_3	–	0.25	512	>1024	>1024	5.08 ± 0.15
12	CH_3	CH_3	–	0.5	512	>1024	>1024	4.91 ± 0.38
13	H	$C(CH_3)_3$	–	0.5	512	>1024	>1024	5.17 ± 0.13
14	H	H	H	128	>1024	>1024	>1024	201.94 ± 21.67
15	H	H	CH_3	1	>1024	1024	>1024	26.98 ± 0.43
16	H	CH_3	CH_3	2	>1024	512	>1024	66.59 ± 4.11
17	CH_3	H	H	8	>1024	>1024	>1024	82.1 ± 3
18	CH_3	H	CH_3	16	>1024	>1024	>1024	199 ± 3
19	CH_3	CH_3	CH_3	256	>1024	>1024	>1024	>5000
FMDP	–	–	–	>1024	>1024	>1024	>1024	4.03 ± 0.26

Table 23. Antimicrobial activity of A) keto-ester 11-13; B) amide-ester 14-19 derivatives of FMDP (Pawlak et al., 2016).

The most recent report on inhibitory activities of di- and tri- (**Nva-FMDP and Lys-Nva-FMDP**), hexa-, hepta-, deca- and undeca-peptides incorporating FMDP against wild-type and wild-type derived peptide permease deficient mutants of *Candida albicans* demonstrated that, phenotypic resistance acquired against oligopetides transported by oligopeptide permeases (OPT) was triggered by environmental factors, whereas di- and tri-peptides transported (PTR) by peptide transporters had genetic bases (Schielmann et al., 2017). Importantly, activity of the oligopeptides was diminished when the minimal media containing ammonium sulfate or L-glutamine as the nitrogen source were used. This effect was attributed to downregulated expression of the OPT genes. Notably, formation of isolated resistant colonies was observed in the inhibitory zones induced by di- and tri- peptides but not of those induced by hexa-, hepta and undeca-peptides.

While all FMDP-oligopeptides showed high inhibitory activity in YNB-SG (Yeast Nitrogen Base w/o amino acids and ammonium sulfate + 2% glucose + 0.2 g L^{-1} sodium glutamate) medium. In YNB-AS (Yeast Nitrogen Base w/o amino acids (contains ammonium sulfate 5 g L^{-1}) + 2% glucose) medium, while Nva-FMDP and Lys-Nva-FMDP activities were low, FMDP-oligopeptides showed 8-10 times higher activity. In RPMI-1640 (w/o sodium bicarbonate, with L-glutamine + 2% glucose + 3.45% MOPS, pH

adjusted to 7.0) medium, all the FMDP-oligopeptides demonstrated much lower growth inhibitory activity in RPMI-1640 but hexa-, hepta- and undeca-oligopetides totally lost their activity. Therefore, components of the RPMI-1640 medium that might have influenced the growth inhibition were tested in YNB media where the oligopeptides showed high activity. Strong effect was found when YNB medium was supplemented with the amino acids having the same composition in RPMI-1640. In YNB + amino acids medium, hexa-, hepta- and undeca-peptides lost their activity while di- and tri-peptides preserved their activity same as in original YNB-SG medium. Activity of F6, F7, and F11 were diminished in the presence of 300 $mg.L^{-1}$ L-glutamine, (the same concentration as in RPMI-1640) in growth medium buffered to pH = 7.0. Impact of pH differences between the growth media were also tested. RPMI-1640 buffered to 5.0, 6.0, and 7.0 (which was originally 7.0) and YNB-AS buffered to 4.5, 5.5, and 6.5 (which was originally 5.4). All FMDP-oligopeptides exhibited lower MICs at lower pH values. In YPD (1% yeast extract, 2% peptone, and 2% glucose) medium, FMDP-oligopeptides had no inhibitory activity. Similarly, when the YNB-AS and YNB-SG were supplemented with Bacto Peptone, 5 g L−1, growth inhibitory activity of all FMDP oligopeptides were completely eliminated.

Significant decrease in inhibitory activity of FMDP-oligopeptides in amino acid mixture and L-glucosamine supplemented media was found consistent with the known phenomenon of repression of OPT genes expression in the presence of high concentrations of the preferred, nitrogen sources (ammonium, L-Glucosamine or urea). Stronger glutamine effect in pH 7 than pH 5-YNB medium was susceptibility to hydrolysis of amino acids in acidic conditions.

The study also pointed out that transport and intracellular cleavage rates of the FMDP-oligopeptides were lower than the di- and tripeptides, which resulted in lower antifungal *in vitro* activity for oligopeptides. However, despite the FMDP-containing di- and tripeptides demonstrated the highest anticandidal activity, they easily induced specific resistance. Relatedly, despite the anticandidal activity of oligopeptides were strongly affected by pH and a nitrogen source, specific resistance induced uptake deficiency were less likely for oligopeptides.

1.2.3.2 Summary

- FMDP was reported to be the most active inhibitor of GlcN-6-P in cell free extracts, particularly to the enzyme extracted from *Candida albicans* (Milewski et al., 1985; Andruszkiewicz et al., 1986).
- Due to toxicity of FMDP to the living cells, dipeptide-FMDP structures were studied in the concept of "warhead delivery". By means of incorporating FMDP into lipophilic peptides containing aliphatic chains, achieving higher inhibitory activity was aimed (Andruszkiewicz et al., 1987). C-terminal dipeptides were more active than their N-terminal isomers, where **Nva-FMDP exhibited the highest inhibitory activity** in comparison to other peptides but also well-known drugs tested in this study.
- It was shown that there are two different permeases in *Candida albicans;* one responsible from di- and tripeptides and the other one from tri-, tetra-, penta-, hexa-peptides. While the **Nva-FMDP induced some spontaneous resistant mutants**, they were no more able to take tripeptides. Tripeptides were suggested to be the most efficient peptides since they were transported by both permeases (Milewski et al., 1988).
- **Lys-Nva-FMDP was found to be the most effective tripeptide form of FMDP exhibiting high inhibitory activity against clinical isolates of *Candida albicans*** (Andruszkiewicz et al., 1990a).The study also pointed out that **Nva-FMDP induced the highest amount of spontaneous resistant mutants in *Candida albicans*.**
- Replacing FMDP with N^3-iodoacetyl derivatives of L-2,3-diaminopropanoic acid showed that Lys and Nva residues were essential for effective transport into fungal cells. However, N^3-iodoacetyl derivatives generally exhibited lower antifungal activity than FMDP-peptides (Andruszkiewicz et al., 1990b).
- A systematic approach to determine the factors determining the anticandidal activity of FMDP-dipeptides, 21-different dipeptide forms of FMDP studies. It was shown that the transport velocity is a more important determinant of peptides' anticandidal activity than the intracellular cleavage velocity (Milewski

et al., 1991). **Nva-FMDP inhibitory one more time outperformed the activities of all other peptides included in the study**.

- After the proven superior activity of Nva-FMDP, it was tested against human cancer cell lines (L1210 murine Leukemia, HeLa S_3 cervical carcinoma and LL_2 murine Lewis carcinoma) (Bontemps-Gracz et al., 1991). **Up to 100 μg/ml concentration of Nva-FMDP, no cytotoxic effects were observed against any of the cell lines**. Notably, cell free-extracts of GlcN-6 P from L1210 cells (0.05 unit) required only 10 x 10^{-6} M for free FMDP or 241 x 10^{-6} M for Nva-FMDP, whereas the enzyme from *Candida albicans* (0.04 unit, (Milewski et al., 1985)) required 4 x 10^{-6} M free FMDP (values are from IC_{50} tests). Nevertheless, the study showed that Nva-FMDP uptake rate was quite high. Therefore, that **inactivity of the peptide was attributed to the slow peptide cleavage rates**.
- When the L-2,3-diaminopropanoic acid backbone was acylated at N^3 amino groups by ketoacids to form derivatives of FMDP that are more prone to hydrolysis (as opposed sensitive methyl ester group of FMDP), ***N^3*-trans-4-oxo-4-phenyl-2-butenoyl-L-2,3-diaminopropanoic acid (BADP) derivative was found to be the most effective inhibitor after FMDP** (Andruszkiewicz et al., 2000). The following prodrug approach by esterification/amidation of FMDP demonstrated that acetoxymethyl and pivaloyloxy-methyl ester derivatives of FMDP had inhibitory activities comparable to FMDP. Therefore, **it was suggested that the prodrug approach could replace the "warhead delivery" approach with peptides** (Zgódka et al., 2001b).
- Since **pure FMDP had very poor MIC values *in vitro* (0,625 mg/ml against *Candida albicans,* 1,25 mg/ml against *Candida glabrata* and 2,5 mg/ml against other *Candida spp.*)**, combinatory therapy with Amphotericin B was considered (Janiak et al., 2002). However, this approach increased the inhibitory effect of FMDP only by 20%.
- When the prodrug approach via derivatization of BADP phenyl ring by lipophilic substitutions was considered, no correlation was found between the MIC values of derivatives and their lipophilicity; and none of the drug showed better activity than BADP. On the other hand, Nva dipeptides of the selected derivatives showed good activity against *Candida glabrata* but not *Candida albicans.*

Notably, dipeptides were non-toxic to HL-60 human promyelocytic leukemia cells (Walkowiak et al., 2005).

- In order to overcome the resistance acquired against the peptides, more lipophilic *N*-acylated dipeptides of FMDP were studied to facilitate free-diffusion to cells. **DecLys(Dec)NvaFMDP peptide exhibited very good activity against numerous standard *Candida spp.* tested but also against fluconazole resistant (Gu4) and the drug efflux protein (Cdr1p and Cdr2p) containing clinical strains of *Candida albicans*. Peptides were non-toxic to human promyelocytic leukemia cell line HL-60 even in very high concentrations** (Andruszkiewicz et al., 2005).
- Thionated analogues of biologically active peptides were known to be more stable against hydrolyses and also transported via cell membranes with higher efficiencies. However, thionated Nva-FMDP and Lys-Nva-FMDP derivatives did not show any activity even at elevated concentrations (Nowak-Jary and Andruszkiewicz, 2009).
- More recent studies focused on lipophilic prodrug approach. Number of lipophilic but efficiently water soluble bis-*N,N*-(2-hydroxyethyl)glycine (bicine) derivatized FMDP conjugates were shown to be more effective against *Candida albicans, Candida glabrata* and *Candida tropicalis* (Koszel et al., 2012) On the other hand, FMDP derivatized as simple amides or ester with simple keto and amide functions exhibited elevated inhibitory activities, and performed much better than FMDP against *Candida albicans*. (Pawlak et al., 2015, 2016)
- The latest study demonstrated that the resistance of *Candida albicans* to oligopetides were induced by environmental factors such as pH and contents of the medium of choice. Activity of oligopeptides were diminished by L-glutamine in RPMI-1640 medium. Study showed that the oligopeptides had low *in vitro* activity because of their slow transport and intracellular cleavage rates. Notably, **di- and tri-peptides (Nva-FMDP and Lys-Nva-FMDP), which were shown to be the most effective peptide forms of FMDP with good anticandidal activity in previous and in this particular study, easily induced specific resistance** in *Candida albicans* (Schielmann et al., 2017).

1.3 Chemical and physical background

1.3.1 Preparation Iron oxide nanoparticles (IONPs) and core-shell nanoparticles

Iron oxide nanoparticles (IONPs) were the nanoparticle of choice to investigate in the concept of thesis. The primary reason of the choice was based on the facts that the IONPs were the only FDA-approved inorganic/metallic nanoparticles for medical purposes to the date; and they are the most promising materials in nanomedical research as the most widely studied nanomaterials in biological applications (Bobo et al., 2016; Ventola, 2017).

Iron oxides in multiple polymorphs can be synthesized to be useful in wide variety of applications (Guo and Barnard, 2013). The most common iron oxides are: α-Fe_2O_3, γ-Fe_2O_3 and Fe_3O_4. While hematite α-Fe_2O_3 nanoparticles are commonly found suitable for various physical applications (as catalysts, high-density magnetic storage media, pigments, anticorrosive agents, water splitting, water purification, solar energy conversion and oxygen sensors (Shin et al., 2005; Cesar et al., 2006; Prucek et al., 2009; Rettig and Moos, 2010), maghemite γ-Fe_2O_3 and magnetite (Fe_3O_4) nanoparticles, due to low cytotoxicity (Caruso et al., 1999; Breen et al., 2001; Yonghui Deng et al., 2007; Amara et al., 2012) are used in magnetic resonance imaging (MRI) as contrast agents, ferrofluids, targeted drug delivery, hyperthermia anticancer therapy, cell labelling and environmental remediation. The physical and chemical properties of iron oxide nanoparticles (IONPs) are greatly affected by the synthesis method and show significant diversity in terms of their oxidation state (Vayssieres et al., 2005; Pol et al., 2010; Andrzejewski et al., 2014). Despite of variety of different synthesis procedures such as: co-precipitation method, sonochemical method, sol–gel synthesis, thermal decomposition of organometallic compounds etc. (Navrotsky et al., 2008) it is very difficult to achieve phase pure compound. Additionally, magnetite is very difficult to preserve for long periods of time, since it transforms to maghemite at very high rates during few hours of storage, so keeping the structural integrity of the particles while protecting them for degradation is a very important task. Therefore, the incorporation of a protective coating which preserves their magnetic properties is very desirable, especially if the coating provides improved bifunctional properties and easy

dispersibility in water. More importantly, from the biomedical application perspective, several aspects need to be addressed in order to fully exploit the multifunctional properties of magnetic NPs, among the most important are: *i)* dispersibility *ii)* low agglomeration, *iii)* stability *iv)* high magnetic response and *v)* high diffusion in tissues and cells (Shapiro et al., 2015). Particularly, it has been proposed that high diffusion has two main interdependent aspects; the first one is size of the NPs, which controls the resistance of the particle against tissue and brings mobility, and the second one is magnetic response, which provides the ‘‘propulsion” for the NPs (Nacev et al., 2011; Tadyszak et al., 2017).

Among the numerous chemical methods for large-scale synthesis of iron oxide nanoparticles, **thermal decomposition** is a most widely adopted high-temperature synthesis method capable of producing highly monodisperse, uniform and high degree crystallinity IONPs in large-scale (Hyeon, 2003; Ling and Hyeon, 2013). While various approaches of thermal decomposition method using iron cupferron, iron acetylacetonate, iron oleate or iron pentacarbonyl as the precursors of iron oxide nanoparticles, iron oleate stands out as the most widely accepted method to produce hydrophobic oleate-capped iron oxide nanoparticles (OA-IONPs) in different sizes (5-22nm) with narrow size variations (Park et al., 2004). However, despite the synthesis of magnetic IONPs is rather straightforward thanks to highly efficient thermal decomposition method, hydrophobicity of the resulting oleate-capped IONPs is the major drawback of the method limiting most of its chemical processing applications to non-aqueous environments. Hydrophobic coating also makes their use in biological applications impossible. As a result of the extensive attempts to render hydrophobic IONPs dispersible in aqueous environments in a permanent manner, coating the nanoparticle surfaces with hydrophilic silicon oxide layer has been long-known as an attractive approach to prepare iron oxide/silica core-shell nanoparticles (IONPs@SiO_2) (Philipse et al., 1994; Santra et al., 2001; Sun et al., 2005; Ma et al., 2007). Resulting IONPs@SiO_2 structures can exhibit both chemical and physical resistance to the external impacts by the shielding effects of silicon oxide, which also provides extended chemical functionality by the readily available variety of organo-silica precursors.

Stöber method (Stöber et al., 1968), from the technical from point of view, is the simplest and the most well-known approach to form silica shells around IONPs (Wang

et al., 2008). However the role of ionic surfactants, as templating or structure-directing agents, cannot be disregarded since the approach has been one of the most commonly utilized methods to the date, not only for IONPs but also non-magnetic nanoparticles with hydrophobic coating (Nooney et al., 2002, 2003; Fan, 2004; Kim et al., 2008b). In this context, the use of cetyltrimethylammonium (CTA^+) salts as charged surfactants, which have been extensively utilized in sol-gel science of siliceous materials, based on the well-described pioneering techniques have had a great impact on the development of core-shell nanostructures that incorporate silica as their coating (shell) material (Yanagisawa et al., 1990; Beck et al., 1992; Kresge et al., 1992). The mechanisms underlying these coating processes rely in both micellization aspects and the ionic nature of CTA^+ to act as template for the silica formation in varying morphologies (Huo et al., 1994).

Due to fact that the structurally well-tuned nanoparticles (including OA-IONPs) can be obtained only by surface stabilization by highly hydrophobic components (Brust et al., 1994; Hyeon et al., 2001; Park et al., 2004), phase transition process has been an additionally important factor in the preparation of siliceous core-shell nanostructures of OA-IONPs (Gittins and Caruso, 2001; Swami et al., 2003; Fan, 2004). In this context, CTA^+ surfactant temptation of OA-IONP surfaces provide the initial aqueous conditions necessary for the silica formation process. Relatedly, employment of hydrophobic OA-IONPs by thermal decomposition method (Park et al., 2004) has been one of the most prominent examples of silica coating processes where the CTA^+ molecules act as phase transfer agent for OA-IONPs and structure directing agent for the formation of iron oxide-silica core-shell (IONPs@SiO_2) structures (Kim et al., 2008b).

Phase transition of OA-IONPs with in the presence of CTA^+ is known to be a concentration dependent process, determining the interactions of the OA-IONPs with each other in an oil-in-water system (Qiu et al., 2010). The increased CTA^+ and OA-IONPs concentrations can lead to formation of CTA^+ stabilized OA-IONP clusters (CTA^+-OA-IONPCs) (Qiu et al., 2010) as opposed to low surfactant and IONPs concentrations that lead to CTA^+ assisted, individually dispersed OA-IONPs (CTA^+-OA-IONPs) (Kim et al., 2008b). The mechanism behind the formation of individual, single core IONPs@SiO_2 formations are dependent on whether the phase transfer process yielded CTA^+-OA-IONPCs or CTA^+-OA-IONPs. While the individual, non-agglomerated core containing

IONPs@SiO_2 formations were formed only in the presence of non-clustered IONPs (CTA^+-OA-IONPs) (Kim et al., 2008b; Qiu et al., 2010), initially clustered IONPs (CTA^+-OA-IONPCs) induce the formation of multi-cored IONPs@SiO_2 core-shell structures (Qiu et al., 2010).

1.3.2 Magnetic properties of iron oxide nanoparticles

When the dimensions of magnetic materials reach to nanometric scale, the structure of the magnetic domains of the material becomes dependent on the size of the material. Such behavior is called superparamagnetism. Magnetic domains are the regions where mutual alignment of all magnetic dipole moments exists in the same direction of any ferro- or ferri-magnetic material below their Curie temperature (Soler and Paterno, 2017). In other words, upon application of an external magnetic field, nanoparticles exhibiting superparamagnetic behavior are magnetized up to their saturation magnetization and no residual magnetic interaction is exhibited by these particles upon the removal of external magnet. Such behavior is known to be limited to particles having 10-20 nm size distributions. When the particles are so small, they become “single magnetic domains” (as opposed to “multiple magnetic domains” found in bulk magnets) and exhibit high magnetic susceptibility. Thus, superparamagnetic nanoparticles can more strongly and rapidly respond to external magnetic fields with negligible residual magnetization (remanence) and coercivity (the field required to bring the magnetism to zero) become negligible (Wahajuddin and Arora, 2012).

Superparamagnetic cubic ferrites (e.g., magnetite, maghemite; known as superparamagnetic iron oxide nanoparticles - SPIONs), as the most widely studied materials since excellent control over their size distribution and almost perfect physical properties (shape, composition, crystallinity) by simple wet chemistry methods were further investigated in the concept of the thesis to reveal the effect of thick silica coating on magnetic behavior of nanoparticles. Magnetic properties were studied by vibrating sample magnetometry (VSM) and alternating current magnetic susceptibility (ACMS) measurements.

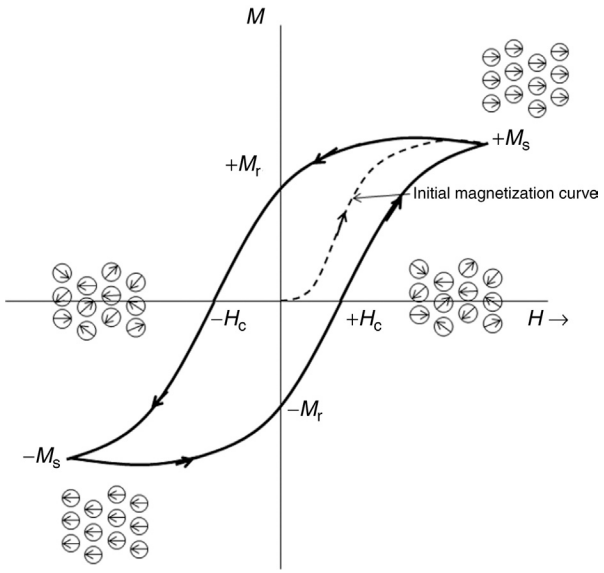

Figure 7. Explanation of a magnetic hysteresis curve (Soler and Paterno, 2017).

Magnetic domains of the ferromagnetic materials that are spontaneously present magnetization at room temperature. They are also responsible from saturation magnetization and hysteresis. Above the critical (Curie) temperature (T_c), spontaneous magnetization disappears, and material becomes paramagnetic. M versus H graph ($M \times H$ curve) is used to present saturation magnetization (M_s) above determined value of the applied field (Figure 7). Phenomenon that occurs when the magnetization is not reduced upon the decrease of the applied field to zero upon saturation is known as hysteresis. Soler and Paterno explains this phenomenon as follows: " ..*If the field is applied to a magnetic material at its demagnetized state, then the magnetization will have a value that ranges from zero to M_s when the field increases in the positive direction. When the field is reduced after saturation, the magnetization decreases to M_r (the remanent magnetization). the field applied in the opposite direction needed to reduce the magnetization to zero is known as the coercive field or coercivity, H_c. Magnetic materials are classified as hard or soft depending on their coercivity value. A hard magnet requires the application of a large field to reduce the remanence to zero or to saturate the magnetization. A soft magnet reaches saturation with small fields and is easily demagnetized. When the reverse field is increased further, magnetization*

saturation is reached with the opposite orientation. When the ferromagnet is demagnetized, the magnetization vectors in the different domains have random orientations and the total magnetization is equal to zero. the magnetization process causes the orientation of all domains to be the same" (Soler and Paterno, 2017) .

Another important parameter to describe superparamagnetic nature of the particle is the blocking temperature (T_B), at which the magnetic anisotropy energy barrier of nanoparticle is overcome by thermal activation energy. T_B can be determined experimentally from the temperature dependent magnetization in zero-field cooled/field cooled (ZFC-FC) measurements (Tadyszak et al., 2017). When a magnetic sample cooled below the blocking temperature, magnetic moments are oriented along the applied magnetic field. Consequently, in a FC measurement, magnetization is larger than the in a ZFC measurement below the blocking temperature. Coincident point of magnetization curves above the irreversibility temperature gives the blocking temperature (Mørup et al., 2011).

Additionally, AC susceptibility (χAC) can be used as is complementary to the measurements in the static (DC) to study the phase transitions and magnetic relaxation of materials. Differential dM/dH response of the magnetization (M) of the sample to an oscillating magnetic field (H) defines the AC susceptibility the material. Methods is useful for operating frequencies vary from 1 Hz to 10 kHz. Beside suitability of method for investigation of the relaxation effects, spin reorientation, transitions to the ordered state or metamagnetic transitions, change in anisotropy energy can be also analyzed by this method (Bałanda, 2013).

1.3.3 Synthesis of antifungal agents their nanoparticle conjugates

As described in section 1.2.3.1, synthetic methods to obtain different GlcN-6-P synthase inhibitors, in good-to-excellent yields, were already described. Among numerous inhibitors reported earlier, FMDP as the most studied inhibitor and its ketoacid derivative BADP with improved resistance to hydrolysis, have been selected to study in the concept of thesis (Milewski et al., 1985; Andruszkiewicz et al., 1986, 2000).

As described by Milewski *et al.* and Andruszkiewicz *et al., s*ynthesis of FMDP and BADP consist of 3 steps, which include: *i)* preparation of *N*-succinimidyl ester derivatives

of α,β-unsaturated acids (mono-methyl fumarate and *trans*-benzoyl acrylic acid); *ii)* reaction of N^2-*tert*-butoxycarbonyl-2,3-diaminopropanoic acid with *N*-succinimidyl esters; *iii)* removal of *tert*-butoxycarbonyl protecting group (Figure 8).

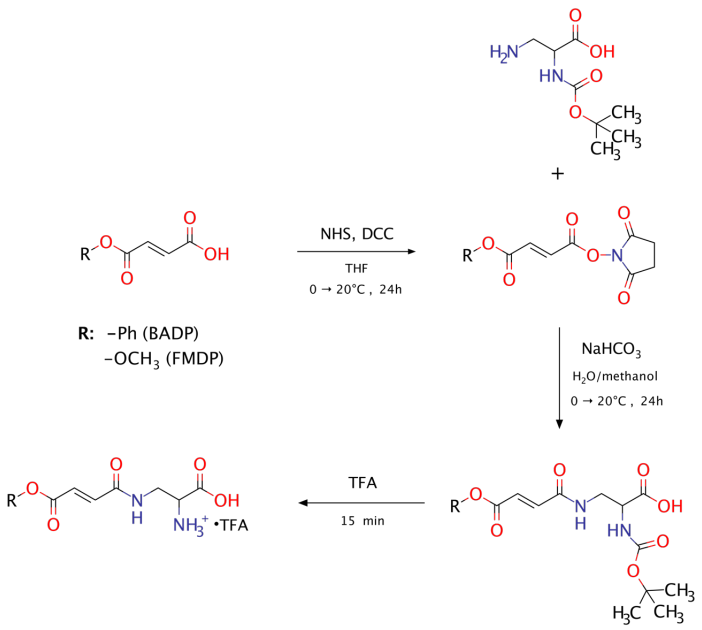

Figure 8. Original synthesis pathway of FMDP and BADP

Despite the synthetic procedure of FMDP and BADP was well-described, the original *tert*-butoxycarbonyl protected forms of the inhibitors does not offer any functionality that could make them quantifiable by any method after their attachment to nanoparticles. On the other hand, removal of *tert*-butoxycarbonyl group that was achieved by HCl-dioxane treatment is not suitable for nanoparticles because HCl can easily dissolve iron oxide nanoparticles (Kim et al., 2008a; Ye et al., 2012). Moreover, removal of protection by TFA would not be suitable since we showed that silica shell is sensitive to acetic acid treatment (see section 5.1). TFA, as a stronger acid than acetic acid, can easily alter the structure of CSNPs. For these reasons, new derivatives of FMDP and BADP with Fmoc protection have been studied in the concept of thesis. Mild conditions required for Fmoc removal (1-20% piperidine-DMF), but also the ease of cleaved-Fmoc protecting group detection by UV-Vis absorption spectroscopy (please see section 5.6) were the reasons behind this choice.

1.4 Objectives of the thesis

The main objective of the thesis was developing a nanoparticle-based platform for the delivery of anticandidal agents, N^3-4-(methoxyfumaroyl)-2,3-diaminopropanoic acid (FMDP) and N^3-trans-4-oxo-4-phenyl-2-butenoyl-L-2,3-diaminopropanoic acid (BADP), to their sub-cellular target, glucoseamine-6-phosphate synthase enzyme. In order to achieve this objective, thesis was aimed to explain following issues:

- **Understanding the mechanisms behind the formation of monodispersed iron oxide-silica core-shell nanoparticles (CSNPs) to develop a biologically compatible material (CHAPTER 3)**
  - Synthesis of monodispersed oleate-capped iron oxide nanoparticles (OA-IONPs) according to previously reported thermal-decomposition method
  - Synthesis of CSNPs having amine functions, based on previously reported microemulsion methods, where the cetyltrimethylammonium bromide surfactants were used as structure directing agents
  - Development of the CSNP preparation method by studying the concentration dependent behavior of OA-IONPs. Development process consist of giving particular attention to conditions inducing the formation of CTA^+-OA-IONPCs and CTA^+-OA-IONPs structures. Formation of CTA^+-OA-IONPs and CTA^+-OA-IONPCs is studied in depth to develop the most suitable structure for biological studies
  - Investigation of surface properties of CSNPs by EELS to assess the suitability of CSNP in surface functionalization studies
  - Investigation of CSNP formation mechanism by detailed structural analysis by HRTEM (EELS) to develop the previously hypothesized mechanisms or propose a new mechanism.

- **Determination of magnetic properties of monodispersed iron oxide-silica core-shell nanoparticles (CSNPs) to reveal their suitability for advanced biological studies in later stages (CHAPTER 4)**

- Investigation of the superparamagnetic state in CSNPs, which is considered as the most favorable functional property for magnetic nanoparticles used in nanomedical application; aimed for future studies which are out of the main topic and objectives of this thesis.

- **Qualitative and quantitative assessment of CSNPs for further organic functionalization studies and development of the GlcN-6-P synthase inhibitors (FMDP and BADP) suitable for the qualitative and quantitative detection of the inhibitors in nanoparticle formulations (CHAPTER 5)**
  - Determination of free amino groups on CSNP surfaces for further chemical functionalization via amide bonding of optically active fluorenylmethyloxycarbonyl (Fmoc) groups.
  - Synthesis of novel derivatives of FMDP and BADP with fluorescent Fmoc protection group to develop an optically detectable drug loading protocol
  - Preparation of OH-PEG-CSNP derivatives via amide bonding to ensure the biocompatibility of CSNPs in highest level and provide free OH groups to prepare inhibitor-CSNP conjugates (Fmoc-FMDP/BADP-PEG-CSNPs) through esterification.

- **Determination of *in vitro* biological activity of GlcN-6-P synthase inhibitor-CSNP conjugates (CHAPTER 6)**
  - Determination of OH-PEG-CSNP uptake efficiency by HeLa, FaDu, MSU1.1 and *Candida albicans* by TEM imaging.
  - Determination of *in vitro* activity of the FMDP-PEG-CSNP and BADP-PEG-CSNP conjugates against human cell lines and *Candida albicans to* define the activity of FMDP and BADP in nanoparticle formulations.

CHAPTER 2

Experimental Section

2.1 Chemicals and Materials

Following reagents, solvents and materials were acquired from Sigma-Aldrich: OH-PEG5K-NHS (average M_n 5000), piperidine (ReganentPlus®, 99%), *N,N'*-diisopropylcarbodiimide (DIC, 99%), N_α-Fmoc-L-2,3-diaminopropionic acid (Fmoc-Dap-OH, 97%), *N*-hydroxysuccinimide (98%), *N,N'*-dicyclohexylcarbodiimide (98%), Fmoc-Osu (Novabiochem®), mono-methyl fumarate (97%), CTAB (≥98%), ethyl acetate (anhyd. 99.8%), chloroform, tetraethylorthosilicate (TEOS, 99%), 3-(aminopropyl)triethoxysilane (APTES, ≥98%), n-hexane (99%), diethyl ether (99.5%), iron(II) acetate (95%), and dialysis tubing (cellulose ester membrane with molecular weight cutoff =14 000). Ethane (≥99.95%) was obtained from Linde. The following reagents and solvents were purchased from Avantor Performance Materials Poland S.A. (formerly POCH S.A.): 2-propanol (99.7%), sodium hydroxide (99.8%), nitric acid (65%), hydrochloric acid (35–38%), ethanol (96%), acetic acid (glacial), and 2-propanol (99.7%). Epoxy resin used for biological experiments was Embed-it low viscosity epoxy kit (Polysciences). The following reagents were purchased from Alfa Aesar: ethyl isonitrosocyanoacetate (oxyma, 97%), *trans*-4-oxo-4-phenyl-2-butenoate (predominantly *trans*, 97%)

2.2 Methods

2.2.1 TEM imaging and structural HRTEM analysis

For time-resolved TEM studies of the silica-coating process, the samples collected at different time intervals of the process were acidified with aqueous 5% HNO3 solution to stop the silica condensation, and then they were centrifuged at 0−5 °C with 13.2 rpm force to remove the reaction medium. The resulting concentrated sample was re-dispersed in ethanol (5 s sonication), then directly applied on 300 mesh copper (carbon film only) TEM grids and left to dry under vacuum. The images were acquired on a JEOL JEM- 1400 transmission electron microscope.

High-resolution TEM (HRTEM) images, scanning TEM high-angle annular dark field (STEM-HAADF) images, and electron energy loss spectroscopy spectrum images

(EELS-SI) were acquired by means of a JEOL ARM200 transmission electron microscope equipped with a field emission gun and a Gatan GIF Quantum EELS spectrometer. Elemental maps and quantification of the EELS data were performed with Gatan DigitalMicrograph software. Obtained SI were quantified using the Egerton method (Egerton, 2011) after denoising by the principal component analysis.

For cryo-TEM experiments, vitrified specimens were prepared in a semiautomated Cryoplunge 3 system from Gatan. A microliter drop of the sample was deposited onto lacey carbon grids (Ted Pella) previously treated with a plasma cleaner to ensure high hydrophilicity of the supporting film. Excess water was removed by gentle blotting with a filter paper and then rapidly plunged into liquid ethane cooled by liquid nitrogen. Such prepared grids were transferred to a Gatan 626 cryo-holder and maintained at −170°C. Cryo-TEM experiments were carried out with a JEOL JEM-1400 transmission electron microscope equipped with a 3k × 4k Gatan camera.

2.2.2 FTIR and Raman spectroscopy

FTIR spectra were recorded with a Tensor 27 (Bruker Optics) spectrometer. Samples were prepared as KBr pellets by applying pressure under a hydraulic press. Before each spectral acquisition session, the background was recorded with pure KBr pellets, and the recorded background spectra were subtracted from each spectrum. Water and CO_2 peaks were automatically removed by the OPUS software used to operate the spectrometer. The spectra were recorded with 2 cm^{-1} resolution by 512 scans in the 4000−200 cm^{-1} range.

Raman spectroscopy measurements were performed with 488, 514 and 633 nm laser excitation using a Renishaw Raman spectrometer attached to a Leica optical microscope with a 50× objective lens. The spectra were recorded over 200−3200 cm^{-1} range with 10 s exposure to 5% laser power (~0.85 mW for 633 nm He−Ne laser) in extended modes.

2.2.3 Dynamic light scattering (DLS) nanoparticle tracking analysis (NTA)

DLS measurements were performed by means of a standard ALV DLS setup consisting of a laser (Coherent OBIS 660 nm, operating at 5 mW), an ALV goniometer, an ALV 7000 digital correlator, and a PerkinElmer avalanche photodiode SPCM-AQR 13. CONTIN algorithm (Provencher, 1982) was applied to analyze the measured correlation functions and obtain the size distribution functions. The measurements were performed at room temperature.

NTA measurements were performed by means of a NanoSight NS500 system (Malvern) equipped with 405 nm laser. Experiments were recorded in 90-215 s time range in scattered light mode, using pure water.

2.2.4 X-Ray Photoelectron Spectroscopy

For the experiments described in section 3.6, analysis performed by XPS-SPECS-Sage HR 100 system, working with a non-monochromatic X-ray source (Al Kα line of 1486.6 eV energy and 350 W). Particles were drop-casted on gold-coated glass (150 nm) and allowed to degas under vacuum.

For the experiments described in section 5.8, analysis performed by SCIENTA R3000 hemispherical photoelectron spectrometer equipped with monochromatic Al K source operating at 300W. The base pressure in the analysis chamber was better than 1x10-10 mbar. All acquired spectra were calibrated to adventitious carbon C1s at 285eV. The overall resolution of the spectrometer during measurements was 0.65eV as a full width of half maximum (FWHM) of the Ag3d5/2 line. After subtraction of the Shirley-type background, the core-level spectra were decomposed into main components with mixed Gaussian–Lorentzian lines (70% G + 30% L for majority of photo-peaks) by a non-linear least squares curve-fitting procedure, using CasaXPS software.

2.2.5 Vibrating sample magnetometry measurements

Magnetic properties of CSNPs nanoparticles were measured using Quantum Design PPMS platform equipped with VSM (Vibrating Sample Magnetometer) for DC and ACMS (Alternating Current Magnetic Susceptibility) probe for AC magnetic susceptibilities. VSM measurement of hysteresis loops were analyzed in the

temperature range of 300 to 4 K, using a maximum applied magnetic field ± 5 T. Zero Field Cooling (ZFC) and Field Cooling (FC) curves were taken for several applied magnetic field (0.01 - 1 T) from 4 to 300 K. VSM magnetic measurements are calculated to the Fe_3O_4 mass respectively. Measurements of the AC magnetic susceptibility were performed at 4 - 300 K temperature range in 10 Hz - 10 kHz frequency window.

2.2.6 NMR analysis

^{1}H and ^{13}C standard spectra, as well as the 2D measurements were recorded by Agilent DD2 800 spectrometer (Agilent Technologies, Santa Clara CA, USA) operating at a frequency of 799.890 MHz for ^{1}H and 201.151 MHz for ^{13}C which was equipped with a $^{1}H/^{13}C$ 5 mm probe head. For all measurements, pure DMSO-d_6 was used as solvent.

2.2.7 ICP-MS analysis of functionalized CSNPs

ICP-MS analyses were carried out separately for OH-PEG-CSNPs, FMDP-PEG-CSNPs and BADP-PEG-CSNPs samples according to PN-EN ISO 17294-2:2016-11 standards. From each aqueous stock sample, 100 µl was transferred to a glass vial and dried at 80-90 °C till the water completely evaporated. Then the dry particles were firstly digested in 0,2 ml piranha solution (3:1, 96% H_2SO_4 – 30% H_2O_2) under 30s sonication in a sonication bath and cooled in liquid nitrogen till it freezes. Then, frozen piranha solutions were mixed with 0,2 ml aqua regia (3:1 HCl - HNO_3) and sonicated for another 30s. Finally, the acid solutions were diluted to 10 ml by addition of Milli-Q water. ICP-MS samples were prepared by diluting 2 ml of the digestion solutions to 10-15 ml in milli-Q water. For each sample 3 different dilutions were prepared, and the ICP-MS analysis results were averaged.

2.2.8 UV-Vis spectroscopy analysis

Absorption spectra were recorded by UV/Vis/NIR LAMBDA 950 spectrophotometer (Perkin Elmer) at 200 – 350 nm region (1 nm intervals) using 700 µl quartz vials having 2 mm path length. For each measurement, background was removed by using identical solvents/ solvent mixtures from respective chemical reactions.

2.3 Synthesis of nanoparticles

2.3.1 Iron oxide nanoparticles

2.3.1.1 IONPs prepared by thermal decomposition method (OA-IONPs)

Oleic acid capped hydrophobic iron oxide nanoparticles (OA−IONPs) were synthesized by the thermal decomposition of the iron oleate complex, according to a previously described method (Park et al., 2004). The iron oleate complex was prepared by dissolving 1.08 g of $FeCl_3 \cdot H_2O$ and 3.65 g of sodium oleate in ethanol/water/n-hexane (3:4:7, v/v/v) and refluxing the mixture at 70 °C for 4 h. When the emulsion cooled down to room temperature, the iron oleate complex was separated from the aqueous phase. To make the phase separation faster, diethyl ether was used. The extracted organic phase was washed several times with Milli-Q water (18 MΩ· cm) and finally evaporated under vacuum. OA−IONPs were prepared by refluxing 3.6 g of the iron oleate complex and 0.57 g of oleic acid in 20 g of 1-octadecene at 325 °C. After cooling the resulting nanoparticle suspension down to room temperature, the nanoparticles were separated from 1- octadecene by diluting the dispersion in 1 part of n-hexane, which was followed by precipitation with 5 parts of ethanol upon centrifugation. This procedure was repeated until a clean supernatant was obtained. The resulting OA−IONPs with an oily appearance were dispersed in n-hexane and stored at 4 °C for later use (Kertmen et al., 2017).

Three different OA-IONPs were prepared by changing the reaction times (25 and 35 and 45 min reactions). Reaction periods were specified as the time passed after the moment that reaction temperature reached 320-325°C.

2.3.1.2 Iron oxide nanoparticle clusters (IONPCs)

IONPCs were prepared by a phase transfer of OA−IONPs under high [CTAB]/[IONP] ratio conditions according to a slightly modified version of the method reported by Qiu *et al*. (Qiu et al., 2010). Briefly, 0.28−0.34 mg of 12.4 nm OA−IONPs in hexane (depending on the concentration, it equals 15−40 µl of hexane stock solution) was further dispersed in 2 ml of chloroform, and this dispersion was added to a 20 ml round flask containing 5.5 ml of 0.135 M CTAB aqueous solution. The resulting emulsion was mixed with a magnetic stirrer until a homogenous mixture was obtained. The

organic phase was removed by heating the mixture to 60 °C under a N_2 flow. A complete removal of the organic solvents was performed *in vacuo* (Kertmen et al., 2017).

2.3.1.3 IONPCs after saponification reaction (Ac-IONPs) and dried oleic acid-capped iron oxide nanoparticles (dOA-IONPs)

To investigate the role of acetate ions as carboxylate ligands, ethyl acetate saponification reaction was carried out in the presence of IONPCs. After preparation of IONPCs described above, the volume of aqueous IONPC dispersion was increased to 50 ml using Milli-Q water in a 100 ml, two-necked round flask. The pH value of this dispersion was adjusted to 11−12 with 300 µl of 2M NaOH solution. The alkaline dispersion of the IONPCs was then heated to 60 °C in an oil bath. Addition of 3 ml of ethyl acetate was followed by a controlled temperature increase to 72−76 °C, and the dispersion was refluxed for 3.15 h while stirring with a magnetic stirrer at 750 rpm stirring rate. Then, the resulting nanoparticle suspension was slowly cooled down to room temperature under continuous magnetic stirring (while keeping the flask in the oil bath). When the suspension cooled down to room temperature, the resulting acetate-capped iron oxide nanoparticles (Ac−IONPs) were placed into a cellulose membrane tubing and dialyzed against Milli-Q water for at least 4−5 days to remove excess CTA^+ molecules and by-products. The dialysis solvent (water) was refreshed every 18−24 h during the dialysis process (Kertmen et al., 2017).

To convert the oily form of OA−IONPs into a dry (powdered) form, the particles were dispersed in a chloroform/hexane mixture and centrifuged at least five times. Each chloroform/hexane dispersion of OA−IONPs was precipitated from ethanol by centrifugation. In each subsequent washing process, the amount of hexane was reduced by 20%. After the last chloroform/hexane wash, the nanoparticle precipitate was rinsed with pure acetone. After evaporation of the solvents, the resulting powder of OA−IONPs was kept at 4 °C for further use. The nanoparticles obtained through the above-described procedure are hereinafter called “dried oleic acid-capped iron oxide nanoparticles” (dOA−IONPs) (Kertmen et al., 2017).

2.3.2 Core – shell nanoparticles (CSNPs)

2.3.2.1 CSNPs prepared by microemulsion (low concentration) method

To understand the effect of **low** [CTAB]/[IONP] ratio conditions in silica shell formation, silica-condensation reaction was performed by addition of ethyl acetate **after** the silica precursors. This method was based on conditions originally described by Kim *et al.* (Kim et al., 2008b) and Ye *et al*. (Ye et al., 2012) to prepare individually CTAB-encapsulated OA−IONPs (CTA^+−OA−IONPs) instead of IONPCs (Qiu et al., 2010). This methos is hereinafter referred to as "microemulsion process". For the phase transfer of OA−IONPs, 60% reduced amount of CTAB (∼45 mM) and approximately 40% reduced amount of OA−IONPs were used in comparison to concentrations used in the nanoemulsion process. The values of other parameters were kept unchanged. After the dilution of CTA^+−OA−IONPs to 50 ml using Milli-Q water, pH of the dispersion was adjusted to 11−12 with the addition of 0.3 ml of 2 M NaOH solution. It was followed by addition of 0.3 ml of TEOS, 50 µl of APTES, and 3 ml of ethyl acetate consecutively. Then, the mixture was refluxed at 70−80 °C for 3.15 h while stirring with a magnetic stirrer. The resulting nanoparticle suspension remained under continuous magnetic stirring for 1 h while slowly cooling down. The nanoparticles were separated from the aqueous solution by centrifugation at 18 000−24 000 rpm at 0 °C and washed three times with ethanol and two times with 2:1 ethanol/water (v/v) mixture with repeated centrifugal separations at −5 °C. Finally, the resulting core−shell structures were dispersed in ethanol and stored at −20 °C for further use (Kertmen et al., 2017).

2.3.2.2 CSNPs prepared by nanoemulsion (high concentration) method

To understand the effect of **high** [CTAB]/[IONP] ratio conditions in silica shell formation, which lead to formation of CTA^+ stabilized OA-IONP clusters (CTA^+-OA-IONPCs), silica-condensation reaction was performed by addition of ethyl acetate **before** the silica precursors. Aqueously dispersible IONPCs formed in **high** [CTAB]/[IONP] ratio conditions were prepared by increasing the water content of the stock IONPCs dispersion to 50 ml using Milli-Q water in a 100 ml three-necked round flask. The pH value of the IONPC dispersion was adjusted to 11−12 by adding 0.3 ml of 2 M NaOH solution. Then 3 ml of ethyl acetate, 0.3 ml of TEOS, and 50 µL of APTES were

consecutively added, and the mixture was refluxed at 72− 76 °C in an oil bath for 3.15 h. The reaction mixture was stirred with a magnetic stirrer at 750 rpm rate. After cooling down the resulting nanoparticle suspension for 1 h under continuous magnetic stirring (while keeping the flask in a warm oil bath), the pH value of the mixture was brought to 3−4 by addition of 1.5 ml of 5% aqueous HNO_3 solution. The nanoparticles were separated from the aqueous solution by centrifugation at 18 000−24 000 rpm at 0 °C and washed three times with ethanol and two times with 2:1 ethanol/water (v/v) mixture with repeated centrifugal separations at −5 °C. Finally, the resulting core−shell structures were dispersed in ethanol and stored at −20 °C for further use (Kertmen et al., 2017). This reaction method is hereinafter referred to as “nanoemulsion process”.

2.3.2.3 Purification of CSNPs prepared by Nanoemulsion method

2.3.2.3.1 Purification by dialysis in concentrated acetic acid solution

To purify the silica-coated nanostructures from excess CTA^+ molecules, a dialysis procedure was performed according to a slightly modified version of a previously described method (Urata et al., 2009). Namely, CSNPs were dispersed in 50 ml of ethanol, 2-propanol, and 2 M acetic acid mixture (1:1:2, v/v/v) and transferred into the dialysis membrane tubing. The nanoparticles were dialyzed against 1 L of the same solvent mixture for 24 h. The process was repeated three times. The amount of CSNPs used in the dialysis was usually half the amount obtained after the nanoemulsion process (Kertmen et al., 2017).

2.3.2.3.2 Purification by dialysis in acetate buffer

In order to purify the silica-coated nanostructures from excess CTA^+ molecules under mild conditions CSNPs, in the amount equal to half the amount obtained after a typical nanoemulsion process, were dispersed in 50 ml of acetic acid/sodium acetate buffer (pH 3.7 – 3.8) and transferred into the dialysis membrane tubing. Nanoparticles were dialyzed against 1 L of the same buffer for seven (7) days. Then solvent was replaced by EtOH-H_2O (1:1, v/v) and dialysis continued for 3 days, followed by dialysis against Milli-Q water for 6-8 h (Kertmen et al., 2017).

2.4 Synthesis of antifungals and their intermediates

Synthesis of antifungal agents, Fmoc-FMDP and Fmoc-BADP, were carried out according to following scheme (Figure 9) based on the original method described in section 1.3.3 and the detailed synthesis procedures explained below:

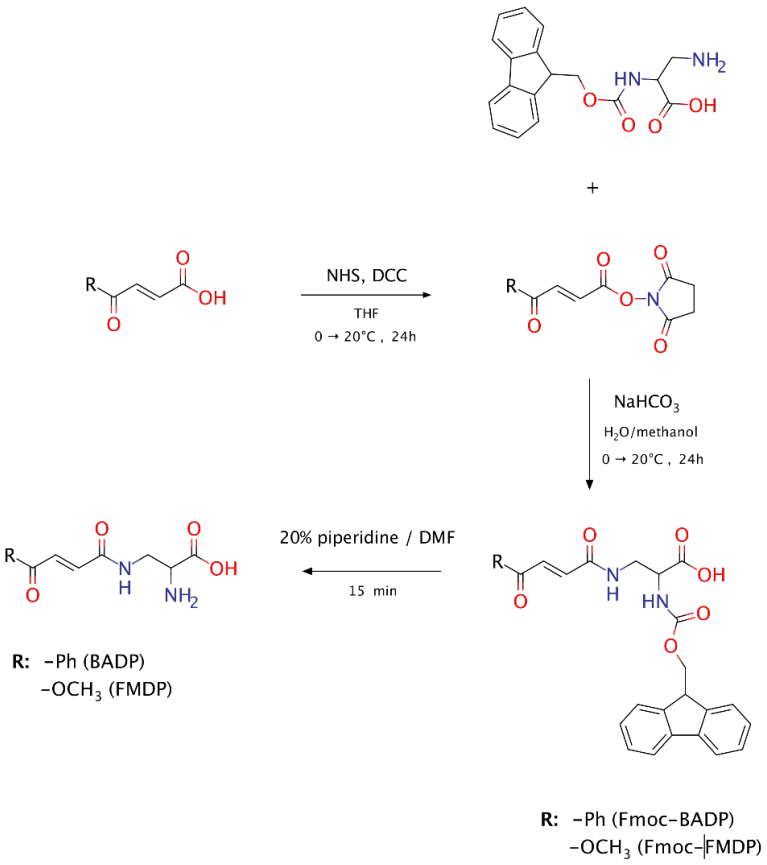

Figure 9. Scheme for synthesis of Fmoc-FMDP, Fmoc-BADP and their intermediates.

2.4.1 *N*-succinimidyl, methyl fumarate

Compound was synthesized according to previously described method (Andruszkiewicz et al., 1986). In details, to the solution of methyl hydrogen fumarate (2.6 g, 20 mmol) in 40 ml tetrahydrofuran, *N*-hydroxysuccinimide (NHS) (2.54 g, 22 mmol) and dicyclohexycarbodiimide (DCC) (4.54 g, 22 mmol) was added at 0°C under stirring. After stirring overnight at room temperature, one of two different methods were flowed: *i)* THF was removed *in vacuo,* resulting white powder including *N,N'*-dicyclohexylurea was re-dispersed in ethyl acetate, *N,N'*-dicyclohexylurea filtered off and residue was crystallized from ethyl acetate/hexane or; *ii)* after *N,N'*-

dicyclohexylurea was filtered off and THF was removed *in vacuo,* residue was crystallized from ethyl acetate/hexane (when the white residue was not fully dissolved in ethyl acetate, it was heated up to boiling point and then hexane was added when it was cooled to room temperature. Crystallization process was initiated at room temperature and continued at 4°C).

2.4.2 *N*-succinimidyl, *trans*-4-oxo-4-phenyl-2-butenoate

Compound was synthesized according to previously described method (Jakubec et al., 2004). In details, to the solution of trans-4-oxo-4-phenyl-2-butenoate (3.53 g, 20 mmol) and *N*-hydroxysuccinimide (NHS) (2.54 g, 22 mmol) in 50 ml THF, DCC (4.54 g, 22 mmol) was added at 0°C under stirring. The mixture was stored at -20°Covernight. *N,N'*-dicyclohexylurea was filtered off and the solvent was removed *in vacuo*. Resulting residue was firstly recrystallized from isopropanol (recrystallization assisted by hot sonication bath) or firstly dissolved in hot isopropanol to let the oily part to precipitate rapidly and then the solution was crystallized from isoporoponal/hexane in a separate flask.

2.4.3 N^2-(Fmoc), N^3-(4-methoxyfumaroyl)-L-2,3-diaminopropanoic acid (Fmoc-FMDP)

Compound was synthesized similarly to previously described method for its *tert*-butoxycarbonyl protected analogue (Andruszkiewicz et al., 1986). In details, to the solution of N_α-Fmoc-L-2,3-diaminopropionic acid (245 mg, 0.75 mmol) and $NaHCO_3$ (630 mg, 7.5 mmol) in 18 ml 2:1 (v/v) water-methanol, *N*-succinimidyl ester of methyl fumarate (170 mg, 0.75 mmol) was added at 0°C under stirring. After 4h, the solvent removed *in vocuo* and replaced by 15 ml water. After adjusting pH with 10% citric acid, product was extracted with ethyl acetate (3x30 ml). After washing the organic phase with saturated NaCl and drying over $MgSO_4$, it was crystallized by addition of hexane.

2.4.4 N^2-(Fmoc), N^3-*trans*-4-oxo-4-phenyl-2-butenoyl-L-2,3-diaminopropanoic acid (Fmoc-BADP)

Compound was synthesized similarly to previously described method for its *tert*-butoxycarbonyl protected analogue (Andruszkiewicz et al., 2000). In details, to the solution of N_α-Fmoc-L-2,3-diaminopropionic acid (326,4 mg, 1 mmol) and $NaHCO_3$ (84 mg, 1 mmol) in 20 ml 1:1 (v/v) water-methanol, *N*-succinimidyl ester of *trans*-4-oxo-4-phenyl-2-butenoate (273 mg, 1 mmol) was added at 0°C under stirring. After stirring overnight, the solvent removed *in vocuo* and replaced by 20 ml water. After adjusting pH with 1 M $KHSO_4$ to pH 2, product was extracted with ethyl acetate (3 x 30 ml). Finally, organic phase was dried over $MgSO_4$. After Addition of minimum amount of methanol to obtain a clear solution, product was crystallized by addition of petroleum ether and ethyl ether.

2.4.5 *cis*-2-(9-Fluorenylmethyloxycarbonyl)amino-cyclopentanecarboxylic acid (Fmoc-cispentacin)

Compound was synthesized according to a combination of previously described methods (LePlae et al., 2001; Caroen et al., 2016). In details, to the solution of 2-aminocyclopentane-1-carboxylic acid (0.375 g, 2.9 mmol) and $NaHCO_3$ (2.44 mg, 14.5 mmol) in 36 ml 2:1 (v/v) acetone-water at 0C, Fmoc-Osu (0.98 g, 2.9 mmol) was added. After stirring overnight at room temperature, reaction mixture was diluted with addition of 12 ml water added and acetone was removed *in vacuo*. Volume of aqueous residue was increased to 50 ml with addition of water and the unreacted content was extracted with 50 ml diethyl ether by stirring for 1h. After the removal of organic layer, aqueous layer was acidified to pH 2 using 1N HCl and the product was extracted with ethyl acetate. Resulting colorless oil was purified by crystallization from n-hexane/chloroform.

2.5 Synthesis of nanoparticle – antifungal conjugates

CSNPs were functionalized according to general scheme shown below (Figure 10):

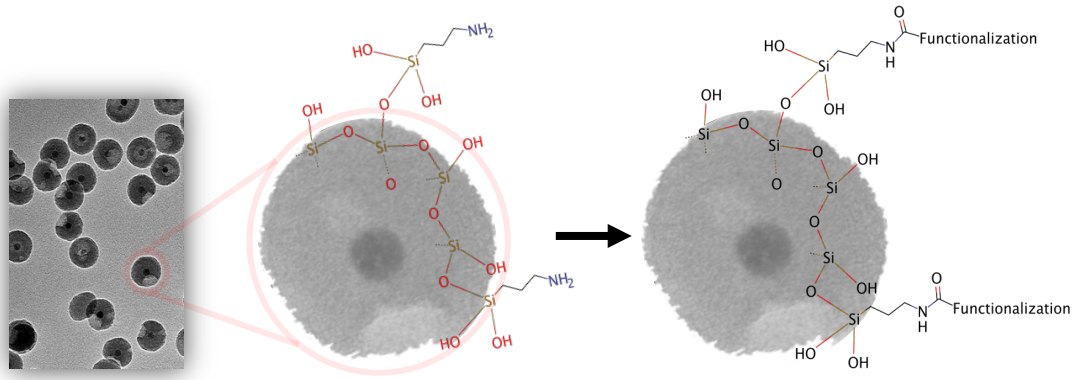

Figure 10. General functionalization scheme of CSNPs via amino groups

2.5.1 Functionalization of CSNPs by Fluorenylmethyloxycarbonyl (Fmoc)

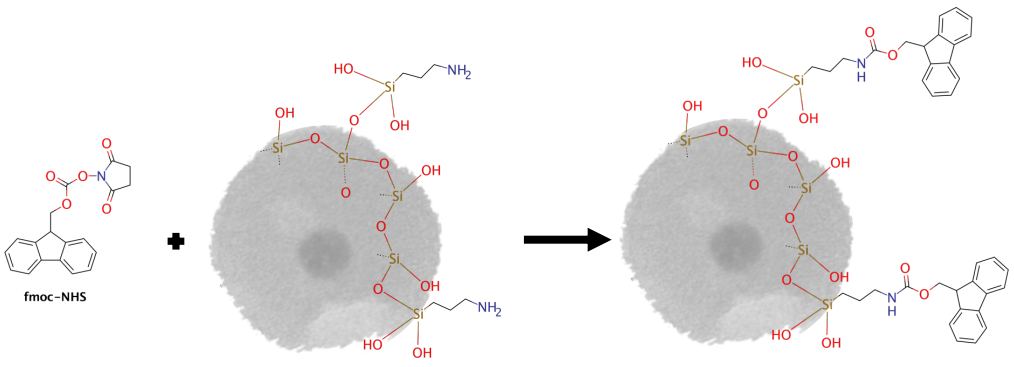

Figure 11. Functionalization of CSNPs by fluorenylmethyloxycarbonyl

Dialyzed CSNPs were directly functionalized by fluorenylmethyloxycarbonyl (Fmoc) groups (Figure 11) in order to determine the amount of active amino groups on the surface particles, according to slightly modified version of a previously reported method (Zhang and Chen, 2012). Briefly, a specific amount of nanoparticles from a stock solution was respectively washed with 1 x EtOH, 1 x H_2O and 1 x 0.1 M NaB buffer (pH 8,15 - 8,50). Then the particles were dispersed in 1 ml 0,1 M NaB buffer and added to 1 ml solution containing 1 mM Fmoc-NHS in a 2 ml Eppendorf. Reaction was carried out for 3h under vigorous shaking in a thermoshaker at room temperature. After the removal of reaction solvents by centrifuge, particles were thoroughly washed with 1:1 NaB – acetonitrile mixture until no absorbance was detectable in Uv-vis spectroscopic measurements. Particles were then dispersed in 1 ml of acetonitrile and added to 1 ml of 1% piperidine-DMF mixture in a 2 ml Eppendorf to release the covalently attached Fmoc group. After 24h of vigorous shaking in a thermoshaker at room temperature, particles were centrifuged and the supernatant containing piperidine-Fmoc adduct was separated into a clean vial.

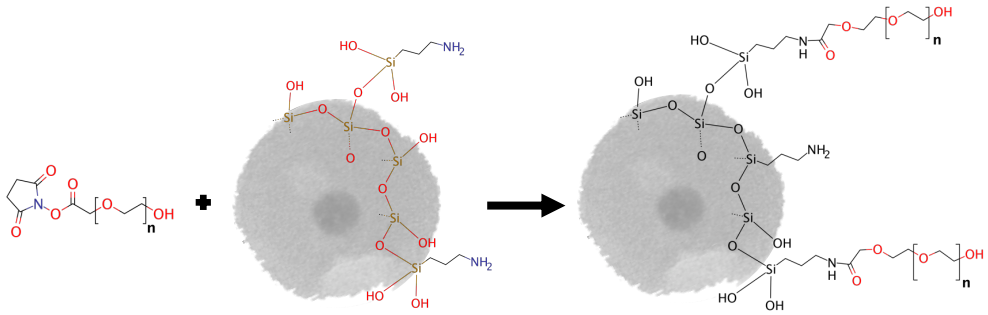

Figure 12. Functionalization of CSNPs by OH-PEG.

Amount of Fmoc group attached to surface of CSNPs were calculated by comparison to a calibration curve separately obtained from piperidine-Fmoc adduct obtained from *cis*-pentacin-piperidine reaction. In order to obtain piperidine-Fmoc adduct, 10.1 µM *cis*-pentacin in 1 M acetonitrile was added to 1 ml of 1% piperidine-DMF mixture in a 2 ml Eppendorf. After 24h of vigorous shaking in a thermoshaker at room temperature, particles were centrifuged and the supernatant containing

piperidine-Fmoc adduct was diluted to 6 (six) different concentrations and absorbance were recorded with UV-vis spectrometer as described.

2.5.2 Preparation of OH-PEG functionalized CSNPs (OH-PEG-CSNPs)

Dialyzed CSNPs were respectively washed with 1 x EtOH, 1 x H_2O and 1 x 0.1 M NaB buffer (pH 8,15 - 8,50). Then the particles were dispersed in 1.75 – 2 ml 0.1 M NaB buffer. After cooling to 0 – 4 °C, particles were added to a 2 ml Eppendorf containing 15-20 mg OH-PEG-NHS. Reactant was added in excess, calculated according to number of amino groups available on CSNP surfaces (see section 5.2 for quantification of amino groups. Since the amount of dialyzed CSNPs used for amino group quantification varies from one experiment to another due to different stock solutions of CSNPs prepared for each experiment, OH-PEG-NHS was used in great excess to make sure that maximum amount of amino groups were functionalized). Reactions were carried out at 4 °C with a thermoshaker for 30-60 min and then continued at room temperature for another 2 – 2.5h. Resulting OH-PEG-CSNPs (Figure 12) were washed with 2 x H_2O and 2 x EtOH. Samples were either immediately used for further synthesis or stored in EtOH at 4°C for later use.

2.5.3 Preparation of Fmoc-FMDP-PEG-CSNPs and Fmoc-BADP-PEG-CSNPs

In order to attach Fmoc-FMDP and Fmoc-BADP to CSNPs, esterification through OH-PEG groups were primarily aimed. However, considering that OH-PEG functionalization might have not proceeded with 100% efficiency, free-amino groups that might be remaining on CSNPs after OH-PEG attachment in first step were also considered for amide formation (Figure 13). Therefore, a method, which was suitable for both esterification and amidation reactions in water containing environment was adopted with some modifications (Wang et al., 2012). Amount of Fmoc-FMDP and Fmoc-BADP to functionalize with OH-PEG-CSNPs were determined by the amount of stock CSNP dispersions used for free-amino group determination as described in section 2.5.1 and shown in section 5.2. In order to make sure that maximum amount of free

amino and OH groups available on the surface of CSNPs were functionalized by Fmoc-FMDP and Fmoc-BADP, excess amount of reagents were used. Briefly, assuming that the amount of amino groups were equal to 1.5 x10^{-8} mol, fifteen-fold excess of Fmoc-FMDP or Fmoc-BADP (2.3 x 10^{-7} mol), 22,5-fold excess of diisopropylcarbodiimide (3.4 x 10^{-7} mol) and oxyma (3.4 x 10^{-7} mol), and 90-folds excess of $NaHCO_3$ were used. In order to adjust the concentrations correctly, 0.68 mM of DIC / oxyma in acetonitirile, 13.6 mM of $NaHCO_3$ in water, 0.45 mM of Fmoc-FMDP or Fmoc-BADP in 5% DMF-acetonitirile were prepared and they were added to OH-PEG-CSNPs in the ratios of 5:5:1:5:4 (v:v:v:v:v, DIC – oxyma – $NaHCO_3$ – Fmoc-FMDP/Fmoc-BADP - OH-PEG-CSNPs). Reactions were carried out in 2 ml Eppendorfs for 8 h at room temperature.

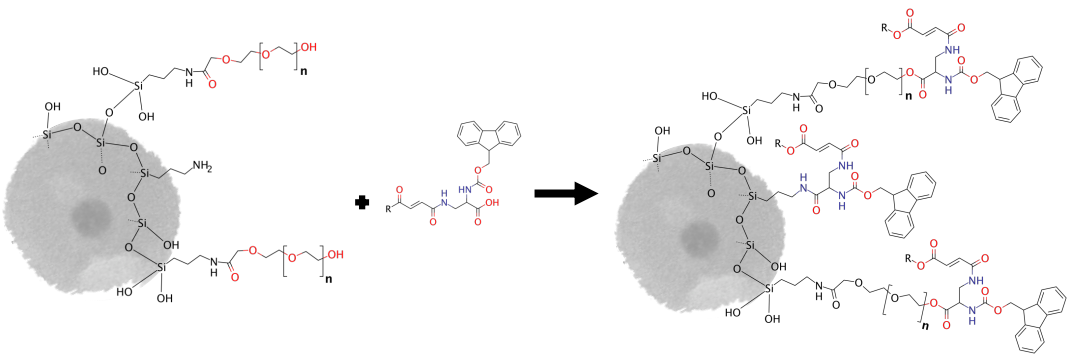

Figure 13. Functionalization of CSNPs by Fmoc-FMDP or Fmoc-BADP via ester and amide bonds. R: -OCH_3 or -Ph

2.5.4 Preparation of FMDP-PEG-CSNPs and BADP-PEG-CSNPs

Fmoc groups were cleaved by addition of either 1% (for 24h) or 20% (for 15 min) piperidine-DMF solutions to the solutions of pure Fmoc-cispentacin, Fmoc-FMDP and Fmoc-BADP in acetonitrile. Release of Fmoc groups were determined by recording the absorption spectra of resulting piperidine-Fmoc adducts.

2.6 *In vitro* Biological experiments

2.6.1 Cell lines and cell culture conditions

Human cervical cancer (HeLa), hypopharyngeal carcinoma (FaDu) cell lines and *Candida albicans* were obtained from American Type Culture Collection (ATCC). Human

fibroblast (MSU1.1) cell line was obtained from Prof. C. Kieda (CBM, CNRS, Orleans, France). Cells were cultured in a complete medium (Dulbecco's Modified Eagle's Medium (DMEM) or Minimum Essential Medium (MEM- FaDu cell line) supplemented with 10 % fetal bovine serum (FBS), 100 units/ml penicillin, 100 µg/ml streptomycin and grown at 37 °C in humidified atmosphere containing 5% CO_2. Growth medium of human cells were supplemented by L-alanyl-L-glutamine dipeptide (glutamax).

2.6.2 Cytotoxicity and viability assays of human cells

Hypopharyngeal carcinoma cell line (FaDu) and normal fibroblasts (MSU1.1) were used for *in vitro* cellular toxicity studies of OH-PEG-CSNPs, FMDP-PEG-CSNPs and BADP-PEG-CSNPs functionalized with drugs. Cells (1×10^3 cells/100 µl) were seeded onto 96-well plates and incubated overnight at 37 °C under a 5 % CO_2 atmosphere. The medium in the wells was then replaced with fresh medium containing increasing concentrations of OH-PEG-CSNPs, FMDP-PEG-CSNPs and BADP-PEG-CSNPs (2.5 - 50 µg/ml) and incubation continued for 24 h. The medium without any nanoparticles and with 50% DMSO were used as a negative and positive control, respectively. The cytotoxic effect of nanoparticles on human cell lines was determined by WST-1 assay according to manufacturer's instructions (Takara, Clonetech). Briefly, 10 µl of WST-1 solution was added to each well and the plates were further incubated. After 2 h, the absorbance was measured with a microplate reader (Anthos Zenyth 340rt) at 450 nm and 650 nm as reference. The mitochondrial function and, by extension, the relative cell viability (%) related to the negative control were calculated by test sample/negative control×100%. Results are reported as the average ± standard deviation (SD) of wells performed in triplicate.

2.6.3 Growth kinetics and viability of *Candida albicans.*

Candida albicans strain ATCC-10231 (wild type, intrinsically resistant to multiple drugs) was used in this study. For routine culture, cells from stocks stored at -80 °C were propagated by streaking onto Yeast-peptone-dextrose (YPD) agar plates, and incubation overnight at 30°C. From these, a loopful of the overnight Candida growth was inoculated into flasks containing 8 ml of YPD liquid media in an orbital shaker at 200 rpm and 30 °C

for 16 h. *Candida albicans* cells were diluted between 2.5 x 10^5 and 5x10^5 cells/ml in YPD medium. 50 µl of the cell suspension were then added to each well of a 96-well plate, then the appropriate concentrations of OH-PEG-CSNPs, FMDP-PEG-CSNPs and BADP-PEG-CSNPs (0-50 µg/ml) were added and placed at 30°C incubator. Turbidity of the suspension, a measure of fungal growth, was measured spectrophotometrically at 570 nm (OD_{570nm}) with a microplate reader (Anthos Zenyth 340rt) at every 2 h interval up to 10 h and then up to 24h. To avoid potential interference during optical measurements, caused by the light scattering properties of the nanoparticles, the same liquid medium without microorganism, but containing the same concentration of nanoparticles were used as blank controls. The readings obtained were plotted and comparative studies were performed between control with and without nanoparticles. Data are reported as the average ± standard deviation (SD) of wells performed in triplicate.

2.6.4 Cellular internalization studies

Internalization of OH-PEG-CSNPs was assessed by TEM analysis. Both *Candida albicans* and human cancer cell line (HeLa cells) were exposed to 25 µg/ml of nanoparticles. After 3h (for *Candida albicans*) or 3h and 24 h (for HeLa), cells were washed three times with PBS, fixed with a 2,5 % glutaraldehyde in PBS for 2h. Washed with PBS. Fixed cells were post-fixed in 2% osmium tetroxide in PBS for 1h, washed 3 x PBS, 2 x D_2O for 10 min, dehydrated through a graded ethanol series (50%, 70%, 80%, 90%, 2x 100%) followed by acetone for 10 min, and embedded in epoxy resin. After 48 h incubation at 60º C, ultrathin sections (100 nm) were prepared using RMC ultramicrotome. Then, the ultrathin sections were stained with 2% uranyl acetate to improve the contrast before observation under JEM 1400 transmission electron microscope.

CHAPTER 3

Preparation of Nanoparticles

3.1 Morphological analysis of nanoparticles by TEM imaging

3.1.1 IONPs prepared by thermal decomposition method (OA-IONPs)

OA-IONP size distribution were extracted from measurements of ≥500 individual particles using Fiji software (Schindelin et al., 2012). Histogram of the 30 min thermal decomposition reaction demonstrated that the OA−IONPs had an average diameter of 12.4 ± 0.87 nm (Figure 14) (Kertmen et al., 2017).

Histogram of the 25 min thermal decomposition reaction demonstrated that the OA−IONPs had an average diameter of 7.92 ± 0.11 nm (Figure 15), whereas the particles from 45 min thermal decomposition reaction were highly polydisperse, having a very broad size distribution with 2-27 nm particles (Figure 16) (Kertmen et al., 2017).

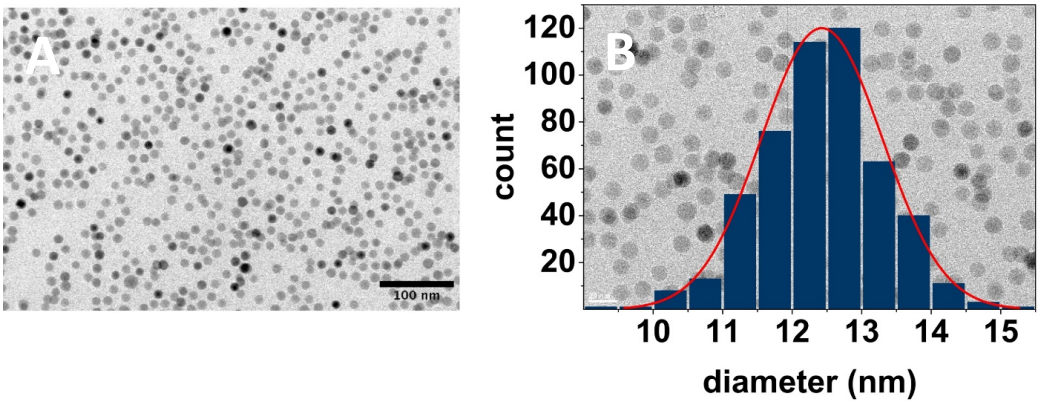

Figure 14. (A) Low-magnification TEM image of 30 min synthesized OA−IONPs and, (B) high-magnification TEM image of OA−IONPs where the overlapping graph shows their size distribution.

TEM observations of the highly-dispersible OA−IONPs synthesized by the thermal decomposition method showed that the particles of 30 min (~12 nm sized, Figure 14) and 25 min (~ 8 nm sized, Figure 15) processes were in nearly monodispersed form. Narrow size distributions and sensitive size tuning of the particles (4 nm variance between the preparations); as well as the highly dispersible nature of the particles in

organic solvents, such as hexane and chloroform, makes the thermal decomposition process a highly valuable method; which all together proved that the OA-IONPs good candidates for silica coating processes in two-solvent systems. Despite the fact that the 45 min thermal decomposition process showed that the extended reaction times leads to high particle size distribution and polydispersity, 25 and 30 min processes were the most promising methods to be adopted.

Figure 15. (A) Low-magnification TEM image of 25 min synthesized monodispersed

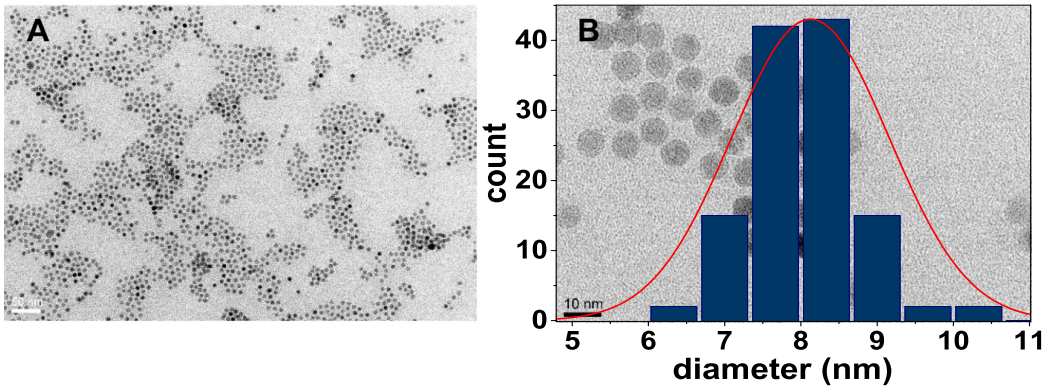

OA–IONPs and, (B) high-magnification TEM image of OA–IONPs.

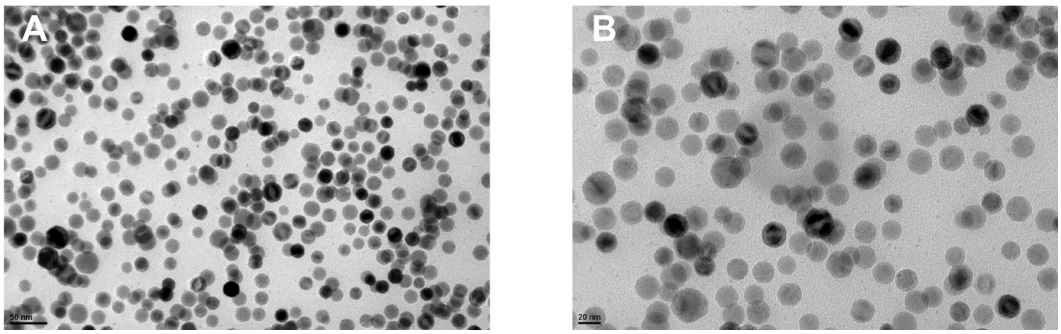

Figure 16. (A) Low-magnification TEM image and, (B) high-magnification TEM image of 45 min synthesized OA–IONPs OA–IONPs.

3.1.2 Iron oxide nanoparticle clusters (IONPCs)

Cryo-TEM observations confirmed that the physical encapsulation of OA–IONPs by CTAB molecules under high [CTAB]/[IONP] ratio conditions resulted in the formation of IONPCs having 100–200 nm diameter (Figure 17) (Kertmen et al., 2017).

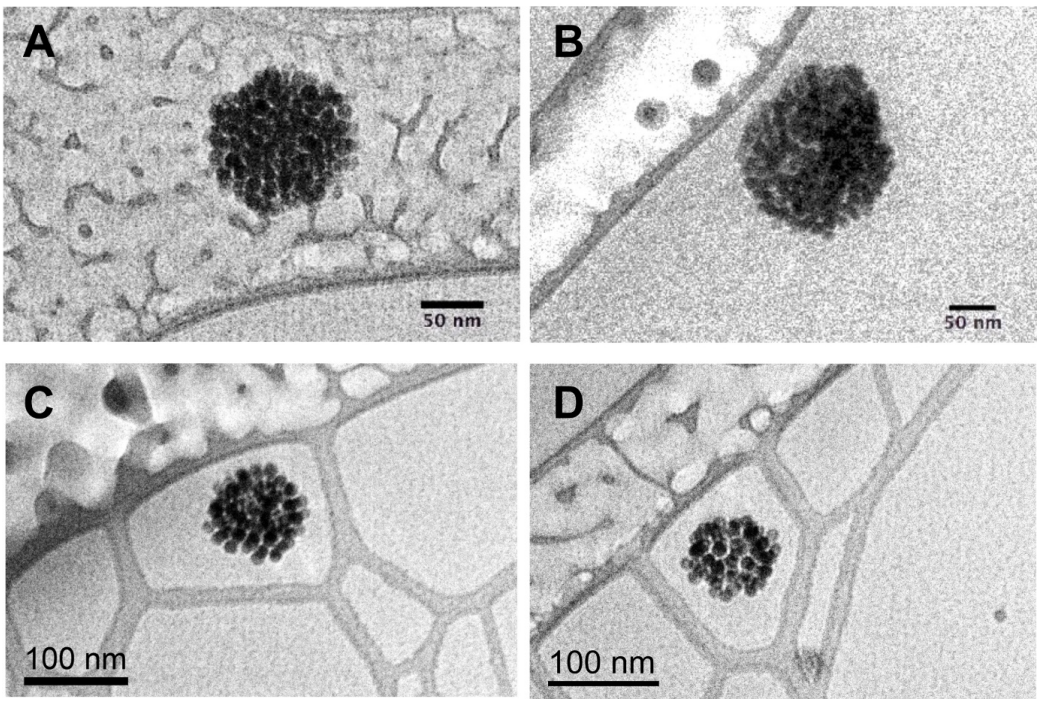

Figure 17. A-D) cryo-TEM images of IONPCs (grids were prepared using highly diluted dispersions of IONPCs).

Cryo-TEM observations confirmed that the physical encapsulation of OA−IONPs by CTAB molecules under high [CTAB]/[IONP] ratio conditions resulted in the formation of IONPCs having 100−200 nm diameter (Figure 17A-D).

3.1.3 Core – shell nanoparticles by microemulsion versus nanoemulsion method

A typical microemulsion process using low [CTAB]/[IONP] ratio and by addition of EtOAc after silica precursors showed that low ratio conditions resulted in highly porous silica formations with uneven edges and a highly agglomerated state (Figure 18A). Iron oxide cores were not centered within the silica shells (Figure 18B). It was even possible to observe some silica shells that lost their iron oxide cores, thereby having empty cores (Figure 18C). Observed structures rarely consisted of single IONP cores but mostly of multiple (clustered) cores and many empty silica structures or uncoated clusters(Figure 18D-F) (Kertmen et al., 2017).

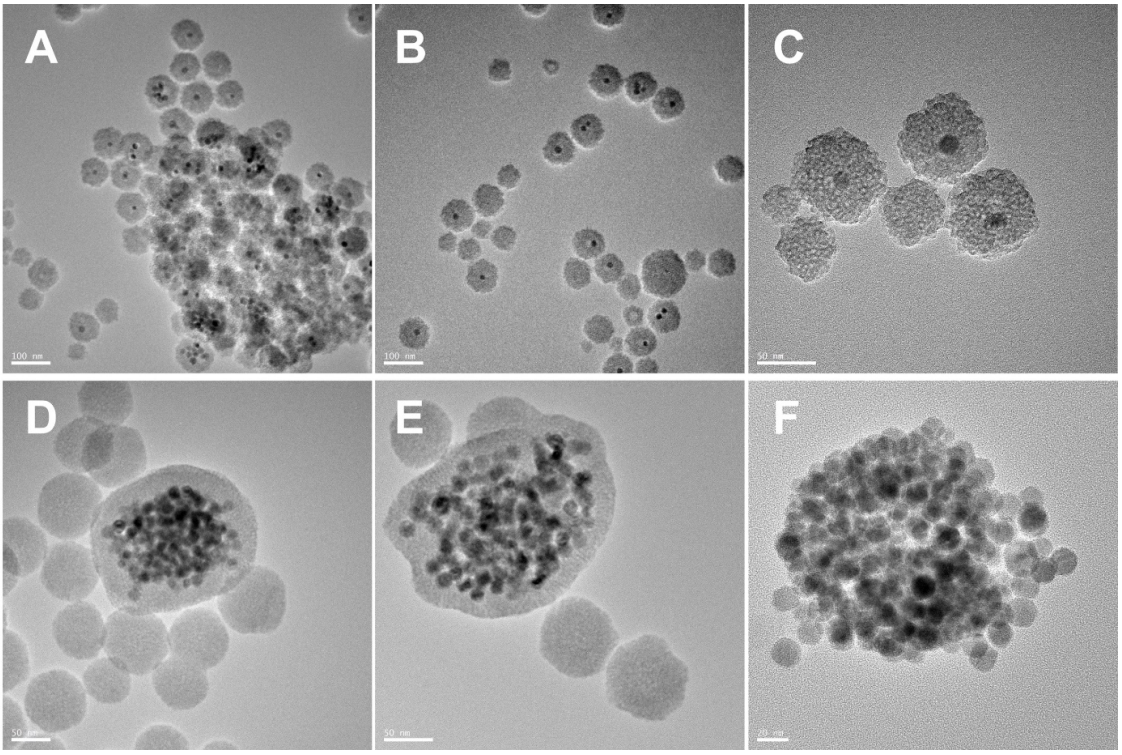

Figure 18. A,B) low-magnification and, C-F) high magnification HR-TEM images of CSNPs prepared by microemulsion method

Nanoemulsion process, as the modified version of the microemulsion process by addition of silica precursors (TEOS and APTES) after ethyl acetate, was analyzed by TEM. Majority of the nanoparticles had single iron oxide cores, whereas few structures appeared to be having double or very rarely multiple cores (Figure 19A–C). The size distribution histogram was created by analyzing 1000 single-core structures. The normal size distribution model fitted to the histogram had a mean value of 58 and 4.2 nm full width at half-maximum (Kertmen et al., 2017).

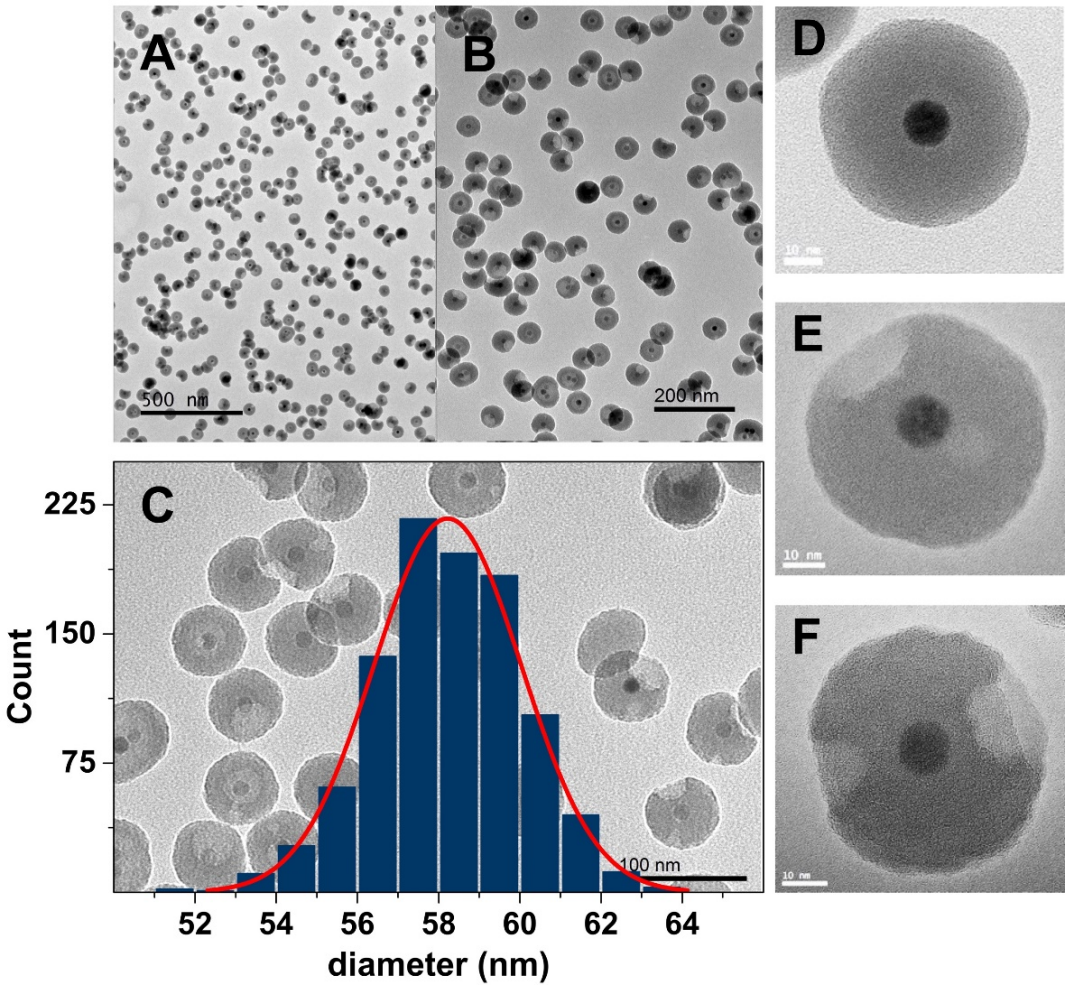

Figure 19. A,B) CSNPs shown in different levels of low-magnification, (C) high magnification TEM image of CSNPs prepared by nanoemulsion method. Overlapping graph shows their size distribution, and (D-F) High magnification HR-TEM images of the individual CSNPs prepared by nanoemulsion method.

When the polydisperse IONPs from 45 min thermal decomposition method was used, overall nanoemulsion process resulted in highly agglomerated core-shell structures. Red arrows indicate the very small OA-IONPs formed as a result of the extended thermal decomposition process (Figure 20).

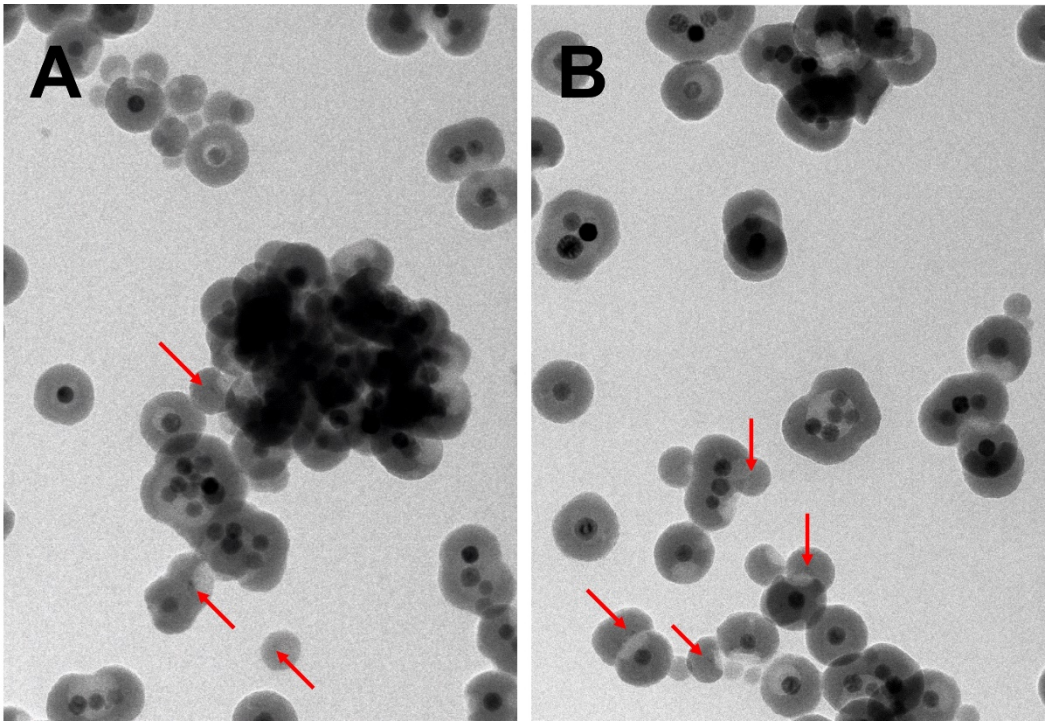

Figure 20. A,B) Nanoemulsion reaction performed with OA-IONPs having very wide size distribution (polydisperse). Red arrows indicates the silica shells with the tiniest iron oxide cores.

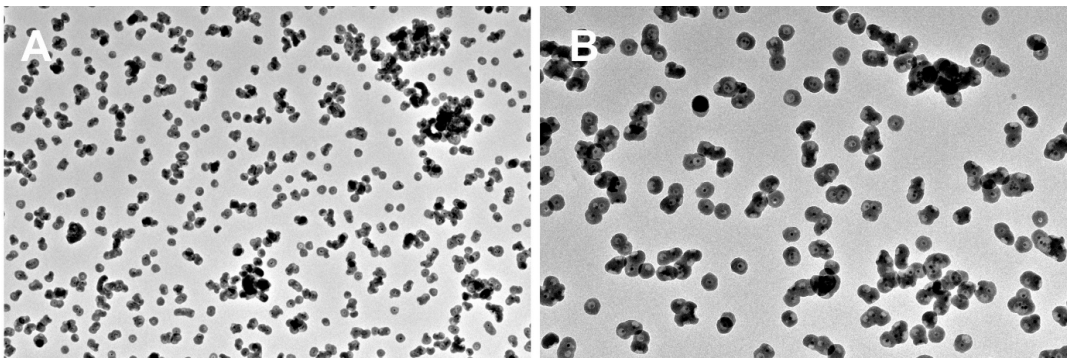

Figure 21. A,B) CSNPs synthesized by nanoemulsion method in the presence of elevated amounts of CTAB (6x CTAB than typical microemulsion method and 2xCTAB than typical nanoemulsion method).

By using 12 nm sized OA-IONPs from thermal decomposition process, low and high [CTAB]/[IONP] ratio conditions were employed in microemulsion and

nanoemulsion processes to form silica shells around OA-IONPs. A typical, well-known two solvent (microemulsion) system in low [CTAB]/[IONP] conditions, where the ethyl acetate as oil phase was used by addition after the silica precursors, efforted highly mesaporous silica structures (Figure 18). Most of the silica structures formed by this process were either empty/coreless and agglomerated or multiple cored silica shells. Despite the fact that therein used method is called "microemulsion method", in comparison to true microemulsion systems where a hydrophobic solvent creates an oily phase in water, ethyl acetate does not fully capable of forming an oily phase because of saponification reaction induced by highly basic aqueous continues phase (pH of aqueous base was adjusted to 11-12 before addition of reagents and reactants. Please see section 2.3.2.1). Thus, microemulsion term was found to be quite misleading to name the process. On the other hand, the hydrolysis kinetics of the TEOS is well-known to be proceeding rapidly in basic conditions (Stöber et al., 1968); which could be the reason of empty silica formations in microemulsion system (there is not enough time to coat OA-IONPs. In other words, formation of coreless silica particles is more favored than coating IONPs).

The impact of EtOAc saponification on silica coating in high [CTAB]/[IONP] ratio system was studied by simply addition of EtOAc as the first step, before the silica precursors (APTES and TEOS) are added. This process was termed as **"nanoemulsion method"** to distinguish it from the general microemulsion process. By allowing saponification reaction of EtOAc at first step, formation of "true emulsions" in continues water phase was aimed. When saponification reaction was fully employed at first place, the pH of system was buffered to pH 7 upon EtOAc hydrolysis. Adjustment of pH ensured that silica precursors in the next step were not rapidly hydrolyzed. However, more importantly, it was ensured that the addition of silica precursors into pH 7 system enabled the formation of oil-in-water emulsions by silica precursors by making use of immiscibility gap between water and hydrophobic TEOS (Donatti and Vollet, 1996; Vollet et al., 1996; Kertmen et al., 2017).

TEM observations after the nanoemulsion process demonstrated that the CSNPs were highly uniform and monodispersed with "apple bite-like" cavities on their surfaces. The majority of the nanoparticles had single iron oxide cores, whereas few structures appeared to be having double, or very rarely multiple cores (Figure 19). The

size distribution histogram was created by analyzing 1000 single-core structures. The normal size distribution model fitted to the histogram had a mean value of 58 and 4.2 nm full width at half-maximum, which confirmed the high-degree monodispersity achieved by the nanoemulsion process. Notably, using 45 min synthesized OA-IONPs with high size distribution caused the silica shells to be fused to each other (Figure 20); while using the much higher [CTAB]/[IONP] ratios resulted in non-spherical silica shell formations with different level of silica shell fusing problems (Figure 21); which emphasized that the quality (monodispersity) of OA-IONPs and CTAB concentrations are primarily and equally important (Kertmen et al., 2017).

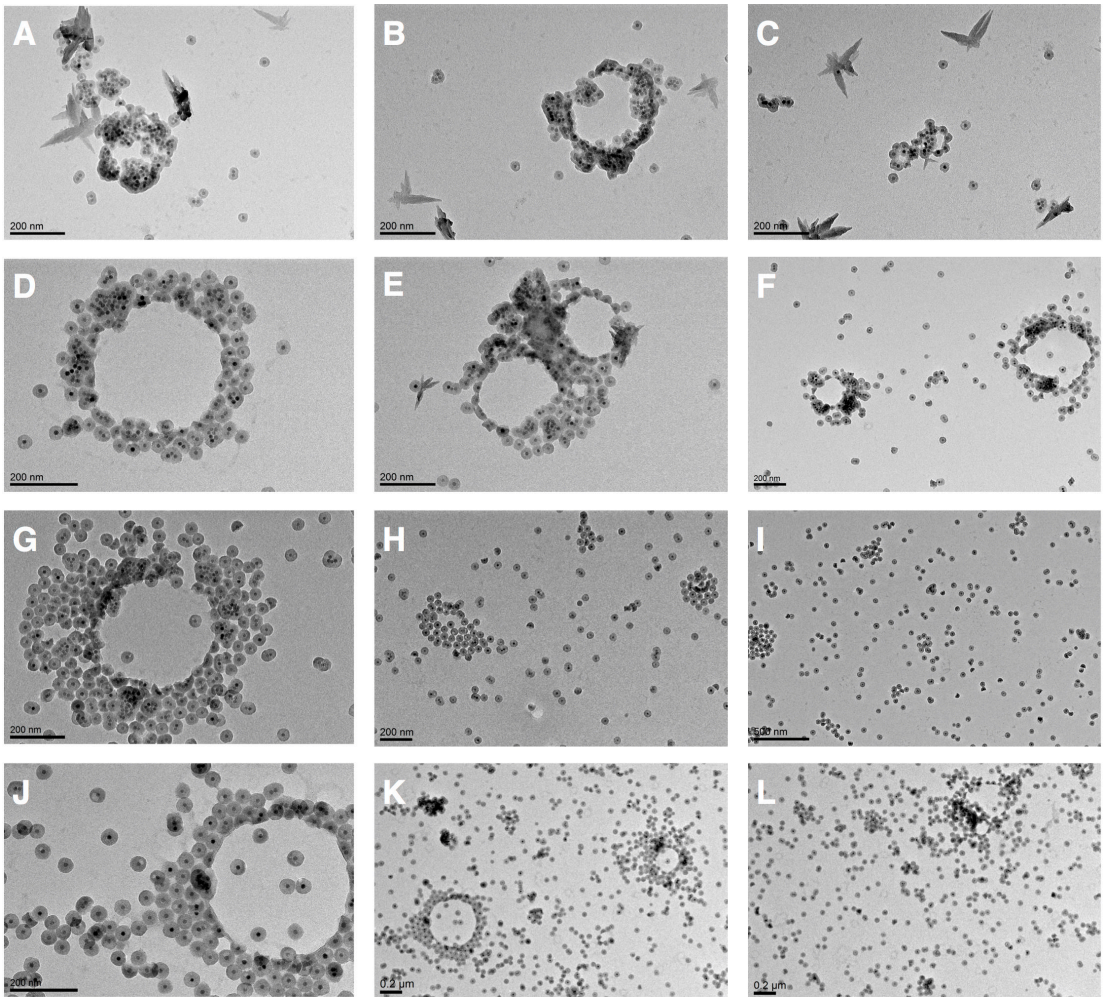

Figure 22. Time-resolved TEM observation of the silica-coating reaction progress: (A−C) 180 min after the silica precursor addition; (D−F) 195 min after the silica precursor addition; (G−I) 210 min after the silica precursor addition; and (J−L) 225 min after the silica precursor addition.

3.2 Time-resolved TEM and cryo-TEM observations of CSNP formation

Samples from nanoemulsion process were collected in intervals of 15 min, between 180 and 225 min after initiating the nanoemulsion process and analyzed by TEM (Figure 22). Images showed formation of ring-like hollow structures 400−600 nm in diameter. The rings were formed by thin but heavily iron oxide-loaded silica shells at 180 min (Figure 22A,B). However, these iron oxide agglomerations were seen undergoing a deagglomeration process by spreading beside the rings that resulted in an increase in the ring widths till 210 min (Figure 22A−I). At 210 min, larger rings were seen to be still intact by keeping the core−shell structures attached (Figure 22G), however, smaller rings were already collapsed and started to release core−shell structures to the environment (Figure 22H). At 225 min, the number of particles around the rings started to decrease by the release of individual core−shell structures (Figure 22J,K). Core− shell structure release after 225 min gave rise to the highest amount of independent core−shell structures observed (Figure 22L). As the time progressed, the increase in the number of individual core−shell structures can be clearly observed (Figure 22C,F,I,L) (Kertmen et al., 2017).

Acidification of the nanoemulsion reaction environment results in rapid reaction quenching and increases the silica sol rigidity. Acidification procedure was carefully performed during each subsequent centrifugal sample preparation process to make sure that maximum silica condensation and rigidity were achieved. Consequently, conventional TEM images of the acidified samples corresponding to 180−225 min of a typical nanoemulsion process revealed hemispherical IONPC formations (Figure 23A−D) (Kertmen et al., 2017).

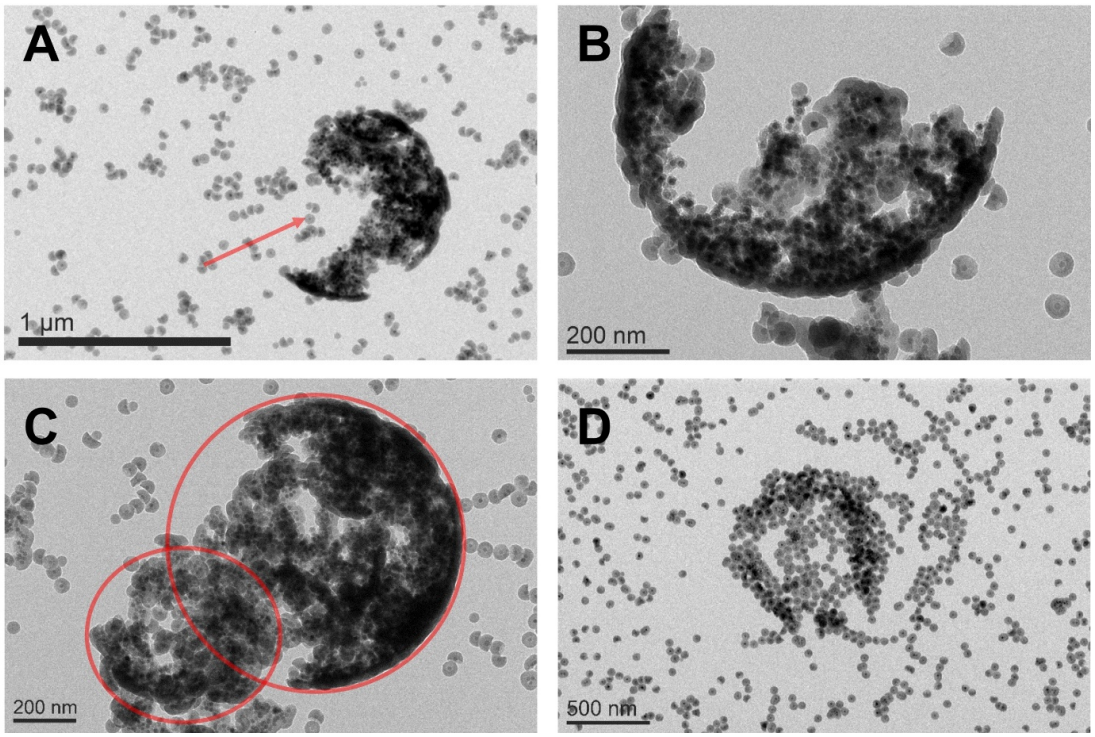

Figure 23. A–C) Hemispheres of IONPCs partially coated with silica formed after 180 min of the nanoemulsion process. Red circles in image "C" indicate the positions of two hemispheres overlapping, D) Hemi- sphere of IONPCs with almost full silica coating on every single IONP building block formed around 225 min of the nanoemulsion process. Hollow opening of the hemisphere positioned perpendicularly to the viewing angle. If "image A" was observed from the angle shown with the red arrow, the hemisphere would be positioned like the one in "image D"

Samples collected at 120 min of the typical nanoemulsion process for cryo-TEM observations showed the existence of vesicular (nanoemulsion) structures (Figure 24). Fusion of nanovesicles to the IONPCs was observed to change the spherical morphology of the clusters (Figure 24A,B). However, a completed fusion process was found to result in a nearly spherical hybrid nanovesicle–IONPC formation (Figure 24C) (Kertmen et al., 2017).

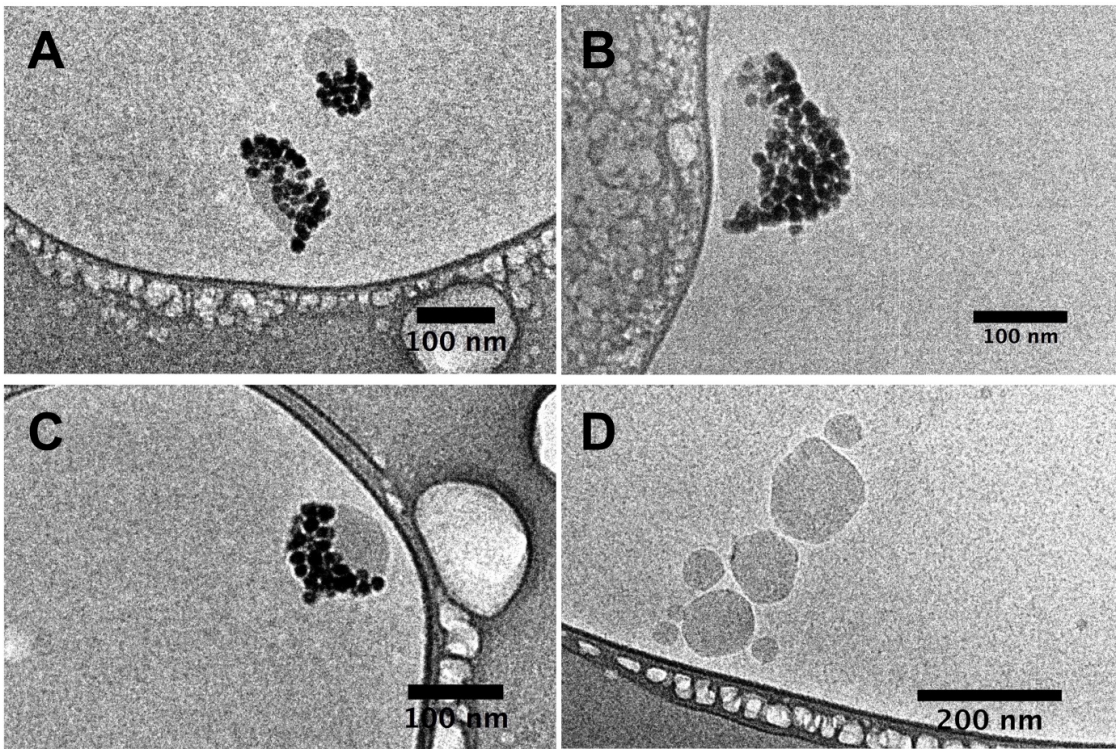

Figure 24. A–C) Cryo-TEM images of the nanoemulsion process collected at 120 min of the reaction show the fusion of IONP clusters and silica nanovesicles (nanoemulsions) and, D) independently coexisting nanovesicles found in the same sample before coalescence to IONPCs.

As important as achieving a true emulsion system, significant attention was paid to the behavior of the OA-IONPs in high [CTAB]/[IONP] ratio conditions. The use of low [CTAB]/[IONP] ratios were previously reported to be crucial to obtain monodisperse CSNPs (Kim et al., 2008a; Qiu et al., 2010; Ye et al., 2012) and high [CTAB]/[IONP] ratios were previously reported to yield IONPCs-silica core–shell structures (IONPCs@SiO_2) (Qiu et al., 2010). Because both methods were based on the base-catalyzed silica condensation in an oil-in-water system, it was sensible to assume that [CTAB]/[IONP] ratios play a key role in monodisperse CSNP preparation. Correspondingly, cryo-TEM observations just after the encapsulation of OA-IONPs by CTAB molecules in high [CTAB]/[IONP] ratio conditions showed that OA-IONPs form IONPCs as it was reported earlier (Qiu et al., 2010). As seen in Figure 17, the physical encapsulation of OA–IONPs by CTAB molecules under high [CTAB]/[IONP] ratio conditions resulted in the formation of IONPCs having 100–200 nm diameter. However, strikingly, it was possible to obtain

monodispersed CSNPs (Figure 19) from IONPCs by means of employing saponification reaction with EtOAc and allowing silica precursors to form emulsions; which was regarded as an important finding to be investigated in depth (Kertmen et al., 2017).

When based on earlier reports, it is clear that addition of silica precursors directly into pH 12 aqueous system catalyzes the silica precursor hydrolysis mediates the formation monodispersed CSNPs **in low [CTAB]/[IONP] ratio conditions** (Kim et al., 2008a; Qiu et al., 2010; Ye et al., 2012) and IONPCs@SiO_2 structures **in high [CTAB]/[IONP] ratio conditions** (Qiu et al., 2010). However, in our case, in a non-catalyzed silica hydrolysis system (by addition of silica precursors after EtOAc to the pH 7 buffered system), **in high [CTAB]/[IONP] ratio conditions,** formation of the monodispersed CSNPs (Figure 19) in high yield (with high success rates) was obviously important key finding to be further investigated. Strikingly, unlike in low [CTAB]/[IONP] conditions, using high [CTAB]/[IONP] ratios in an uncatalyzed oil-in-water system were seen to be inducing "apple bite-like" cavity formations on silica shells, which was considered as the key point of investigation behind the silica shell formation in non-catalyzed high [CTAB]/[IONP] ratio conditions. Correspondingly, investigations on the mechanism behind the formation apple bite-like cavities were carried out by performing time-resolved TEM observations (Figure 22) for a typical nanoemulsion reaction (typical as referred to reactions condition described in section 2.3.2.2). When the innermost core−shell nanoparticle layers of ring-like structures are closely observed, it is clearly seen that these core−shell particles are coated with hemispherical silica shells. Considering the highly hydrophilic nature of silica, it can be concluded that the inner (hollow) region of the ring-like structures consists of a hydrophobic phase. On the other hand, the core−shell structures at the outer level of rings, which are far from the inner phase, have nearly full-spherical silica shells. However, the outermost particles are still connected with the adjacent particles via "necks" between the respective silica shells. These observations suggest that the silica shell necking and the phase separation by the hydrophobic inner phase are the origin of the apple bite-like cavities observed on the silica shells. It is noteworthy to mention that the ring-like structures shown in Figure 22 appear to be quite identical to the "on-grid" appearance of IONP-loaded polymersomes reported by Sanson *et al.* (Sanson et al., 2011). The same appearance was reported for the polymersomes and magnetoliposomes having hydrophobic or hydrophilic lumens

prepared with hydrophobic IONPs (Beaune et al., 2011; Arosio et al., 2013). As reported by Sanson *et al.* (Sanson et al., 2011) ring-like structures can be observed as a consequence of the collapse of spherical magneto- polymersomes when the samples are dried on a TEM grid. To make sure whether a similar collapsing issue was experienced with the structures observed in Figure 22, an additional time-resolved TEM analysis was carried out. In comparison to flexible polymers used by Sanson et al. (Sanson et al., 2011), using silica as the rigid coating material was advantageous that preserved the morphology of the nanoparticle clusters. By taking this advantage into account, more attention to acidification of the nanoemulsion reaction environment was paid at final step that resulted in rapid reaction quenching and increases the silica sol rigidity. Acidification procedure was carefully performed during each subsequent centrifugal sample preparation process to make sure that maximum silica condensation and rigidity were achieved. Consequently, conventional TEM images of the acidified samples corresponding to 180−225 min of a typical nanoemulsion process revealed hemispherical IONPC formations (Figure 23). This also explains that the ring-like structures, as it was for the case of Sanson et al. (Sanson et al., 2011), originated from the collapse of these hemispheres on the TEM grid. Collapse of the hemispheres took place, most likely because they were dried before the silica shells reached their full rigidity. Therefore, the large ring-like, hollow formations presented in Figure 22 must be regarded as a consequence of the collapsing hemispherical structures on TEM grids. Figure 23D clearly represents a preserved (non-collapsed) hemisphere structure in contrast to collapsed hemispheres in Figure 22G, J (Kertmen et al., 2017).

The origin of ring-like structures and hemispheres shown in Figure 22 and Figure 23 were further investigated by cryo-TEM. These observations were carried out to detect and understand how they appear in an aqueous medium. Samples collected at 120 min of the nanoemulsion process gave an important clue that a fusion process took place between the IONPCs and independently coexisting vesicular structures (Figure 24). Notably, the existence Fusion of vesicular structures (nanoemulsions) to the IONPCs was observed to change the spherical morphology of the clusters (Figure 24A,B). However, a completed fusion process was found to result in a nearly spherical hybrid nanovesicle −IONPC formations (Figure 24). Detection of these hybrid structures suggested that the ring-like structures (Figure 22) were formed after the drying process on the TEM grid.

The morphological transformations that IONPCs undergo after fusion with nanovesicles indicate that the nanovesicles were particularly attracted to the interior of the IONP clusters. In other words, the hydrophobic nanovesicle phase had an affinity to the phase within the interior of IONPCs. Such an affinity relation highly resembles the coalescence of two "Janus colloidal capsules" that can be clearly observed on the microscale (Rozynek et al., 2014). When two Janus colloidal capsules coalesce, colloids undergo a reorganization at the interface of an enlarged oil droplet and the surrounding liquid medium (Rozynek et al., 2014). From Figure 24C, a very similar behavior is observed. Nanovesicle−IONPC hybrid morphology recovers to a nearly spherical shape when the fusion process is completed. Consequently, herein observed morphological transformations are altogether strong indicators of IONPCs actually being oil-in-water "Janus colloidal capsules." (Rozynek et al., 2014) Nevertheless, the reason IONPCs appear to be hemispherical after fusion to the nanovesicles could be attributed to the viscosity changes in the nanovesicle phase because viscosity changes are known to play an important role in the coalescence dynamics of Janus colloidal capsules (Rozynek et al., 2014). Changes in the nanovesicle viscosity due to condensation of silica precursors most likely inhibit the IONPCs to undergo a full rearrangement around the nanovesicles. Rapid condensation of silica precursors after fusion would be the most accurate scenario responsible from the viscosity increase. Although the "colloidal capsule" definition has been very recently suggested as the most universal term to describe Pickering-type emulsions (Bollhorst et al., 2017), IONPCs could be more specifically classified as "colloidosomes" (Dinsmore et al., 2002). This is because the colloidosomes are described as stabilized Pickering emulsions (Morse et al., 2016). When it is taken into account that IONPCs consist of OA−IONPs constrained at the oil−water interfaces by CTA^+ molecules, the "colloidosome" classification would be the most suitable term to describe IONPCs. Previously reported water-in-oil colloidosomes of iron oxide nanoparticles prepared in a similar manner in the presence of oil-soluble surfactants also strongly support the colloidosome nature of the herein reported IONPCs (Bollhorst et al., 2015) (Kertmen et al., 2017).

3.3 FT-IR and Raman spectroscopy analysis of IONPs and CSNPs

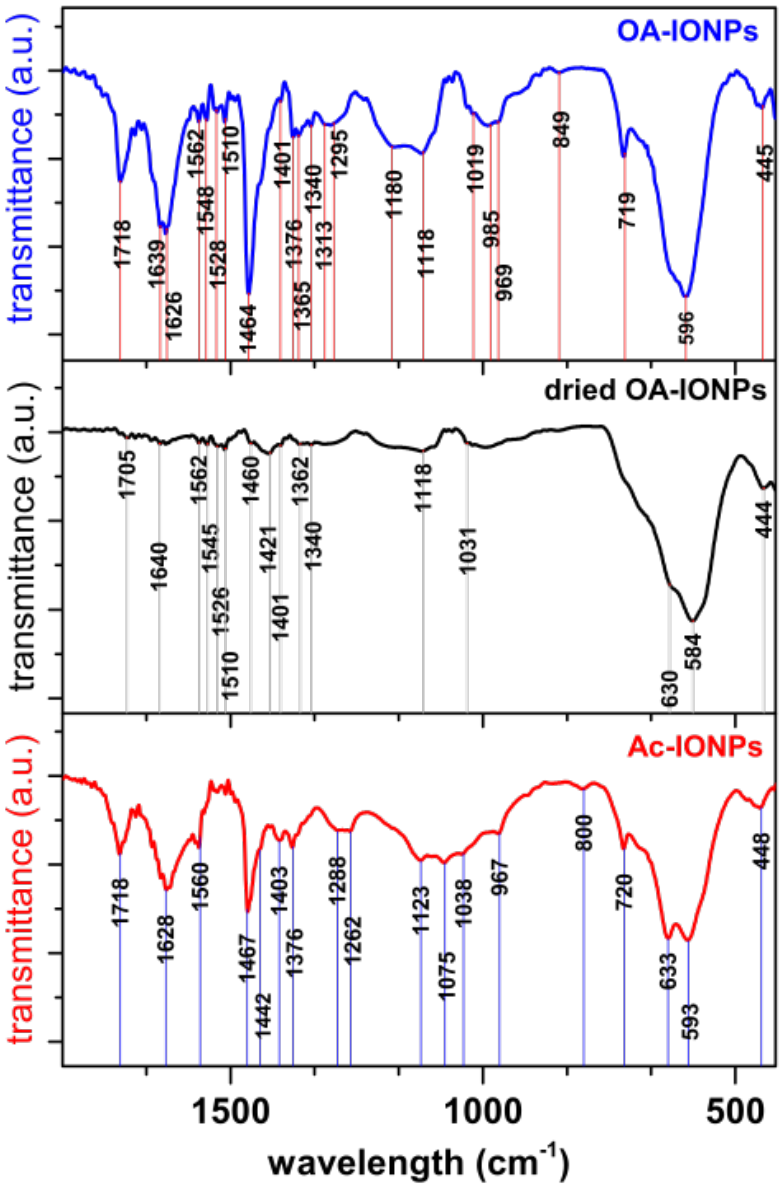

Figure 25. FT-IR spectroscopy analyses of OA-IONPs, dried OA-IONPS and Ac-IONPs.

Regarding CSNPs of nanoemulsion process, another important approach to clarify the mechanism behind the formation of apple-bite like cavities was investigation of the EtOAc saponification impact on IONPCs in the absence of silica precursors. Such investigation was simply made by keeping all other reaction parameters of a typical nanoemulsion process same while not adding any silica precursors (please see section 2.3.1.3 for saponification reaction details employed in the presence of only IONPCs).

Correspondingly, impact of the in situ formed acetate species on IONPCs, after saponification of EtOAc, as potential carboxylate ligands was investigated by vibrational spectroscopies (Kertmen et al., 2017).

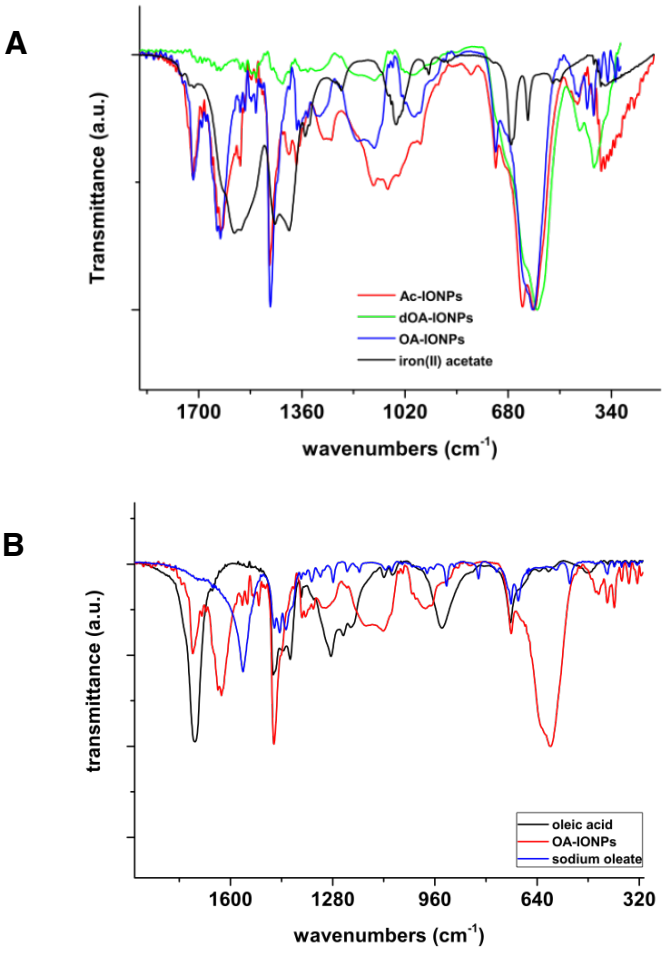

Figure 26. FT-IR spectroscopy comparison of OA- and Ac-IONPs with oleic acid, sodium oleate and iron(II) acetate.

The FT-IR spectroscopy analyses of OA-IONPs and the acetate coated IONPs (Ac-IONPs) shown in Figure 25 clearly indicates the existence of iron oxide (Fe-O) mode for both samples at 596 and 593 cm^{-1}, which are in agreement with the literature data of magnetite structure (Xuan et al., 2007), while the existence of 444, 584 cm^{-1} and 584, 630 cm^{-1} pairs for the dOA-IONPs could be regarded as the indications of magnetite structure (Liu et al., 2009; Sundar et al., 2014). However, the same peaks can also point the maghemite formation due the interactions of carboxylate groups and the iron under

elevated pressure during the KBr disk preparations for FT-IR experiments (Jing and Wu, 2004). Although the latter two peaks are observed also for OA- and Ac-IONPs, from electron microscopy studies that the Ac- and OA- IONPs are perfectly crystalline magnetite species.

Since acetate and oleate ligands are both carboxylic acids, the IR spectra of both ligands shows similar features, although with considerable intensity band splitting differences. The asymmetric and symmetric carboxylate stretching modes (ν_s[COO-] and ν_{as}[COO-]) were assigned to 1628, 1467 cm^{-1} and 1560, 1403 cm^{-1} pairs; which were found to be in agreement with the molecular iron acetate species reported in the (Long et al., 1973; Paul et al., 1978; Edwards and Lewis, 1993). The 1560, 1404 pair was also reported in a previous study as ν_s[COO-] and ν_{as}[COO-] modes of magnetite nanoclusters synthesized with acetate ligands (Shouhu Xuan Yi-Xiang J. Wang and Leung, 2009). 1718 cm^{-1} band of Ac-IONP sample was regarded as the indication of the stretching modes of non-complexed carbonyl groups (ν[C=O]) (Lindegren et al., 2009) which was also observed for the complexation studies with various forms of iron oxides (Rose et al., 2002). This band should be taken into consideration along with the the ν_s[C-O] band appearing at 1288-1262 cm^{-1}, which is observed for non-ionized, hydrogen bonded acetic acid complexes (Chapados and Max, 2004) or for basic Iron(III) acetate containing an OH- ligand but not for iron(II) acetate (SDBS). Consequently, it can be confirmed by the existence of hydrogen bonded acetate species through non-complexed C=O bonds (Rose et al., 2002). When all of the carboxylate interactions with ν_{as}[COO-]— ν_s[COO-] assignments are taken into account, acetate ions are found to have Δ values (ν_{as}[COO-] - ν_s[COO-]) consistent with bridging, bidentate and unidentate complexation modes on the surface of IONPs (Deacon, 1980; Nakamoto, 2009). OA-IONPs show identical features with Ac-IONPs however the appearance of weak ν_{as}[COO-] and ν_s[COO-] peaks at 1560 and 1401 cm^{-1} suggests a substantial decrease in the amount of complexation modes of oleic acid in comparison to Ac-IONPs. The shift of ν_a[C-O] band to 1313-1265 cm^{-1}, on the other hand, is an important indication of difference in the type of physiosorbed carboxylate species with varying bond strengths (acetate vs oleate). Additionally, OA-IONPs revealed several additional peaks in the 1560-1510 cm^{-1} and 1464-1340 cm^{-1} regions. These suggest that the oleate complexation might have several different additional modes in comparison to acetate ligand. At this point, comparison

with dOA-IONP sample provides an entirely different panorama where truly complexed oleate species actually give rise to the 1510-1526 and 1421 cm^{-1} ν_{as}[COO-] - ν_{s}[COO-] peaks, since rest of the peak intensities observed in carboxylate region of the OA-IONPs were substantially decreased to almost disappearance after drying process. This observation confirms that the peaks observed at 1718-1464 cm^{-1} region represents the non-complexed, adsorbed species; at least in case of oleic acid. Because the removal of the adsorbed species was facilitated by a simple cold solvent washing for oleic acid; whereas the acetate species were subjected to a long dialysis process. However, acetate species were obviously resistant to desorption, despite undergoing dialysis up to a week, they still hold the same features in 1718-1467 cm^{-1} region. This observation once more indicates the difference in carboxylate species observed in OA- and Ac-IONPs; where the acetate exhibits stronger complexation and physisorption behavior (Kertmen et al., 2017).

1376-1340 cm^{-1} region is known for representing the -CH_3 deformations in various acetate complexes of iron (Rochester and Topham, 1979; Johnson et al., 1981; Edwards and Lewis, 1993), iron(II) and basic iron (III) acetates (SDBS). While this band is represented as a single peak at 1376 cm^{-1} for Ac-IONPs, oleic acid shows additional 1365 and 1340 cm^{-1} peaks in the same region. The 1075 and 1038 cm^{-1} peaks represent the -CH_3 group vibrations of acetate (Paul et al., 1978; Edwards and Lewis, 1993) which are absent in oleate samples, were regarded as the most important support for the existence of acetate species. Their origin was correlated by comparison to Fe(II) acetate (Figure 26A) where they were assigned to -CH_3 symmetric stretching vibrations (Alcock et al., 1976). 1121 cm^{-1} feature that has not been reported for the acetate species previously, however a similar peak is observed for basic Fe(III) acetate around 1150 cm^{-1} region; although it was not indicated (SDBS). It is thought to be related to complexation of iron with carboxylates (C-O-Fe). This postulation is supported with the existence of the 1118 cm^{-1} peak in OA-IONPs as a part of a broad band formed together with 1180 cm^{-1} peak, which is seen intensifying after the complexation of oleic acid with iron oxide that is evident from a comparison made between OA-IONPs, pure oleic acid and sodium oleate (Figure 26B). Similar intensity increase can be also observed at the 1019 and 985 cm^{-1} peaks, which altogether suggest a relation between complexation of carboxylates with iron. The most important reason of suggesting a relation between iron- carboxylate

complexation associated to these peaks is their disappearance in sodium oleate salt. At last, the 967 cm^{-1} band of the Ac-IONPs on the other hand, is in very good agreement with the C-C stretching vibrations reported for the acetate complexes formed with iron and various other metals (Alcock et al., 1976; Paul et al., 1978) (Kertmen et al., 2017).

Existence of the acetate/ acetic acid species was evident from the highly hydrophilic nature of the IONPs after the reaction of IONPCs with ethyl acetate. Existence of the acetate/ acetic acid species identified by FTIR was evident from the highly hydrophilic nature Ac-IONPs (Figure 27) (Kertmen et al., 2017).

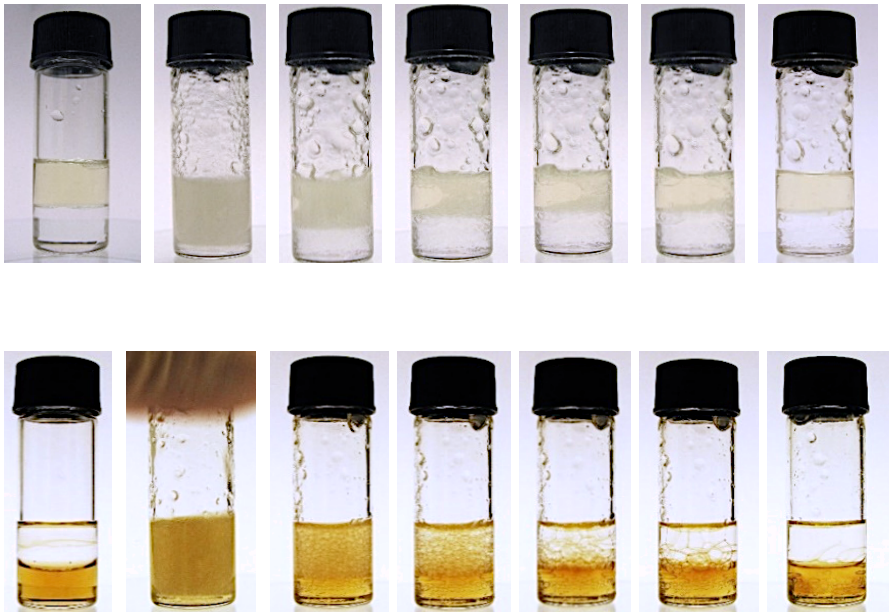

Figure 27. A) Demonstration of the phase separation between the upper aqueous phase containing Ac-IONPs and lower chloroform phase. Images from left to right shows the rapid phase separation after vigorous shaking, B) Demonstration of the phase separation between the lower chloroform phase containing OA-IONPs and upper aqueous phase. Images from left to right shows the rapid phase separation after vigorous shaking.

Raman spectroscopy analysis was carried out separately for (inorganic) iron oxide and the organic content fingerprint regions in comparison to a series of reference organic compounds. These comparisons provided a much clearer evidence of the acetate/oleate ligand exchange. Raman spectral band assignments were made according to the literature data found for experimental and calculated/simulated

spectroscopic properties of iron oxide structures (Figure 28) (White and DeAngelis, 1967; de Faria et al., 1997; Gasparov et al., 2000; Shebanova and Lazor, 2003; Chamritski and Burns, 2005; Jacintho et al., 2009).

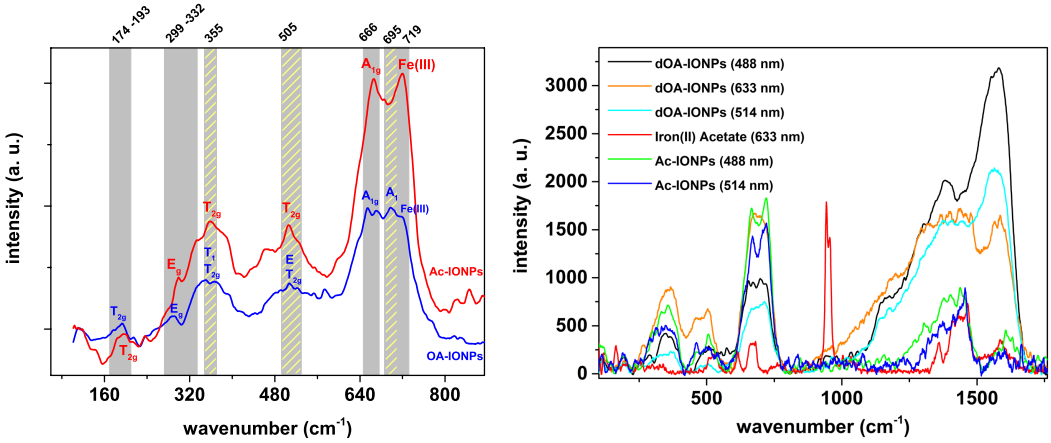

Figure 28. A) Raman spectroscopy analysis of dOA−IONPs in comparison to oleic acid, sodium oleate, iron oleate, and iron(II) acetate and the list of the peaks found in spectra (Kertmen et al., 2017).

The 200−700 cm^{-1} fingerprint region of the iron oxide structures for Ac−IONPs and dOA−IONPs revealed at least five Raman active modes ($3T_{2g} + E_g + A_{1g}$) that belong to cubic inverse-spinel structure of magnetite (Figure 28A). The spectrum of dAO−IONPs shows identical band patterns as Ac−IONPs, however, the former resembles a convoluted form of the latter. Generally, Ac−IONP Raman spectrum showed similarities to the previously reported citrate-coated magnetite (Da Silva et al., 2003) spectrum, which strongly supports the existence of carboxylate species. The strongest peak of the Ac−IONP spectrum at 666 cm^{-1} was assigned to the A_{1g} mode, which is a clear indication of the magnetite form along with the bands observed at 174−193, 355, and 505 cm^{-1} for T_{2g} modes and 299−332 cm^{-1} for the E_g mode (where the 460−480 cm^{-1} band could be alternatively regarded as a T_{2g} band) (Figure 28A). On the other hand, the bands representing 355, 505, and 695 cm^{-1} could be regarded as the indication of T_1, E, and A_1 modes of maghemite. The strong peak observed at 719 cm^{-1} was attributed to the oxidation of Fe(II) to Fe(III) at the octahedral sites. Both the maghemite features and the oxidation at octahedral sites could be attributed to locally elevated temperatures

induced by the micro-Raman technique, which is known to induce the change from magnetite to maghemite (Chamritski and Burns, 2005) (Kertmen et al., 2017).

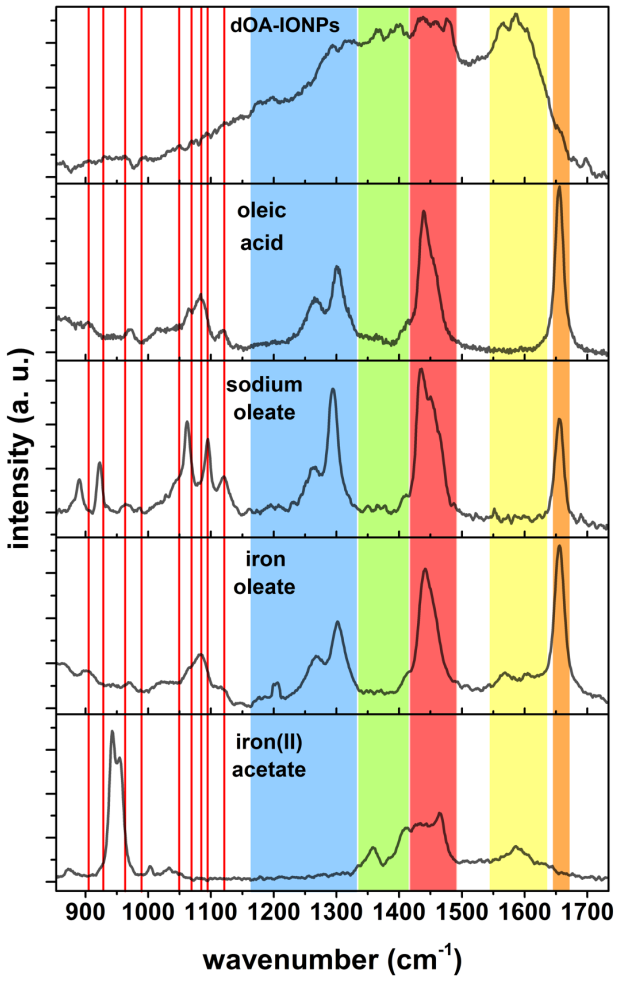

dOA-IONPs	OA	sodium oleate	iron oleate	iron acetate
1658	1656	1657	1656	-
-	-	-	-	1632
1604	-	-	1603	-
1585	-	-	-	1587
1565	-	-	1570	1564
-	-	1552	-	-
1475	-	1467	-	1466
1458	1456	1450	1454	1447
1438	1439	1435	1439*	1432
1401	1413	1411	1409	1412
1385	-	-	-	1384
1369	1363	1363	1369	1358
-	-	1351	-	-
1314	1319	-	1313	-
1294	1300	1295	1300	-
1256	1265	1266	1265	-
-	-	1206	1206	-
1198	-	1195	1186	-
1178	-	1173	1175	-
1121	1121	1121	1121	-
1094	-	1094	-	-
1083	1083	1083	1083	-
1068	1062	1062	1062	-

Figure 29. A) Raman spectroscopy analysis of dOA–IONPs and Ac–IONPs at the iron oxide fingerprint region, B) comparison of the dOA–IONPs and Ac– IONPs under different laser excitations. Raman spectroscopy analysis of Ac- and OA-IONPs (Kertmen et al., 2017)

Analysis in the 850–1750 cm^{-1} organic fingerprint region for dOA–IONPs could be performed only for 633 nm laser excitation because the 488 and 514 nm laser excitations did not provide the same band resolution in this region. On the other hand, Ac–IONPs exhibited a good band resolution under 488 and 514 nm excitations but suffered from a strong fluorescence background under 633 nm excitation. Therefore, the organic fingerprint region analysis of dOA–IONPs and Ac–IONPs is presented separately in Figure 28A and Figure 29. In Figure 29, 633 nm excited dOA–IONPs were compared to oleic acid, sodium oleate, iron oleate (OA-IONP precursor), and iron(II)

acetate to distinguish the differences between the complexation of oleate and acetate species with iron. The spectrum of dOA−IONPs was analyzed in five different regions and highlighted in different colors). In Figure 29, the orange band indicates the C=C bond of oleic acid (Otero et al., 2014), which is observed as a minor shoulder in dOA−IONPs. The yellow band is particularly important because it represents the asymmetric carboxylate vibrations. This is due to the fact that only iron oleate and iron acetate reveal these peaks, whereas oleic acid and sodium oleate lack them. The green region, where the dOA−IONPs have very intense peaks in comparison to all oleic acid/oleate references in the graph, was assigned to the symmetric stretching vibrations of carboxylates. This region also features very intense peaks for iron(II) acetate at 1412 and 1358 cm^{-1}, which have been assigned to both symmetric carboxylate stretching and CH3 deformation modes for the iron(II) acetate complex (Edwards and Lewis, 1993). On the other hand, for a cobalt acetate complex, a 1358 cm^{-1} peak was attributed to the symmetric carboxylate stretching (Nickolov et al., 1995). Because of the different peak assignments made in previous studies and the distinct peak intensity exhibited by dOA−IONPs in this region, both 1401 and 1369 cm^{-1} peaks of dOA−IONPs were attributed to symmetric stretching vibrations of the carboxylates. The red band indicates the CH_3 stretching and bending vibrations. Peaks observed in this region for iron(II) acetate were found to be in agreement with the peaks previously reported for acetate complexes (Edwards and Lewis, 1993; Nickolov et al., 1995). For the reference oleate/oleic acid compounds and dOA−IONPs, the red and blue regions are the indicators of the $-CH_2$ deformations, in agreement with the fatty acid metal complex vibrations (Otero et al., 2014). Below the blue band region, strong C−C stretching and CH_2 rocking vibrations are observed. To make a clear visual comparison with all other samples, the peaks found for dOA−IONPs in this region are highlighted with red lines (Figure 29). The band assignments made in Figure 29 were also used as a guide for the analysis in Figure 28B, where the 488 and 514 nm-excited Ac−IONPs were compared to 488, 514, and 633 nm dOA−IONPs. This comparison clearly demonstrates the spectral intensity differences between the samples. In this comparison, following properties were observed: (i) ν_{as}[COO−] intensities (which corresponds to the yellow band region of Figure 29 increase with the decreasing laser wavelengths for dOA−IONPs; (ii) increasing the wavelength from 488 to 514 nm results in a shift for the green and yellow band regions of the Ac−IONPs. The

distance between the green and yellow band regions decreased without any notable difference in the peak intensities; and (iii) the identical spectral shapes of the Ac−IONPs and iron(II) acetate remarkably demonstrate the acetate−iron complex origin of Ac−IONPs. Vibrational modes in the iron oxide fingerprint region with minor shifts were found to be in agreement with all wavelengths used. Briefly, FTIR and Raman analyses evidenced that the ethyl acetate saponification in the presence of IONPCs results in a ligand-exchange reaction between acetate ions and oleate on the surface of IONP building blocks of IONPCs, without altering the magnetite structure of IONPs (Kertmen et al., 2017).

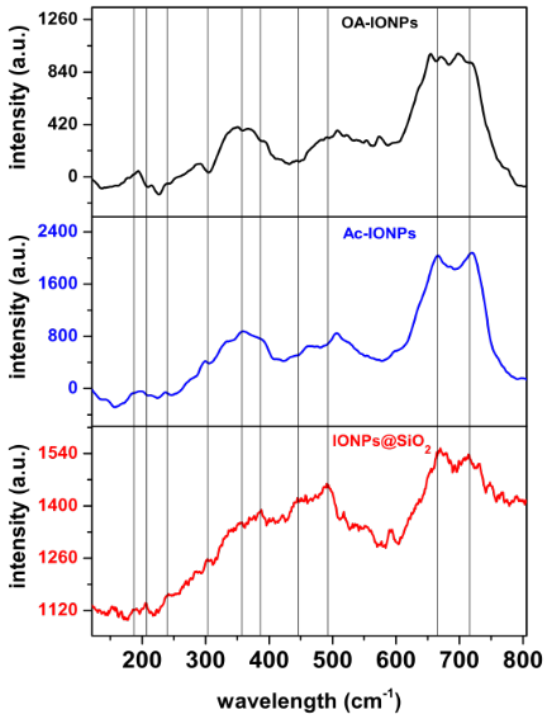

Figure 30. Raman spectroscopy comparison of OA-IONPs, Ac-IONPs and CSNPs of the nanoemulsion process (Kertmen et al., 2017).

CSNPs of nanoemulsion process compared to Ac−IONPs and dOA−IONPs, in terms of the Raman spectrum in the iron oxide fingerprint region, showed only minor differences (Figure 30). A_{1g} and Fe(III) bands are seen to match with those from Ac−IONPs and OA−IONPs (Figure 28A). However, $3T_{2g}$ and E_g bands observed at 190, 386, 492, and 303 cm^{-1} exhibited negligible shifts but significant intensity changes. Such

results suggest that the silica coating had no chemical or physical influence on the IONP structure.

3.4 Structural TEM analysis of IONPs and CSNPs of nanoemulsion process

3.4.1 Crystallographic properties

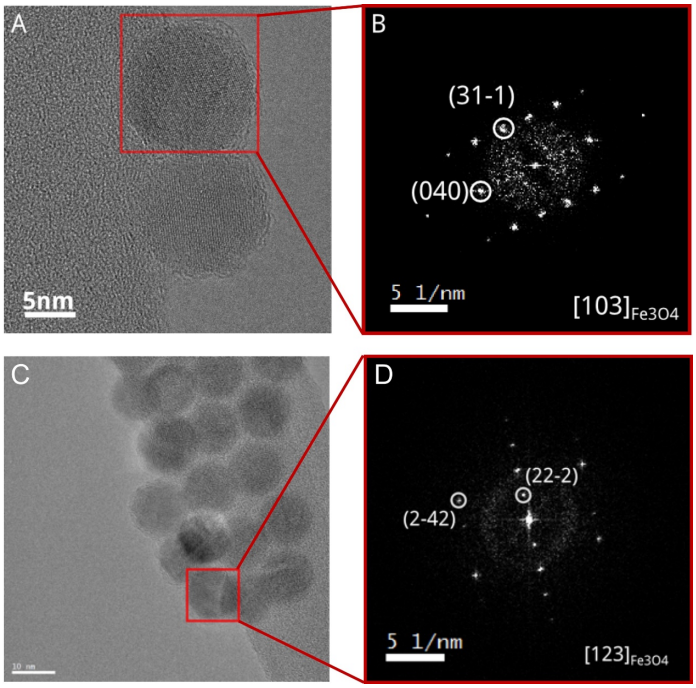

Figure 31. A,B) HR-TEM and corresponding FFT of the Ac-IONPs showing that the iron oxide structures is magnetite; C,D) HR-TEM and corresponding FFT of the OA-IONPs showing that the iron oxide structures is magnetite; E) Oxygen and Iron content analysis of Ac- and OA-IONPs shows that the composition of the structures are identical and ligand exchange did not result in any significant modification in magnetite structure.

In order to support the Raman and FTIR analyses that evidenced the acetate/oleate exchange (section 3.3), HRTEM and EELS measurements were carried out on OA−IONPs and Ac−IONPs. Fast Fourier transform (FFT) images of Ac−IONPs and OA−IONPs show that both samples contained only magnetite (Figure 31) while their oxygen K edge and Fe L edge spectral comparison confirmed the structure of magnetite was unaffected from ligand exchange Figure 32.

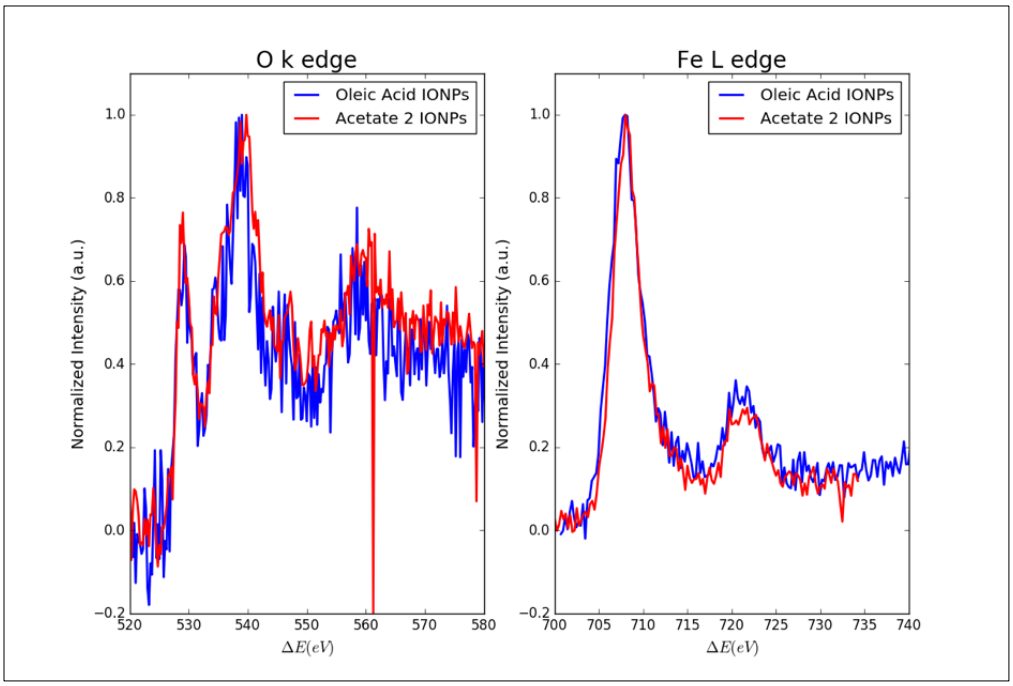

Figure 32. Oxygen and Iron content analysis of Ac- and OA-IONPs shows that the composition of the structures is identical and ligand exchange did not result in any modification in magnetite structure.

The Fe_3O_4 core composition is also supported by the HRTEM images of the core−shell structures and their corresponding FFTs (Figure 33). Comparison of the two core−shell structures showed that there was no difference between their iron oxide compositions. Note that one of the core−shell structures was imaged through its apple bite-like cavity, showing no differences.

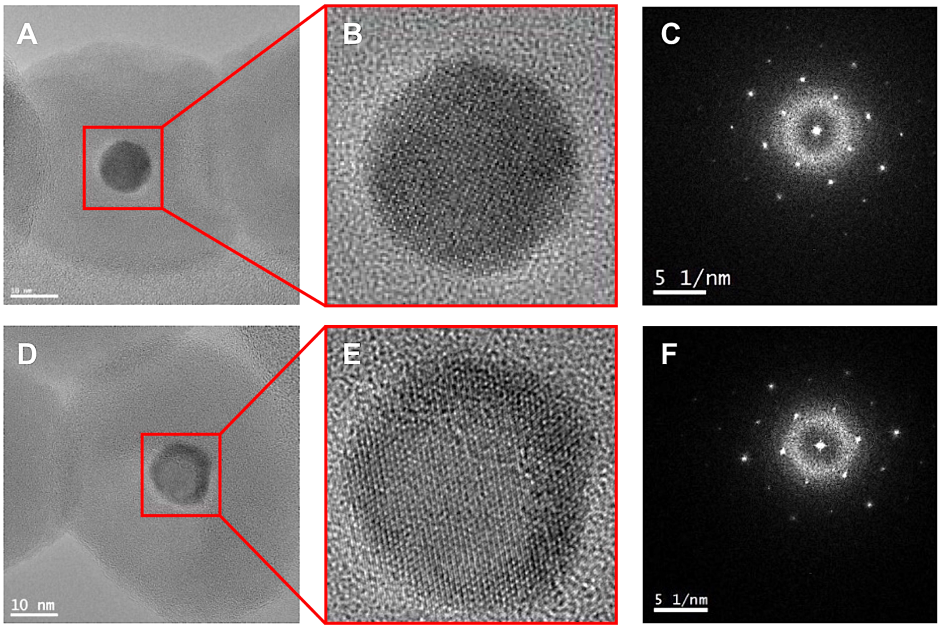

Figure 33. A, D) HRTEM images of CSNPS structures of nanoemulsion process; B,E) magnified views of the regions highlighted by red squares thereof and corresponding FFT images; C,F) images unambiguously show that the core of the nanoparticles are perfectly crystalline and observed crystal lattice is consistent with magnetite (Fe_3O_4) and the silica shells are found to be amorphous. In “images D” and “E” the cavity in silica shell is facing up.

3.4.2 Surface coating analysis

Oxygen and iron content analyses by EELS confirmed that the composition of Ac−IONPs and OA−IONPs was identical (Figure 32). This means that the ligand-exchange process mediated by ethyl acetate does not alter the structure of IONPs. On the other hand, the carbon content analysis by EELS demonstrated that the Ac−IONPs were coated with a uniform, amorphous-looking carbon shell in comparison to the OA−IONPs having brush-like, scattered carbon content (Figure 34). Notably, despite the huge difference between the acetate and oleic acid hydrocarbon contents (1:17), deposition of acetate in large amounts was evident from the similar carbon shell thicknesses in Ac−IONPs and OA−IONPs.

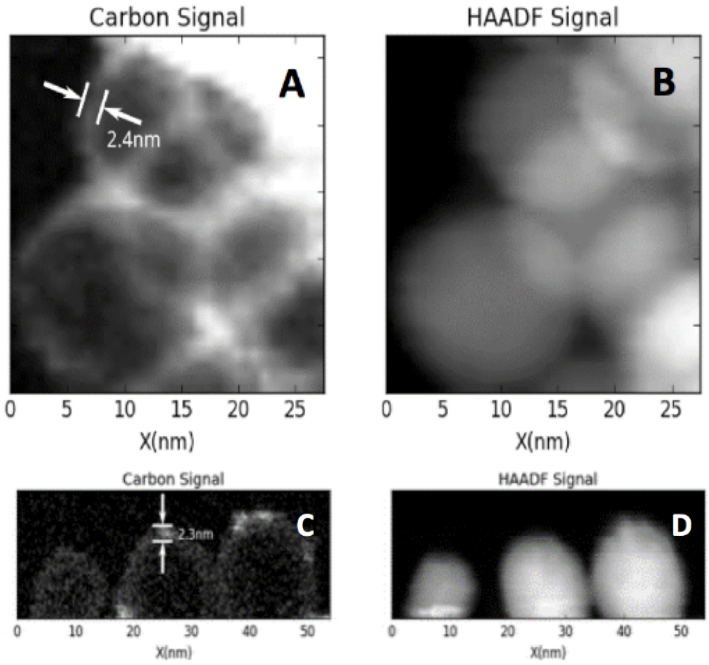

Figure 34. EELS analyses of carbon content: A,B) acetate-coated IONPs and, C,D) oleic acid-coated IONPs.

The existence and location of the carbon content have great importance to elucidate the long- considered role of CTA^+ as a structure-directing agent in siliceous material preparation. This information can demonstrate how surfactant molecules template the silica growth on the hydrophobic metal nanoparticle surfaces. As suggested by previously reported studies, aliphatic chains of the CTA^+ molecules interact with the aliphatic fatty acid chains covering the nanoparticle surface to form the oleate–CTA^+ bilayer (Fan, 2004; Kim et al., 2008b; Ye et al., 2012). Then, the cationic head groups of the CTA^+ molecules provide aqueous dispersibility. However, CTA^+ molecules later on interact with water-solubilized silicates to condense them into silica (Fan, 2004; Kim et al., 2008b; Ye et al., 2012) in various morphologies (Yanagisawa et al., 1990; Beck et al., 1992; Kresge et al., 1992). In other words, the oleate–CTA^+ bilayer is physically capped by the silica shell as a consequence of the silica formation mechanism. On the other hand, nanoemulsion process starts with the acetate/oleate exchange, and it was shown that the ligand exchange creates an acetate-based thick carbon shell in the absence of a silica shell. However, the fate of the initial acetate shell was unclear after the silica coating. When the previous hypotheses and our recent observations on

acetate-induced ligand-exchange processes were taken into account all together, some carbon content is expected between the silica shell and iron oxide core of the CSNPs of the nanoemulsion process. To investigate the existence of this carbon content, either related to the oleate− CTA^+ bilayer or the acetate layer, detailed EELS analyses were performed on the individual core−shell structures prepared by the nanoemulsion process.

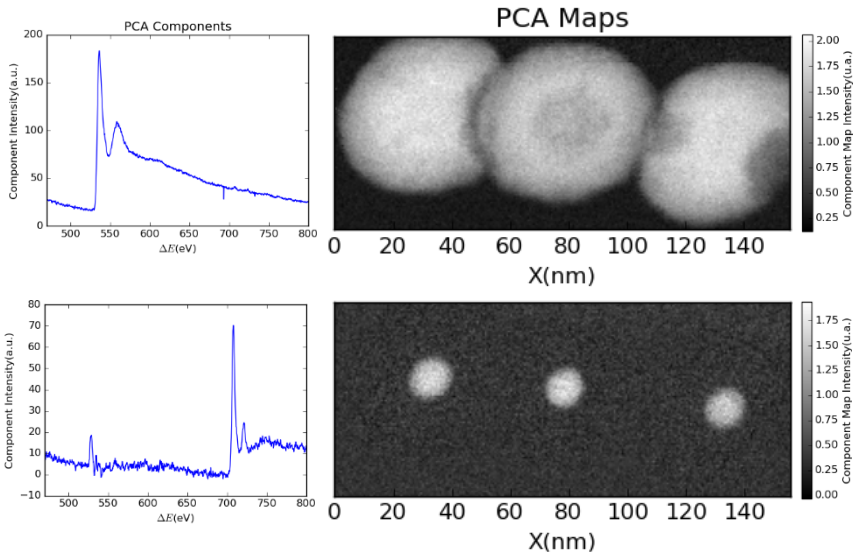

Figure 35. PCA decomposition maps. This demonstrates uniform composition of SiO_2 (upper left and right) shells and Fe_3O_4 cores (lower left and right).

The chemical composition of the resulting CSNPs obtained from the typical nanoemulsion process reaction was further investigated by EELS measurements. Elemental analysis maps demonstrated that the core−shell structures were composed of pure amorphous silicon oxide shells and iron oxide in the form of magnetite (Fe_3O_4) (Figure 35) (the Fe_3O_4 core composition was also supported by the HRTEM images of the core−shell structures and their corresponding FFTs in Figure 33). Comparison of the CSNPs showed that there was no difference between their iron oxide compositions. Note that one of the CSNPs was imaged through its apple bite-like cavity, showing no differences. EELS fine structure parameters of the oxygen and iron edges were separately mapped (Figure 36). A prepeak in the oxygen K edge was observed for all samples, which is characteristic of magnetite. The prepeak intensity maps revealed

homogenous composition of the iron oxide core. The same conclusion was obtained from the Fe $L_{2,3}$ white line parameter maps. Moreover, perfectly matching Fe $L_{2,3}$ edge spectral analysis of OA-IONPs and CSNPs additionally proves that iron oxide cores did not change their chemical composition after the coating process (inset of Figure 36A).

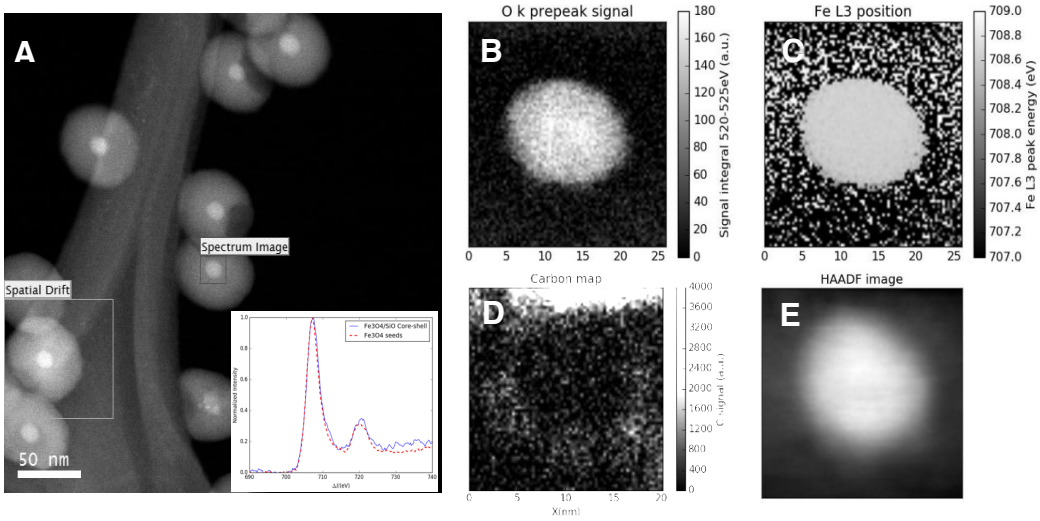

Figure 36. A) HAADF image of CSNPs of nanoemulsion process. Inset is the Fe $_{L2,3}$ edge spectra obtained from the core shell particles and from the seeds. The spectra where calibrated with the oxygen K edge and normalized. It confirms that no detectable chemical change happened to iron oxide cores after silica coating.; B,C) EELS fine structure parameter maps. Shifts in the Fe L_3 position of 1-2eV are known to be related to changes in the oxidation state of iron. Also the presence of a pre-peak in the oxygen edge in FeOx consistent with the iron core being Fe_3O_4. The homogeneity in these parameters maps indicates that oxidation state of the iron oxide cores is homogenous; D) Carbon EELS signal map after PCA de-noising. Note that the bright region at the top of the image corresponds to the surface of the hole in the silica populated with high concentration of carbon. However, carbon signal can be still seen surrounding the iron oxide core; E) co-acquired HAADF image showing the region where EELS SI was taken from.

Analysis shown in Figure 37 demonstrates that the outermost surface of silica shells is coated with carbon. The thick carbon shell seen at the particle edges (Figure 37C,E) was regarded as a clear indication of the CTA^+-templated silica growth mechanism. The colored relative carbon composition map, including the IONP core, evidenced that the core was completely coated with silica (Figure 37E). Oxygen content

from the silica shell confirmed its uniform structure (Figure 37B). A careful investigation of Figure 37D revealed the carbon content concentrated around the core (an additional image of carbon concentrated around the core, obtained for a different particle, can be seen in Figure 36D). Further EELS analyses carried out on a particle after removal of surface CTA^+ molecules by dialysis confirmed that the outermost surface carbon content of CSNPs was removed to a great extent, and an inner carbon content indeed existed between the IONP core and the silica shell (Figure 38).

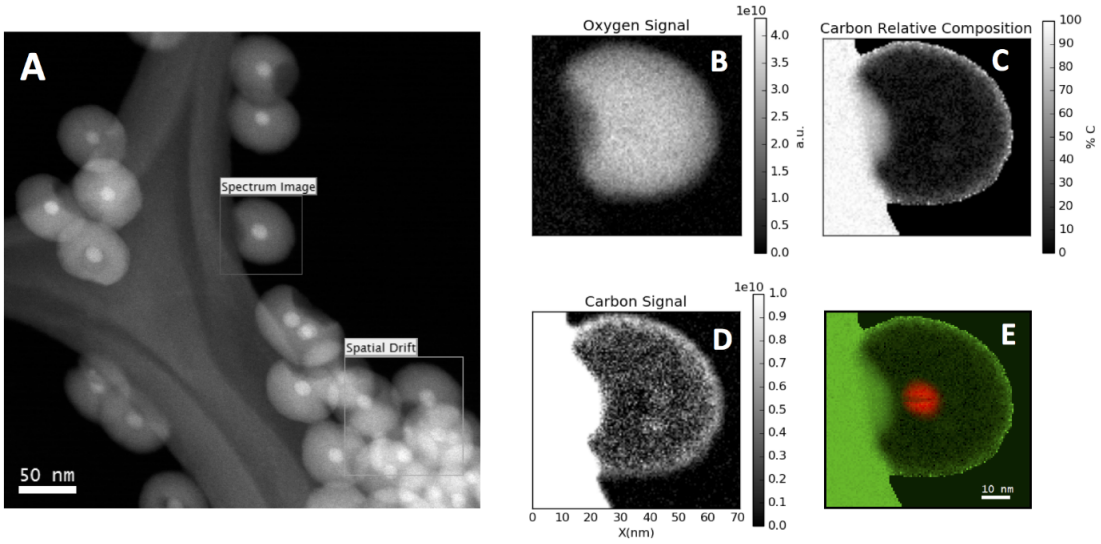

Figure 37. A) HAADF image with a highlighted region where an EELS spectrum image was taken; B) oxygen signal coming from silica; (C) carbon relative composition from the EELS SI; D) carbon signal; and E) coloured map of carbon relative composition (green) with iron oxide core (red).

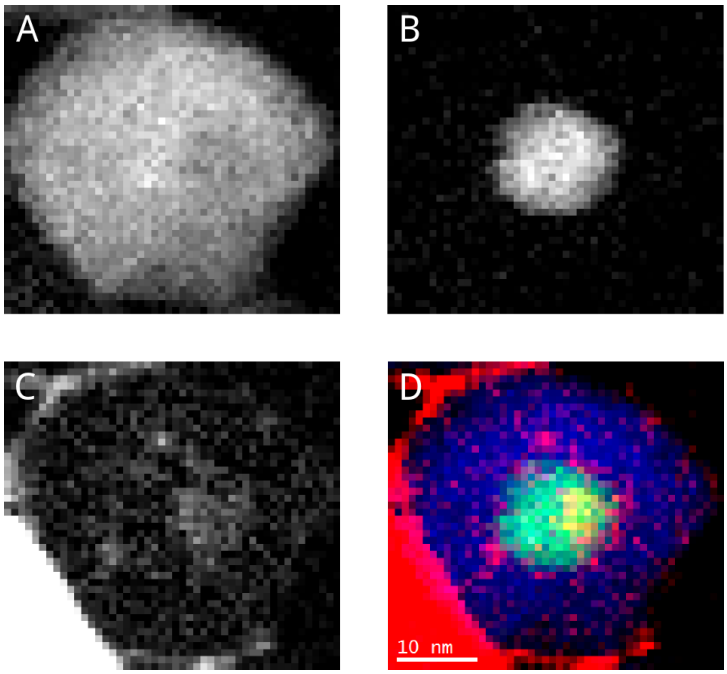

Figure 38. EELS analysis showing A) oxygen signal, B) iron signal, C) carbon signal, and D) colored map of oxygen (blue), iron (green), and carbon (red).

More detailed EELS analyses carried out on a particle after removal of surface CTA^+ molecules by dialysis confirmed that the outermost surface carbon content of CSNPs was removed to a great extent, and an inner carbon content existed between the IONP core and the silica shell (Figure 38). In some cases, even after the harsh dialysis process, some carbon content was observed between the adjacent particles (Figure 39).

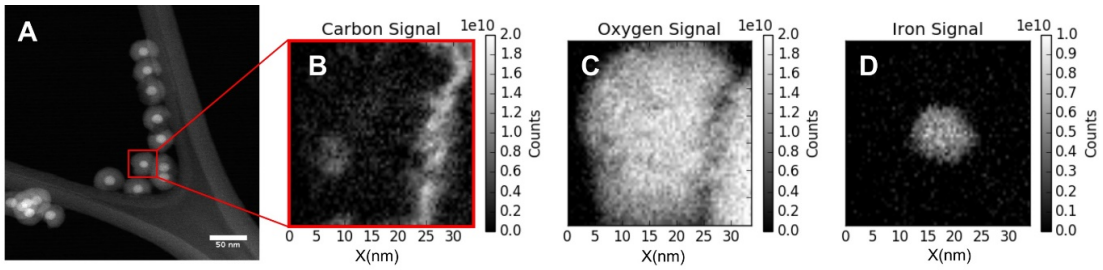

Figure 39. A) a HAADF image of the adjacent CSNPs of nanoemulsion process, B) EELS carbon analysis of two adjacent CSNPs shown in “image A”, C) EELS oxygen analysis of two adjacent CSNPs shown in “image A”, D) EELS iron analysis of two adjacent CSNPs shown in “image A”

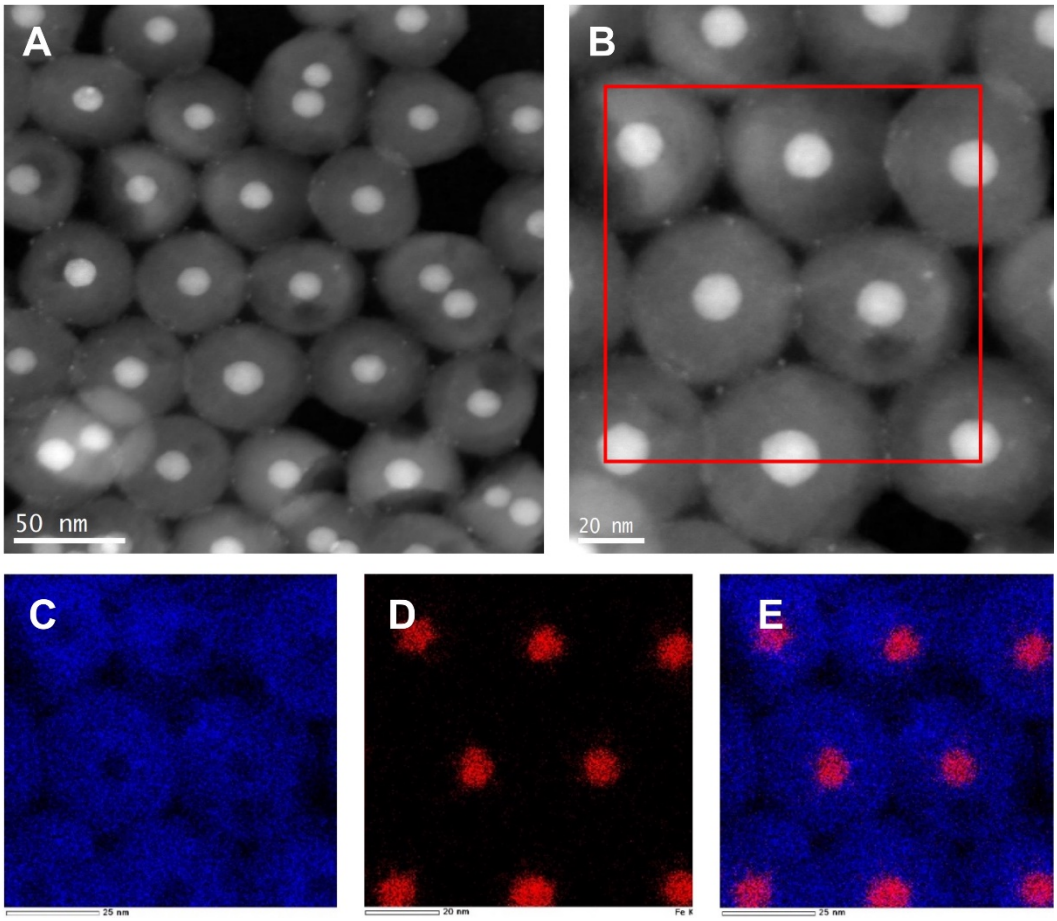

Figure 40. A) HAADF image taken from the ring formations in 3.30 h of nanoemulsion process; B) a magnified view of the "image A"; C) EDX analysis of silicon content in the area shown in red frame in image B; D) EDX analysis of iron content within the area shown in red frame in image B; E) Overlapped view of the image C and D; F) Elemental composition of the sample.

3.4.3 Elemental analysis of CSNPs

Careful observations made on TEM images obtained from 180 min of the nanoemulsion process revealed that the silica-condensation reaction induced the formation of tiny iron oxide particles (Figure 40). To confirm that such particles were indeed iron oxide and not any other contaminant or byproduct of the synthesis procedure, further EDX analyses were carried out on the 180 min sample. Because the TEM images were collected in a dark field, they allowed a clear differentiation of the higher atomic number iron cores from the lighter silica shells (Figure 40A,B). EDX spectra collected over the same area show that the only elements present on the sample are

Fe, Si, and O (C and Cu being part of the grid), which clearly shows that the small particles had indeed iron oxide origin (Figure 40C-E). Additionally, cryo-TEM analysis of samples obtained from 120 min of the nanoemulsion process confirmed the existence of a thin shell covering each IONP building block of the IONPC hemisphere (Figure 40C,D). When the sample orientation was disturbed by melting the icy media with an intense electron beam, it was observed that these thin shells created tiny clusters (Figure 40E,F). The tiny clusters, formed as a consequence of the melting ice, were similar to tiny iron oxide particles observed in the 180 min sample (Figure 40A,B).

Existence of the tiny iron oxide nanoparticles at 120 min of the nanoemulsion process suggests that their formation was a consequence of the acetate/oleate ligand exchange because it was evidenced from cryo-TEM images collected at 120 min that silica condensation did not start at 120 min (Figure 41). Especially, the existence of a thin iron oxide shell observed in the cryo-TEM images suggests that the removal of oleate ligands from the IONPs cannot be simply described under the terms of a conventional "ligand exchange". Acetate/oleate exchange seems to proceed rather by removal of the outermost iron oxide surface from the IONPs by breakage. Such destructive effects of acetate ions on various iron oxide structures were previously reported (Rose et al., 2002). If it is taken into account that the IONPCs were exposed to the acetate-rich reaction medium for 120 min (up to the start of the silica shell formations) at elevated temperatures, acetate- induced damage of IONPs becomes a plausible scenario. However, EELS studies confirmed that the breakage by acetate ions in our study did not cause any observable chemical changes in IONPs (Figure 31 and Figure 33). On the other hand, it was sensible to assume that these tiny iron oxide particles might have been present in the samples before the silica coating, although they were not observed in the TEM analyses in Figure 19. To reassure that the tiny iron oxide particles were the result of breakage by acetate ions or not, the batch of CSNPs prepared with OA−IONPs having wide size distribution (ranging from 2 to 27 nm) could be compared (Figure 20). When the nanoemulsion reaction performed in the presence of these 45 min OA-IONPs, both the smallest and largest iron oxide nanoparticles were coated with silica shells having the same thickness, regardless of their size. This indirect observation clearly suggests that there is an important difference between the tiny iron oxide particles formed as a result of acetate-induced IONP breakage and the formation of small IONPs as the

thermal decomposition product. Because the tiny iron oxide particles observed as a result of acetate breakage did not have silica shells, it can be concluded that the tiny iron oxide particles observed in Figure 41 were formed as a consequence of the acetate-induced breakage.

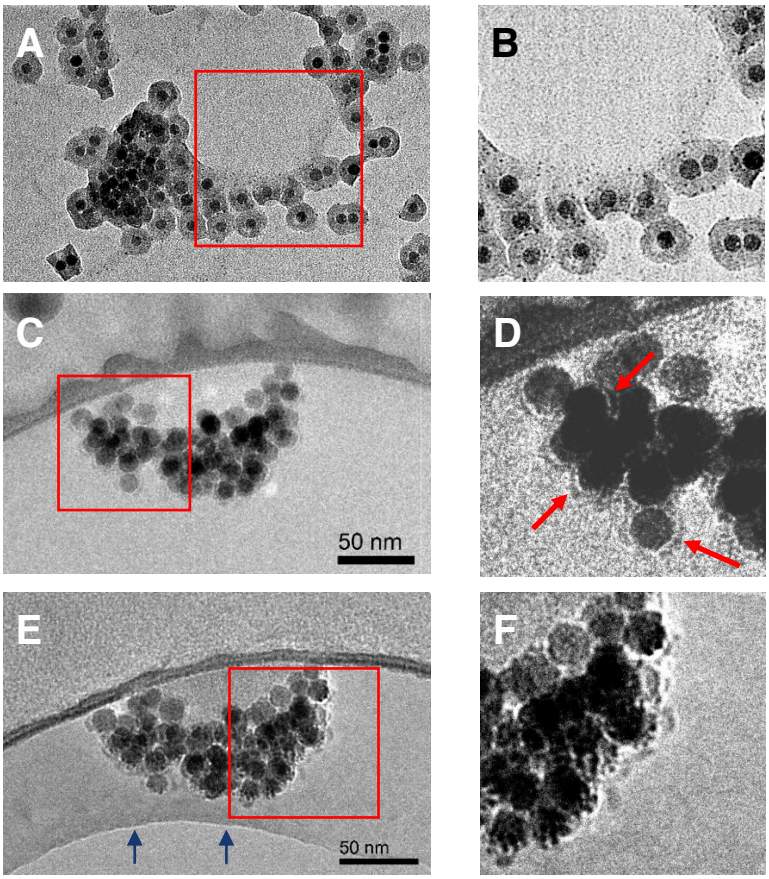

Figure 41. TEM image taken at 180 min of nanoemulsion process, B) magnified view of the region highlighted with red square in image A, C) cryo-TEM image of an CTAB-OA-IONPC at 120 min of nanoemulsion process, D) (C) magnified view of the region highlighted with red square in image C. Red arrows indicates the thin shells created around individual IONPs, E) The same CTAB-OA-IONPC shown in image D was destructed by melting the cryogenic medium with electron beam. Blue arrows indicates the direction of melting medium, F) magnified view of the region highlighted with red square in image C demonstrates the existence of tiny iron oxide particles within shells similar to those seen in image B.

3.5 Dynamic Light Scattering / Nanoparticle Tracking Analyses

3.5.1 DLS analysis of nanovesicle–IONPC hybrids

To make sure that the structures observed in Figure 22 and Figure 23 are also present in the bulk in identical sizes, DLS experiments were performed with the samples collected at 195 min of the nanoemulsion process. DLS analysis confirmed that mainly 400–600 nm sized objects were observable in both highly diluted and concentrated aqueous environments (Figure 42). A wide size distribution was obtained from DLS measurements because the monodispersed core–shell structures start to be released from the clusters at 195 min of reaction, as previously observed from the time-resolved TEM images (Figure 22D-F).

Figure 42A shows a typical correlation function obtained in DLS measurements. CONTIN algorithm was used to calculate the size distribution functions weighted by the scattered light intensity (Figure 42B). For complex samples, it is very difficult to define a relation between the scattered light intensity and weight- or number- concentration of the sample. Therefore, the raw solutions from CONTIN analysis were only multiplied by the mean total scattered intensity of a given sample.

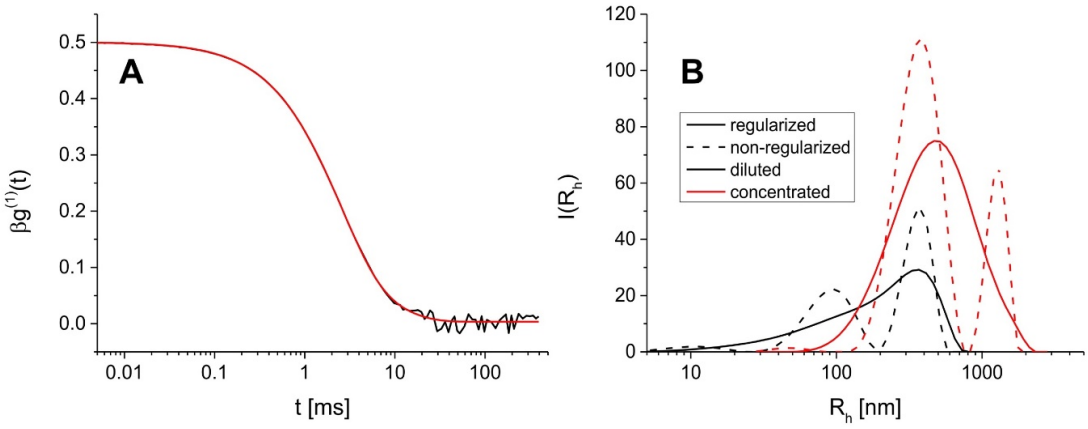

Figure 42. A) typical correlation function with a fit performer using the CONTIN algorithm, B) size distribution obtained from the CONTIN analysis for diluted (black) and concentrated (red) sample. The dashed lines refer to weakly regularized CONTIN solutions.

Apart from the regularized solutions in Figure 42B, the non-regularized ones giving some information about the mean size of the particle fractions present in the samples were shown. Regularization is an inherent procedure of CONTIN algorithm which finds a compromise between the solution accuracy and the complexity of the size distribution. The solution called here “regularized” are suggested by CONTIN as most probable ones, whereas the non-regularized (or weakly regularized) as the ones showing too many (statistically insignificant) details in the distribution function.

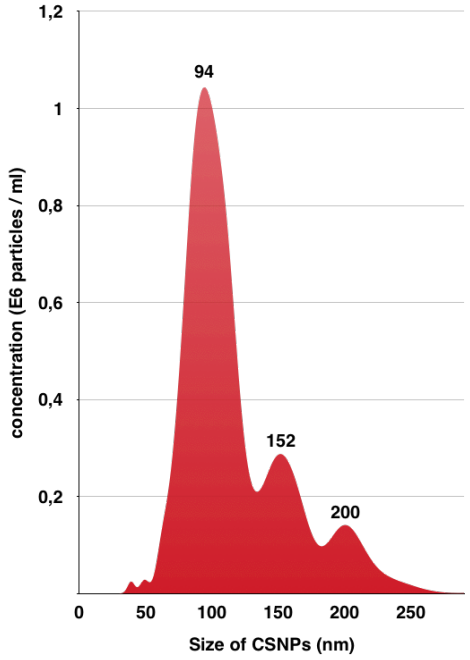

Figure 43. NTA analysis graph of CSNPs from nanoemulsion process.

Two samples were analyzed: one called “diluted” (simply diluted suspension) and one called “concentrated” which was obtained by collecting the magnetic particles with a strong magnet and reducing the volume of “supernatant”. It is clear from Figure 42B that the diluted sample contains a whole distribution of nanoparticles with sizes ranging from ~10 to ~1000 nm. The procedure of concentrating the sample with a magnet lead to a significant increase of concentration of particles with a radius in the region of several hundred nm plus to an appearance of even larger particles (above 1000 nm radius) which either were already present in the diluted sample at very low concentration or appeared as a result of aggregation in the increased concentration conditions. The number of smallest particles probably decreased although their

disappearance might be an artefact due to high intensity of light scattered by the bigger particles.

DLS analysis confirmed that mainly 400−600 nm sized objects were observable in both highly diluted and concentrated aqueous. A wide size distribution was obtained from DLS measurements because the monodispersed core−shell structures start to be released from the clusters at 195 min of reaction, as we observed from the time-resolved TEM. On the other hand, IONPCs formed in various sizes contribute to the wide size distribution observed.

3.5.2 NTA of CSNPs synthesized by nanoemulsion method

NTA analysis of CSNPs from nanoemulsion process (the same particles shown in Figure 19) measured in Milli-Q water revealed that majority of particles were having average hydrodynamic size of 94 nm. The rest of the particles having average 152 – 200 nm were probably due to particles having more than one iron oxide cores (Figure 43).

3.6 X-ray Photoelectron Spectroscopy Analysis

Carbon analysis of the non-etched sample shows mainly two components, which could be attributed to the C-N bond of CTA^+ molecules at 286.69 eV and CH_x (C-C / Si-C) species at 284.8 eV (Figure 44) (Leng et al., 2013; Vuori et al., 2014). The strongest peak (284.8 eV) would arise from APTES, CTA^+ and possibly from oleate. After 240 min etch, CH_x intensity sharply decreases and 240 min etched sample reveals another peak at around 285.7 eV. This peak was attributed to the C-N bonds of APTES because the intensity decrease between the 284.8 peak and the 285.7 peaks are not proportional (Vuori et al., 2014). This reveals that etching process removes the outermost carbon that was attributed to the CTA^+ and oleate but etching the APTES-rich silica shell continue to reveal APTES species. On the other hand, broadening of the peaks from 288 to 290 eV is an important indication of COO- species (Fleutot et al., 2011; Samusawa and Shiotani, 2015).

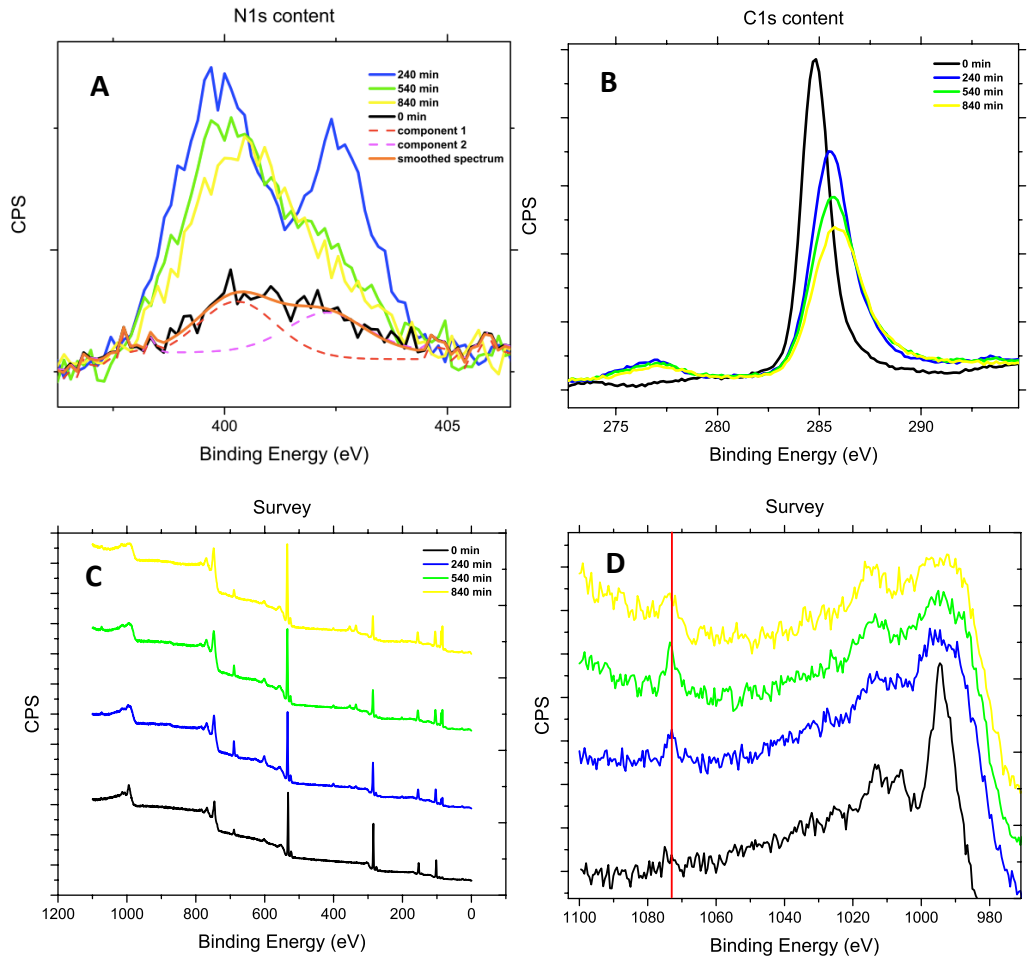

Figure 44. XPS analysis of CSNPs of the nanoemulsion process: A) nitrogen; B) carbon; C,D) General XPS survey. Red line indicates the 1073.38 eV sodium peaks

Nitrogen analysis of the on-etched sample shows a very week, two-component band (Figure 44). While 402.29 was attributed to the CTA^+ nitrogen (Leng et al., 2013), 400,27 was attributed to the nitrogen from APTES species. After etching the sample, intensity of the band significantly increases and the difference between the CTA^+ and APTES nitrogen becomes clearer. For 540-840 min etched samples, CTA^+ nitrogen almost disappear while the APTES nitrogen intensity moderately decreases. The intensity decrease consistent with the decrease of C-N carbon bands also confirms the existence of APTES and distinguish it from the CTA^+ species.

Surprisingly, etching the samples revealed the existence of sodium in particles at 1073.38 eV (Figure 44D). With the increasing etching time, sodium content also

increases. Existence of sodium is also evident in the oxygen region where the Na Auger peaks are usually observed (534-536 eV). Significant broadening in oxygen peaks and shifts to the Na Auger region with increasing etching time is consistent with the increasing sodium content within the silica shell. On the other hand, assigning oxygen peaks to the specific species is difficult since etching process induces the reduction of oxygen in samples. However, sodium content was regarded as additional proof for the existence of acetate species since acetate is the only molecular species that could be the source of sodium within silica shell (in the main text, we explained how the acetate-iron bonding occurs during the acetate-oleate exchange. Due to hydrophobic nature of the nanovesicle-IONPC fusion, only the mechanism that can source the sodium ions is the ethyl acetate saponification reaction inducing sodium acetate species).

3.7 Conclusion of the Chapter

When the chemical reactions taking place in a nanoemulsion process are discussed in detail, the acetate origin of the inner carbon shell can also be easily explained. Previously proposed hypotheses on the CTA^+-templated silica formation mechanisms required the silica precursors to be already hydrolyzed in the aqueous phase (Brinker, 1990; Fan, 2004; Kim et al., 2008b; Ye et al., 2012; Schubert, 2015). Such a hydrolysis prerequisite was considered essential for the interaction of negatively charged hydrolyzed silica precursors with positively charged CTA^+ molecules for silica condensation and growth. The initial hydrolysis of silica precursors can be achieved only by acid or base catalysis. However, acid/base catalyzed conditions do not correspond to nanoemulsion reaction conditions because nanoemulsion process was solely based on stabilizing pH of the reaction solution to neutral (pH ≈ 7) by the initial saponification reaction of ethyl acetate. In other words, the catalyst (NaOH) used in Kim and Ye *et al.* methods (Kim et al., 2008b; Ye et al., 2012) for the hydrolysis of silica precursors was immediately consumed in the nanoemulsion process by rapid ethyl acetate saponification. Hydrolysis of the silica precursor (TEOS) after its addition to neutral aqueous solutions is known to proceed extremely slowly because of the immiscibility gap between water and hydrophobic TEOS (Donatti and Vollet, 1996; Vollet et al., 1996).

Consequently, the introduction of the hydrophobic TEOS to the neutral aqueous solution of emulsifying CTA^+ molecules in the nanoemulsion process indeed promotes nano-sized vesicle formation because of the oil-in-water behavior of the unhydrolyzed TEOS. Formation of these nanovesicles was already evident in Figure 24. Therefore, it can be concluded that the mechanism of silica formation in the nanoemulsion process is different from the previously laid down hypotheses (Fan, 2004; Kim et al., 2008b; Ye et al., 2012) because unhydrolyzed silica precursors carried by the nano-vesicles are not capable of interacting with CTA^+. On the other hand, the above-presented results related to the acetate-induced breakage of the iron oxide particle surface and the thin iron oxide layer formation make the CTA^+–oleate bilayer removal from the nanoparticle surface a plausible scenario. Such a scenario makes it very unlikely that the inner carbon content seen in Figure 38D is related to the CTA^+–oleate bilayer. From the cryo-TEM analyses (Figure 24), we could conclude that the silica condensation did not start up to 120 min of the reaction. However, it was evident that the silica condensation started at some point after the micellar fusion of the IONPCs and nano-vesicles. This means that the pH conditions (acidic or basic) essential for the hydrolysis of silica precursors must have been provided by the IONPCs after fusion with nano-vesicles. Because the nanoemulsion process starts with the ethyl acetate saponification reaction, the pH conditions necessary to trigger the silica precursor hydrolysis were provided by the acetate layer that was already present before the fusion of nano-vesicles with IONPCs. Because the solvolysis of silica precursors by acetic acid is well-known (Orel et al., 2005) acetic acid-induced silica formation stands out as the only possible scenario. Consequently, we can conclude that the inner carbon content observed in Figure 38D was formed by acetate ligands, and therefore, CSNPs of nanoemulsion process are hereinafter referred as iron oxide–acetate–silica core–shell–shell nanoparticles (IONPs@acetate@SiO_2).

When the applicability of as-synthesized CSNPs are considered, the carbon shell in the outermost surface of CSNPs (Figure 37), which was very likely consists of CTA^+ molecules, biocompatibility of CSNPs because of toxic nature of CTAB become questionable. On the other hand, thick carbon coating on the surface would make the free amino groups within silica shell inaccessible.

Exchange of oleate ligands by acetate ions on the IONP surfaces was a very fundamental observation to describe the mechanism behind the silica coating on the individual IONP surfaces. We demonstrated that the nanoemulsion process in the absence of silica precursors resulted in fully acetate-coated IONPs (see section 3.3), and the acetate layer was preserved within the silica shell (Figure 38). Correspondingly, by knowing that the IONPCs are in fact Pickering-type emulsions (colloidosomes) constrained at the oil−water interface, we elucidated that the acetate/oleate exchange leading to silica formation proceeded in five steps (Figure 45):

i. A typical phase transfer of the OA−IONPs from the oil phase to aqueous phase by CTA^+ molecules (Figure 45A) results in the formation of IONPCs (Figure 45B) that we showed in Figure 17. IONPCs are simply formed by the OA−IONPs that are partially encapsulated by CTA^+ molecules at the liquid−liquid interface (Figure 45C). When the ethyl acetate was introduced to the alkaline dispersion of IONPCs, the unhydrolyzed excess of the ethyl acetate phase directly interacted with the CTA^+−oleate bilayer on the IONP surfaces (Figure 45C,D). Formation of oil-in-water emulsion of ethyl acetate that was induced by the excess CTA^+ surfactant molecules would make such interactions highly possible (Yang and Li, 2014). However, a large fraction of ethyl acetate was immediately hydrolyzed in the aqueous phase because of the saponification reaction. It is highly feasible that ethyl acetate was exchanged continuously between the CTA^+−oleate bilayer and the water phase, which results in the diffusion of acetate ions within the bilayer. As soon as the acetate ions gained access to the IONP surfaces, the acetate/oleate exchange must have proceeded via breakage of the iron oxide particles (Figure 45E);

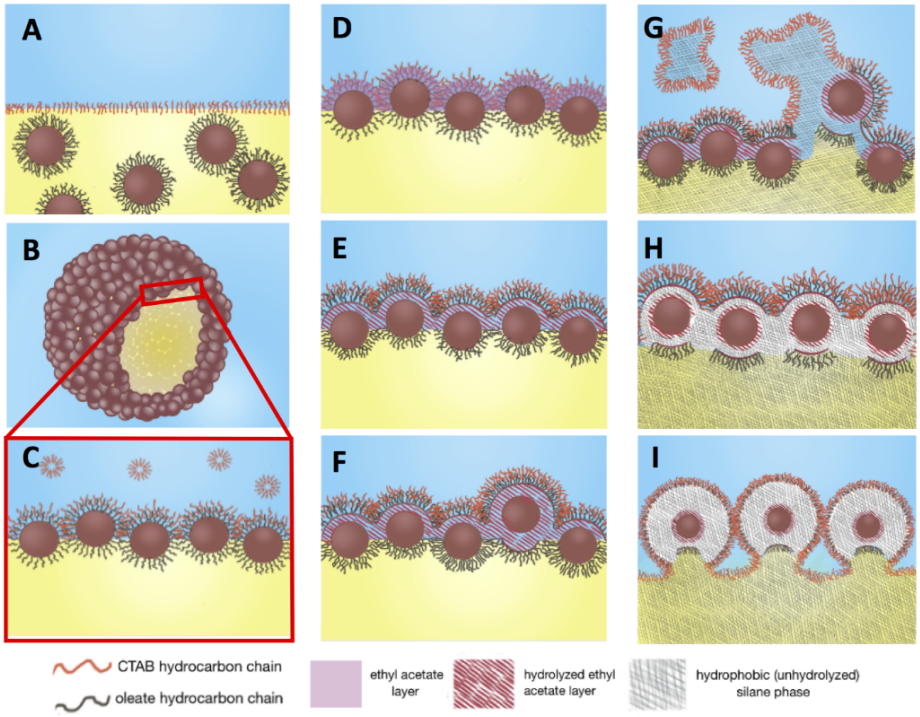

Figure 45. Micellar fusion mechanism leading to the formation of CSNPs of nanoemulsion process (IONPs@acetate@SiO_2 structures): (A initial mixtures of aqueous CTAB solution and OA–IONPs dispersion in chloroform showing the phase separation between the aqueous (blue) and hydrophobic (yellow) phase oil. CTAB molecules create a monolayer at the liquid–liquid interface; B) after the evaporation of the organic phase, OA–IONPs are stabilized at the liquid– liquid interfaces, which results in the formation of IONPCs encapsulating the hydrophobic phase; C) IONP building blocks of IONPCs at the liquid–liquid interface and some micellar structures of CTA^+ in the aqueous phase; D) upon ethyl acetate addition into the solution, it is dispersed within the CTA^+–oleate bilayer on the surface of the clusters; E) after ethyl acetate saponification, the resulting acetate ions interact with the iron oxide surface and break the iron oxide structure. The breakage results in thin iron oxide shell formations stabilized by the CTA^+–oleate bilayer; F) later, the acetate layer penetrates the hydrophobic phase and removes the oleate-only coated surface of the IONPs. This results in fully dynamic IONP formations as seen for the fourth IONP from the left; G) after addition of silica precursors, they form nanovesicles with excess CTAB molecules/micelles in solution. They eventually attack the dynamic sites of the IONPCs (fourth IONP from the left), which they use as tiny gates to fuse with the hydrophobic core of the clusters. The fusion process takes place by the coalescence of CTA^+ monolayers of nanovesicles to the CTA^+–oleate bilayers; (H) encapsulated silica precursors start to accumulate to space between the dynamic CTA^+–oleate bilayer and acetate-coated IONPs. Silica eventually starts to form, initially in the agglomerated form as observed in Figure 22A-C I) as time progresses, silica shell continues to grow, which will eventually lead to the formation of monodispersed IONPs@acetate@SiO_2 (Kertmen et al., 2017).

ii. We showed that the acetate/oleate exchange proceeded by breakage of iron oxide nanoparticles. Then, the broken iron oxide particles create a thin layer above the IONP surfaces (Figure 41C,D). Correspondingly, when the tiny iron oxide particles were formed by the acetate-induced breakage, the CTA^+− oleate bilayer must have been carried away along with the tiny iron oxide nanoparticles (Figure 45E). The attraction of iron-based thin shell to the IONP cluster surface could be assisted by the ionic and hydrogen bonds between the thin iron oxide shells and acetate ions on the IONP surfaces. Meanwhile, the hydrophobic portion of the IONPs that are still coated with oleate and oriented toward the hydrophobic phase within the IONPCs must have protected the IONPCs from undergoing a disassembly;

iii. Eventually, the acetate-induced breakage must have taken place underneath the hydrophobic portion of the IONPs (Figure 45F). This must have removed the oleate-only coated portions of the IONPs that are oriented toward the hydrophobic core of the IONPCs. When the removal of oleate took place, individual iron oxide particles in clusters must have started to disassemble. Dynamic motions obtained by IONPCs after the disassembly must have facilitated the movement of their IONP building blocks toward the continuous aqueous phase. This also means that the CTA^+−oleate bilayer holding the thin iron oxide shells must have undergone dynamic rearrangements. Consequently, the displaced IONP building blocks of the IONPCs must have served as tiny gates between the nanovesicles of silica precursors and the hydrophobic phase in the core of the IONPCs. It must be pointed out that the existence of “tiny gates” is the most accurate scenario because IONPCs were stable till 120 min of the nanoemulsion process when the nanovesicle−IONPC hybrids start to form (Figure 24). In other words, IONPCs do not undergo a full disassembly process because of removal of the acetate/oleate bilayer from the surface;

iv. Dynamic rearrangement of the CTA^+−oleate bilayer and formation of the tiny gates opening to the hydrophobic cores of IONPCs must have been the driving force for the fusion of nanovesicles to the IONPCs. This appears to be an accurate scenario because similar fusion interactions of surfactant vesicles to the dynamic ligands on the nanoparticle surfaces are already known (Lee et al., 2013). When

the fusion process started (Figure 45G), the hydrophobic phase of silica precursors must have been transferred into the hydrophobic core of the IONPCs, and two hydrophobic phases must have merged inside the clusters (as in the case of coalescence of Janus colloidal capsules (Rozynek et al., 2014)). This could be the explanation why we observed that the emulsions seemed to be invading the IONP clusters in the cryo-TEM images (Figure 24A,B). Consequently, the rearrangement of IONPCs around the nanovesicle phases must have resulted in the formation of IONPC−nanovesicle hybrids that we observed in Figure 24C. Notably, additional CTA^+ molecules supplied to the IONPCs by nanovesicles must have provided additional flexibility and dynamicity to the CTA+−oleate bilayer for the dynamic rearrangement;

v. Hydrolysis of the silica precursors must have started as soon as the IONPCs and nanovesicle fusion was complete. What facilitated the formation of silica shells in spherical morphologies must have been the additional CTA^+ molecules supplied by the nanovesicles to the CTA^+−oleate bilayers. This scenario is consistent with the observation of a thick carbon template around the silica shells in Figure 37C-E. These thick carbon shells in such high concentrations could be provided only by the CTA^+ surfactant molecules that are the largest source of carbon in the nanoemulsion process. Eventually, the hydrolysis of silica precursors on the IONP surfaces must have been catalyzed by the acetate ions (Orel et al., 2005). The continuous accumulation of silica precursors from the hydrophobic core of the IONPCs to the space between the oleate−CTA^+ bilayer and IONP cores must have grown the silica shells (Figure 45H). Condensation of the precursor into silica around the IONP cores must have continued till the CTA^+−oleate bilayers lost their mobility (elasticity) and collapsed when the silica shells reached their maximum size (~60 nm). Release of individual IONPs@acetate@SiO_2 core−shell structures from the nanovesicle−IONPC hybrids must have finally started, when the unity of CTA^+−oleate bilayers was lost (Figure 45I).

CHAPTER 4

Magnetic properties of CSNPs

4.1 Vibrating sample magnetometry (VSM)

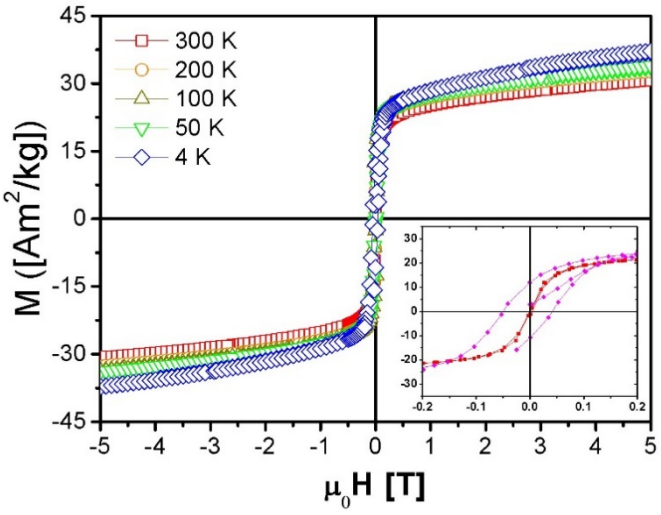

Figure 46. Hysteresis loop measured at different temperatures from 300 K - 4 K range, inset shows the coercive field for 300 K and 4 K measurement.

The temperature dependence of hysteresis loops measured in range 300–4 K are shown in Figure 46. At room temperature sample displays the characteristic behavior of superparamagnetic nanoparticles. The decrease of temperature promotes a noticeable increase in the coercivity H_c, as a result of the blocking of the nanoparticle magnetization (Larumbe et al., 2012), the most visible changes are observed between high (300 K) and low (4 K) temperatures (Figure 46 inset), inset shows low field part of hysteresis). Room temperature curve shows zero remanence and coercivity while at 4 K it exhibits finite coercivity of 0.0414 T. This is a typical characteristic of nanosized particles which are superparamagnetic. Magnetic loops do not saturate in any temperatures confirming the occurrence of core/shell model. Hence, we assume that in this model the spins at the surface area are highly disordered due to high surface

anisotropy. Thereby it is harder to align surface spins on applied magnetic field (Parekh et al., 2009). It should be remarked that the magnetization even at 5 T is below the typical bulk value (≈92 Am^2/kg) (Vergés et al., 2008), for our samples the magnetization for 4 K at 5 T is equal to ∼37.5 Am^2/kg. Such a decrease may result from lack of coordination for the surface ions which can lead to spin disorder (Aquino et al., 2005) or even spin canting at surfaces (Coey, 1971; Zboril et al., 2002). The reduction of magnetization can be also considered as a result of silica coating hindering the exchange interaction between the magnetic sublattices of the Fe_3O_4 nanoparticles (Coşkun et al., 2010), nevertheless it is a common observation in similar systems (Guo et al., 2016).

Blocking temperature T_B was also determined. As Figure 47a shows zero-field cooling (ZFC open symbol) and field cooling (FC solid symbol) magnetization curves exhibit characteristic superparamagnetic behavior. With the magnetic field increase (from 0.01 to 1 T) TB shifts into the lower temperatures exhibiting the typical superparamagnetic behavior. Moreover, the effect of silica coating is strongly exhibited for high applied magnetic fields (0.5 and 1 T at Figure 47b) at low temperatures and it is manifested as strong increase of magnetization with lowering of temperature. Insert of Figure 47b shows that, at low temperatures magnetization deviates from the Bloch law $M_S(T) = M_S(0)(1 - BT^{\alpha})$. For our samples, α deviates from 1.5 and its equal to ≈2. It is found that for sufficiently small particles, deviations from the Bloch law $T^{3/2}$ have been observed [as shown by Linderoth *et al.* on 3.1 nm amorphous Fe-C particles (Hendriksen et al., 1993; Linderoth et al., 1993), and by Aquino *et al.* in magnetic fluids based on ferrite nanoparticles (Aquino et al., 2005)]. Also calculations made by Hendriksen *et al.* (Hendriksen et al., 1992) show that α changes from 3.0 for smallest clusters to the 1.5 for bulk. In magnetic systems the temperature dependence of magnetization is related to the spin waves, or magnons, and this approach is the base for Bloch law of $T^{3/2}$, in our case α deviates from 3/2 and it is equal to 2.

These deviations are related to the size effect, since in the nanoparticles the spatial confinement reduces the number of degrees of freedom and generates a gap in the corresponding spin wave spectrum as it is shown by Hendriksen et al. (Hendriksen et al., 1992). The blocking temperature dependency is explained by decreasing particle size. In the system, there is a point, in which the NPs magnetic energy becomes comparable to the thermal energy. As a result, thermal fluctuations of the magnetic

moment of particles arise, and this strongly influence their magnetic properties. For sufficiently small particle size, magnetic anisotropy energy may become comparable, or less influential, than the thermal energy, even at low temperatures. Application of an external magnetic field to such particles causes rotation of magnetization direction according to the field. After application of an external magnetic field to the superparamagnetic particles, they are trying to arrange their magnetic moments to the direction of the field, however, in paramagnets, thermal energy will be the main competitor and thus disrupting this arrangement. The stronger the magnetic field is applied, the easier it sets direction of magnetic moment of particles. Therefore, the stronger the magnetic field is applied, the lower blocking temperature is achieved. This behavior is very well known in the case of super- paramagnetic systems such as the ones presented in this publication. Finally, due to their nanometric size, the deviation from an ideal spherical shape predominant, although visible round, any imperfection of the surface at the nanoscale level would be highly influential in the structure, thus contributing to the K1 value shown here.

4.2 Alternating Current Magnetic Susceptibility (ACMS)

To get a better insight into the nature of magnetic interactions, we investigated the temperature dependence of the AC susceptibility for frequency range 10–10 000 Hz. AC susceptibility is useful technique in characterization of small particles which exhibit superparamagnetism. Figure 48a shows real part of magnetic susceptibility χ' (T) and it is clearly seen that we observe one broad peak, which shifts to the higher temperatures with increasing frequency. Frequency depended changes of position of maximum are shown on Figure 48b. These features clearly indicate superparamagnetic behavior in CSNPs. The observed frequency sensitivity of the χ' maximum may be attributed to the superparamagnetic blocking process of isolated, non-interacting, and weak-interacting nanoparticles (Néel, 1955; Dormann et al., 1997). A useful quantity that characterizes relaxation property is parameter Φ defined as (Binder and Young, 1986):

$$\Phi = \frac{\Delta T_{max}}{T_{\max}(f)\Delta \log(f)} \qquad (1)$$

f [Hz]	Φ
36	0.041
50	0.048
100	0.075
361	0.060
500	0.063
1000	0.065
3612	0.057
5000	0.060
10000	0.062

Table 24. Parameter Φ determined based on the Eq. (1) for 36–10 000 Hz frequencies.

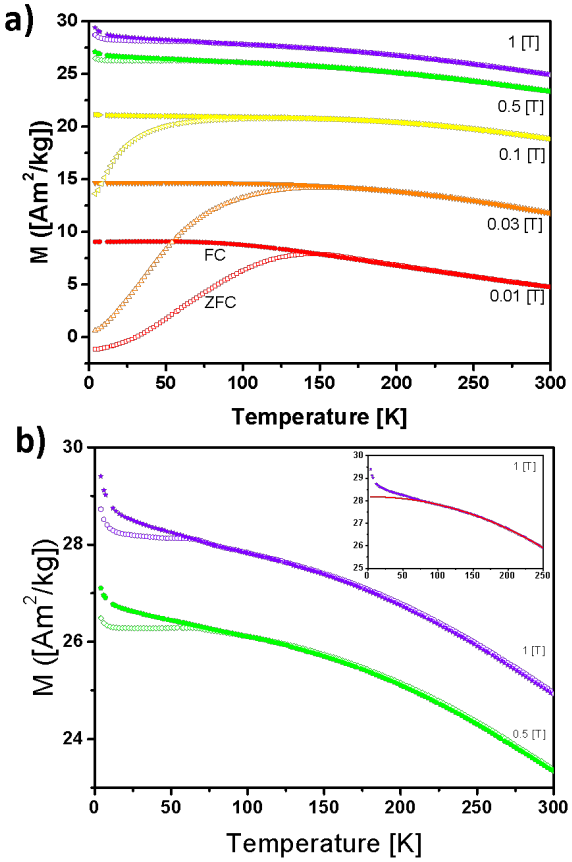

Figure 47. a,b) shows zero field cooling (ZFC open symbol) and field cooling (FC solid symbol) magnetization curves exhibit characteristic superparamagnetic behaviour, with the magnetic field increase (from 0.01 to 1 T) T_B shifts into the lower temperatures.

This parameter relates the shift of the temperature of the χ' maximum with measurement frequency. For superparamagnetic system value of Φ is ~0.3, for noninteracting nanoparticles between 0.10–0.13 and 0.05–0.13 for interacting nanoparticles (Hüser et al., 1986; Dormann et al., 1997). Also the observed frequency dependent behavior in the χ'_{AC} may be attributed to the spin-glass system, however for spin-glass the Φ value is quite small in comparison to the superparamagnetic one and it is <0.005 (Tholence, 1980; Synoradzki and Toliński, 2012), thus base on this parameter we can clearly distinguish these two states. Table 24 present values of Φ obtained for our CSNPs for all frequencies. These values are slightly less than the typical value for non-interacting superparamagnetic nanoparticles which may indicate slight dipole interactions.

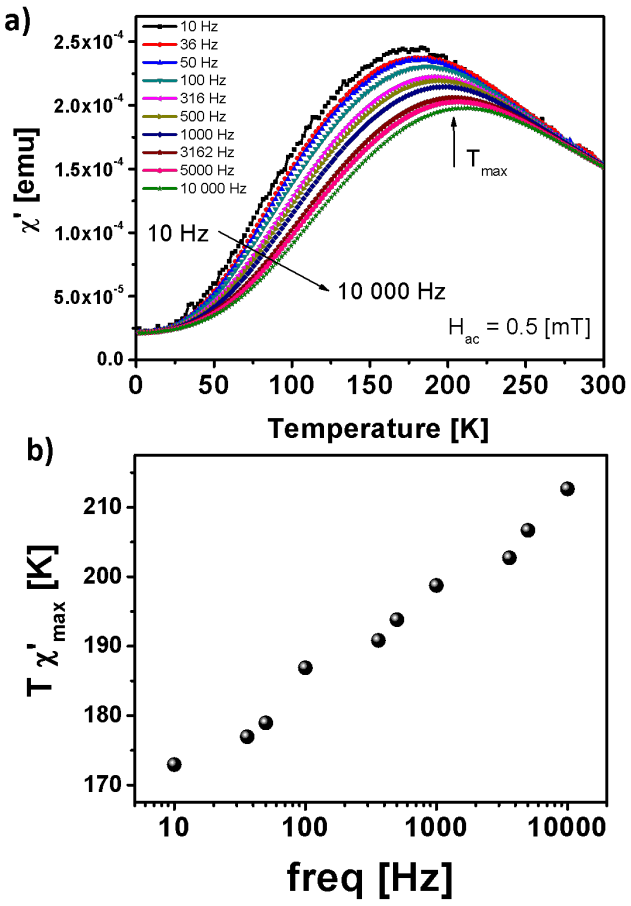

Figure 48. a) Real part χ' of AC susceptibility as a function of temperature for 10-10 000 Hz frequencies, b) T_{max} as a function of frequency.

CHAPTER 5

Organic Synthesis and Nanoparticle Functionalization

5.1 Surface purification of CSNPs by dialysis

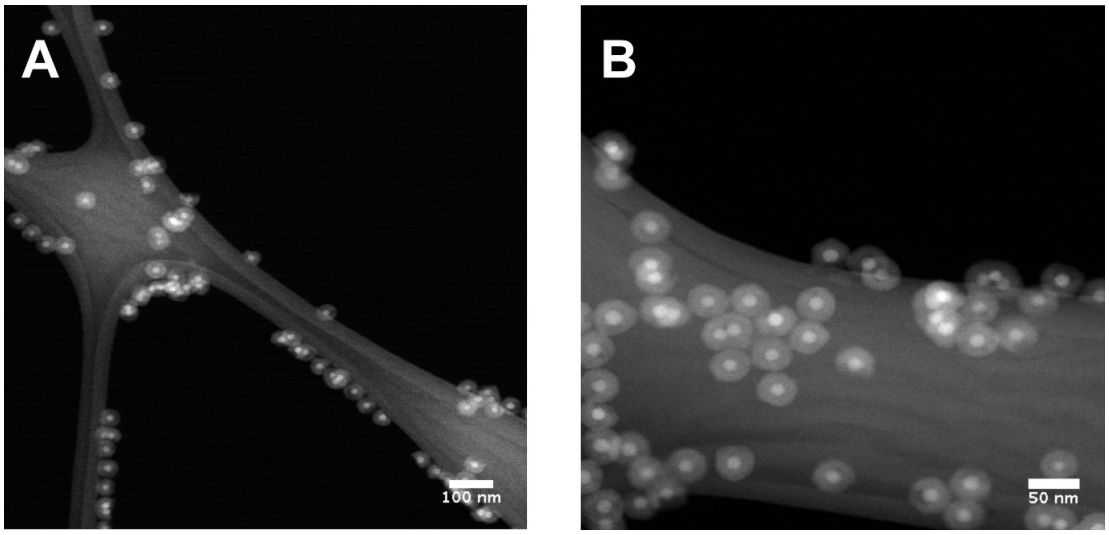

Figure 49. A) Low magnification and, B) high magnification dark-field HR-TEM image of CSNPs after dialysis in acetic acid solution

Previous HRTEM observations made via EELS evidenced the thick carbon coatings at the outermost surface of the CSNPs (Figure 37). Such thick carbon coating, of which origin was attributed to the CTA^+ molecules as the most abundant carbon source in nanoemulsion process, would possess problems in surface functionalization process of CSNPs; but also in biological studies because of the toxic nature of CTA^+ molecules (Zhang et al., 2015). Correspondingly, removal of the carbon coating was performed by dialysis method.

Dialysis of the CSNPs (produced by typical nanoemulsion process) in 2 M acetic acid solution resulted in decrease in thickness of the silica coatings. Figure 49 shows that the particle sizes were significantly reduced as a result silica shell etching by acetic acid. The thickness of the CSNPs after dialysis were reduced to ~12.5 nm [shell thickness was measured as 22±1,5 nm before dialysis in acetic acid solution (Tadyszak et al., 2017)].

TEM images of the CSNPs of the nanoemulsion process after dialysis in acetate buffer demonstrated that the particles were still intact, having mean particle size of 46.5±1,8 nm, with lower degree of size reduction in silica shells when compared to acetic acid dialyzed CSNPs (Figure 50). Particles were overlapping due to increased hydrophilicity after dialysis that caused aggregation on hydrophobic carbon TEM grid used in imaging. However, there were no silica necking between particles which could cause permanent aggregation. Black dots observed on particles in image B were due to unwashed acetic acid contamination because TEM sample were prepared directly dialysis from acetate buffer.

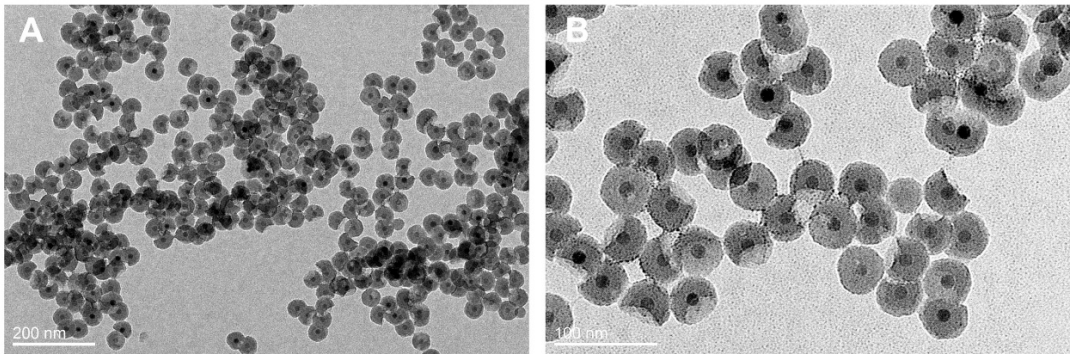

Figure 50. A) Low magnification TEM image and, B) higher magnification TEM image of CSNPs of nanoemulsion process dialyzed in acetate buffer.

5.2 Determination of free amino groups on CSNP surfaces by UV-vis spectroscopy

Fmoc-NHS was used to functionalize the dialyzed CSNPs to assess the carbon shell removal efficiency in dialysis process, which would be directly correlated by the accessibility of free amino groups within silica shell of CSNPs. Positive accessibility assessment of amino groups would also confirm the employability of CSNPs in further antifungal conjugation studies and their applicability in biological studies.

Absorption spectroscopy was used to quantify the free amino groups within the silica shell of CSNPs of nanoemulsion process to determine the minimum amount of OH-PEG-NHS functionalization through amide bonds. The same information used in the next step to determine the minimum amount of Fmoc-FMDP and Fmoc-BADP to derivatize the OH-PEG functionalities on the surface. On the other hand, same method was

employed to quantify the amount of FMDP and BADP covalently attached to CSNPs by releasing their Fmoc protections.

In these experiment, absorbance spectra of solutions containing 3,2 – 19 mmol Fmoc-piperidine adduct obtained from Fmoc-cispentacin-piperidine (%1) solutions; and the solution from %1 piperidine dispersion of Fmoc-CSNPs were recorded (Figure 51). Calibration curve constructed for the absorption spectra on left (Figure 51). The amount of Fmoc directly attached to surface of CSNPs was equal to 15,2 nmol. It is noteworthy to mention that, the reason of employing Fmoc-cispentacin was the ease of compound preparation (one-step reaction) and its (although non-proteogenic) amino acid nature that would allow to develop this method later for analysis of more complex, laborious to produce, costly Fmoc-BADP and Fmoc-FMDP molecules.

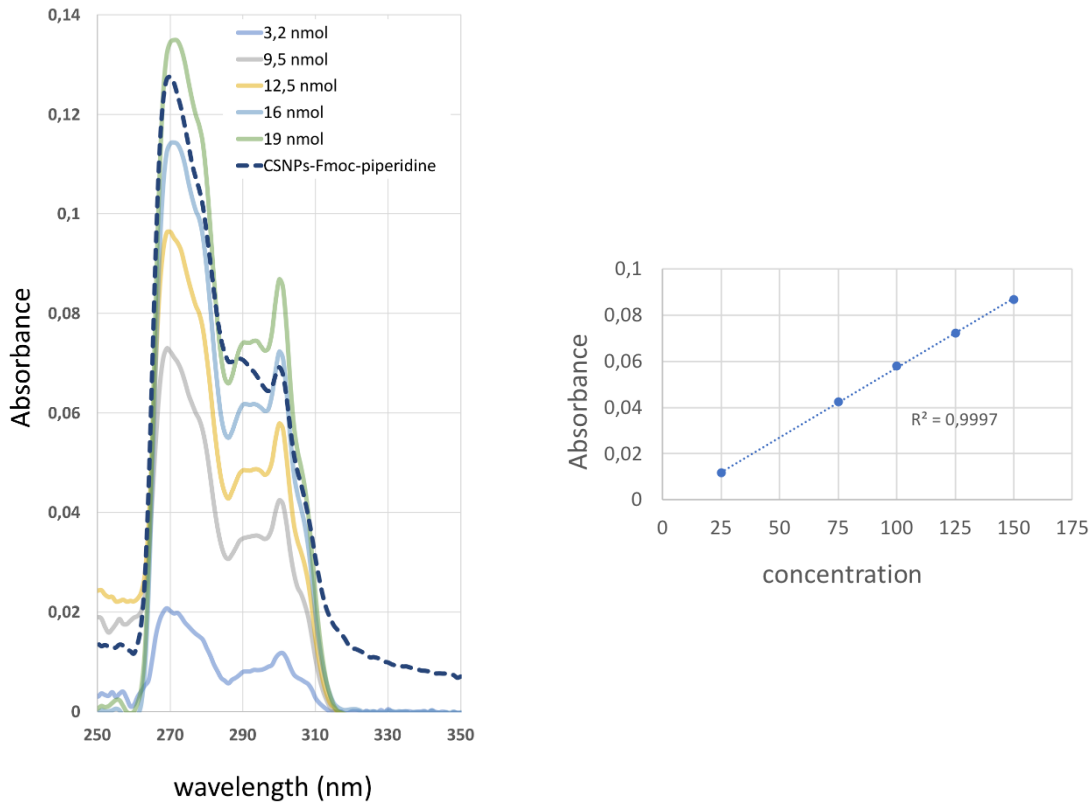

Figure 51. Absorbance spectra and its calibration curve obtained for Fmoc-piperidine adduct from Fmoc-cispentacin, fitted to absorption spectrum of Fmoc-piperidine adduct released from CSNPs. CSNPs-Fmoc-piperidine stands for Fmoc released from CSNPs

5.3 Determination of OH-PEG attachment to the CSNPs by FT-IR analysis

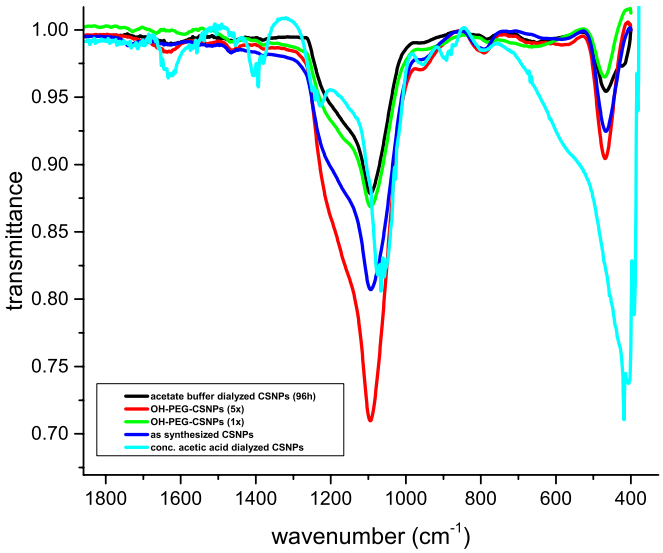

Figure 52. FTIR analysis of as-synthesized, dialyzed and OH-PEG functionalized CSNPs of the nanoemulsion process.

When the OH-PEG functionalized (OH-PEG-CSNPs) and dialyzed CSNPs (dia-CSNPs) are compared to as-synthesized CSNPs, it was seen that all the significant vibrations of Si-O-Si, C-O-C and C-C vibrations were concentrated at 900-1300 cm^{-1} band (Figure 52). However, the difference between the acetic acid and the acetate buffer dialyzed samples revealed the small differences between C-C vibrations of CTA^+ and Si-O-Si vibrations of silica shells. In section 3.4, EELS analysis demonstrated that most of the CTA^+ molecules are positioned at the outer surface of the CSNPs (Figure 37). However, acetic acid dialysis removes ~12.5 nm of silica shell along with the CTA^+ molecules (see section 5.1), although some CTA^+ molecules still remains at the inter-particle spaces (Figure 39). Obviously, removal of ~12.5 nm layer shifts revealed that vibrations at 1066 cm^{-1} belongs Si-O-Si bonding, while a significant reduction in bad intensity at 1100-1200 cm^{-1} region appeared; which was obviously related to removed CTA^+ molecules. On the other hand, in comparison to as-synthesized CSNPs, not the band shape but only the intensity of band significantly changed for the acetate buffer dialyzed and OH-PEG functionalized samples, where the 1096 cm^{-1} become the only

obvious vibration. Taking into account that there was no difference between the as-synthesized and PEG functionalized samples, it was obvious that the C-C vibrations of both PEG and CTA^+ molecules are concentrated at this region. This conclusion was also supported by the CSNPs functionalized with different amounts of OH-PEG (1x or 5x), that resulted in significant change in band intensity at 1096 cm^{-1} while the band shape was retained.

5.4 ICP-MS analysis of OH-PEG-CSNPs

Total amount of silicon and iron concentration in OH-PEG-CSNPs samples determined by ICP -MS analysis was equal to 213,3 µg/ml. This sample was later used for *in vitro* biological experiments.

5.5 NMR analysis of Fmoc-FMDP, Fmoc-BADP and their intermediates

Antifungal agents and their intermediates were prepared in good yields according to detailed procedure given in CHAPTER 2. Each compound was identified by standard ^1H and ^{13}C NMR analysis along with their HSQC and HMBC analysis.

5.5.1 N-succinimidyl, methyl fumarate

White solid, yield 70%. ^1H NMR (800MHz, DMSO-d_6): δ = 2.85 (s, 4H, CH_2-CH_2), 3.79 (s, 3H, OCH_3), 7.08-7.13 (m, 2H, CH=CH); ^{13}C NMR (800MHz, DMSO-d_6): δ = 169.88 (2 x C=O-N), 163.95 (C=O-O), 160.63 (C=O-O), 137.91 (**C**H=CH), 126.97 (CH=**C**H), 52.61 (OCH_3), 25.50 (CH_2-CH_2)

Original ^1H, ^{13}C and HSQC spectra can be found in appendixes 1-3.

5.5.2 N-succinimidyl, trans-4-oxo-4-phenyl-2-butenoate

Yellow solid, yield: 70%. ^1H NMR (800MHz, DMSO-d_6): δ = 2.88 (s, 4H), 7.03 (dd, 1H, *J* = 15.7), 7.60 (dd, 2H, *J* = 8.1 , 7.6), 7.74 (dt, 2H, *J* = 8.4 , 1.1), 8.08 (dd, 1H, *J* = 8.3 , 1.1), 8.29 (d, 1H, *J* = 15.7); ^{13}C NMR 188.57 (**C=**OAr), 170.0 (2 x C=O-N), 161.2 (C=O-O), 142.3 (**C**H=CH), 135.5 (CHAr), 134.4 (CHAr), 129.1 (4 x CHAr), 124.8 (CH=**C**H), 25.5 (CH_2-CH_2).

Original ^1H, ^{13}C, HMBC and HSQC spectra can be found in appendixes 4-7.

5.5.3 N^2-(Fmoc), N^3-(4-methoxyfumaroyl)-L-2,3-diaminopropanoic acid (Fmoc-FMDP)

White solid, yield: 74.5%. ^{1}H NMR (800MHz, DMSO-d_6): δ = 8.67 (t, J = 5.9 Hz, 1H), 7.89 (d, J = 7.5 Hz, 2H), 7.71 (d, J = 6.4 Hz, 2H), 7.63 (d, J = 8.5 Hz, 1H), 7.42 (t, J = 7.4 Hz, 2H), 7.33 (t, J = 7.4 Hz, 2H), 7.03 (d, J = 15.5 Hz, 1H), 6.58 (d, J = 15.5 Hz, 1H), 4.29 (d, *J* = 7.3 Hz, 1H), 4.23 (t, *J* = 7.1 Hz, 1H), 4.19 – 4.14 (m, 1H), 3.72 (s, 1H), 3.62 (dt, *J* = 13.4, 5.5 Hz, 1H), 3.41 (ddd, *J* = 13.7, 7.9, 6.1 Hz, 1H); ^{13}C NMR (800MHz, DMSO-d_6): δ = 171.78 (C=O-O), 165.46 (**C**=O-OCH_3), 163.19 (C=O-N), 156.00 (C=O-N), 143.75 (2 x CHAr), 140.68 (2 x CHAr), 137.35 (**C**H=CH), 128.24 (CH=**C**H), 127.61 (2 x CHAr), 127.05 (2 x CHAr), 125.23 (2 x CHAr), 120.10 (2 x CHAr), 65.74 (CH-O), 53.40(C-COO), 51.99 (-CH_3O), 46.58 (**C**H-CH_2COOH), 40.03 (C-NH).

Original ^{1}H, ^{13}C, HMBC and HSQC spectra can be found in appendixes 12-15

5.5.4 N^2-(Fmoc), N^3-trans-4-oxo-4-phenyl-2-butenoyl-L-2,3-diaminopropanoic acid (Fmoc-BADP)

White solid, yield 60%. ^{1}H NMR (800MHz, DMSO-d_6): δ = δ =3.45 (m, 1H), 3.66 (m, 1H), 4.20-4.15 (m, 1H), 4.25-4.20 (t, 1H), 4.33-426 (dd, 1H), 7.00 (d, 1H, *J* = 15.3), 7.35-7.28 (m, 2H), 7.42-7.37 (m, 2H, *J*), 7.57 (t, 2H, *J* = 7.8), 7.63 (d, 1H, *J* = 8.1), 7.72-7.67 (m, 3H), 7.74 (d, 1H, *J* = 12.3), 7.88 (d, 2H, *J* = 7.6 , 1.1), 8.01-7.96 (m, 2H, *J* = 8.3 , 1.1), 8.73 (t, 1H, *J* = 5.8); ^{13}C NMR (800MHz, DMSO-d_6): δ = 189.8 (**C=**OAr), 171.8 (C=OOH), 163.8 (C-**C**=O-N), 156.0 (O-**C**=O-N), 143.75 (CHAr), 140.68 (CHAr), 136.54 (C-Ar), 136.13 (CH=**C**H), 133.74 (CHAr), 132.12 (**C**H=CH), 128.98 (CHAr), 128.60 (CHAr), 127.61 (CHAr), 127.06 (CHAr), 125.20 (CHAr), 120.10 (CHAr), 65.74 (CH-O), 53.55 (C-COO), 46.69 (**C**H-CH_2COOH), 40,20 (C-NH)

Original ^{1}H, ^{13}C, HMBC and HSQC spectra can be found in appendixes 8-11.

5.5.5 *cis*-2-(9-Fluorenylmethyloxycarbonyl)amino-cyclopentanecarboxylic acid

White solid, yield: 83%. ^{1}H NMR (800 MHz, DMSO-d_6): δ= 11.99 (s, 1H, OH), 7.89 (d, *J* = 7.5, 2H, CHAr), 7.75 – 7.68 (dd, *J* = 7.5, 7.5, 4H, CHAr), 7.36 – 7.29 (m, 3H, CHAr +

NH), 4.24 (dd, *J* = 8.7, 5.5, 1H, NH-C**H**), 4.21 – 4.13 (m, 3H, OCH_2CH), 2.83 (q, *J* = 7.7 Hz, 1H, C**H**-COO), 1.93 – 1.50 (m, 6H, $-CH_2-CH_2-CH_2-$); ^{13}C NMR (800MHz, DMSO-d_6): δ = 174.26, 155.54, 144.02, 143.73, 140.66, 127.59, 127.58, 127.10, 127.04, 125.45, 125.25, 120.05, 120.03, 65.52, 53.98, 47.43, 46.69, 31.33, 26.38, 21.64.

Original ^1H, ^{13}C, HMBC and HSQC spectra can be found in appendixes 16-19.

5.6 Determination of Fmoc-FMDP and Fmoc-BADP attachment to the OH-PEG-CSNPs by FT-IR

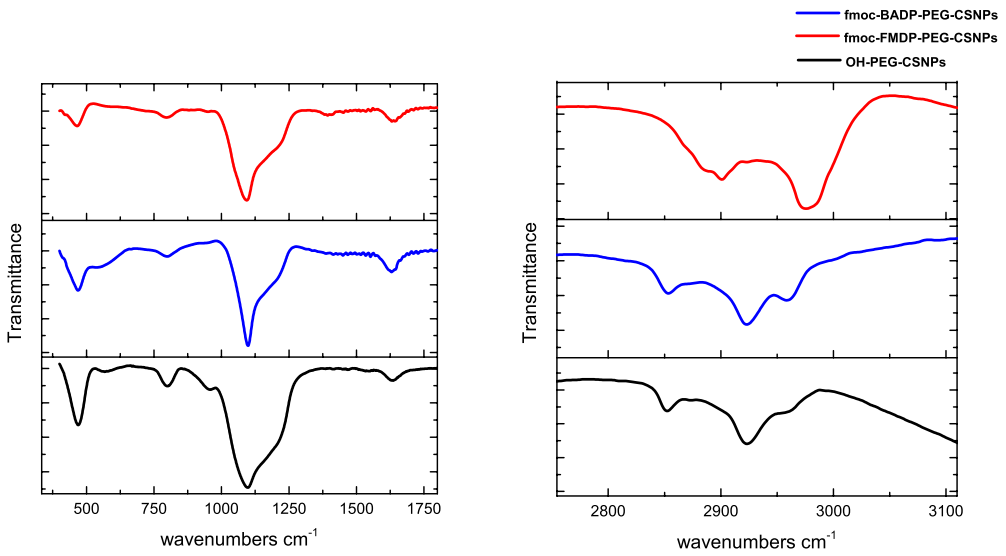

Figure 53. FTIR analysis of Fmoc-FMDP-PEG-CSNPs and Fmoc-BADP-PEG-CSNPs

FTIR analysis of Fmoc-FMDP-PEG-CSNPs and Fmoc-BADP-PEG-CSNPs in comparison to OH-PEG-CSNPs did not provide any conclusive information since all the aliphatic C-H vibrations, including Si-O-Si and C-O-C vibrations were concentrated at 1000-1250 cm^{-1} band. Only the difference observed for Fmoc-FMDP-PEG-CSNPs was the appearance of additional weak peak at 1394 cm^{-1}, which was attributed to do the exitance of $-OCH_3$ vibrations from FMDP (NIST). On the other hand, apart from slightly shifted bands of Fmoc-FMDP-PEG-CSNP sample, there were no significant difference at 2800-3000 cm^{-1} region to distinguish the C-H stretching vibrations.

5.7 Determination of the amount of FMDP and BADP attachment to CSNPs by UV-Vis spectroscopy

After the determination of free amino groups and functionalization of CSNPs by OH-PEG, Fmoc-BADP and Fmoc-FMDP reaction were carried out with amounts more than 15,2 nmol (amount calculated for free amino groups on CSNPs in section 5.2. Assuming that OH-PEG reactions proceeded with 100% efficiency and some free amino groups might have remained due to changes in number of particles used between the different reaction batches, excess amounts of Fmoc-BADP and Fmoc-FMDP were used).

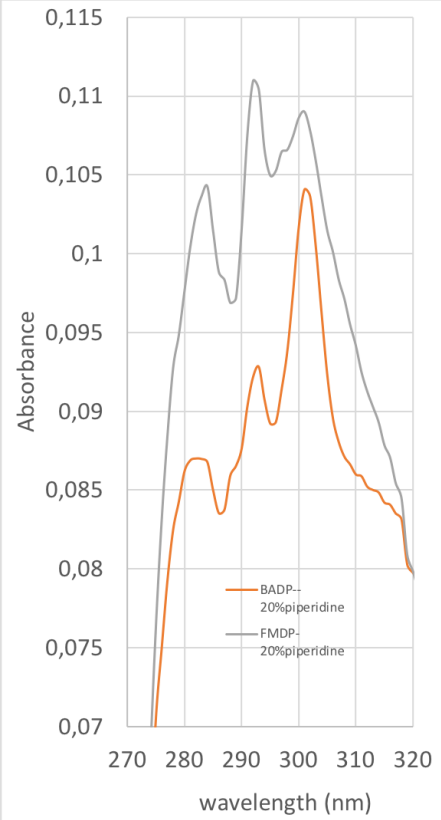

Figure 54. Absorbance spectra of Fmoc-piperidine adducts obtained from Fmoc-BADP-PEG-CSNPs and Fmoc-FMDP-PEG-CSNPs.

After the reactions, Fmoc protecting groups of the FMDP and BADP molecules attached to OH-PEG-CSNPs were released by 20% piperidine-DMF solution. Both samples exhibited the characteristic absorbance peak of Fmoc-piperidine adduct at 301 nm (Figure 54).

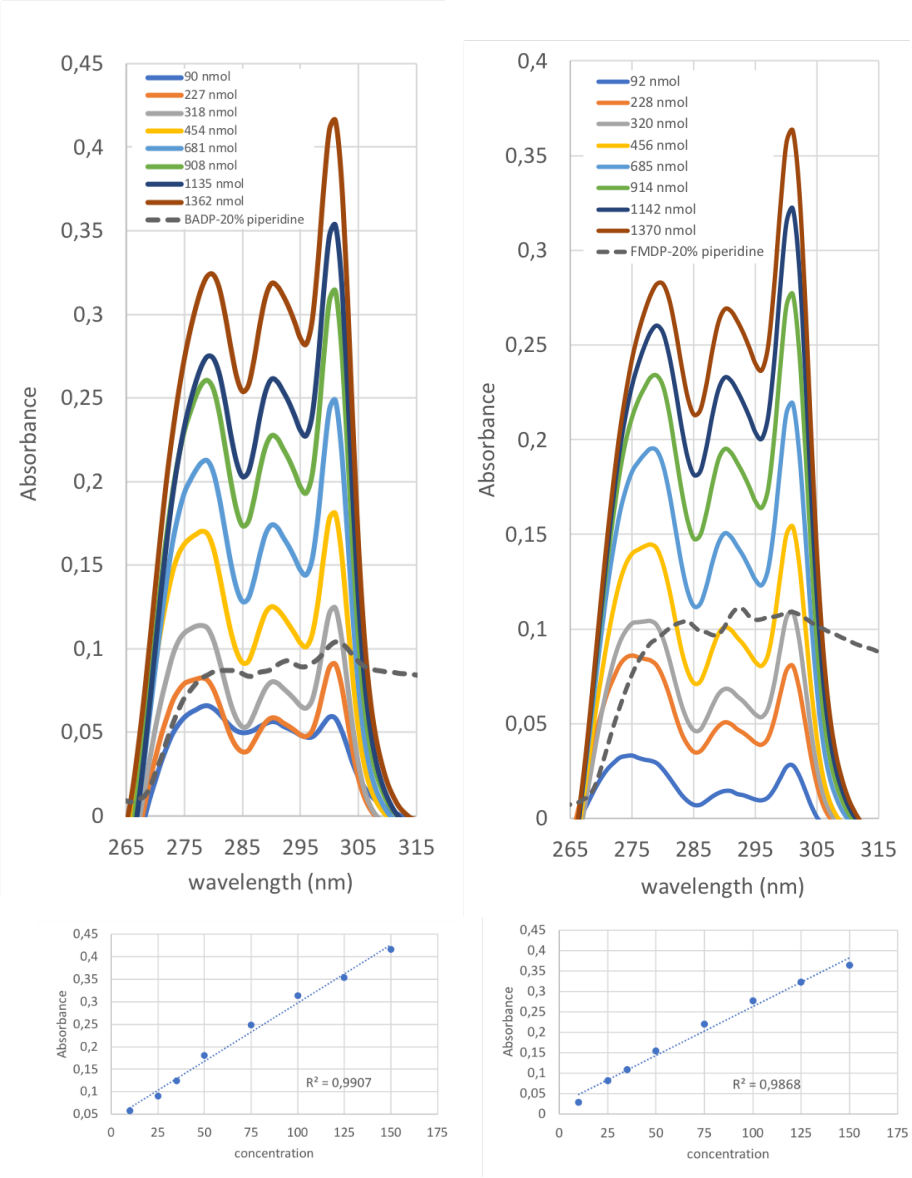

Figure 55. Absorbance spectra and calibrations curves obtained for Fmoc-piperidine adduct from pure Fmoc-BADP and Fmoc-FMDP, fitted absorption spectrum of Fmoc-piperidine adducts released from Fmoc-BADP-PEG-CSNPs and Fmoc-FMDP-PEG-CSNPs. "BADP-20% piperidine" and "FMDP-20% piperidine" stand for absorbance curves of Fmoc-piperidine released from Fmoc-BADP-PEG-CSNPs and Fmoc-FMDP-PEG-CSNPs.

In the next step, absorbance spectra of solutions containing 90 – 1362 nmol Fmoc-piperidine adduct obtained from Fmoc-BADP/20% piperidine and 92 – 1370 nmol Fmoc-FMDP/20% piperidine reactions (Figure 55). Calibration curves constructed absorption spectra are shown below the respective graphs. Then, absorbance spectra

obtained from Fmoc-BADP-PEG-CSNPs and Fmoc-FMDP-PEG-CSNPs were fitted to these calibration spectra. From these measurements, amount of BADP and FMDP attached to CSNPs was calculated as 260 and 308 nmol (205,3 µM and 173.3 µM), respectively. Apart from the quantitative analysis of BADP and FMDP, qualitative measurement of the Fmoc absorbance is the strongest confirmation for the successful attachment of inhibitors to CSNPs.

5.8 X-ray Photoelectron analysis of Fmoc-FMDP-PEG-CSNPs, Fmoc - BADP-PEG-CSNPs and OH-PEG-CSNPs

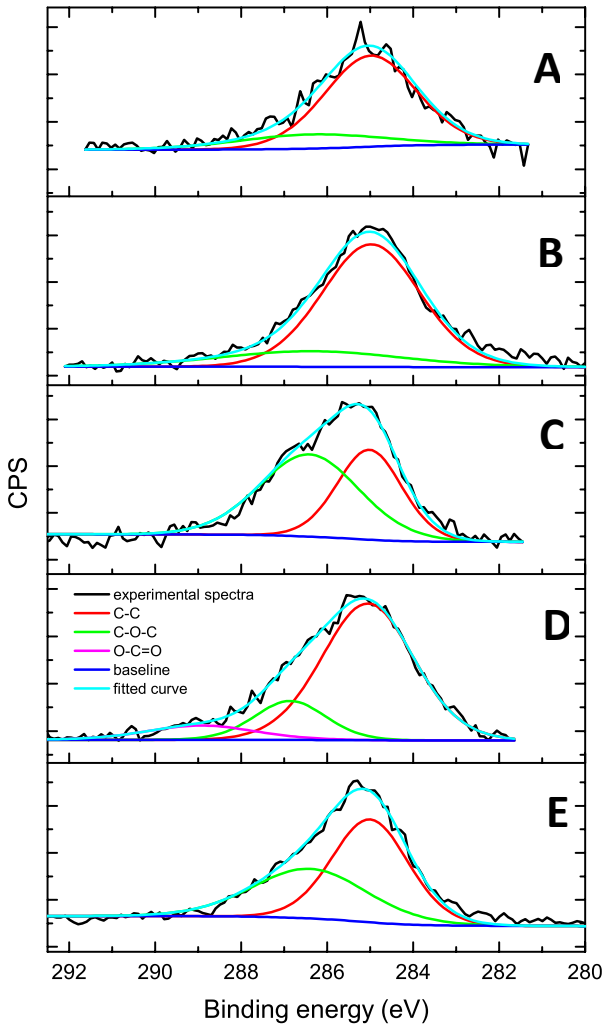

Figure 56. C1s analysis of as-synthesized CSNPs from nanoemulsion process (A), purified CSNPs by dialysis against acetic acid buffer (B), OH-PEG-CSNPs (C), Fmoc-FMDP-PEG-CSNPs (D), and Fmoc-BADP-PEG-CSNPs (E)

Despite the qualitative measurement of the Fmoc-piperidine adducts obtained from Fmoc-BADP-PEG-CSNPs and Fmoc-FMDP-PEG-CSNPs were the strongest indication of FMDP and BADP covalently attached to CSNPs, further confirmation was sought by high-resolution XPS analysis.

Sample	C-C			C-O, C-O-C		
	Energy	fwhw	%	Energy	fwhw	%
As-synthesized CSNPs	284,99	2,507	80,29	286,39	3,956	19,71
Dialyzed CSNPs	284,98	2,688	80,87	286,38	5	19,13
OH-PEG-CSNPs	285,01	1,774	41,53	286,41	2,731	58,47
Fmoc-FMDP-PEG-CSNPs	284,98	2,486	58,96	286,38	3,532	41,04
Fmoc-BADP-PEG-CSNPs	285	2,086	57,97	286,4	3,136	42,03

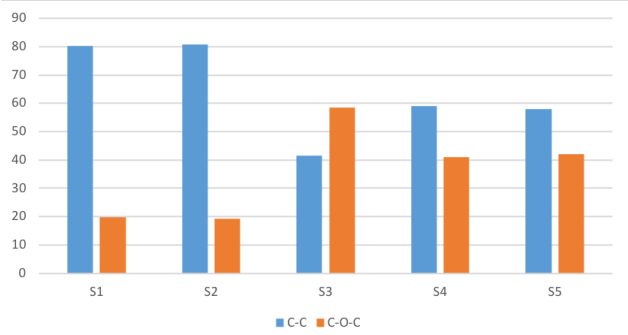

Table 25. Relative C-C and C-O-C binding energy ratios of samples and their graphical presentation (O-C=O included in C-O-C).

C1s analysis of Fmoc-BADP-PEG-CSNPs and Fmoc-FMDP-PEG-CSNPs in comparison to as-synthesized CSNPs, dialyzed (acetic acid buffer) CSNPs and OH-PEG-CSNPs clearly evidenced that OH-PEG was successfully attached to CSNPs (Figure 56). This information was retrieved from the significant increase observed in the intensity of C-O/C-O-C binding energy of OH-PEG-CSNPs at 286,4 eV relative to C-C binding energy of as-synthesized and dialyzed CSNPs ~285 eV (Table 25). O-C=O binding energy visible in Fmoc-FMDP-PEG-CSNPs spectrum was regarded as the indication of -OCH_3 groups of FMDP molecules since this energy level is missing from Fmoc-BADP-PEG-CSNP sample. Comparable C-C / C-O ratios of as-synthesized and dialyzed CSNPs, despite the fact that

surface CTA^+ molecules were removed from as-synthesized CSNPs in a great extent by dialysis (Figure 38), was attributed to the exposed propyl groups of APTES species and the acetate species adsorbed on the surface of CSNPs after dialysis process. Notably, despite the samples contained aromatic Fmoc groups and BADP contained additional phenyl ring in its structures, no aromatic binding energy level was observed.

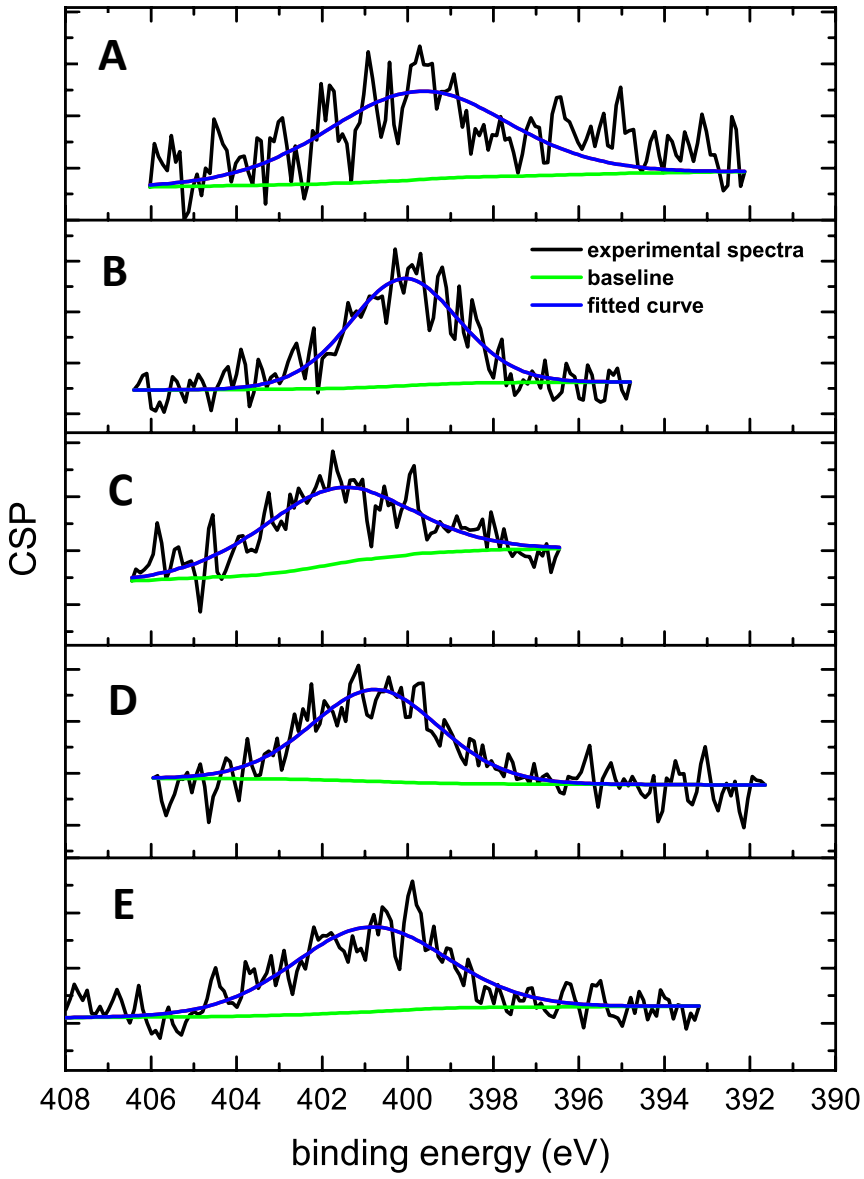

Figure 57. N1s analysis of as-synthesized CSNPs from nanoemulsion process (A), purified CSNPs by dialysis against acetic acid buffer (B), OH-PEG-CSNPs (C), Fmoc-FMDP-PEG-CSNPs (D), and Fmoc-BADP-PEG-CSNPs (E).

N1s analysis of the samples (Figure 57), on the other hand, gives a totally different impression than the XPS spectra obtained for as-synthesized CSNPs earlier discussed in section 3.6. While 402.29 eV was assigned to C-N species of CTA^+ molecules, 400,27 eV was assigned to amino groups of the APTES molecules. However, being differently than the previous XPS measurement where the surface of CSNPs was cleaned/etched by ion sputtering, herein a mild chemical cleaning procedure was applied. Chemical process could be expected to introduce additional chemical species that can alter binding energies. Interaction of acetate species with amino groups during the dialysis process is one of the most probable scenarios. Correspondingly, the new XPS spectra obtained after dialysis shows an improvement in the intensity of nitrogen species with a negligible shift in binding energy (399.7 eV for as-synthesized CSNPs and 400.09 eV for dialyzed CSNPs). However, notably, after the attachment of OH-PEG species to CSNPs, a significant shift to 401.7 eV was observed. This binding energy can be undoubtedly attributed to the formation of amide bonds (N-C=O). On the other hand, equal 400.08 eV binding energy for Fmoc-FMDP-PEG-CSNPs and Fmoc-BADP-PEG-CSNPs is in agreement with the fact that both molecules carry the same N1s species that results in 1eV shift from OH-PEG-CSNP spectrum.

O1s analysis of the samples give important information about the nature of oxygenated species (Figure 58). When it is considered that the relative amount of oxygen content of the samples was calculated as 50.14% (as-synthesized CSNPs), 48.38% (dialyzed CSNPs), 47.93% (OH-PEG-CSNPs), 48.74% (Fmoc-FMDP-PEG-CSNPs) and 48.84% (Fmoc-BADP-PEG-CSNPs), it is clear that the amount of oxygen removed with the silica layer after dialysis was replaced by other species. In accordance with the N1s and C1s data hinting the interaction of acetate and amino groups on the surface of CSNPs after dialysis, oxygen rich acetate species might have replaced the lost SiO_2 oxygen atoms. This fact was also clear from the equal amount of C-O species found in C1s data. Acetate species must have replaced not only oxygen but also the C-C energies lost after the removal of CTA^+ molecules by dialysis (taking into account that CTA^+ molecules consist of 19 carbon atoms, a large amount of acetate molecules must have been adsorbed). From the spectra obtained for OH-PEG-CSNPs and as-synthesized CSNPs, peak at ~534,6 eV is indicator of water content. Thus, these spectra seem shifted to higher energy levels that might be the consequence of the interactions with water.

For dialyzed and Fmoc-FMDP/BADP-PEG-CSNPs samples, the peak at 533.4 eV is an indicator of O-C=O bonds of ester species. Such observation is particularly important since it reveals the existence of ester bonds after dialysis. Considering that the acetate buffer removed around 10 nm of silica shell during dialysis, the breakage of the Si-O-Si bonds seems to be proceeded by formation of ester bonds between Si-O and acetate species.

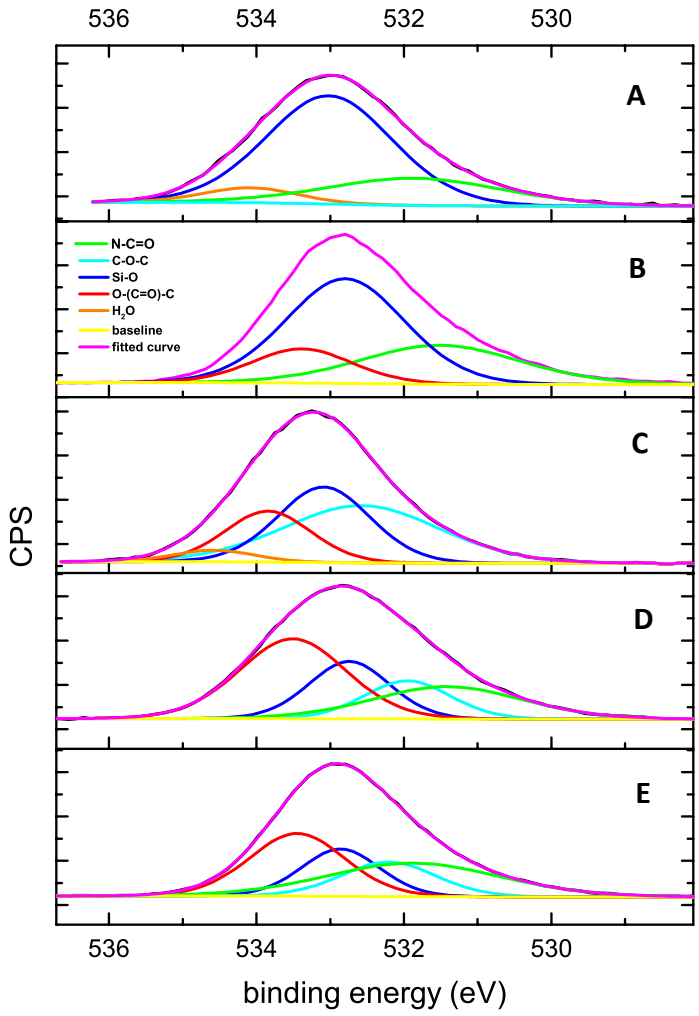

Figure 58. O1s analysis of as-synthesized CSNPs from nanoemulsion process (A), purified CSNPs by dialysis against acetic acid buffer (B), OH-PEG-CSNPs (C), Fmoc-FMDP-PEG-CSNPs (D), and Fmoc-BADP-PEG-CSNPs (E).

At ~532.5 eV, appearance of a new band for OH-PEG-CSNPs was attributed to the energy levels of C-O-C species from PEG chain in the presence of water. The same band appears at 531.9 – 532.1 range for Fmoc-FMDP/BADP-PEG-CSNPs samples in the absence of water. On the other hand, O-C=O species energy level observed for Fmoc-FMDP-PEG-CSNPs and Fmoc-BADP-PEG-CSNPs 533.4 eV was significantly increased in intensity; confirming that the conjugation of Fmoc-FMDP/BADP to OH-PEG-CSNPs was successful. At last, observation of 531.4-531.8 eV bands for all samples, except OH-PEG-CSNPs, were regarded as the indication of N-C=O bonds. While these species can be attributed to the amides formed by acetate species for as-synthesized and dialyzed samples, they are the indication of the amide bonds in Fmoc-FMDP and Fmoc-BADP species. The absence of these bonds in OH-PEG-CSNPs could be the consequence of the shift to higher energy levels caused by the presence of water (N1s data evidenced the amide formation).

5.9 ICP-MS analysis of BADP-PEG-CSNPs and FMDP-PEG-CSNPs

Total amount of silicon and iron concentrations in FMDP-PEG-CSNPs and BADP-PEG-CSNPs samples determined by ICP -MS analysis were equal to 40.5 µg/ml and 78.9 µg/ml, respectively. These samples were later used for *in vitro* biological experiments.

5.10 Conclusion of the chapter

In this chapter, it was shown that the simple purification process of CSNPs by dialysis against acetate buffer was a very effective, mild process to obtain CSNPs in monodispersed form. Acetate buffer dialysis, in contrast to previously reported concentrated acetic acid dialysis, was proven to be much more effective and less destructive to CSNPs.

Fmoc-piperidine absorbance method used to determine the number of free amino groups available for further functionalization of CSNPs was shown to be a very efficient quantification protocol for chemical processing of CSNPs. For the first time, method has been used to prove that, from the chemical point of view, CSNPs produced by nanoemulsion process were highly suitable materials for drug loading via covalent linkages.

Fmoc-piperidine absorbance method was also adopted for the quantification of FMDP/BADP-PEG-CSNP conjugation efficiencies. Detailed NMR analysis showed that the Fmoc-FMDP and Fmoc-BADP derivatives prepared for this purpose can be obtained in quite good yields. Fmoc-piperidine quantification method presented in this chapter proved that concentration of FMDP and BADP can be easily determined by UV-vis absorption spectroscopy. Herein developed method is very likely to constitute a quantitative analysis protocol for further studies that might be carried out with different derivatives of GlcN-6-P synthase inhibitors and CSNPs.

While Fmoc-piperidine absorbance method was proven to be an effective qualitative determination of chemical derivatization of CSNPs with GlcN-6-P synthase inhibitors, further support sought by FTIR analysis did not provide any additional information other than a strong indication of successful PEG derivatization of CSNPs. This was a consequence of the aliphatic nature of the GlcN-6-P synthase inhibitors that overlaps with strong PEG and Si-O-Si vibrations in the same region. However, high resolution XPS analysis provided valuable information about the successful attachment of PEG chains to CSNPs. Significant increase observed in O-C=O chemical binding energies after Fmoc-FMDP and Fmoc-BADP attachment to OH-PEG-CSNPs evidenced the successful conjugation of the inhibitors to CSNPs via esterification (Figure 58).

Notably, when the ratio of nanoparticle concentrations expressed as silicon+iron content and the molarity of FMDP/BADP attached to CSNPs are compared, it was seen that the FMDP conjugation efficiency was ~2.5-times more efficient than the BADP.

CHAPTER 6

In vitro Biological Studies

6.1 Cytotoxicity and viability assays of human cells

Impact of 2.5-50 µg/ml -PEG-CSNPs on human hypopharyngeal carcinoma (FaDu), human cervical cancer (HeLa) and normal fibroblast (MSU1.1) cell lines were tested by determining their mitochondrial activity with WST-1 test. In these tests, OH-PEG-CSNPs did not show any cytotoxic effects against any of the cell lines. FMDP-PEG-CSNPs and BADP-PEG-CSNPs at 2.5-10 µg/ml exhibited quite comparable, non-toxic effects similar to OH-PEG-CSNPs towards HeLa and FaDu. At 10 µg/ml, effects of FMDP-PEG-CSNPs started to be slightly observed against MSU1.1, killing ~20% of the cells. At 25 µg/ml, FMDP-PEG-CSNPs killed 82% of FaDu and 90% of MSU1.1 whereas ~50% of the HeLa cells were still viable. At 2.5-25 µg/ml range, BADP-PEG-CSNPs had no impact on any of the cell lines. However, 2-folds increase in the amount of BADP-PEG-CSNPs (50 µg/ml) killed 36% of FaDu and 63% of MSU1.1 and ~70% HeLa cells. (Figure 59-Figure 61).

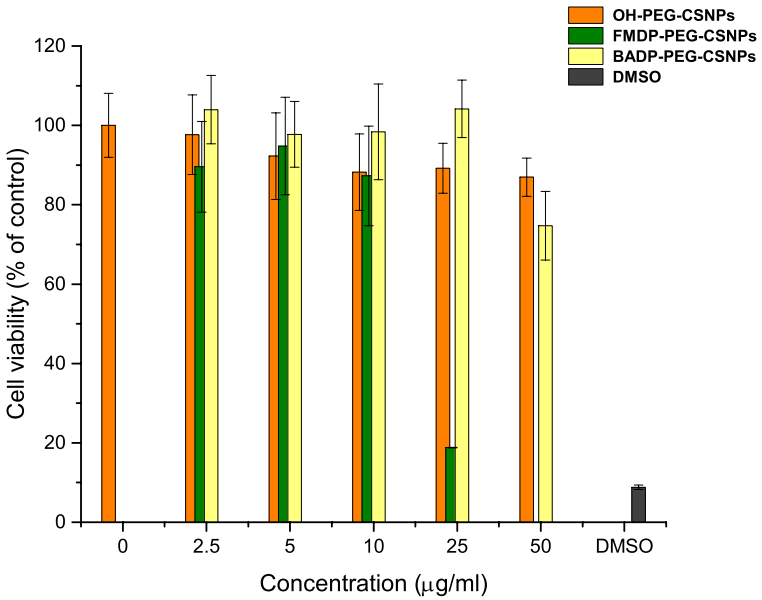

Figure 59. FaDu viability: FMDP-PEG-CSNPs tested for 2.5-25 µg/ml and BADP-PEG-CSNPs tested for 2.5-50 µg/ml in comparison to 2.5-50 µg/ml OH-PEG-CSNPs.

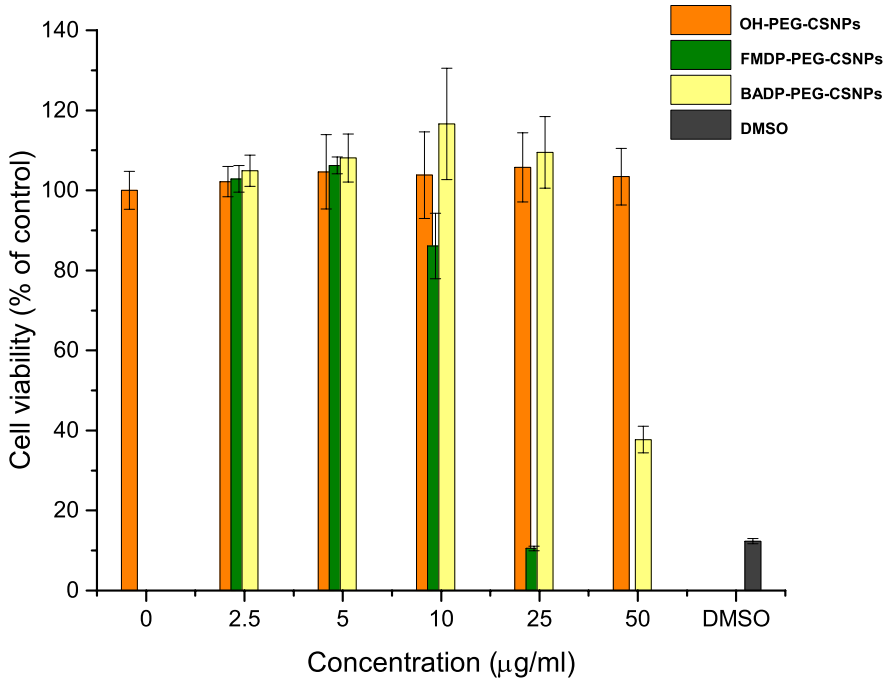

Figure 60. MSU-1.1 viability: FMDP-PEG-CSNPs tested for 2.5-25 μg/ml and BADP-PEG-CSNPs tested for 2.5-50 μg/ml in comparison to 2.5-50 μg/ml OH-PEG-CSNPs.

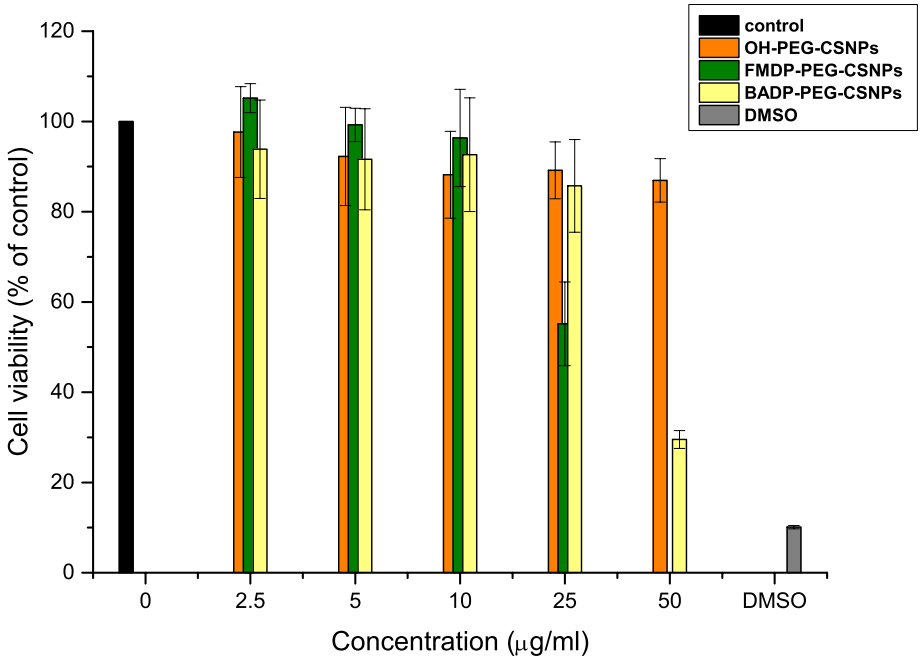

Figure 61. HeLa viability: FMDP-PEG-CSNPs tested for 2.5-25 μg/ml and BADP-PEG-CSNPs tested for 2.5-50 μg/ml in comparison to 2.5-50 μg/ml OH-PEG-CSNPs.

6.2 Growth kinetics and viability of *Candida albicans*

After determination of the maximum FMDP/BADP-PEG-CSNP concentrations required the kill more than 50% of the cancer and normal human cells, the same range of the particle concentrations were tested against *Candida albicans.*

Growth kinetics *of Candida albicans* was assessed by the turbidity of the cell suspension as a measure of fungal growth, which was measured spectrophotometrically at 570 nm (OD_{570nm}) with a microplate reader. The data collected at every 2 h interval up to 10 h and then up to 24h demonstrated that the OH-PEG-CSNPs at concentration ranging between 1-50 µg/ml had no negative impact on cell growth (Figure 62).

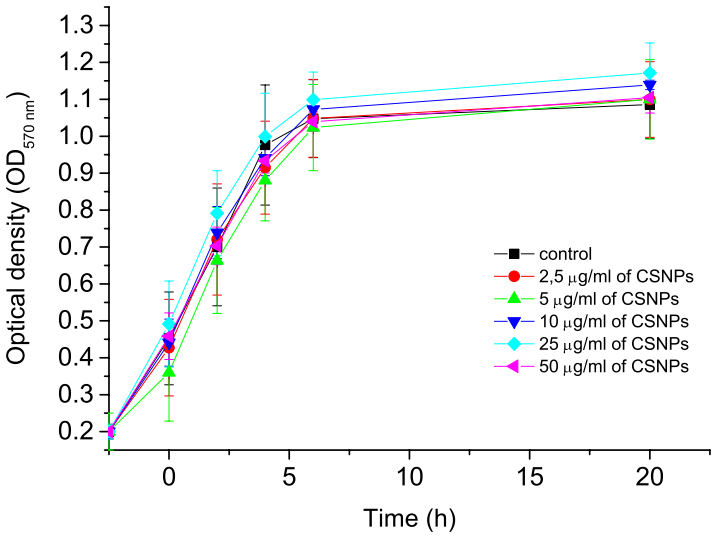

Figure 62. *Candida albicans* growth kinetics in the presence of 1-50 µg/ml concentration of CSNPs. The results are expressed as the mean of three independent experiments and the error bars show the standard deviation.

Using the same method, viability of Candida albicans reassessed up to 22h in the presence of 0,4-25 µg/ml FMDP-PEG-CSNPs, BADP-PEG-CSNPs and OH-PEG-CSNPs. While FMDP-PEG-CSNPs caused 14% decrease in number of cells in comparison to control, BADP-PEG-CSNPs caused 20% decrease (Figure 63). Number of Candida albicans gradually decreased with minor changes at 6.5-25 µg/ml particle concentrations. As a last attempt, increasing the concentration of BADP-PEG-CSNPs (2-folds, to 50 µg/ml) also did not result in any significant changes (between 12.5, 25 and 50 µg/ml

concentrations there were only 2-3% decrease in number of cells). On the other hand, growth inhibitory activity were tested up to 24h with 25 µg/ml FMDP-PEG-CSNPs and 50 µg/ml BADP-PEG-CSNPs in comparison to 25 µg/ml OH-PEG-CSNPs demonstrated that at 20-24 hour, BADP-PEG-CSNPs caused 28% decrease in Candida albicans growth kinetics whereas FMDP-PEG-CSNPs caused 17% decrease (Figure 64).

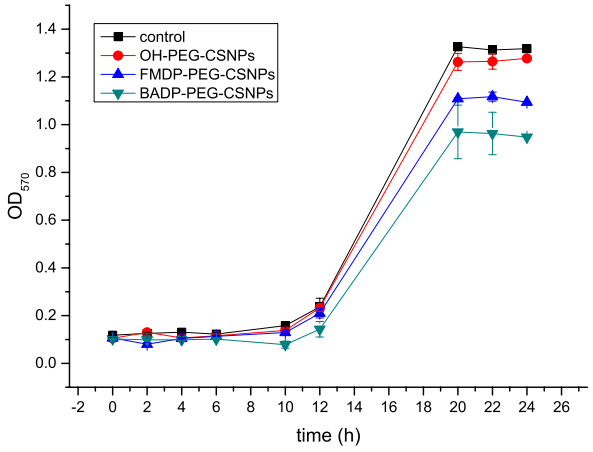

Figure 63. Viability of *Candida albicans* in the presence of 0.4-25 µg/ml OH-PEG-CSNPs and 0.4 -50 µg/ml FMDP-PEG-CSNPs and 50 µg/ml BADP-PEG-CSNPs.

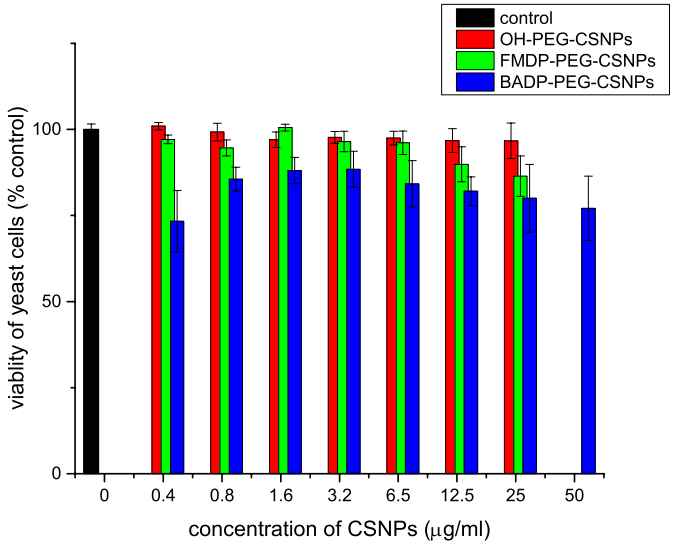

Figure 64. Growth inhibitory activity of 25 µg/ml FMDP-PEG-CSNPs and 50 µg/ml BADP-PEG-CSNPs against *Candida albicans* in comparison to 25 ul OH-PEG-CSNPs.

6.3 Determination of CSNP internalization by TEM imaging

6.3.1 TEM imaging of HeLa cells

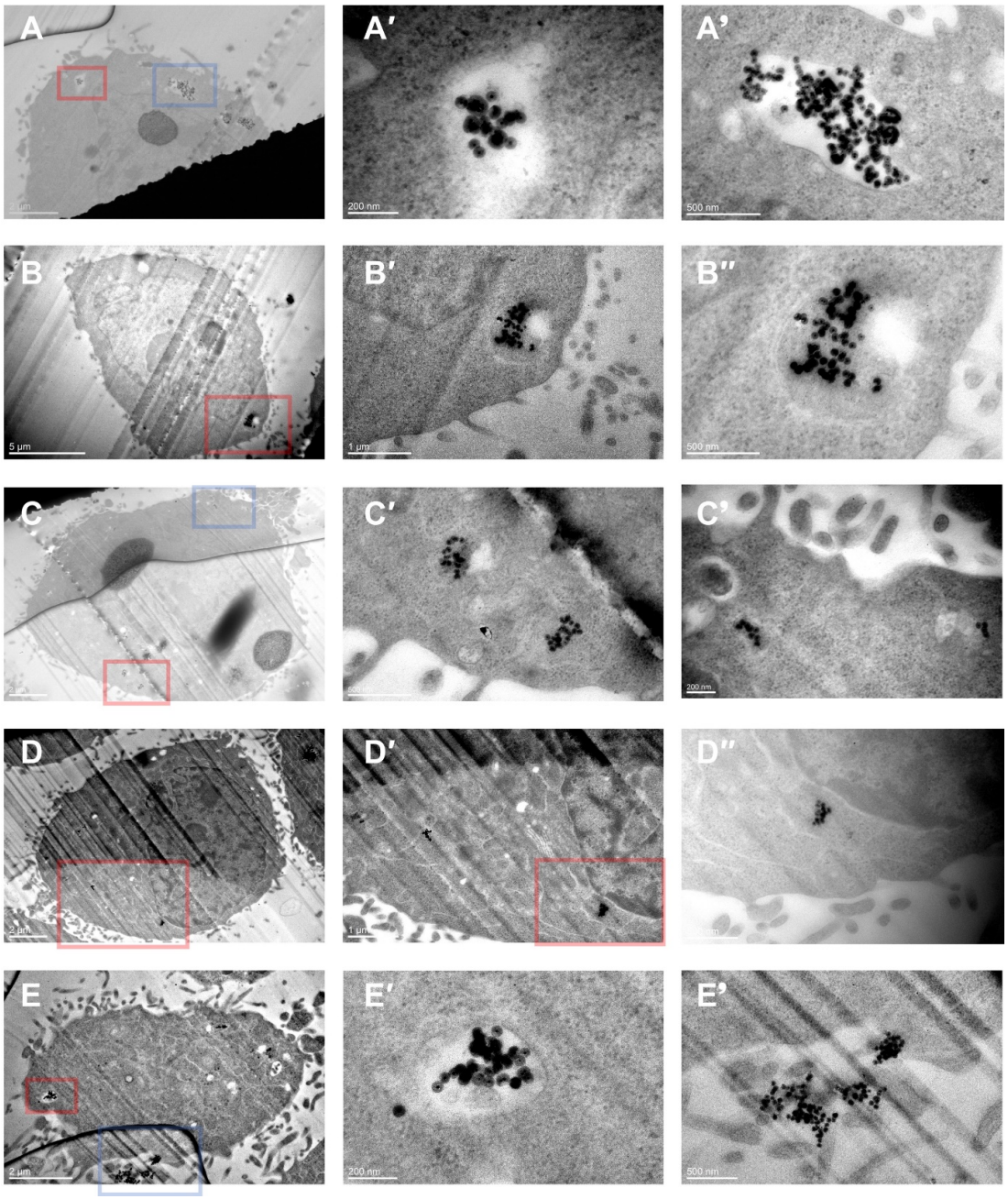

Figure 65. TEM images of HeLa cells after 3-24h incubation with 25 µg/ml OH-PEG-CSNPs. X' and X'' represents the different levels of magnification of one selected area in image X. X' represents the magnified view of the second selected area in image X.

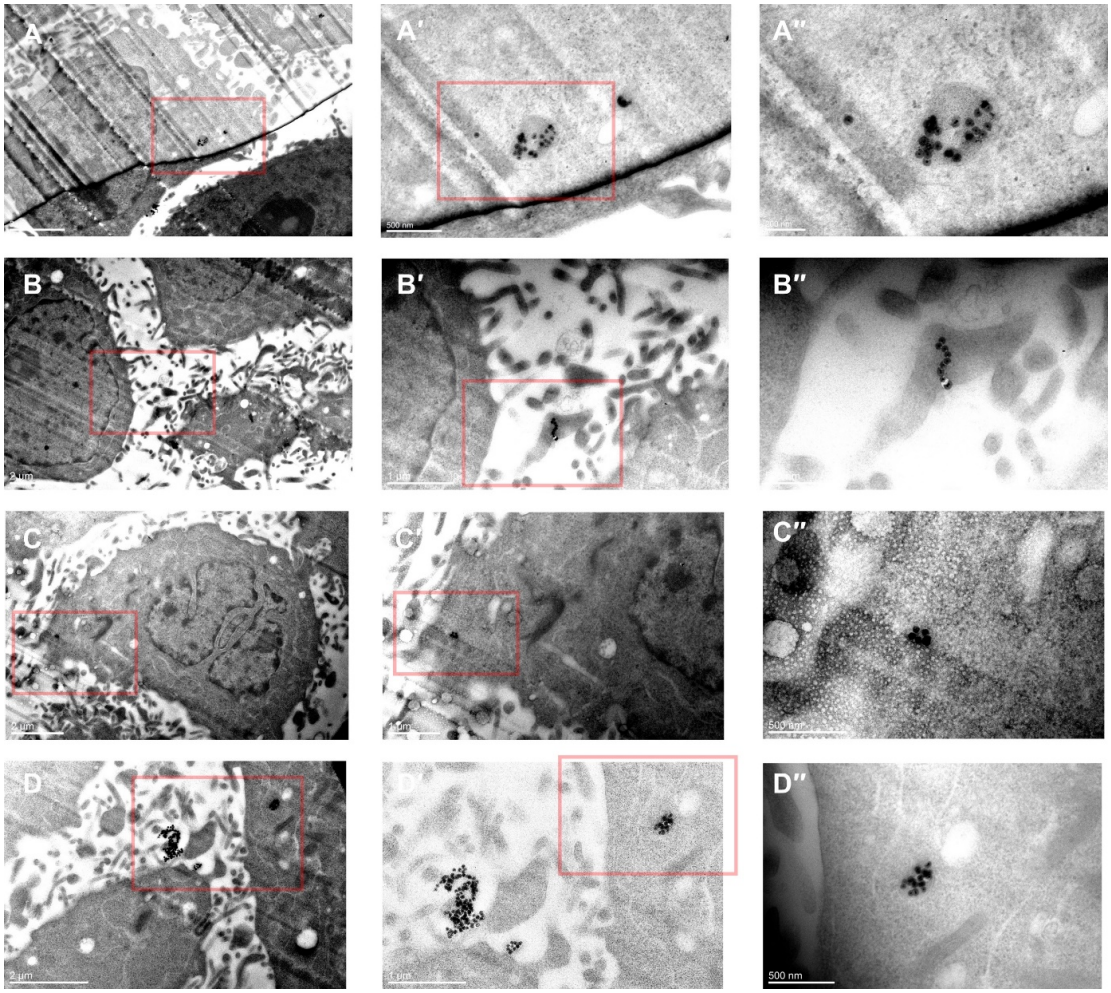

Figure 66. TEM images of HeLa cells after 3-24h incubation with 25 µg/ml OH-PEG-CSNPs. X' and X'' represents the different levels of magnification of one selected area in image X.

Internalization efficiency of OH-PEG-CSNPs into human cervical cancer (HeLa) and hypopharyngeal carcinoma (FaDu) cell lines have been investigated by TEM imaging. 3 h and 24 h incubated HeLa cells did not show significant differences in terms of number of internalized nanoparticles. Figure 65 and Figure 66 shows that large amounts of nanoparticles were encapsulated into intracellular departments. In contrast, 3h and 24h incubated FaDu cells exhibited significant difference in nanoparticle internalization efficiency. 3h incubated FaDu cells (Figure 68A-C) were only able to internalize individual nanoparticles or they were in the beginning of internalization process, which gave the impression of an internalization process by phagocytosis. On the other hand, 24h incubated cells were occupied with large amounts of OH-PEG-CSNPs (Figure 68B-I and

Figure 69). Among the 24h incubated cells it was also possible to observe the intracellular compartments encapsulating the nanoparticles (Figure 68D and Figure 69A' and B'). Nevertheless, FaDu cells imaged in the absence of CSNPs as control did not show any morphological differences in comparison to cells incubated with particles. Figure 67 shows the images of FaDu taken in the absence of nanoparticles, where the high-contrast cellular compartments were highlighted to distinguish them from nanoparticles.

6.3.2 TEM imaging of FaDu cells

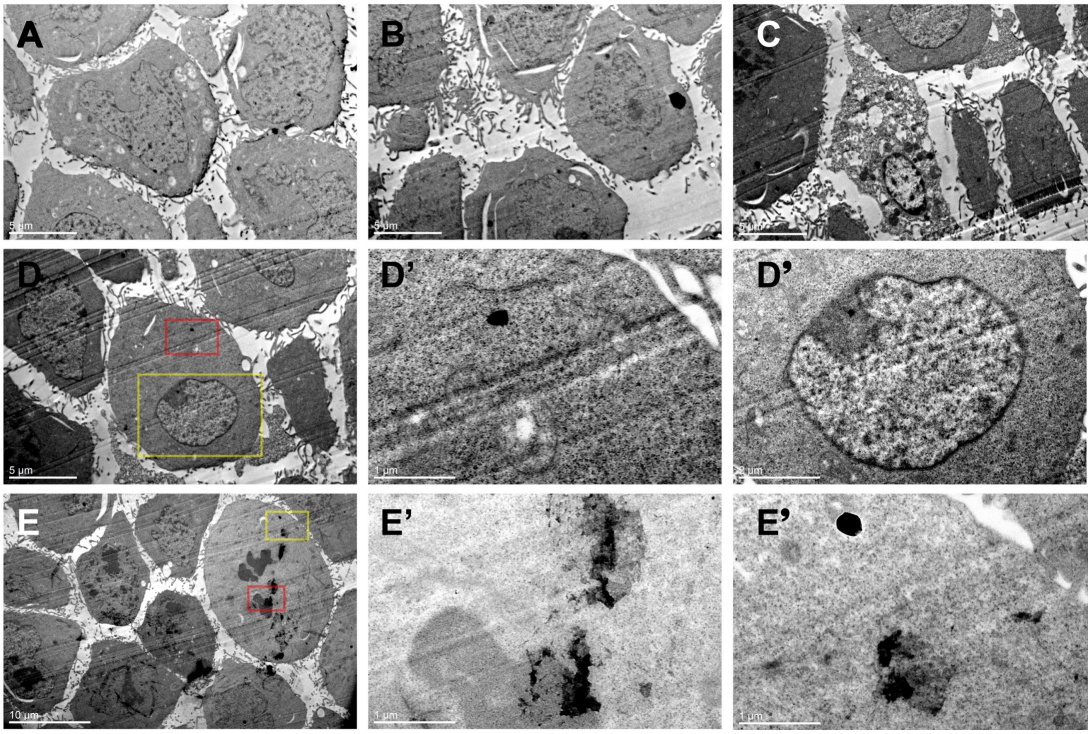

Figure 67. TEM images of FaDu cells in the absence of nanoparticles, presented as control sample. X' and X'' represents the different levels of magnification of one selected area in image X. Magnified view if the second selected area in image X is represented by X'.

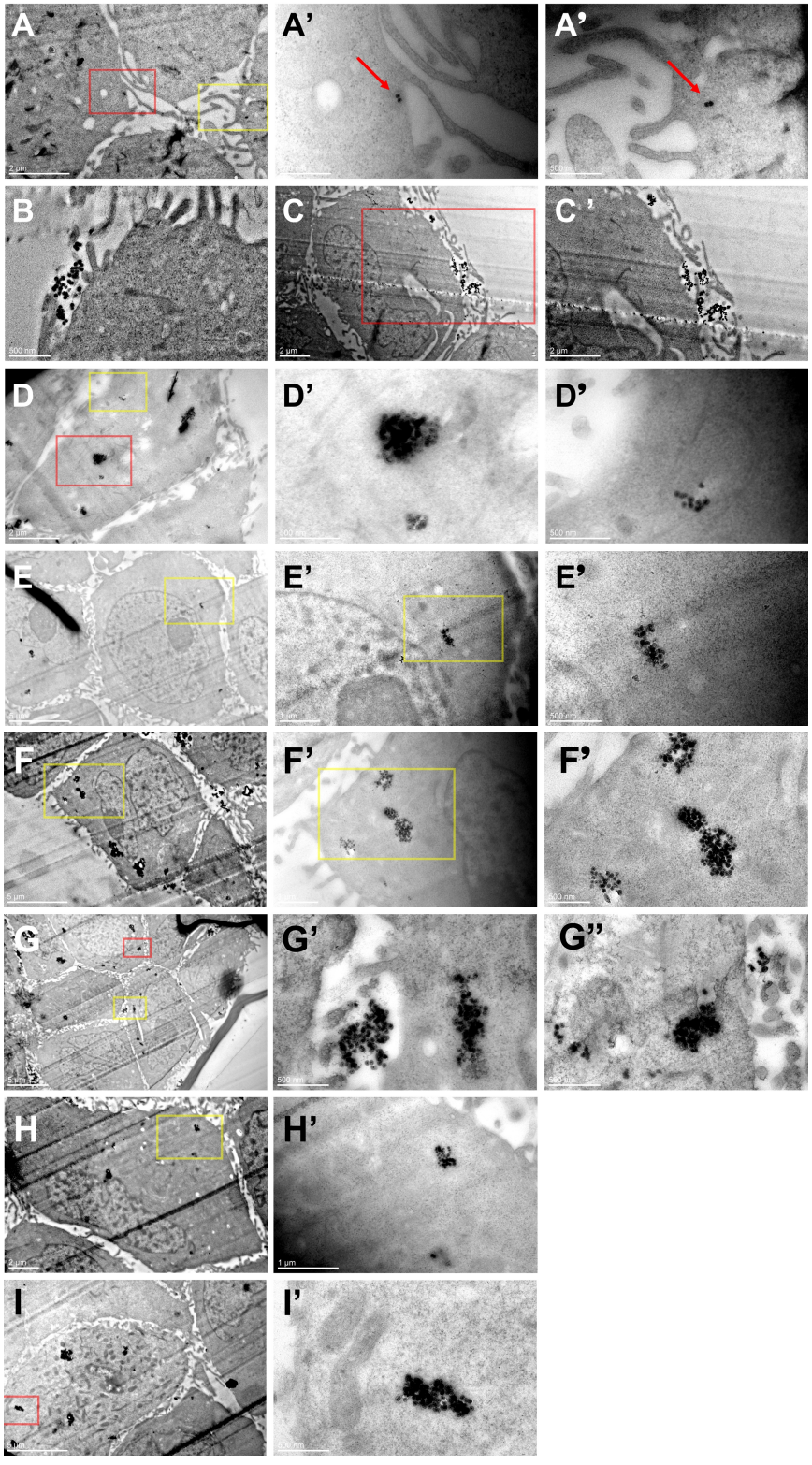

Figure 68. TEM images of FaDu cells after 3h (A-C) and 24h incubation with 25 µg/ml OH-PEG-CSNPs (B-I). X' and X'' represents the different levels of magnification of one selected area in image X. Magnified view if the second selected area in image X is represented by X'.

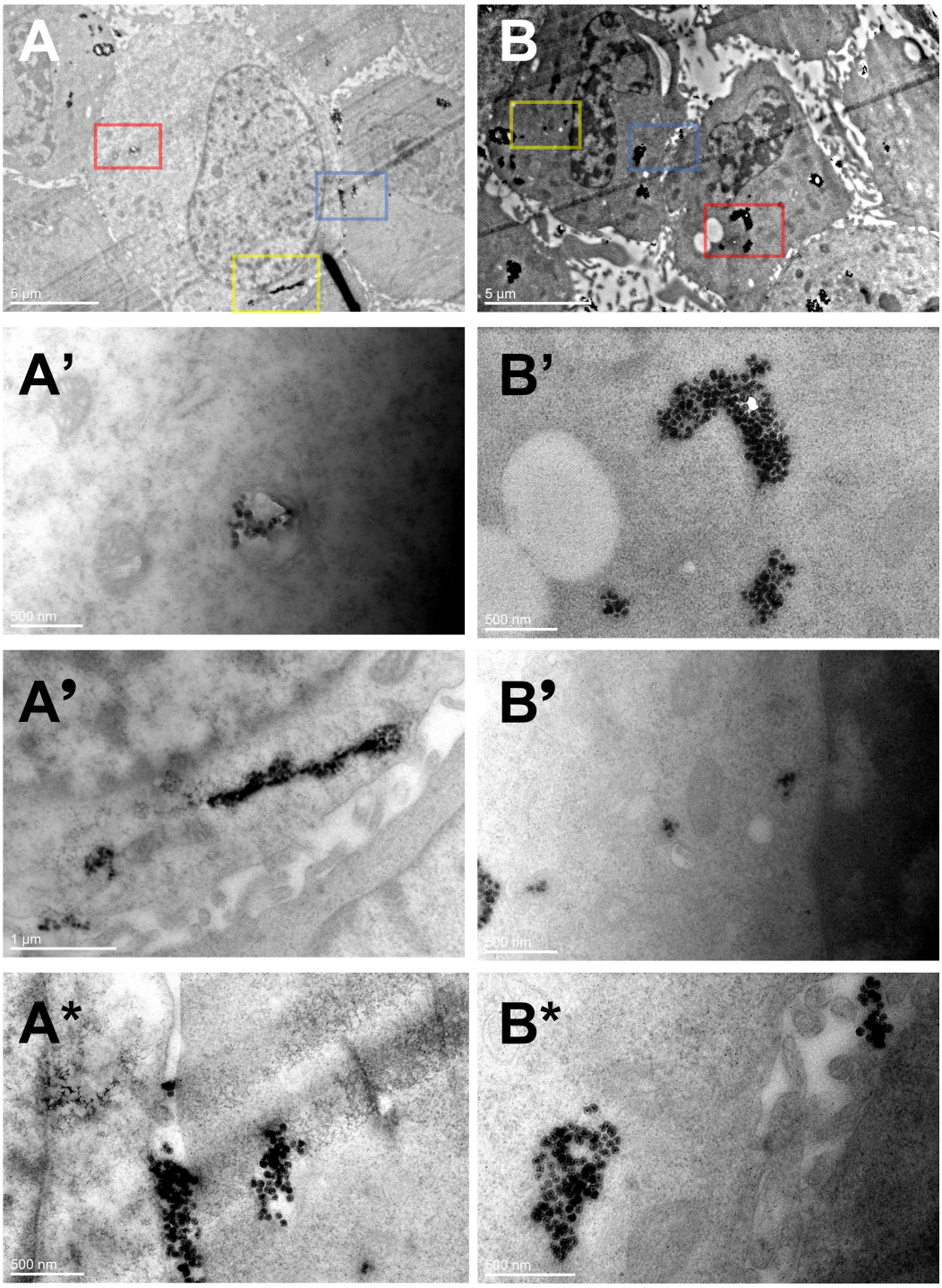

Figure 69. TEM images of FaDu cells after 24h incubation with 25 µg/ml OH-PEG-CSNPs. X' and X'' represents the different levels of magnification of one selected area in image X. Magnified view if the second selected area in image X is represented by X'.

6.3.3 TEM imaging of Candida albicans

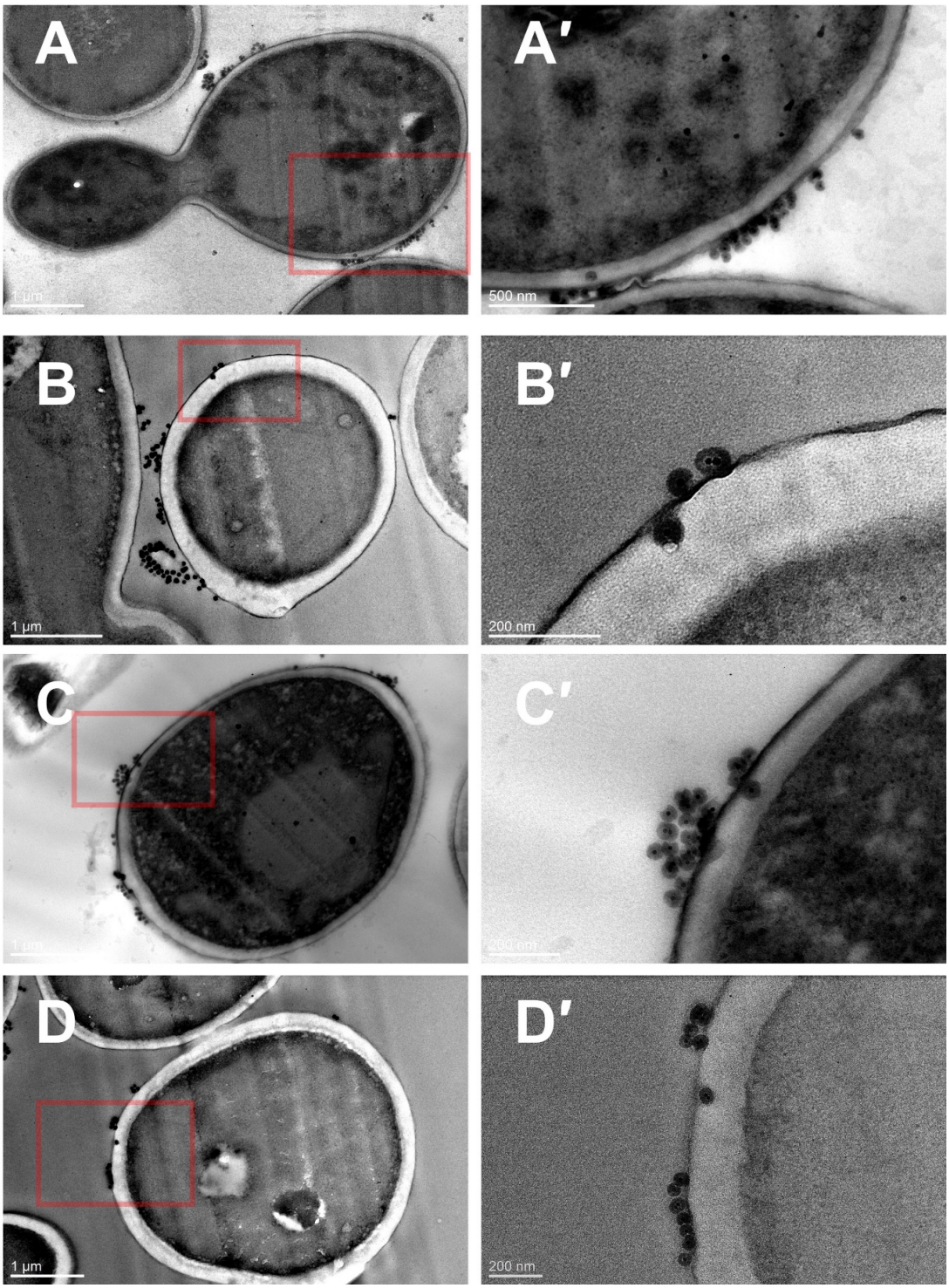

Figure 70. TEM images of *Candida albicans* after 24h incubation with 25 µg/ml OH-PEG-CSNPs showing the particles passing through to cell-wall to cell membrane

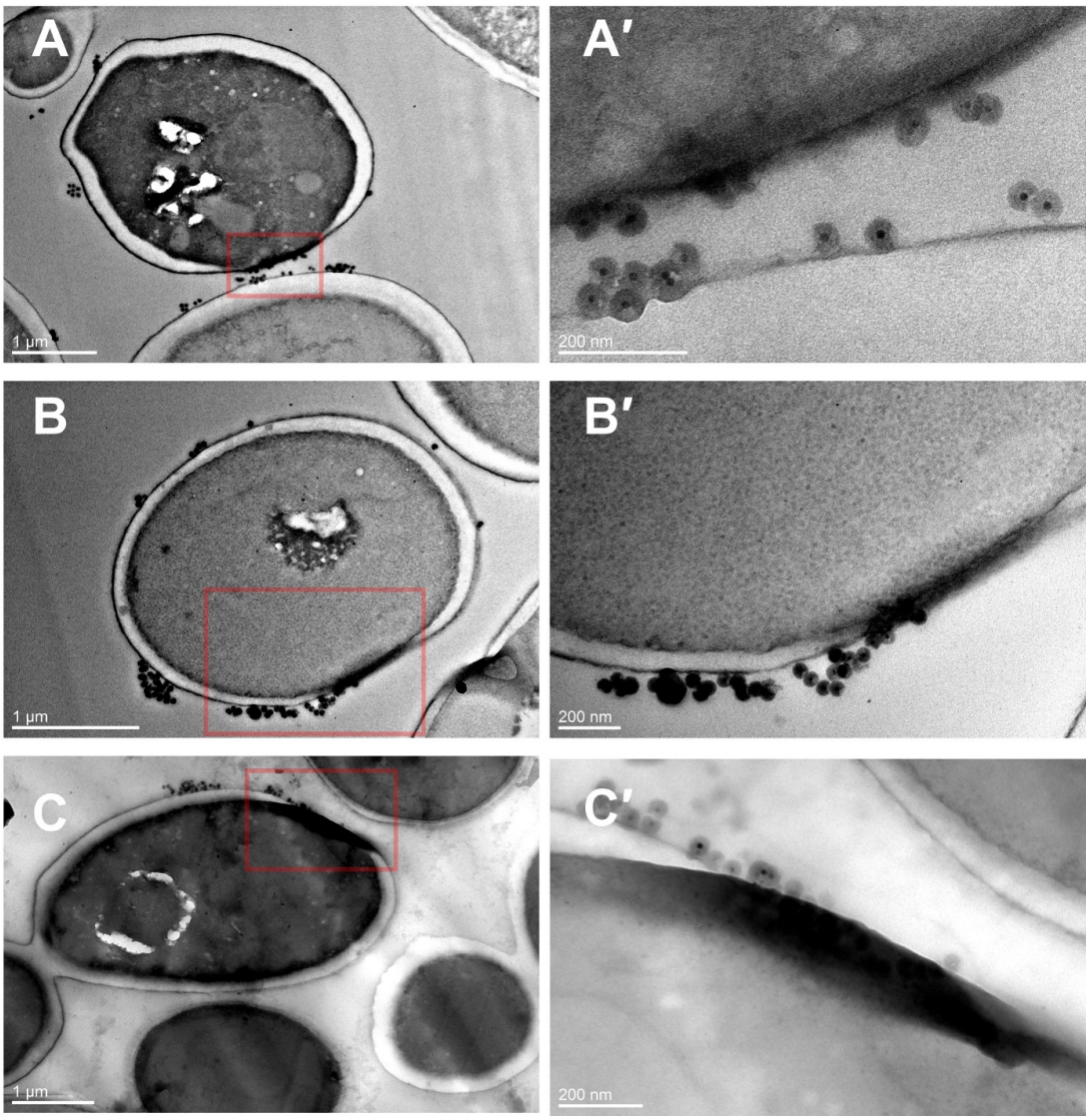

Figure 71. TEM images of *Candida albicans* after 24h incubation with 25 µg/ml OH-PEG-CSNPs showing internalization of particles by shifted cytoplasm.

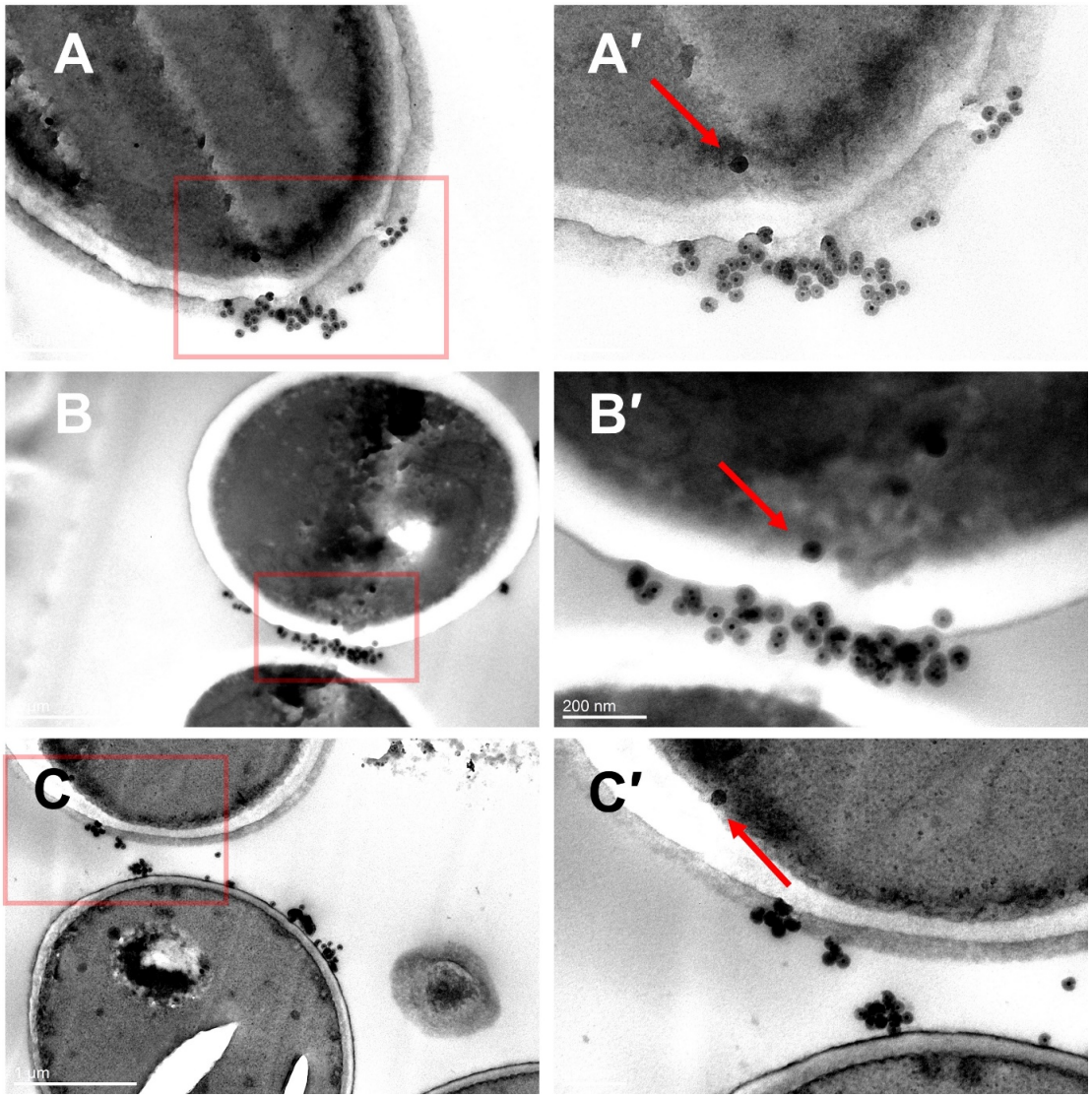

Figure 72. TEM images of *Candida albicans* after 24h incubation with 25 µg/ml OH-PEG-CSNPs showing the particles passed through cell membrane and reached to cytoplasm.

Nanoparticle internalization efficiency of *Candida albicans* in 24h, in comparison to HeLa and FaDu cell lines, was too low. Although most of the nanoparticles were cluttered around *Candida albicans* cell walls, images in Figure 70 demonstrated that the particles were capable of passing through the cell wall and got stuck in cell membranes. On the other hand, images in Figure 71 showed that the cytoplasm of some cells were shifted towards to directions where there were large amounts of nanoparticles. These images demonstrated *Candida albicans* upon particle internalization action. Nevertheless, images in Figure 72 showed the nanoparticles that were able to pass through the cell wall and cell membrane, and finally reached cell cytoplasm.

From TEM images, it was obvious that 3-24h was enough for human cells to internalize significant amounts of nanoparticles whereas *Candida albicans* were just in the beginning of internalization process. When the large amounts of particles internalized by the HeLa cells in comparison to small amounts internalized by *Candida albicans,* it was clear that the higher amounts of FMDP and BADP delivered to human cells is the reason why the human cells were easily inhibited while *Candida albicans* were still alive.

CONCLUSIONS

Due the fact that IONPs@SiO_2 structures (CSNPs) bearing amino functionalities, in monodispersed form, have never been reported in literature for drug delivery purposes; development of CSNPs in highest biocompatibility was primarily aimed in this thesis. Nanoparticle preparation in thesis was based on the three previously reported CSNP preparation procedures by microemulsion method. The process of development was started by studying the organic capping agent stability / ligand exchange potentials within the reaction environment that CSNP are prepared. It was demonstrated that *in situ* formed acetate ions in the presence of IONPCs were efficient agents for ligand exchange with oleate-capping agents of the OA−IONPs. The acetate/oleate ligand exchange has been shown to be an efficient way of obtaining hydrophilic Ac−IONPs from hydrophobic OA−IONPs. Considering that the existence of hydrophobic oleate coating on the surface of as-synthesized OA-IONPs is the biggest obstacle to their use in biological applications, acetate/oleate ligand exchange can be regarded as a very efficient and non-destructive method to obtain hydrophilic IONP particles in highest quality.

Very importantly, pH values stabilized by ethyl acetate/acetate buffer in high [CTAB]/[IONP] ratios have been shown to induce the formation of nanovesicles (nanoemulsions) of silica precursors, which were stable up to 2-3h under refluxing conditions. This stability of the nanoemulsions facilitated the observation of the affinity of IONPCs to the hydrophobic phase in aqueous environment, which gave strong indications of IONPCs being oil-in-water Pickering-type emulsions; more specifically,

"colloidosomes." The capability of IONPCs to encapsulate a hydrophobic medium in an aqueous environment and release it in the form of high-quality, monodispersed, hydrophilic core−shell nanostructures allowed to develop nanoemulsion process and create a "true-emulsion system" in comparison to generally known microemulsion process. The nanoemulsion process can be expected to offer new venues for targeted drug-delivery of hydrophobic active agents.

On the other hand, discovery of acetate ions within the CSNPs elucidated that the formation of silica proceeds differently than the previously suggested inorganic surface-capping mechanisms in so-called (oil-in-water) microemulsion systems (Kim et al., 2008a; Ye et al., 2012) or complete ligand exchange in water-in-oil (reverse-microemulsion) systems (Darbandi et al., 2005; Koole et al., 2008; Vogt et al., 2010; Ding et al., 2012). More specifically, CSNPs having apple bite-like cavities have been identified as iron oxide− acetate−silica core−shell−shell (IONPs@acetate@SiO_2) structures, which seem to be involving both covalent and physical interactions between iron oxide, acetate, and silicon oxide species. On the other hand, some features of the silica growth process have helped to conclude that the formation of CSNPs in the monodisperse form was primarily dictated by the presence of acetate ions and ethyl acetate/acetate-buffered pH stabilization, rather than the [CTAB]/ [IONP] ratio alone, as previously suggested (Qiu et al., 2010; Ye et al., 2012). Consequently, a novel silica-condensation mechanism based on the existence of a dynamic CTA^+−oleate bilayer was proposed, which constitutes the most experimentally supported hypothesis on the formation of CSNPs in an oil-in-water system in literature. In general, silica condensation was mediated by acetate ions, and the IONPCs were expected to serve as the most efficient and high-yielding method known to the date, for the preparation of high-quality IONPs@acetate@SiO_2 nano-structures by herein described nanoemulsion method.

In order to facilitate the quantification and detection of FMDP/BADP-PEG-CSNP conjugation efficiencies by absorption spectroscopy, FMDP and BADP inhibitors were synthesized with rather new, fluorescent Fmoc protecting groups. It was shown that the oxyma catalyzed dual esterification/amidation procedure in water containing environment was a highly efficient procedure that can be applied for solid-state chemistry (Wang et al., 2012). High-resolution XPS analysis quantification and

qualitative Fmoc-piperidine absorption analysis of FMDP/BADP-PEG-CSNP conjugates confirmed the attachment of FMDP and BADP to the CSNPs.

The DC and AC magnetic measurements confirmed the existence of the superparamagnetic state of CSNPs, followed by the temperature dependence of the real part of the magnetic susceptibility χ', recorded for multiple frequencies. Typical superparamagnetic features in the FC/ZFC measurements were also found. Furthermore, magnetic data confirmed the effect of silica coating and surface spin disorder is evidenced. From the AC magnetic measurements, we can conclude that parameter Φ has slightly less value than for the non-interacting superparamagnetic nanoparticles, which may indicate slight dipole interactions. Overall, the paramagnetic response, coupled with the ~60 nm size, makes the particles presented in this study excellent candidates for complex biomedical applications in which high concentration, low agglomeration and fast membrane penetration is needed.

Despite the successful CSNP development process and chemical inhibitor conjugation studies, FMDP/BADP-PEG-CSNP conjugates found to be having an entirely different fate under *in vitro* conditions when compared to activities of previously reported FMDP-peptide and FMDP-prodrug structures. Although the primary aim of the thesis was constructing a nanoparticle delivery platform for improved transport of GlcN-6-P synthase inhibitors to their subcellular target in *Candida albicans,* FMDP/BADP-PEG-CSNP conjugates did not provide any improvement to the previously reported antifungal activity of free FMDP and BADP. As a result of the fact that the inhibitory activity of FMDP and BADP were expressed as MIC values in previous reports, it is difficult to compare the results presented in the thesis, since the maximum concentrations of FMDP/BADP-PEG-CSNP conjugates used against *Candida albicans* were determined by the minimum concentration killed more than 50% of human cells. Such an approach about concentrations was followed because the nanomedical treatments are primarily intended for human cells and thus, it was initially more important to assess the impact of FMDP/BADP-PEG-CSNP on human cells. This is reasoned by the much higher potential of mammalian cells that are capable of internalizing higher amounts of particles.

TEM imaging studies carried out to observe the CSNP internalization efficiency evidenced that the cell wall of the *Candida albicans* was very efficient in their mechanism of acting as an impermeable barrier. However, in the light of current

literature, it is noteworthy to highlight that CSNPs in such high quality in terms of biocompatibility as herein reported, have never been used against *Candida albicans* (wild-type, intrinsically multi-drug resistance); and it was shown for the first time that nanoparticles having 50 nm average size can pass through the cell wall and cell membrane and actually reach the cytoplasm of fungal *Candida albicans* cells. However, the low efficiency of the nanoparticle internalization raised questions, such as, whether the "biocompatibility" in the concept of "nanoparticle based antifungal therapy" is a valid concept or not. Rejection of CSNPs by fungal *Candida albican* cells despite the highly improved biocompatibility of CSNPs as presented in this thesis suggests that the development of more lipophilic (less biocompatible) nanoparticle formulation strategy that was previously followed for FMDP prodrugs and peptides could be the solution for better nanoparticle internalization by fungal cells.

Although the above conclusion about biocompatibility sounds to be the ideal approach when biocompatibility of "only" fungal cells is considered; however, it must be also remembered that the biocompatibility of host environment, which is usually surrounded by healthy human cells cannot be disregarded. Correspondingly, we have demonstrated that OH-PEG-CSNPs were shown to be perfectly biocompatible with healthy and cancer human cells. However, the viability tests carried out with FMDP-PEG-CSNPs have demonstrated that the FaDu cancer cells and MSU1.1 healthy fibroblasts were easily killed while the HeLa cells were found to be quite resistant in equivalent concentrations. On the other hand, FaDu cells were much more resistant to BADP-CSNPs than the HeLa and MSU1.1. The current results obtained for CSNP conjugates, by being in conflict with the previously reported non-toxic *in vitro* activity of FMDP derivatives against human cell lines, complicates the GlcN-6-P synthase targeted antifungal fungal therapy even further. It is very important to highlight that even the use of a glutamine (L-alanyl-L-glutamine dipeptide) analog during the *in vitro* viability studies was not able to reverse the function of GlcN-6-P synthase enzyme, as it was the case in many other FMDP-based GlcN-6-P synthase inhibition studies. This might also mean that inhibition of glucosamine biosynthesis was not the only pathway that was inhibited by FMDP and BADP action.

It is a fact that GlcN-6-P synthase enzyme is present in almost every kind of cell however, FMDP based antifungal therapy that was previously shown to be safe for

human cell lines, now seems to be posing a new threat to other cell lines by unspecific mechanism of action. Herein presented results suggests that the fate of GlcN-6-P synthase inhibitors were changed by nanoparticle mediated delivery.

Bibliography

Alcock, N. W.; Tracy, V. M.; Waddington, T. C. Acetates and Acetato-Complexes. Part 2. Spectroscopic Studies. *J. Chem. Soc. Dalt. Trans.* **1976**, No. 21, 2243.

Amara, D.; Grinblat, J.; Margel, S. Solventless Thermal Decomposition of Ferrocene as a New Approach for One-Step Synthesis of Magnetite Nanocubes and Nanospheres. *J. Mater. Chem.* **2012**, *22* (5), 2188–2195.

Ames, B. N.; Ames, G. F.-L.; Young, J. D.; Tsuchiya, D.; Lecocq, J. Illicit Transport: The Oligopeptide Permease. *Proc. Natl. Acad. Sci.* **1973**, *70* (2), 456–458.

Anderson, G. W.; Zimmerman, J. E.; Callahan, F. M. The Use of Esters of N-Hydroxysuccinimide in Peptide Synthesis. *J. Am. Chem. Soc.* **1964**, *86* (9), 1839–1842.

Andruszkiewicz, R.; Chmara, H.; Milewski, S.; Borowski, E. Synthesis of N3-Fumaramoyl-L-2,3-Diaminopropanoic Acid Analogues, the Irreversible Inhibitors of Glucosamine Synthetase. *Int. J. Pept. Protein Res.* **1986**, *27* (5), 449–453.

Andruszkiewicz, R.; Chmara, H.; Milewski, S.; Borowski, E. Synthesis and Biological Properties of N3-(4-Methoxyfumaroyl)-L-2,3-Diaminopropanoic Acid Dipeptides. A Novel Group of Antimicrobial Agents. *J. Med. Chem.* **1987**, *30* (10), 1715–1719.

Andruszkiewicz, R.; Milewski, S.; Zieniawa, T.; Borowski, E. Anticandidal Properties of N3-(4-Methoxyfumaroyl)-L-2,3-Diaminopropanoic Acid Oligopeptides. *J. Med. Chem.* **1990a**, *33* (1), 132–135.

Andruszkiewicz, R.; Chmara, H.; Milewski, S.; Zieniawa, T.; Borowski, E. Antimicrobial Properties of N3-(Iodoacetyl)-L-2,3-Diaminopropanoic Acid-Peptide Conjugates. *J. Med. Chem.* **1990b**, *33* (10), 2755–2759.

Andruszkiewicz, R.; Jędrzejczak, R.; Zieniawa, T.; Wojciechowski, M.; Borowski, E. N 3 - Oxoacyl Derivatives of L-2,3-Diaminopropanoic Acid and Their Peptides; Novel Inhibitors of Glucosamine-6-Phosphate Synthase. *J. Enzyme Inhib.* **2000**, *15* (5), 429–441.

Andruszkiewicz, R.; Zieniawa, T.; Walkowiak, A. Anticandidal Properties of N-Acylpeptides Containing an Inhibitor of Glucosamine-6-Phosphate Synthase. *J. Enzyme Inhib. Med. Chem.* **2005**, *20* (2), 115–121.

Andrzejewski, B.; Bednarski, W.; Kaźmierczak, M.; Łapiński, A.; Pogorzelec-Glaser, K.; Hilczer, B.; Jurga, S.; Nowaczyk, G.; Załęski, K.; Matczak, M.; et al. Magnetization Enhancement in Magnetite Nanoparticles Capped with Alginic Acid. *Compos. Part B Eng.* **2014**, *64*, 147–154.

Aoki, Y.; Kamiyama, T.; Fujii, T.; Yamamoto, M.; Ohwada, J.; Arisawa, M. Design of an Antifungal Methionine Inhibitor Not Antagonized by Methionine. *Biol. Pharm. Bull.* **1995**, *18* (9), 1267–1271.

Aquino, R.; Depeyrot, J.; Sousa, M. H.; Tourinho, F. A.; Dubois, E.; Perzynski, R. Magnetization Temperature Dependence and Freezing of Surface Spins in Magnetic Fluids Based on Ferrite Nanoparticles. *Phys. Rev. B - Condens. Matter Mater. Phys.* **2005**, *72* (18).

Arendrup, M. C.; Patterson, T. F. Multidrug-Resistant Candida: Epidemiology, Molecular Mechanisms, and Treatment. *J. Infect. Dis.* **2017**, *216* (3), S445–S451.

Arosio, P.; Thévenot, J.; Orlando, T.; Orsini, F.; Corti, M.; Mariani, M.; Bordonali, L.;

Innocenti, C.; Sangregorio, C.; Oliveira, H.; et al. Hybrid Iron Oxide-Copolymer Micelles and Vesicles as Contrast Agents for MRI: Impact of the Nanostructure on the Relaxometric Properties. *J. Mater. Chem. B* **2013**, *1* (39), 5317.

Bałanda, M. AC Susceptibility Studies of Phase Transitions and Magnetic Relaxation: Conventional, Molecular and Low-Dimensional Magnets. *Acta Phys. Pol. A* **2013**, *124* (6), 964–976.

Beaune, G.; Levy, M.; Neveu, S.; Gazeau, F.; Wilhelm, C.; Ménager, C. Different Localizations of Hydrophobic Magnetic Nanoparticles within Vesicles Trigger Their Efficiency as Magnetic Nano-Heaters. *Soft Matter* **2011**, *7* (13), 6248.

Beck, J. S.; Vartuli, J. C.; Roth, W. J.; Leonowicz, M. E.; Kresge, C. T.; Schmitt, K. D.; Chu, C. T.-W.; Olson, D. H.; Sheppard, E. W.; McCullen, S. B.; et al. A New Family of Mesoporous Molecular Sieves Prepared with Liquid Crystal Templates. *J. Am. Chem. Soc.* **1992**, No. 114, 10834–10843.

Berkow, E.; Lockhart, S. Fluconazole Resistance in Candida Species: A Current Perspective. *Infect. Drug Resist.* **2017**, *Volume 10*, 237–245.

Binder, K.; Young, A. P. Spin Glasses: Experimental Facts, Theoretical Concepts, and Open Questions. *Rev. Mod. Phys.* **1986**, *58* (4), 801–976.

Bobo, D.; Robinson, K. J.; Islam, J.; Thurecht, K. J.; Corrie, S. R. Nanoparticle-Based Medicines: A Review of FDA-Approved Materials and Clinical Trials to Date. *Pharm. Res.* **2016**, *33* (10), 2373–2387.

Bollhorst, T.; Shahabi, S.; Wörz, K.; Petters, C.; Dringen, R.; Maas, M.; Rezwan, K. Bifunctional Submicron Colloidosomes Coassembled from Fluorescent and Superparamagnetic Nanoparticles. *Angew. Chemie Int. Ed.* **2015**, *54* (1), 118–123.

Bollhorst, T.; Rezwan, K.; Maas, M. Colloidal Capsules: Nano- and Microcapsules with Colloidal Particle Shells. *Chem. Soc. Rev.* **2017**, *46* (8), 2091–2126.

Bontemps-Gracz, M.; Milewski, S.; Borowski, E. The Influence of L-Norvalyl-N3-4-Methoxyfumaroyl-L-2,3-Diaminopropanoic Acid, an Antifungal Agent, on Mammalian Cells in Tissue Culture. *Acta Biochim. Pol.* **1991**, *38* (2), 229–239.

Borowski, E. Novel Approaches in the Rational Design of Antifungal Agents of Low Toxicity. *Farm.* **2000**, *55* (3), 206–208.

Breen, M. L.; Dinsmore, A. D.; Pink, R. H.; Qadri, S. B.; Ratna, B. R. Sonochemically Produced ZnS-Coated Polystyrene Core-Shell Particles for Use in Photonic Crystals. *Langmuir* **2001**, *17* (3), 903–907.

Brinker, C. J. Hydrolysis and Condensation I: Nonsilicates. *Sol-Gel Sci. Phys. Chem. Sol-Gel Process.* **1990**, No. 2, 21–96.

Brust, M.; Walker, M.; Bethell, D.; Schiffrin, D. J.; Whyman, R. Synthesis of Thiol-Derivatised Gold Nanoparticles in a Two-Phase Liquid–Liquid System. *J. Chem. Soc., Chem. Commun.* **1994**, No. 7, 801–802.

Butts, A.; Palmer, G. E.; Rogers, P. D. Antifungal Adjuvants: Preserving and Extending the Antifungal Arsenal. *Virulence* **2017**, *8* (2), 198–210.

Campoy, S.; Adrio, J. L. Antifungals. *Biochem. Pharmacol.* **2017**, *133*, 86–96.

Caroen, J.; Clemmen, A.; Kámán, J.; Backaert, F.; Goeman, J. L.; Fülöp, F.; Van Der Eycken, J. Solid-Phase Synthesis of 6,7-Cycloalkane-Fused 1,4-Diazepane-2,5-Diones via a Cyclization/Release Strategy. *Tetrahedron* **2016**, *72* (1), 148–160.

Caruso, F.; Susha, A. S.; Giersig, M.; Möhwald, H. Magnetic Core–Shell Particles:

Preparation of Magnetite Multilayers on Polymer Latex Microspheres. *Adv. Mater.* **1999**, *11* (11), 950–953.

Cesar, I.; Kay, A.; Gonzalez Martinez, J. A.; Grätzel, M. Translucent Thin Film Fe2O3 Photoanodes for Efficient Water Splitting by Sunlight: Nanostructure-Directing Effect of Si-Doping. *J. Am. Chem. Soc.* **2006**, *128* (14), 4582–4583.

Chamritski, I.; Burns, G. Infrared- and Raman-Active Phonons of Magnetite, Maghemite, and Hematite: A Computer Simulation and Spectroscopic Study. *J. Phys. Chem. B* **2005**, *109* (11), 4965–4968.

Chapados, C.; Max, J. J. Infrared Spectroscopy of Aquous Carboxilic Acids- Comparison between Differnt Acids and Their Salts. *J. Phys. Chem. A* **2004**, *108*, 3324–3337.

Cheung, K.-S.; Wasserman, S. A.; Dudek, E.; Lerner, S. A.; Johnston, M. Chloroalanyl and Propargylglycyl Dipeptides. Suicide Substrate Containing Antibacterials. *J. Med. Chem.* **1983**, *26* (12), 1733–1741.

Chmara, H.; Andruszkiewicz, R.; Borowski, E. Inactivation of Glucosamine-6-Phosphate Synthetase from Salmonella Typhimurium LT 2 SL 1027 by N β - Fumarylcarboxyamido-L-2,3-Diaminopropionic Acid. *Biochem. Biophys. Res. Commun.* **1984**, *120* (3), 865–872.

Chmara, H.; Andruszkiewicz, R.; Borowski, E. Inactivation of Glucosamine-6-Phosphate Synthetase from Salmonella Typhimurium LT2 by Fumaroyl Diaminopropanoic Acid Derivatives, a Novel Group of Glutamine Analogs. *Biochim. Biophys. Acta* **1986**, *870* (2), 357–366.

Coey, J. M. D. Noncollinear Spin Arrangement in Ultrafine Ferrimagnetic Crystallites. *Phys. Rev. Lett.* **1971**, *27* (17), 1140–1142.

Coşkun, M.; Korkmaz, M.; Fırat, T.; Jaffari, G. H.; Shah, S. I. Synthesis of SiO2 Coated NiFe2O4 Nanoparticles and the Effect of SiO2 Shell Thickness on the Magnetic Properties. *J. Appl. Phys.* **2010**, *107* (9), 09B523.

Darbandi, M.; Thomann, R.; Nann, T. Single Quantum Dots in Silica Spheres by Microemulsion Synthesis. *Chem. Mater.* **2005**, *17* (23), 5720–5725.

Deacon, G. Relationships between the Carbon-Oxygen Stretching Frequencies of Carboxylato Complexes and the Type of Carboxylate Coordination. *Coord. Chem. Rev.* **1980**, *33* (3), 227–250.

Ding, H. L.; Zhang, Y. X.; Wang, S.; Xu, J. M.; Xu, S. C.; Li, G. H. Fe3O4@SiO2 Core/Shell Nanoparticles: The Silica Coating Regulations with a Single Core for Different Core Sizes and Shell Thicknesses. *Chem. Mater.* **2012**, *24* (23), 4572–4580.

Dinsmore, A. D.; Hsu, M. F.; Nikolaides, M. G.; Marquez, M.; Bausch, A. R.; Weitz, D. A. Colloidosomes: Selectively Permeable Capsules Composed of Colloidal Particles. *Science (80-.).* **2002**, *298* (5595), 1006–1009.

Donatti, D. A.; Vollet, D. R. Study of the Hydrolysis of TEOS-TMOS Mixtures under Ultrasound Stimulation. *J. Non. Cryst. Solids* **1996**, *204* (3), 301–304.

Dormann, J. L.; Fiorani, D.; Tronc, E. *Magnetic Relaxation in Fine-Particle Systems*; 1997; Vol. 98.

Edwards, H. G. M.; Lewis, I. R. Vibrational Spectroscopic Studies of Iron(II) Acetate. *J. Mol. Struct.* **1993**, *296* (1–2), 15–20.

Edwards, J. E. Candida Species. In *Mandell, Douglas, and Bennett's Principles and Practice of Infectious Diseases*; 2015; pp 2879–2894.

Egerton, R. F. *Electron Energy-Loss Spectroscopy in the Electron Microscope*; Springer

US: Boston, MA, 2011.
European Commission. A European One Health Action Plan against Antimicrobial Resistance (AMR). *Eur. Comm.* **2017**, 24.
Fan, H. Self-Assembly of Ordered, Robust, Three-Dimensional Gold Nanocrystal/Silica Arrays. *Science (80-.).* **2004**, *304* (5670), 567–571.
de Faria, D. L. A.; Venâncio Silva, S.; de Oliveira, M. T. Raman Microspectroscopy of Some Iron Oxides and Oxyhydroxides. *J. Raman Spectrosc.* **1997**, *28* (11), 873–878.
Fickel, T. E.; Gilvarg, C. Transport of Impermeant Substances in E. Coli by Way of Oligopeptide Permease. *Nat. New Biol.* **1973**, *241* (110), 161–163.
Fleutot, S.; Martinez, H.; Dupin, J. C.; Baraille, I.; Forano, C.; Renaudin, G.; Gonbeau, D. Experimental (X-Ray Photoelectron Spectroscopy) and Theoretical Studies of Benzene Based Organics Intercalated into Layered Double Hydroxide. *Solid State Sci.* **2011**, *13* (9), 1676–1686.
Gasparov, L. V.; Tanner, D. B.; Romero, D. B.; Berger, H.; Margaritondo, G.; Forró, L. Infrared and Raman Studies of the Verwey Transition in Magnetite. *Phys. Rev. B - Condens. Matter Mater. Phys.* **2000**, *62* (12), 7939–7944.
Ghosh, S.; Blumenthal, H. J.; Davidson, E.; Univer-, D.; Carolina, N. V. Enzymatic Synthesis. **1960**, *235* (6).
Gittins, D. I.; Caruso, F. Spontaneous Phase Transfer of Nanoparticulate Metals from Organic to Aqueous Media. *Angew. Chemie - Int. Ed.* **2001**, *40* (16), 3001–3004.
Grzybowska, J.; Sowinski, P.; Gumieniak, J.; Zieniawa, T.; Borowski, E. N-Methyl-N-D-Fructopyranosylamphotericin B Methyl Ester, New Amphotericin B Derivative of Low Toxicity. *J. Antibiot. (Tokyo).* **1997**, *50* (8), 709–711.
Guo, H.; Barnard, A. S. Naturally Occurring Iron Oxide Nanoparticles: Morphology, Surface Chemistry and Environmental Stability. *J. Mater. Chem. A* **2013**, *1* (1), 27–42.
Guo, X.; Wu, Z.; Li, W.; Wang, Z.; Li, Q.; Kong, F.; Zhang, H.; Zhu, X.; Du, Y. P.; Jin, Y.; et al. Appropriate Size of Magnetic Nanoparticles for Various Bioapplications in Cancer Diagnostics and Therapy. *ACS Appl. Mater. Interfaces* **2016**, *8* (5), 3092–3106.
Hendriksen, P. V.; Linderoth, S.; Lindgård, P.-A. Finite-Size Effects in the Magnetic Properties of Ferromagnetic Clusters. *J. Magn. Magn. Mater.* **1992**, *104–107* (PART 3), 1577–1579.
Hendriksen, P. V.; Linderoth, S.; Lindgård, P.-A. Finite-Size Modifications of the Magnetic Properties of Clusters. *Phys. Rev. B* **1993**, *48* (10), 7259–7273.
Huo, Q.; Margolese, D. I.; Ciesla, U.; Demuth, D. G.; Feng, P.; Gier, T. E.; Sieger, P.; Firouzi, A.; Chmelka, B. F.; Schuth, F.; et al. Organization of Organic Molecules with Inorganic Molecular Species into Nanocomposite Biphase Arrays. *Chem. Mater.* **1994**, *6* (8), 1176–1191.
Hüser, D.; Van Duynevel, A. J.; Nieuwenhuys, G. J.; Mydosh, J. A. Phenomenological Model for the Frequency Dependence of the Susceptibility of Spin Glasses and Related Compounds. *J. Phys. C Solid State Phys.* **1986**, *19* (19), 3697–3717.
Hyeon, T. Chemical Synthesis of Magnetic Nanoparticles. *Chem. Commun.* **2003**, No. 8, 927–934.
Hyeon, T.; Lee, S. S.; Park, J.; Chung, Y.; Na, H. Bin. Synthesis of Highly Crystalline and

Monodisperse Maghemite Nanocrystallites without a Size-Selection Process. *J. Am. Chem. Soc.* **2001**, *123* (51), 12798–12801.

Jacintho, G. V. M.; Brolo, A. G.; Corio, P.; Suarez, P. A. Z.; Rubim, J. C. Structural Investigation of MFe 2 O 4 (M = Fe, Co) Magnetic Fluids. *J. Phys. Chem. C* **2009**, *113* (18), 7684–7691.

Jakubec, P.; Berkeš, D.; Považanec, F. Crystallization-Induced Asymmetric Transformation. Application to Conjugate Addition of Benzylamine to Amides of Benzoylacrylic Acid. *Tetrahedron Lett.* **2004**, *45* (24), 4755–4758.

Janiak, A.; Cybulska, B.; Szlinder-Richert, J.; Borowski, E.; Milewski, S. Facilitated Diffusion of Glucosamine-6-Phosphate Synthase Inhibitors Enhances Their Antifungal Activity. *Acta Biochim. Pol.* **2002**, *49* (1), 77–86.

Jing, Z.; Wu, S. Synthesis, Characterization and Magnetic Properties of γ-Fe2O3 Nanoparticles via a Non-Aqueous Medium. *J. Solid State Chem.* **2004**, *177* (4–5), 1213–1218.

Johnson, M. K.; Powell, D. B.; Cannon, R. D. Vibrational Spectra of Carboxylato Complexes—III. Trinuclear 'Basic' Acetates and Formates of Chromium(III), Iron(III) and Other Transition Metals. *Spectrochim. Acta Part A Mol. Spectrosc.* **1981**, *37* (11), 995–1006.

Kaaniche, F. M.; Allela, R.; Cherif, S.; Algia, N. ben. Invasive Candidiasis in Critically Ill Patients. *Trends Anaesth. Crit. Care* **2016**, *11*, 1–5.

Kertmen, A.; Torruella, P.; Coy, E.; Yate, L.; Nowaczyk, G.; Gapiński, J.; Vogt, C.; Toprak, M.; Estradé, S.; Peiró, F.; et al. Acetate-Induced Disassembly of Spherical Iron Oxide Nanoparticle Clusters into Monodispersed Core–Shell Structures upon Nanoemulsion Fusion. *Langmuir* **2017**, *33* (39), 10351–10365.

Kim, J.; Kim, H. S.; Lee, N.; Kim, T.; Kim, H.; Yu, T.; Song, I. C.; Moon, W. K.; Hyeon, T. Multifunctional Uniform Nanoparticles Composed of a Magnetite Nanocrystal Core and a Mesoporous Silica Shell for Magnetic Resonance and Fluorescence Imaging and for Drug Delivery. *Angew. Chemie - Int. Ed.* **2008a**, *47* (44), 8438–8441.

Kim, J.; Kim, H. S.; Lee, N.; Kim, T.; Kim, H.; Yu, T.; Song, I. C.; Moon, W. K.; Hyeon, T. Multifunctional Uniform Nanoparticles Composed of a Magnetite Nanocrystal Core and a Mesoporous Silica Shell for Magnetic Resonance and Fluorescence Imaging and for Drug Delivery. *Angew. Chemie Int. Ed.* **2008b**, *47* (44), 8438–8441.

King, A. Antibiotic Resistance Will Kill 300 Million People by 2050. *Sci. Am.* **2014**, 1–10.

Kingsbury, W. D.; Boehm, J. C.; Mehta, R. J.; Grappel, S. F. Transport of Antimicrobial Agents Using Peptide Carrier Systems: Anticandidal Activity of m -Fluorophenylalanine-Peptide Conjugates. *J. Med. Chem.* **1983**, *26* (12), 1725–1729.

Kingsbury, W. D.; Boehm, J. C.; Mehta, R. J.; Grappel, S. F.; Gilvarg, C. A Novel Peptide Delivery System Involving Peptidase Activated Prodrugs as Antimicrobial Agents. Synthesis and Biological Activity of Peptidyl Derivatives of 5-Fluorouracil. *J. Med. Chem.* **1984**, *27* (11), 1447–1451.

Koole, R.; Van Schooneveld, M. M.; Hilhorst, J.; De Donegal, C. M.; 'T Hart, D. C.; Van Blaaderen, A.; Vanmaekelbergh, D.; Meijerink, A. On the Incorporation Mechanism of Hydrophobic Quantum Dots in Silica Spheres by a Reverse Microemulsion Method. *Chem. Mater.* **2008**, *20* (7), 2503–2512.

Koszel, D.; Lącka, I.; Kozłowska-Tylingo, K.; Andruszkiewicz, R. The Synthesis and Biological Activity of Lipophilic Derivatives of Bicine Conjugated with N^3-(4-Methoxyfumaroyl)-L-2,3-Diaminopropanoic Acid (FMDP)-an Inhibitor of Glucosamine-6-Phosphate Synthase. *J. Enzyme Inhib. Med. Chem.* **2012**, *27* (2), 167–173.

Kresge, C. T.; Leonowicz, M. E.; Roth, W. J.; Vartuli, J. C.; Beck, J. S. Ordered Mesoporous Molecular Sieves Synthesized by a Liquid-Crystal Template Mechanism. *Nature* **1992**, *359* (6397), 710–712.

Kumar, A.; Jha, A. Anticandidal Agents. In *Anticandidal Agents*; Elsevier, 2017.

Larumbe, S.; Gómez-Polo, C.; Pérez-Landazábal, J. I.; Pastor, J. M. Effect of a SiO2 Coating on the Magnetic Properties of Fe3O4 Nanoparticles. *J. Phys. Condens. Matter* **2012**, *24* (26), 266007.

Lee, H.-Y.; Shin, S. H. R.; Abezgauz, L.; Lewis, S. A.; Chirsan, A. M.; Danino, D.; Bishop, K. J. M. Correction to "Integration of Gold Nanoparticles into Bilayer Structures via Adaptive Surface Chemistry." *J. Am. Chem. Soc.* **2013**, *135* (33), 12476–12476.

Leng, Y.; Li, Y.; Gong, A.; Shen, Z.; Chen, L.; Wu, A. Colorimetric Response of Dithizone Product and Hexadecyl Trimethyl Ammonium Bromide Modified Gold Nanoparticle Dispersion to 10 Types of Heavy Metal Ions: Understanding the Involved Molecules from Experiment to Simulation. *Langmuir* **2013**, *29* (25), 7591–7599.

LePlae, P. R.; Umezawa, N.; Lee, H. S.; Gellman, S. H. An Efficient Route to Either Enantiomer of Trans-2-Aminocyclopentanecarboxylic Acid. *J. Org. Chem.* **2001**, *66* (16), 5629–5632.

Lichliter, W. D.; Naider, F.; Becker, J. M. Basis for the Design of Anticandidal Agents from Studies of Peptide Utilization in Candida Albicans. *Antimicrob. Agents Chemother.* **1976**, *10* (3), 483–490.

Lindegren, M.; Loring, J. S.; Persson, P. Molecular Structures of Citrate and Tricarballylate Adsorbed on α-FeOOH Particles in Aqueous Suspensions. *Langmuir* **2009**, *25* (18), 10639–10647.

Linderoth, S.; Balcells, L.; Labarta, A.; Tejada, J.; Hendriksen, P. V.; Sethi, S. A. Magnetization and Mössbauer Studies of Ultrafine Fe-C Particles. *J. Magn. Magn. Mater.* **1993**, *124* (3), 269–276.

Ling, D.; Hyeon, T. Chemical Design of Biocompatible Iron Oxide Nanoparticles for Medical Applications. *Small* **2013**, *9* (9–10), 1450–1466.

Liu, J.; Sun, Z.; Deng, Y.; Zou, Y.; Li, C.; Guo, X.; Xiong, L.; Gao, Y.; Li, F.; Zhao, D. Highly Water-Dispersible Biocompatible Magnetite Particles with Low Cytotoxicity Stabilized by Citrate Groups. *Angew. Chemie - Int. Ed.* **2009**, *48* (32), 5875–5879.

Long, G. J.; Robinson, W. T.; Tappmeyer, W. P.; Bridges, D. L. The Magnetic, Electronic, and Mössbauer Spectral Properties of Several Trinuclear Iron(III) Carboxylate Complexes. *J. Chem. Soc., Dalt. Trans.* **1973**, No. 6, 573–579.

Ma, D.; Veres, T.; Clime, L.; Normandin, F.; Guan, J.; Kingston, D.; Simard, B. Superparamagnetic FexOy@SiO2 Core−Shell Nanostructures: Controlled Synthesis and Magnetic Characterization. *J. Phys. Chem. C* **2007**, *111* (5), 1999–2007.

Miceli, M. H.; Díaz, J. A.; Lee, S. A. Emerging Opportunistic Yeast Infections. *Lancet.*

Infect. Dis. **2011**, *11* (2), 142–151.
Milewski, S. Glucosamine-6-Phosphate Synthase--the Multi-Facets Enzyme. *Biochim. Biophys. Acta* **2002**, *1597* (2), 173–192.
Milewski, S. Molecular Targets for Anticandidal Chemotherapy. In *Candida albicans: Cellular and Molecular Biology*; Prasad, R., Ed.; Springer International Publishing: Cham, 2017; pp 429–469.
Milewski, S.; Chmara, H.; Andruszkiewicz, R.; Borowski, E. Synthetic Derivatives of Acid Inactivate Glucosamine Synthetase from Candida Albicans. *Biochim. Biophys. Acta - Protein Struct. Mol. Enzymol.* **1985**, *828* (3), 247–254.
Milewski, S.; Andruszkiewicz, R.; Borowski, E. Substrate Specificity of Peptide Permeases in Candida Albicans. *FEMS Microbiol. Lett.* **1988**, *50* (1), 73–78.
Milewski, S.; Andruszkiewicz, R.; Kasprzak, L.; Mazerski, J.; Mignini, F.; Borowski, E. Mechanism of Action of Anticandidal Dipeptides Containing Inhibitors of Glucosamine-6-Phosphate Synthase. *Antimicrob. Agents Chemother.* **1991**, *35* (1), 36–43.
Milewski, S.; Mignini, F.; Micossi, L.; Borowski, E. Antihistoplasmal in Vitro and in Vivo Effect of Lys-Nva-FMDP. *Med. Mycol.* **1998**, *36* (3), 177–180.
Milewski, S.; Mignini, F.; Prasad, R.; Borowski, E. Unusual Susceptibility of a Multidrug-Resistant Yeast Strain to Peptidic Antifungals. *Antimicrob. Agents Chemother.* **2001**, *45* (1), 223–228.
Molloy, B. B.; Boeck, L. D.; Higgens, G. E.; Kastner, R. E.; Huckstep, L. L.; Neuss, N. A New Dipeptide Antibiotic from Streptomyces Collinus, Lindenbein. *J. Antibiot. (Tokyo).* **1972**, *25* (2), 137–140.
Montravers, P.; Mira, J. P.; Gangneux, J. P.; Leroy, O.; Lortholary, O. A Multicentre Study of Antifungal Strategies and Outcome of Candida Spp. Peritonitis in Intensive-Care Units. *Clin. Microbiol. Infect.* **2011**, *17* (7), 1061–1067.
Morse, A. J.; Giakoumatos, E. C.; Tan, S.-Y.; Webber, G. B.; Armes, S. P.; Ata, S.; Wanless, E. J. Giant PH-Responsive Microgel Colloidosomes: Preparation, Interaction Dynamics and Stability. *Soft Matter* **2016**, *12* (5), 1477–1486.
Mørup, S.; Hansen, M. F.; Frandsen, C. Magnetic Nanoparticles. In *Comprehensive Nanoscience and Technology*; Elsevier, 2011; Vol. 1, pp 437–491.
Nacev, A.; Kim, S. H.; Rodriguez-Canales, J.; Tangrea, M. A.; Shapiro, B.; Emmert-Buck, M. R. A Dynamic Magnetic Shift Method to Increase Nanoparticle Concentration in Cancer Metastases: A Feasibility Study Using Simulations on Autopsy Specimens. *Int. J. Nanomedicine* **2011**, *6*, 2907–2923.
Nakamoto, K. Applications in Coordination Chemistry. In *Infrared and Raman Spectra of Inorganic and Coordination Compounds*; John Wiley & Sons, Inc.: Hoboken, NJ, USA, 2009; pp 1–273.
Navrotsky, A.; Mazeina, L.; Majzlan, J. Size-Driven Structural and Thermodynamic Complexity in Iron Oxides. *Science (80-.).* **2008**, *319* (5870), 1635–1638.
Néel, L. Some Theoretical Aspects of Rock-Magnetism. *Adv. Phys.* **1955**, *4* (14), 191–243.
Nickolov, Z.; Georgiev, G.; Stoilova, D.; Ivanov, I. Raman and IR Study of Cobalt Acetate Dihydrate. *J. Mol. Struct.* **1995**, *354* (2), 119–125.
NIST. NIST Standard Reference Database Number 69 https://webbook.nist.gov/chemistry/.
Nooney, R. I.; Dhanasekaran, T.; Chen, Y.; Josephs, R.; Ostafin, A. E. Self-Assembled Highly Ordered Spherical Mesoporous Silica/Gold Nanocomposites. *Adv.*

Mater. **2002**, *14* (7), 529–532.

Nooney, R. I.; Thirunavukkarasu, D.; Chen, Y.; Josephs, R.; Ostafin, A. E. Self-Assembly of Mesoporous Nanoscale Silica/Gold Composites. *Langmuir* **2003**, *19* (18), 7628–7637.

Nowak-Jary, J.; Andruszkiewicz, R. Antifungal Activity of Thionated Analogues of Nva-FMDP and Lys-Nva-FMDP. *Polish J. Microbiol.* **2009**, *58* (4), 295–299.

O 'neill, J. Tackling Drug-Resistant Infections Globally: Final Report and Recommendations the Review on Antimicrobial Resistance. **2016**, No. May.

Orel, B.; Ješe, R.; Lavrenčič Štangar, U.; Grdadolnik, J.; Puchberger, M. Infrared Attenuated Total Reflection Spectroscopy Studies of Aprotic Condensation of (EtO)3SiRSi(OEt)3 and RSi(OEt)3 Systems with Carboxylic Acids. *J. Non. Cryst. Solids* **2005**, *351* (6–7), 530–549.

Otero, V.; Sanches, D.; Montagner, C.; Vilarigues, M.; Carlyle, L.; Lopes, J. A.; Melo, M. J. Characterisation of Metal Carboxylates by Raman and Infrared Spectroscopy in Works of Art. *J. Raman Spectrosc.* **2014**, *45* (11–12), 1197–1206.

Pappas, P. G.; Kauffman, C. A.; Andes, D. R.; Clancy, C. J.; Marr, K. A.; Ostrosky-Zeichner, L.; Reboli, A. C.; Schuster, M. G.; Vazquez, J. A.; Walsh, T. J.; et al. Clinical Practice Guideline for the Management of Candidiasis: 2016 Update by the Infectious Diseases Society of America. *Clin. Infect. Dis.* **2015**, *62* (4), civ933.

Parekh, K.; Upadhyay, R. V; Aswal, V. K. Monodispersed Superparamagnetic Fe3O4 Nanoparticles: Synthesis and Characterization. *J. Nanosci. Nanotechnol.* **2009**, *9* (3), 2104–2110.

Park, J.; An, K.; Hwang, Y.; Park, J.-G.; Noh, H.-J.; Kim, J.-Y.; Park, J.-H.; Hwang, N.-M.; Hyeon, T. Ultra-Large-Scale Syntheses of Monodisperse Nanocrystals. *Nat. Mater.* **2004**, *3* (12), 891–895.

Patterson, T. F. Advances and Challenges in Management of Invasive Mycoses. *Lancet (London, England) 366* (9490), 1013–1025.

Paul, R. C.; Narula, R. C.; Vasisht, S. K. Iron(Ill) Acetates. *Transit. Met. Chem.* **1978**, *3*, 35–38.

Pawlak, D.; Stolarska, M.; Wojciechowski, M.; Andruszkiewicz, R. Synthesis, Anticandidal Activity of N3-(4-Methoxyfumaroyl)-(S)-2,3-Diaminopropanoic Amide Derivatives - Novel Inhibitors of Glucosamine-6-Phosphate Synthase. *Eur. J. Med. Chem.* **2015**, *90*, 577–582.

Pawlak, D.; Schielmann, M.; Wojciechowski, M.; Andruszkiewicz, R. Synthesis and Biological Activity of Novel Ester Derivatives of N3-(4-Metoxyfumaroyl)-(S)-2,3-Diaminopropanoic Acid Containing Amide and Keto Function as Inhibitors of Glucosamine-6-Phosphate Synthase. *Bioorganic Med. Chem. Lett.* **2016**, *26* (15), 3586–3589.

Perfect, J. R. The Antifungal Pipeline: A Reality Check. *Nat. Rev. Drug Discov.* **2017**, *16* (9), 603–616.

Pfaller, M. A.; Diekema, D. J. Epidemiology of Invasive Candidiasis: A Persistent Public Health Problem. *Clin. Microbiol. Rev.* **2007**, *20* (1), 133–163.

Philipse, A. P.; van Bruggen, M. P. B.; Pathmamanoharan, C. Magnetic Silica Dispersions: Preparation and Stability of Surface-Modified Silica Particles with a Magnetic Core. *Langmuir* **1994**, *10* (1), 92–99.

Pol, V. G.; Daemen, L. L.; Vogel, S.; Chertkov, G. Solvent-Free Fabrication of Ferromagnetic Fe3o4 Octahedra. *Ind. Eng. Chem. Res.* **2010**, *49* (2), 920–924.

Prasad, R.; Shah, A. H.; Rawal, M. K. Antifungals: Mechanism of Action and Drug Resistance; 2016; pp 327–349.

Provencher, S. W. CONTIN: A General Purpose Constrained Regularization Program for Inverting Noisy Linear Algebraic and Integral Equations. *Comput. Phys. Commun.* **1982**, *27* (3), 229–242.

Prucek, R.; Hermanek, M.; Zbořil, R. An Effect of Iron(III) Oxides Crystallinity on Their Catalytic Efficiency and Applicability in Phenol Degradation-A Competition between Homogeneous and Heterogeneous Catalysis. *Appl. Catal. A Gen.* **2009**, *366* (2), 325–332.

Qiu, P.; Jensen, C.; Charity, N.; Towner, R.; Mao, C. Oil Phase Evaporation-Induced Self-Assembly of Hydrophobic Nanoparticles into Spherical Clusters with Controlled Surface Chemistry in an Oil-in-Water Dispersion and Comparison of Behaviors of Individual and Clustered Iron Oxide Nanoparticles. *J. Am. Chem. Soc.* **2010**, *132* (50), 17724–17732.

Rettig, F.; Moos, R. α-Iron Oxide: An Intrinsically Semiconducting Oxide Material for Direct Thermoelectric Oxygen Sensors. *Sensors Actuators, B Chem.* **2010**, *145* (2), 685–690.

Richardson, M.; Lass-Flörl, C. Changing Epidemiology of Systemic Fungal Infections. *Clin. Microbiol. Infect.* **2008**, *14 Suppl 4*, 5–24.

Rochester, C. H.; Topham, S. a. Infrared Studies of the Adsorption of Probe Molecules onto the Surface of Goethite. *J. Chem. Soc. Faraday Trans. 1 Phys. Chem. Condens. Phases* **1979**, *75*, 872.

Rose, J.; Cortalezzi-Fidalgo, M. M.; Moustier, S.; Magnetto, C.; Jones, C. D.; Barron, A. R.; Wiesner, M. R.; Bottero, J. Synthesis and Characterization of Carboxylate−FeOOH Nanoparticles (Ferroxanes) and Ferroxane-Derived Ceramics. *Chem. Mater.* **2002**, *14* (2), 621–628.

Rozynek, Z.; Mikkelsen, A.; Dommersnes, P.; Fossum, J. O. Electroformation of Janus and Patchy Capsules. *Nat. Commun.* **2014**, *5* (May), 3945.

Samusawa, I.; Shiotani, K. Influence and Role of Ethanol Minor Constituents of Fuel Grade Ethanol on Corrosion Behavior of Carbon Steel. *Corros. Sci.* **2015**, *90*, 266–275.

Sanson, C.; Diou, O.; Thévenot, J.; Ibarboure, E.; Soum, A.; Brûlet, A.; Miraux, S.; Thiaudière, E.; Tan, S.; Brisson, A.; et al. Doxorubicin Loaded Magnetic Polymersomes: Theranostic Nanocarriers for MR Imaging and Magneto-Chemotherapy. *ACS Nano* **2011**, *5* (2), 1122–1140.

Santra, S.; Tapec, R.; Theodoropoulou, N.; Dobson, J.; Hebard, A.; Tan, W. Synthesis and Characterization of Silica-Coated Iron Oxide Nanoparticles in Microemulsion: The Effect of Nonionic Surfactants. *Langmuir* **2001**, *17* (10), 2900–2906.

Schielmann, M.; Szweda, P.; Gucwa, K.; Kawczynski, M.; Milewska, M. J.; Martynow, D.; Morschhäuser, J.; Milewski, S. Transport Deficiency Is the Molecular Basis of Candida Albicans Resistance to Antifungal Oligopeptides. *Front. Microbiol.* **2017**, *8* (NOV).

Schindelin, J.; Arganda-Carreras, I.; Frise, E.; Kaynig, V.; Longair, M.; Pietzsch, T.; Preibisch, S.; Rueden, C.; Saalfeld, S.; Schmid, B.; et al. Fiji: An Open-Source Platform for Biological-Image Analysis. *Nat. Methods* **2012**, *9* (7), 676–682.

Schubert, U. Chemistry and Fundamentals of the Sol-Gel Process. *Sol-Gel Handb.* **2015**,

1–3, 1–28.
SDBS. *Fe(II) Acetate and Fe(III) Acetate*; Vol. FT-IR spec.
Shallow, D. A.; Barrett-Bee, K. J.; Payne, J. W. Evaluation of the Dipeptide and Oligopeptide Permeases of Candida Albicans as Uptake Routes for Synthetic Anticandidal Agents. *FEMS Microbiol. Lett.* **1991**, *63* (1), 9–14.
Shapiro, B.; Kulkarni, S.; Nacev, A.; Muro, S.; Stepanov, P. Y.; Weinberg, I. N. Open Challenges in Magnetic Drug Targeting. *Wiley Interdiscip. Rev. Nanomedicine Nanobiotechnology* **2015**, *7* (3), 446–457.
Shebanova, O. N.; Lazor, P. Raman Spectroscopic Study of Magnetite (FeFe2O4): A New Assignment for the Vibrational Spectrum. *J. Solid State Chem.* **2003**, *174* (2), 424–430.
Shin, E.-J.; Miser, D. E.; Chan, W. G.; Hajaligol, M. R. Catalytic Cracking of Catechols and Hydroquinones in the Presence of Nano-Particle Iron Oxide. *Appl. Catal. B Environ.* **2005**, *61* (1–2), 79–89.
Shouhu Xuan Yi-Xiang J. Wang, J. C. Y.; Leung, K. C.-F. Tuning the Grain Size and Particle Size of Superparamagnetic Fe3O4 Microparticles. *Chem. Mater.* **2009**, *21* (c), 5079–5087.
Da Silva, S. W.; Melo, T. F. O.; Soler, M. A. G.; Lima, E. C. D.; Da Silva, M. F.; Morais, P. C. Stability of Citrate-Coated Magnetite and Cobalt-Ferrite Nanoparticles Under Laser Irradiation: A Raman Spectroscopy Investigation. *IEEE Trans. Magn.* **2003**, *39* (5 II), 2645–2647.
Soler, M. A. G.; Paterno, L. G. Magnetic Nanomaterials. In *Nanostructures*; Elsevier, 2017; pp 147–186.
Stöber, W.; Fink, A.; Bohn, E. Controlled Growth of Monodisperse Silica Spheres in the Micron Size Range. *J. Colloid Interface Sci.* **1968**, *26* (1), 62–69.
Sun, Y.; Duan, L.; Guo, Z.; DuanMu, Y.; Ma, M.; Xu, L.; Zhang, Y.; Gu, N. An Improved Way to Prepare Superparamagnetic Magnetite-Silica Core-Shell Nanoparticles for Possible Biological Application. *J. Magn. Magn. Mater.* **2005**, *285* (1–2), 65–70.
Sundar, S.; Mariappan, R.; Piraman, S. Synthesis and Characterization of Amine Modified Magnetite Nanoparticles as Carriers of Curcumin-Anticancer Drug. *Powder Technol.* **2014**, *266*, 321–328.
Swami, A.; Kumar, A.; Sastry, M. Formation of Water-Dispersible Gold Nanoparticles Using a Technique Based on Surface Bound Interdigitated Bilayers. *Langmuir* **2003**, *19* (18), 1168–1172.
Sychrová, H. *Yeast Membrane Transport*; Ramos, J., Sychrová, H., Kschischo, M., Eds.; Advances in Experimental Medicine and Biology; Springer International Publishing: Cham, 2016; Vol. 892.
Synoradzki, K.; Toliński, T. Effective Mass Enhancement and Spin-Glass Behaviour in CeCu 4 Mn y Al 1− y Compounds. *J. Phys. Condens. Matter* **2012**, *24* (13), 136003.
Tadyszak, K.; Kertmen, A.; Coy, E.; Andruszkiewicz, R.; Milewski, S.; Kardava, I.; Scheibe, B.; Jurga, S.; Chybczyńska, K. Spectroscopic and Magnetic Studies of Highly Dispersible Superparamagnetic Silica Coated Magnetite Nanoparticles. *J. Magn. Magn. Mater.* **2017**, *433*, 254–261.
Tholence, J. L. On the Frequency Dependence of the Transition Temperature in Spin Glasses. *Solid State Commun.* **1980**, *35* (2), 113–117.

UN. Draft Political Declaration of the High-Level Meeting of the General Assembly on Antimicrobial Resistance. **2016**, *16108* (September), 0–3.

Urata, C.; Aoyama, Y.; Tonegawa, A.; Yamauchi, Y.; Kuroda, K. Dialysis Process for the Removal of Surfactants to Form Colloidal Mesoporous Silica Nanoparticles. *Chem. Commun. (Camb).* **2009**, No. 34, 5094–5096.

Vayssieres, L.; Sathe, C.; Butorin, S. M.; Shuh, D. K.; Nordgren, J.; Guo, J. One-Dimensional Quantum-Confinement Effect in α-Fe2O 3 Ultrafine Nanorod Arrays. *Adv. Mater.* **2005**, *17* (19), 2320–2323.

Ventola, C. L. Progress in Nanomedicine: Approved and Investigational Nanodrugs. *P T* **2017**, *42* (12), 742–755.

Vergés, M. A.; Costo, R.; Roca, A. G.; Marco, J. F.; Goya, G. F.; Serna, C. J.; Morales, M. P. Uniform and Water Stable Magnetite Nanoparticles with Diameters around the Monodomain-Multidomain Limit. *J. Phys. D. Appl. Phys.* **2008**, *41* (13).

Vogt, C.; Toprak, M. S.; Muhammed, M.; Laurent, S.; Bridot, J. L.; Müller, R. N. High Quality and Tuneable Silica Shell-Magnetic Core Nanoparticles. *J. Nanoparticle Res.* **2010**, *12* (4), 1137–1147.

Vollet, D. R.; Donatti, D. A.; Campanha, J. R. A Kinetic Model for the Ultrasound Catalyzed Hydrolysis of Solventless TEOS-Water Mixtures and the Role of the Initial Additions of Ethanol. *J. Sol-Gel Sci. Technol.* **1996**, *6* (1), 57–63.

Vuori, L.; Hannula, M.; Lahtonen, K.; Jussila, P.; Ali-Löytty, H.; Hirsimäki, M.; Pärna, R.; Nõmmiste, E.; Valden, M. Controlling the Synergetic Effects in (3-Aminopropyl) Trimethoxysilane and (3-Mercaptopropyl) Trimethoxysilane Coadsorption on Stainless Steel Surfaces. *Appl. Surf. Sci.* **2014**, *317*, 856–866.

Wahajuddin; Arora, S. Superparamagnetic Iron Oxide Nanoparticles: Magnetic Nanoplatforms as Drug Carriers. *Int. J. Nanomedicine* **2012**, *7*, 3445–3471.

Wakieć, R.; Gabriel, I.; Prasad, R.; Becker, J. M.; Payne, J. W.; Milewski, S. Enhanced Susceptibility to Antifungal Oligopeptides in Yeast Strains Overexpressing ABC Multidrug Efflux Pumps. *Antimicrob. Agents Chemother.* **2008**, *52* (11), 4057–4063.

Walkowiak, A.; Wakieć, R.; Bontemps-Gracz, M. M.; Andruszkiewicz, R. Glutamine Analogues Containing a Keto Function--Novel Inhibitors of Fungal Glucosamine-6-Phosphate Synthase. *J. Enzyme Inhib. Med. Chem.* **2005**, *20* (5), 439–447.

Wang, S.; Cao, H.; Gu, F.; Li, C.; Huang, G. Synthesis and Magnetic Properties of Iron/Silica Core/Shell Nanostructures. *J. Alloys Compd.* **2008**, *457* (1–2), 560–564.

Wang, Y.; Aleiwi, B. A.; Wang, Q.; Kurosu, M. Selective Esterifications of Primary Alcohols in a Water-Containing Solvent. *Org. Lett.* **2012**, *14* (18), 4910–4913.

Whaley, S. G.; Berkow, E. L.; Rybak, J. M.; Nishimoto, A. T.; Barker, K. S.; Rogers, P. D. Azole Antifungal Resistance in Candida Albicans and Emerging Non-Albicans Candida Species. *Front. Microbiol.* **2017**, *7* (JAN), 1–12.

White, W. B.; DeAngelis, B. A. Interpretation of the Vibrational Spectra of Spinels. *Spectrochim. Acta Part A Mol. Spectrosc.* **1967**, *23* (4), 985–995.

WHO. *Antimicrobial Resistance - Global Report on Surveillance*; 2014.

WHO. *20th WHO Model List of Essential Medicines*; 2017; Vol. 20th.

Winterburn, P. J.; Phelps, C. F. The Binding of Substrates and Modifiers to Glucosamine Synthetase. *Biochem. J.* **1971**, *121* (4), 721–730.

Wisplinghoff, H.; Bischoff, T.; Tallent, S. M.; Seifert, H.; Wenzel, R. P.; Edmond, M. B. Nosocomial Bloodstream Infections in US Hospitals: Analysis of 24,179 Cases from a Prospective Nationwide Surveillance Study. *Clin. Infect. Dis.* **2004**, *39* (3), 309–317.

Xuan, S.; Hao, L.; Jiang, W.; Gong, X.; Hu, Y.; Chen, Z. Preparation of Water-Soluble Magnetite Nanocrystals through Hydrothermal Approach. *J. Magn. Magn. Mater.* **2007**, *308* (2), 210–213.

Yanagisawa, T.; Shimizu, T.; Kuroda, K.; Kato, C. The Preparation of Alkyltriinethylaininonium–Kaneinite Complexes and Their Conversion to Microporous Materials. *Bull. Chem. Soc. Jpn.* **1990**, *63* (4), 988–992.

Yang, W.; Li, B. A Novel Liquid Template Corrosion Approach for Layered Silica with Various Morphologies and Different Nanolayer Thicknesses. *Nanoscale* **2014**, *6* (4), 2292–2298.

Ye, F.; Laurent, S.; Fornara, A.; Astolfi, L.; Qin, J.; Roch, A.; Martini, A.; Toprak, M. S.; Muller, R. N.; Muhammed, M. Uniform Mesoporous Silica Coated Iron Oxide Nanoparticles as a Highly Efficient, Nontoxic MRI T2 Contrast Agent with Tunable Proton Relaxivities. *Contrast Media Mol. Imaging* **2012**, *7* (5), 460–468.

Yonghui Deng; Dawei Qi; Chunhui Deng, *; Xiangmin Zhang, and; Zhao*, D. Superparamagnetic High-Magnetization Microspheres with an Fe3O4@SiO2 Core and Perpendicularly Aligned Mesoporous SiO2 Shell for Removal of Microcystins. **2007**.

Zavrel, M.; White, T. C. Medically Important Fungi Respond to Azole Drugs: An Update. *Future Microbiol.* **2015**, *10*, 1355–1373.

Zboril, R.; Mashlan, M.; Petridis, D. Iron(III) Oxides from Thermal Processes-Synthesis, Structural and Magnetic Properties, Mössbauer Spectroscopy Characterization, and Applications. *Chem. Mater.* **2002**, *14* (3), 969–982.

Zgódka, D.; Borowski, E.; Milewski, S. A Diffusible Analogue of N 3-(4-Methoxyfumaroyl)-l-2,3-Diaminopropanoic Acid with Antifungal Activity. *Microbiology* **2001a**, *147* (7), 1955–1959.

Zgódka, D.; Jdrzejczak, R.; Milewski, S.; Borowski, E. Amide and Ester Derivatives of N3-(4-Methoxyfumaroyl)-(S)-2,3-Diaminopropanoic Acid. *Bioorg. Med. Chem.* **2001b**, *9* (4), 931–938.

Zhang, Y.; Chen, Y. Fmoc-Cl Fluorescent Determination for Amino Groups of Nanomaterial Science. *IET Nanobiotechnology* **2012**, *6* (2), 76.

Zhang, Y.; Newton, B.; Lewis, E.; Fu, P. P.; Kafoury, R.; Ray, P. C.; Yu, H. Cytotoxicity of Organic Surface Coating Agents Used for Nanoparticles Synthesis and Stability. *Toxicol. In Vitro* **2015**, *29* (4), 762–768.

Zierhut, M.; Pavesio, C.; Ohno, S.; Orefice, F.; Rao, N. A. *Intraocular Inflammation*; Springer Berlin Heidelberg: Berlin, Heidelberg, 2016.

APPENDIXES

1 *N-succinimidyl, methyl fumarate ^{1}H-NMR*

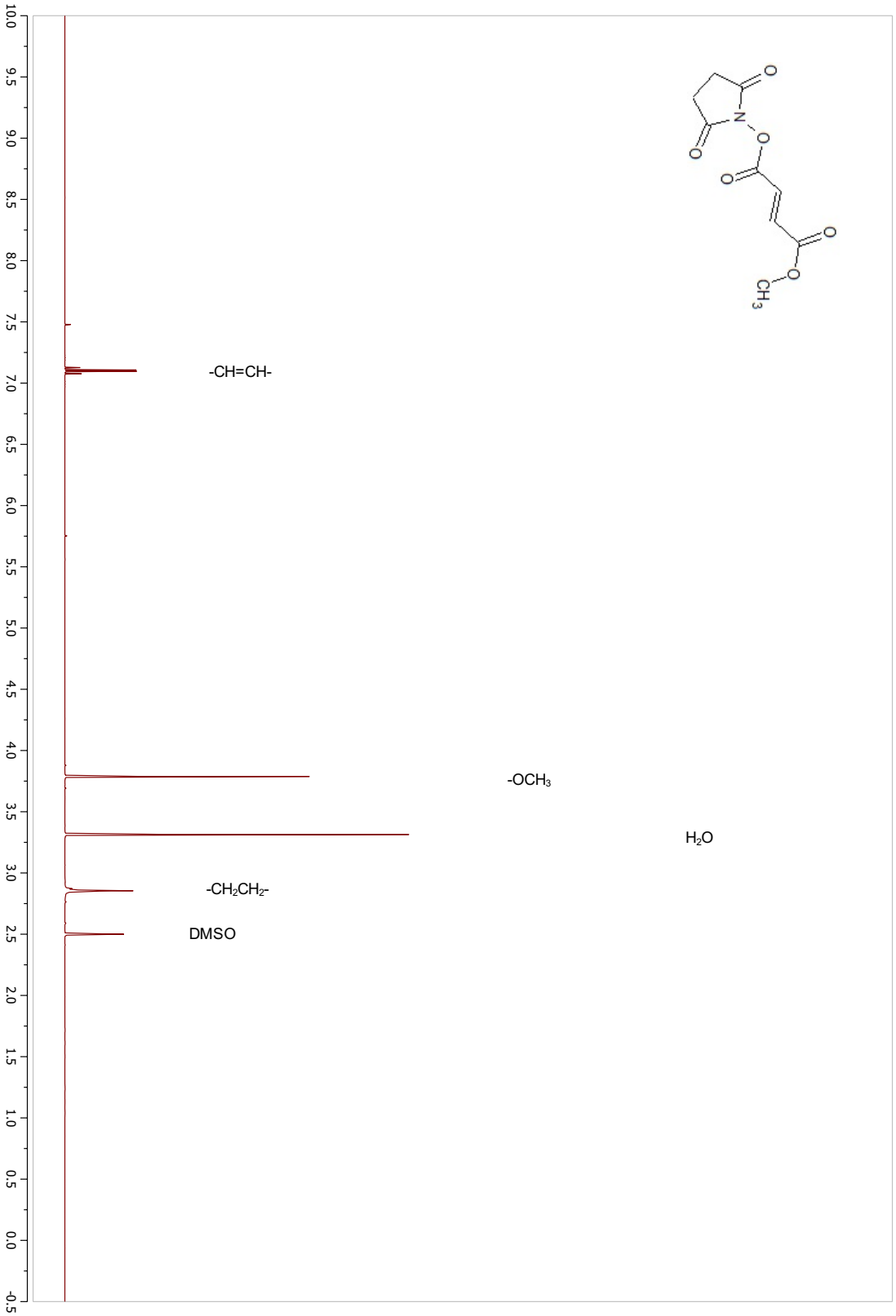

2 *N-succinimidyl, methyl fumarate ^{13}C-NMR*

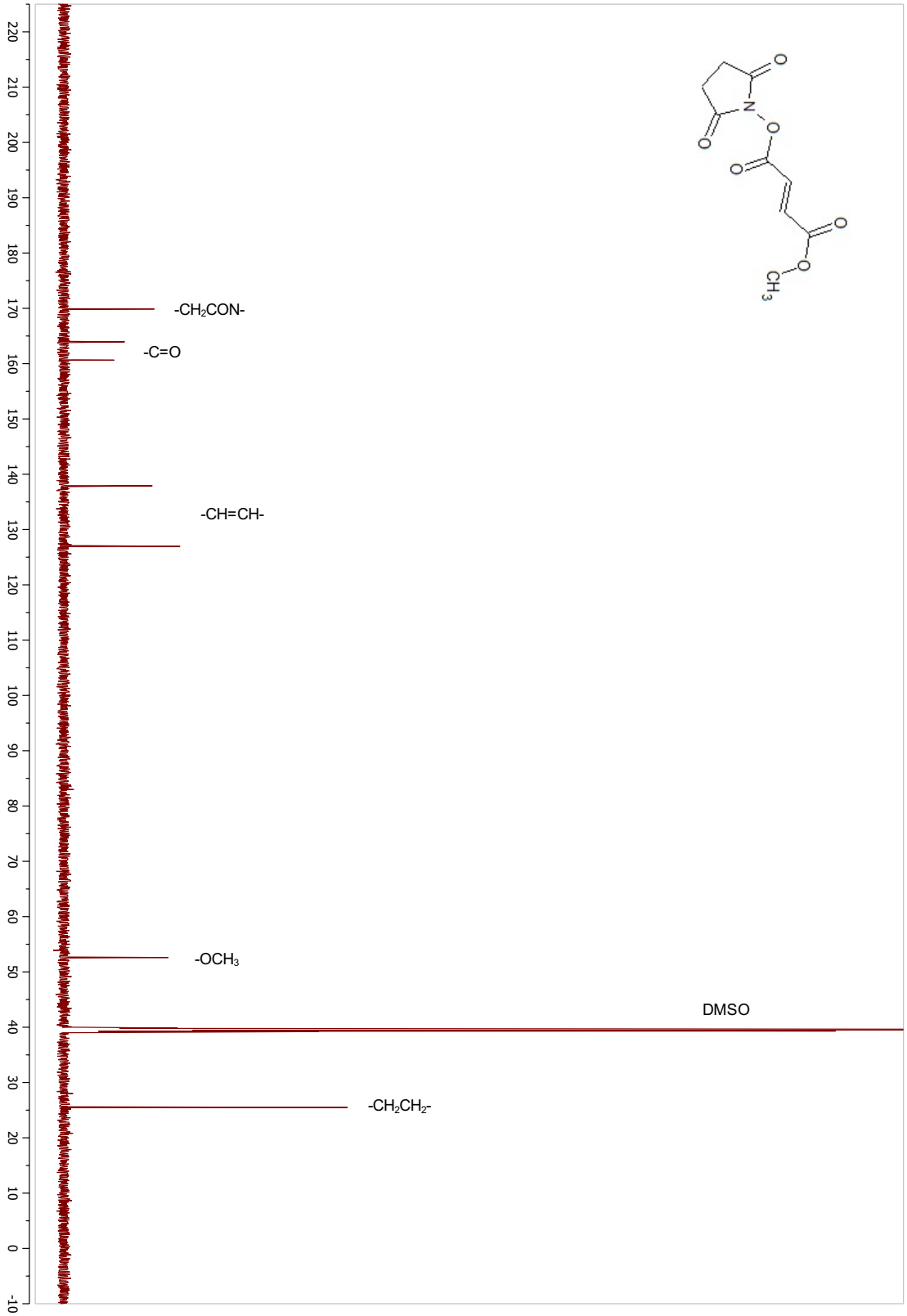

3 ***N-succinimidyl, methyl fumarate HSQC***

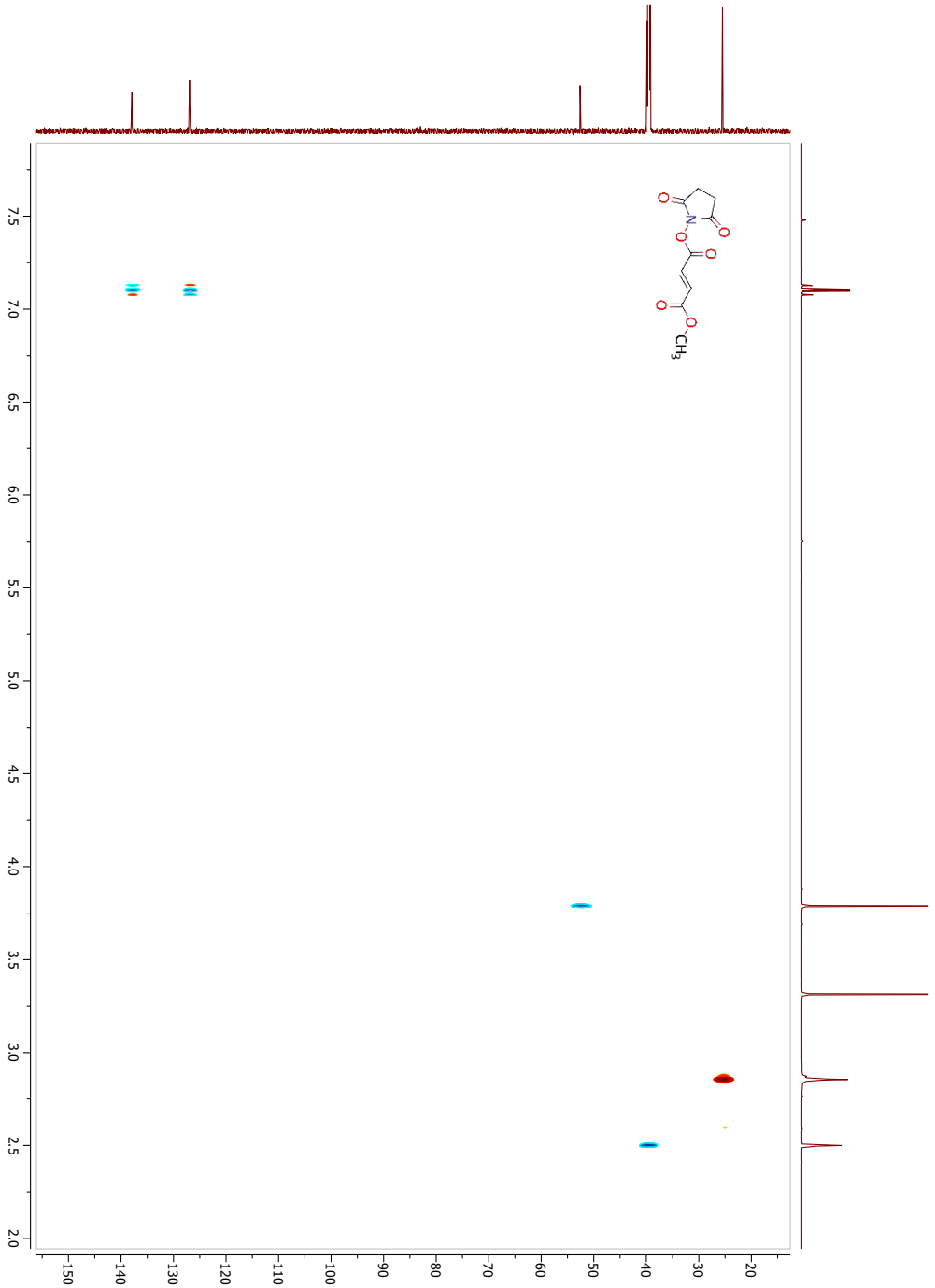

4 *N-succinimidyl, trans-4-oxo-4-phenyl-2-butenoate ^{1}H-NMR*

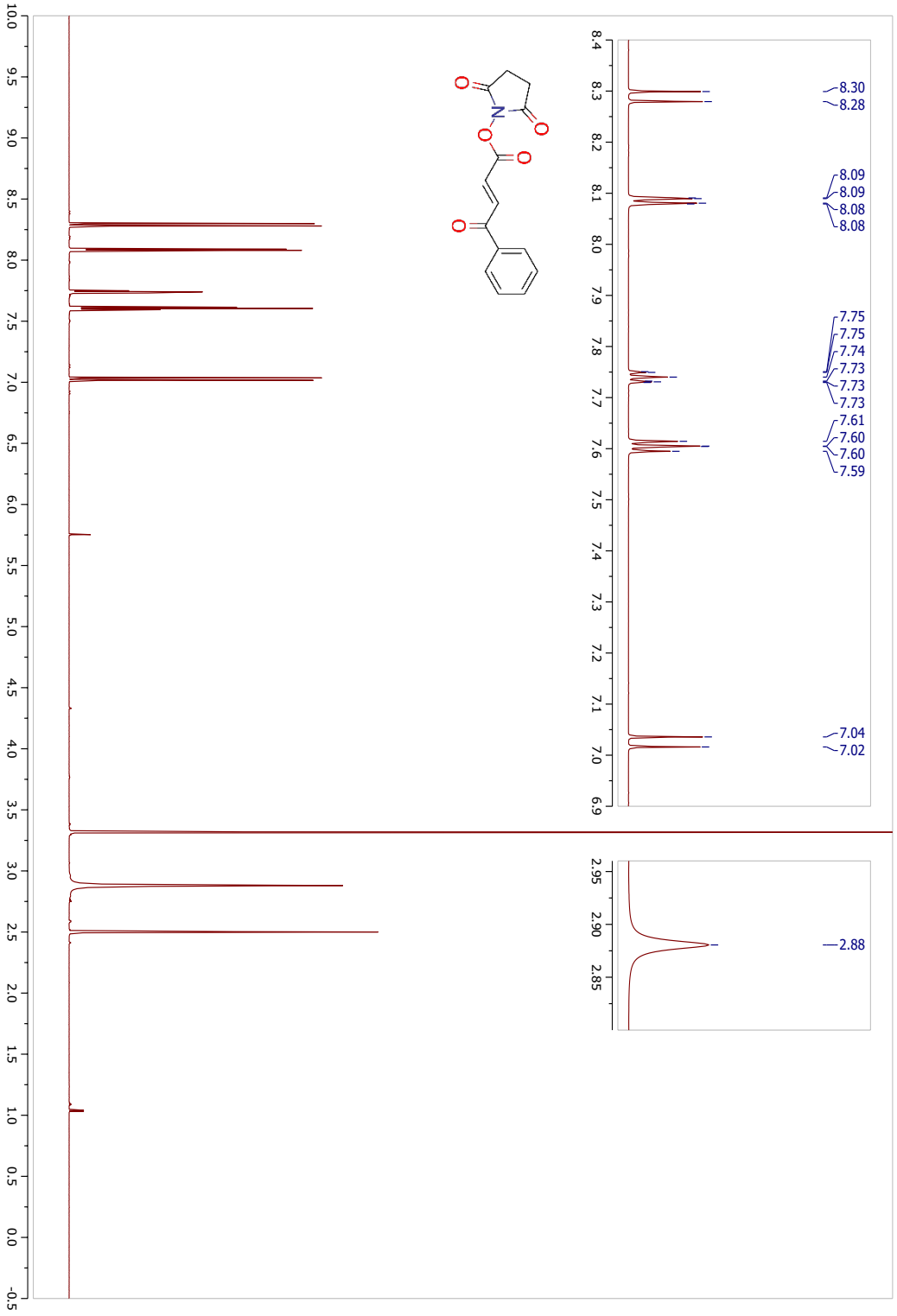

5 *N-succinimidyl, trans-4-oxo-4-phenyl-2-butenoate ^{13}C-NMR*

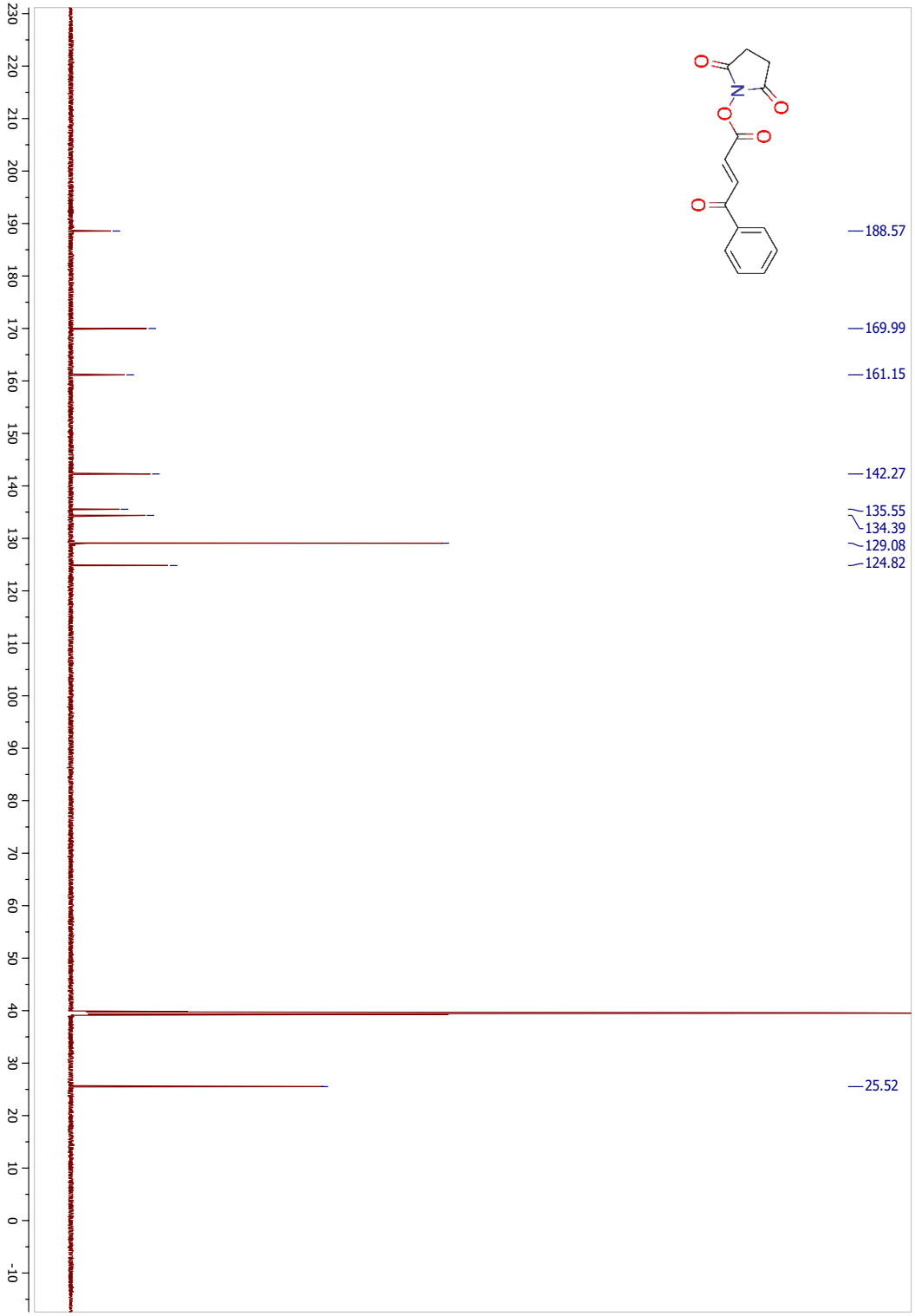

6 *N-succinimidyl, trans-4-oxo-4-phenyl-2-butenoate HSQC*

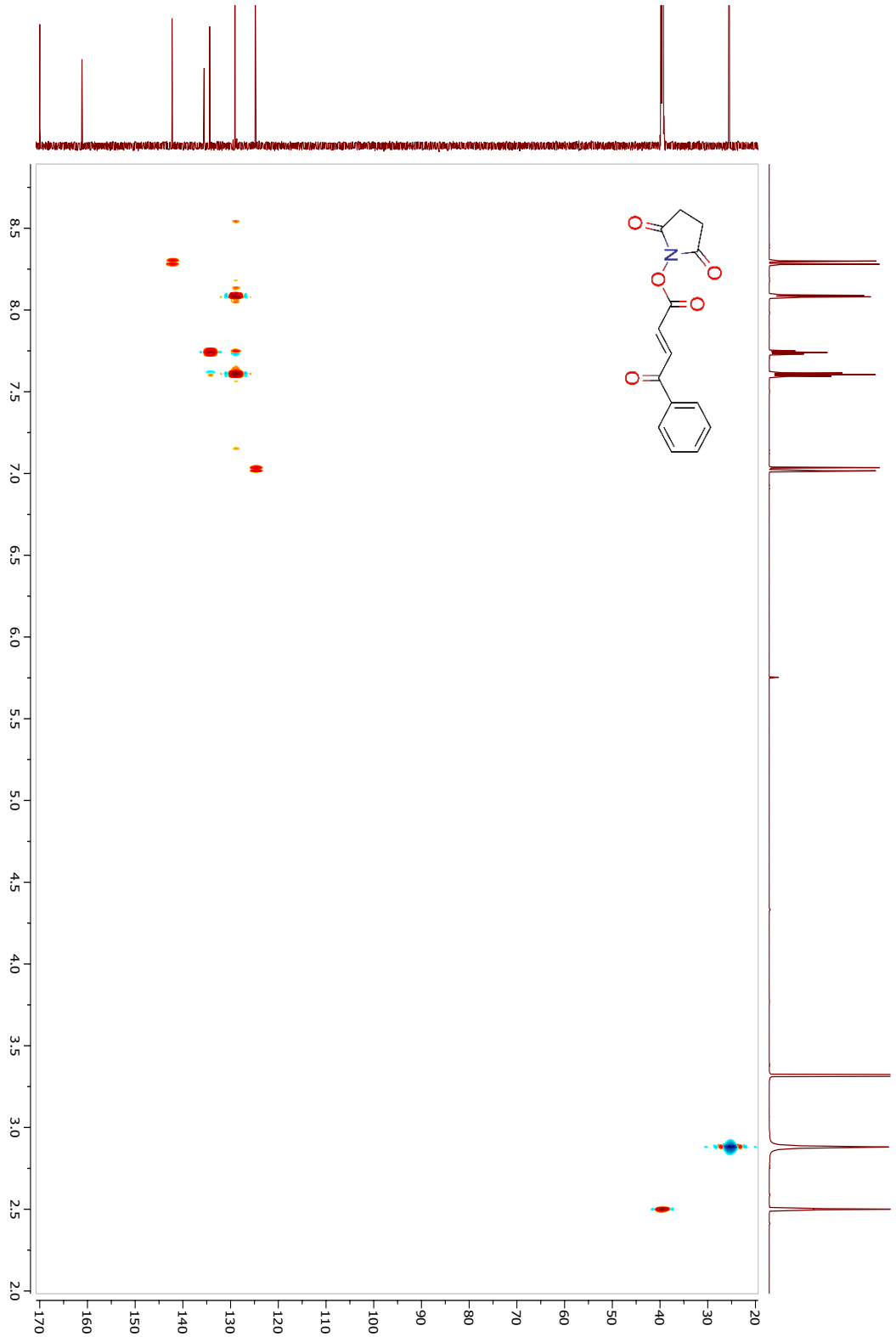

7 *N-succinimidyl, trans-4-oxo-4-phenyl-2-butenoate HMBC*

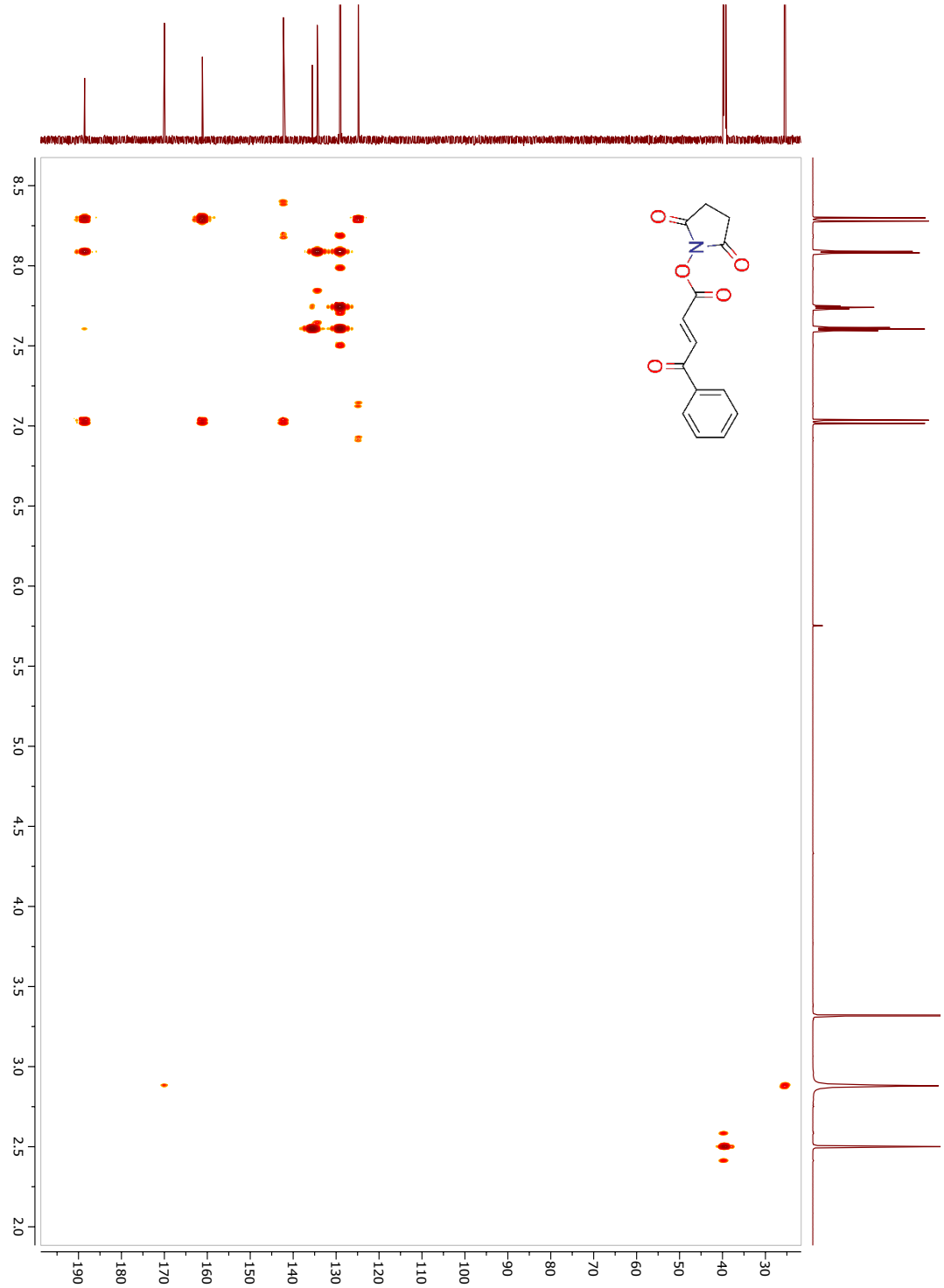

8 *N^2-(Fmoc), N^3-trans-4-oxo-4-phenyl-2-butenoyl-L-2,3-diaminopropanoic acid (Fmoc-BADP) ^{1}H-NMR*

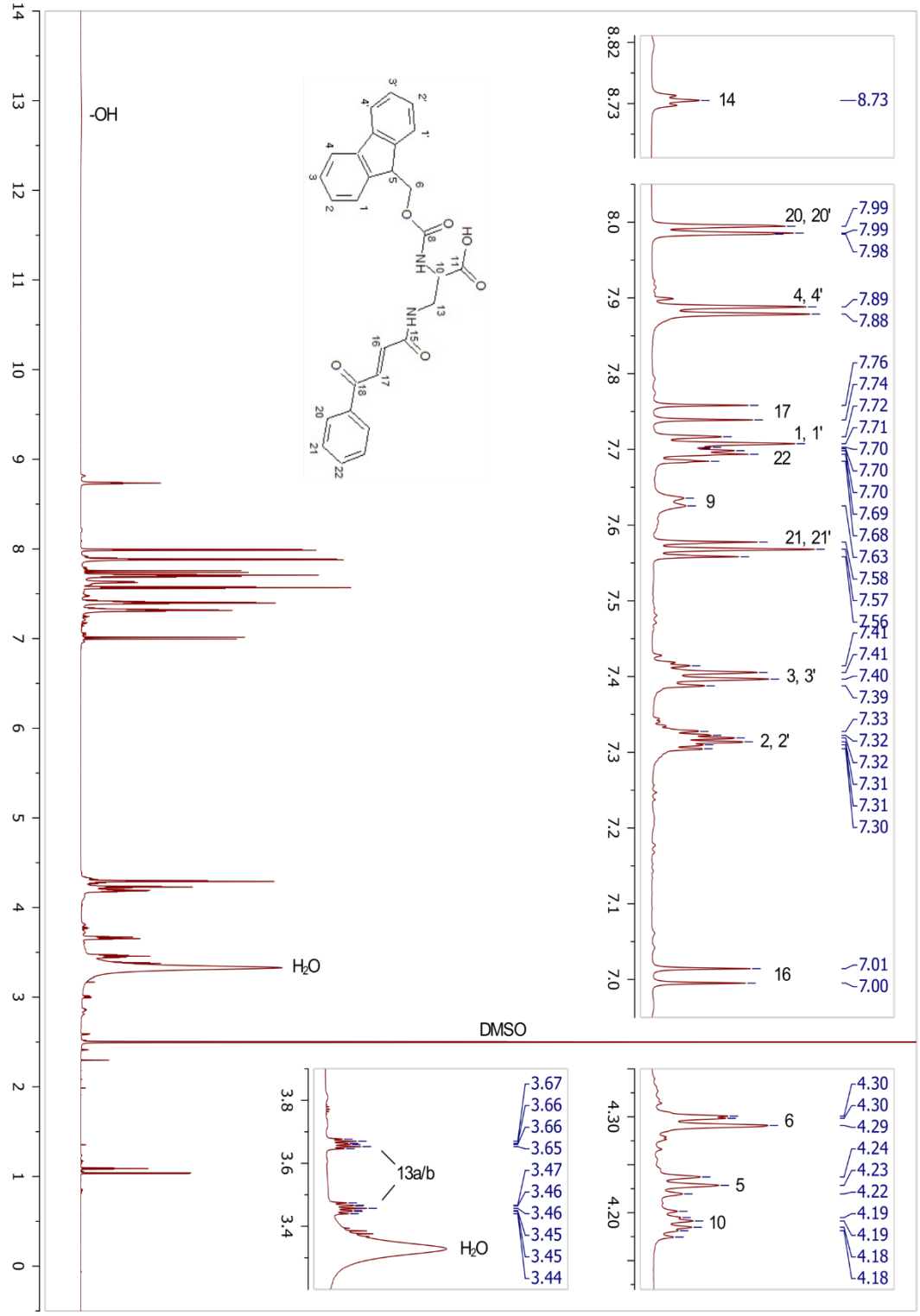

9 *N^2-(Fmoc), N^3-trans-4-oxo-4-phenyl-2-butenoyl-L-2,3-diaminopropanoic acid (Fmoc-BADP) ^{13}C -NMR*

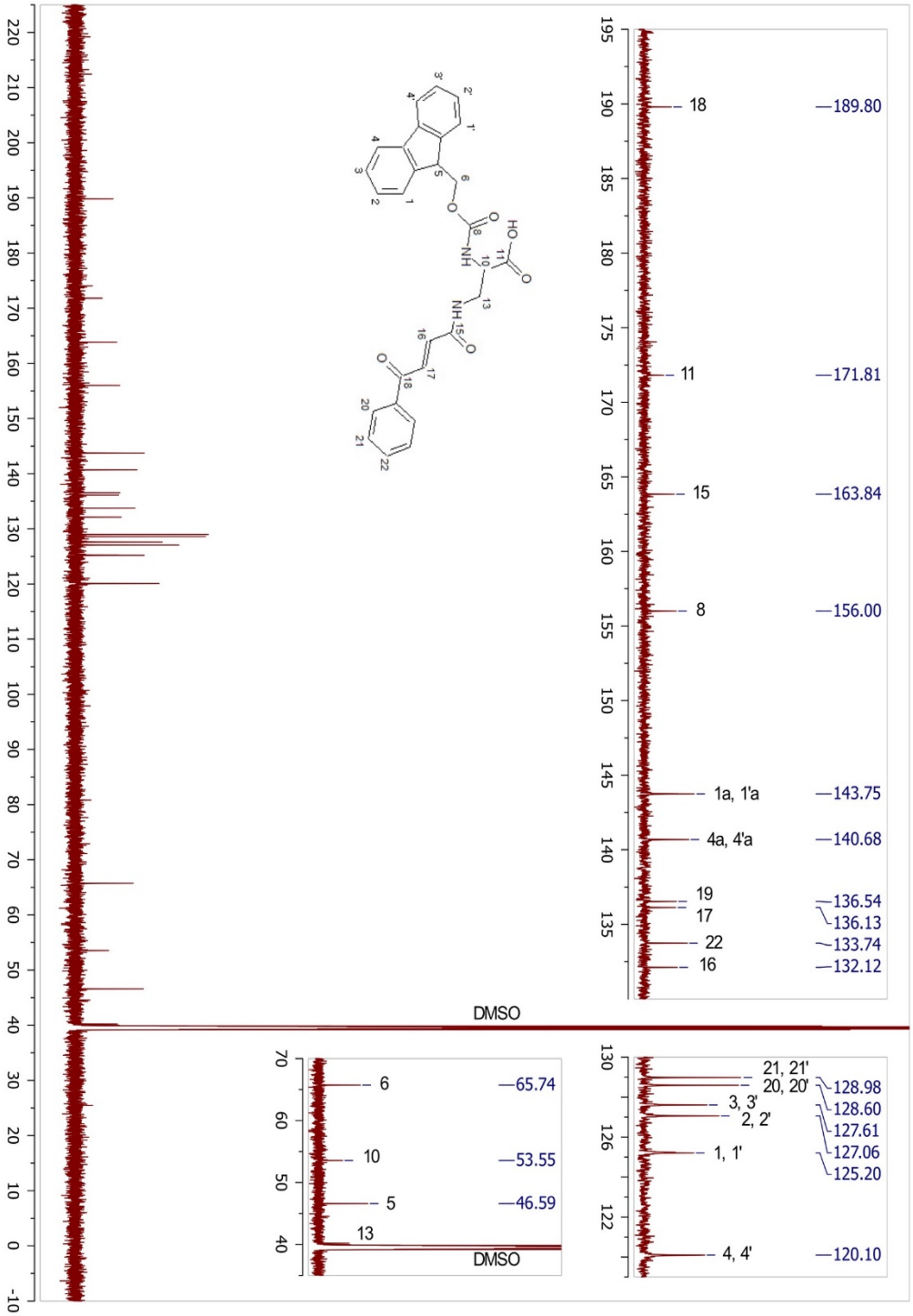

10 ***N^2-(Fmoc), N^3-trans-4-oxo-4-phenyl-2-butenoyl-L-2,3-diaminopropanoic acid (Fmoc-BADP) HSQC***

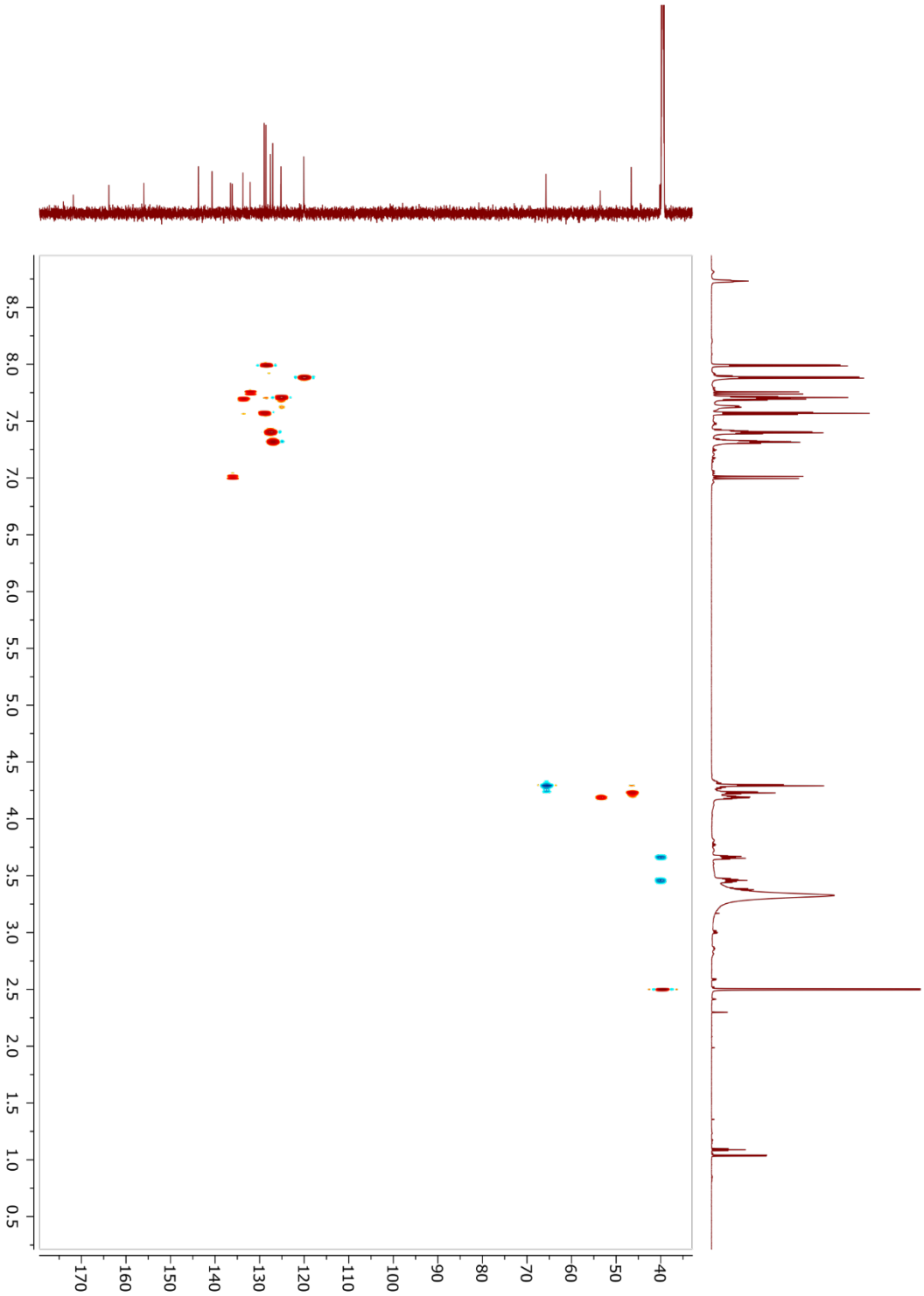

11 ***N^2-(Fmoc), N^3-trans-4-oxo-4-phenyl-2-butenoyl-L-2,3-diaminopropanoic acid (Fmoc-BADP) HMBC***

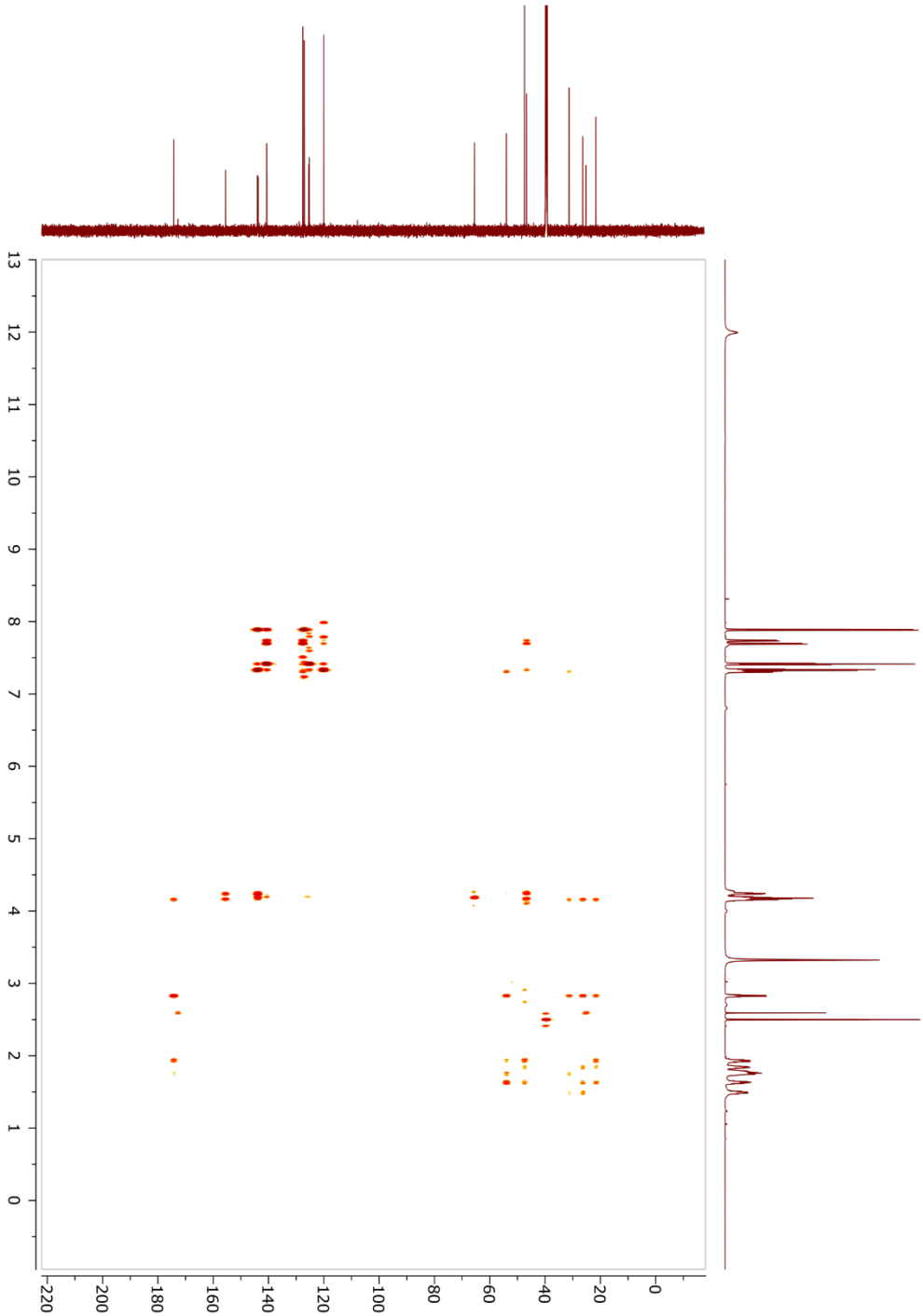

12 *N^2-(Fmoc), N3-(4-methoxyfumaroyl)-L-2,3-diaminopropanoic acid acid (Fmoc-FMDP) ^{1}H-NMR*

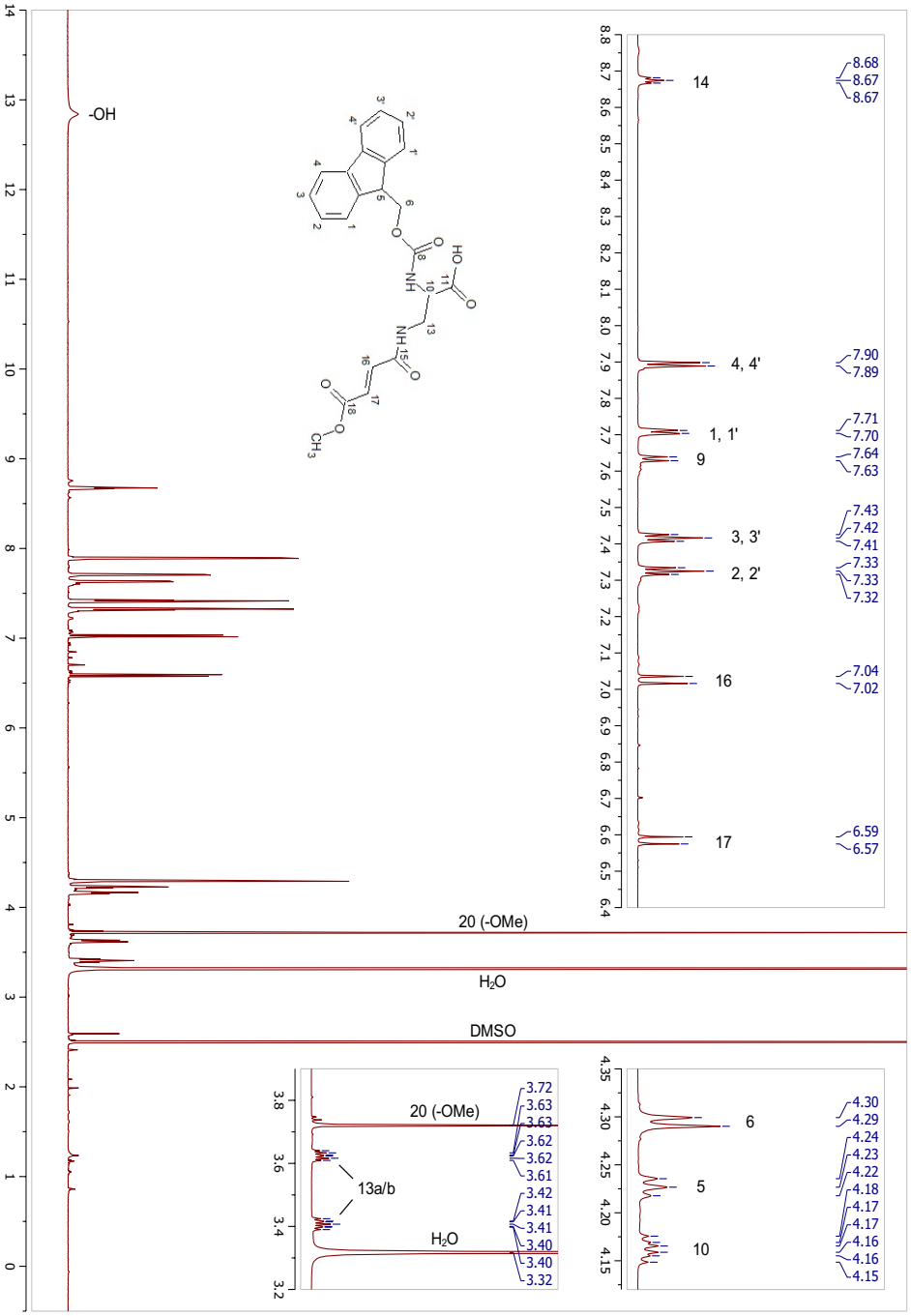

13 *N^2-(Fmoc), N3-(4-methoxyfumaroyl)-L-2,3-diaminopropanoic acid acid (Fmoc-FMDP) ^{13}C-NMR*

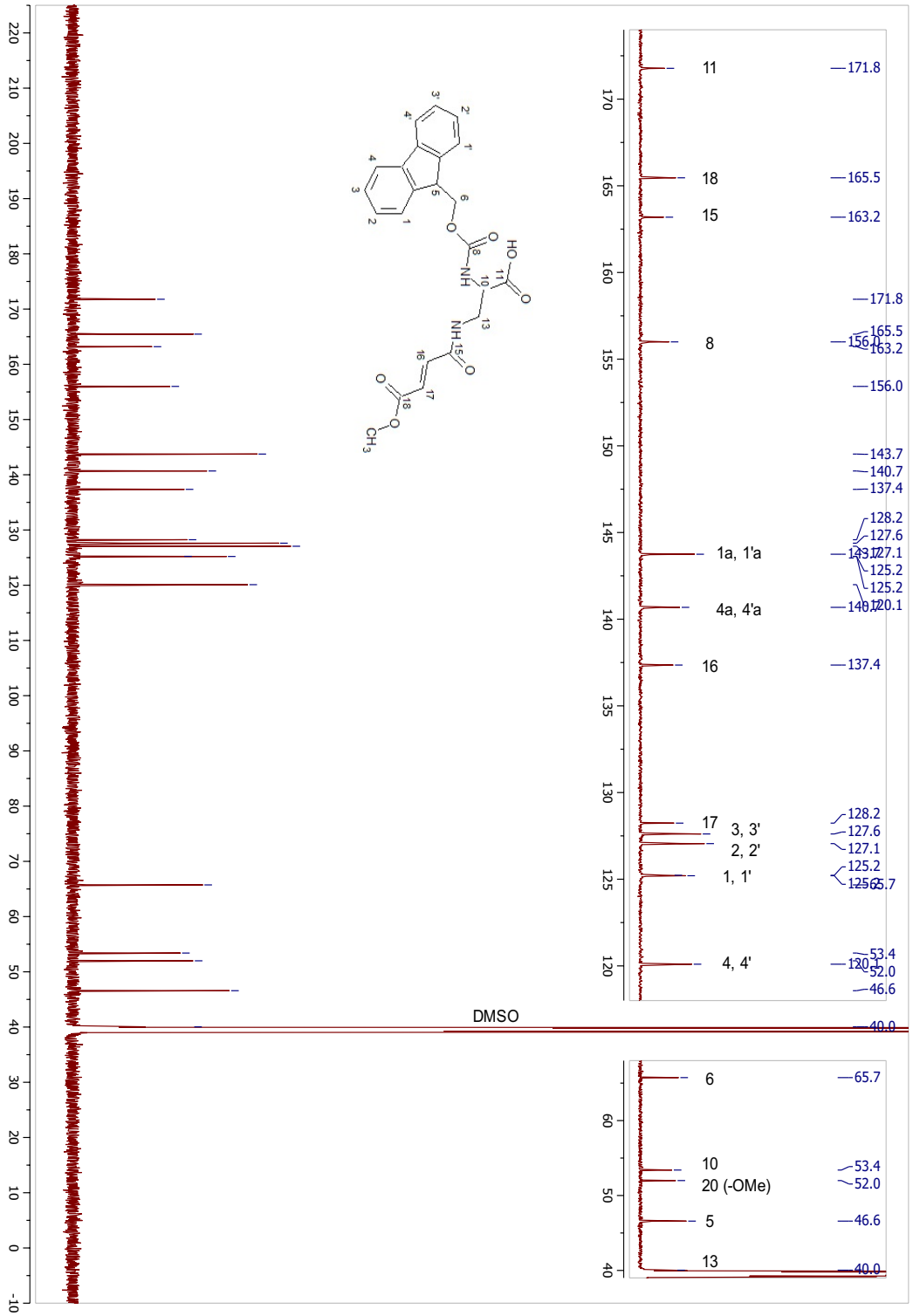

14 ***N^2-(Fmoc), N3-(4-methoxyfumaroyl)-L-2,3-diaminopropanoic acid acid (Fmoc-FMDP) HSQC***

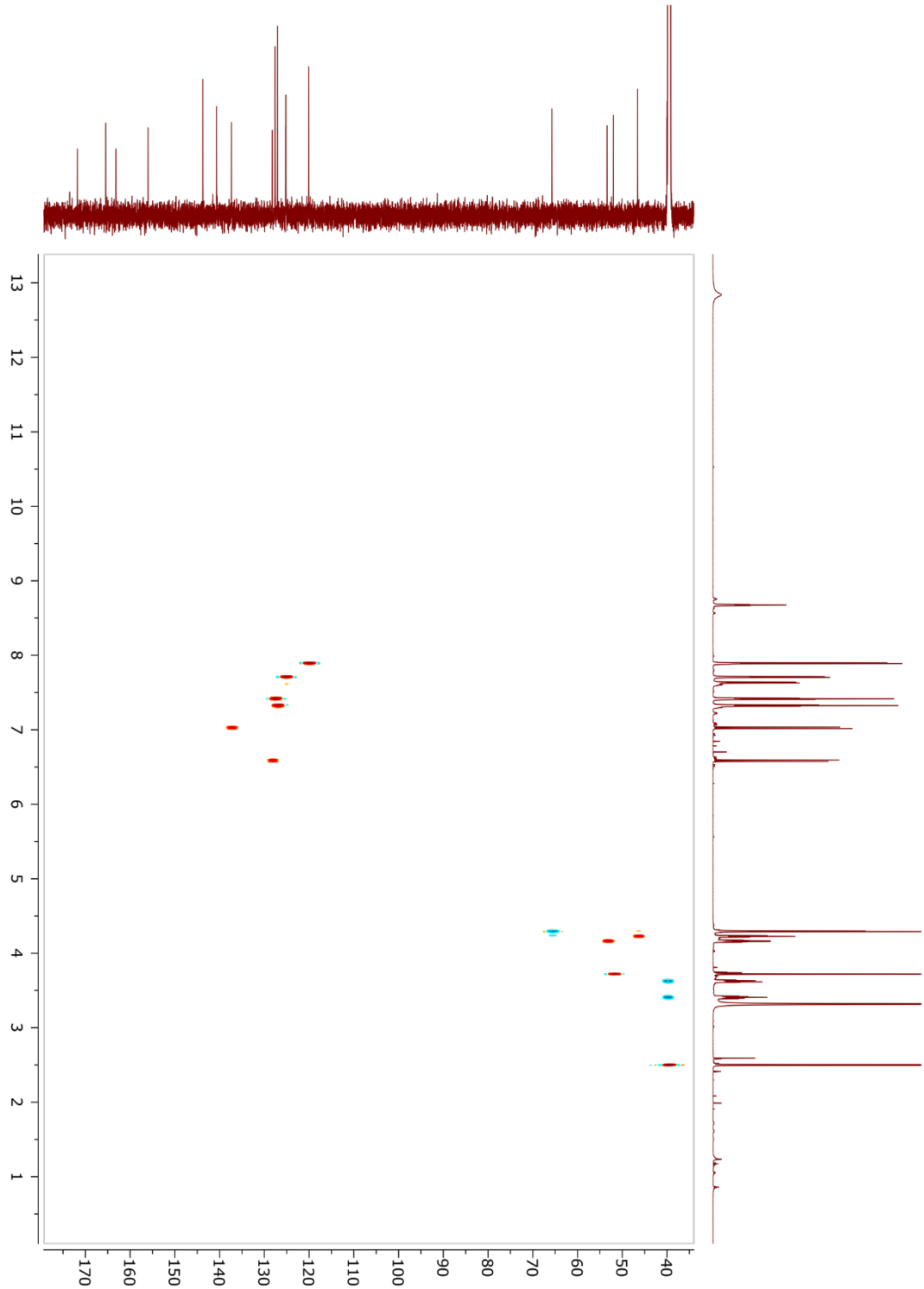

15 ***N^2-(Fmoc), N3-(4-methoxyfumaroyl)-L-2,3-diaminopropanoic acid acid (Fmoc-FMDP) HMBC***

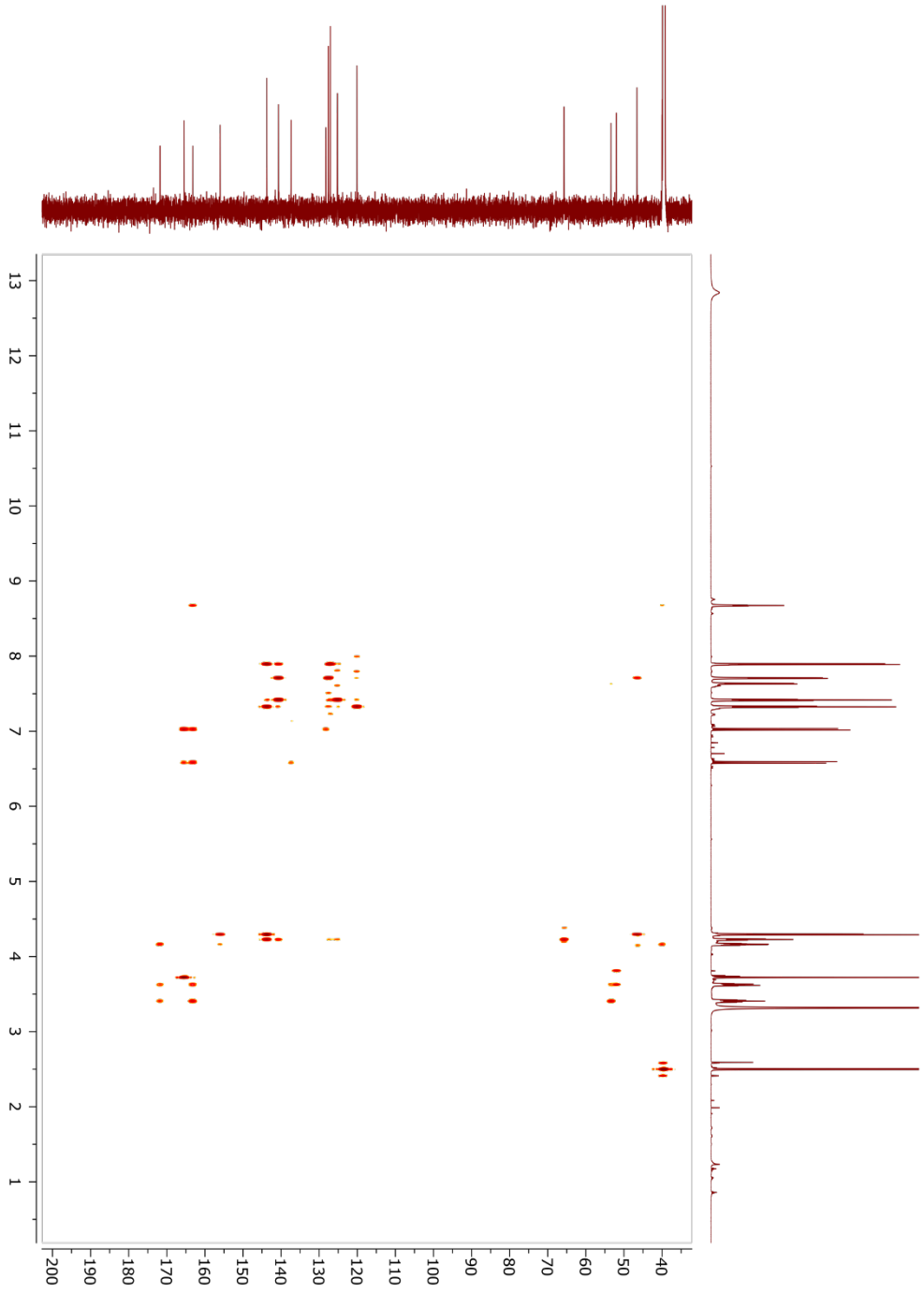

16 ***cis-2-(9-Fluorenylmethyloxycarbonyl)amino-cyclopentanecarboxylic acid (Fmoc-cispentacin)*** ^{1}***H-NMR***

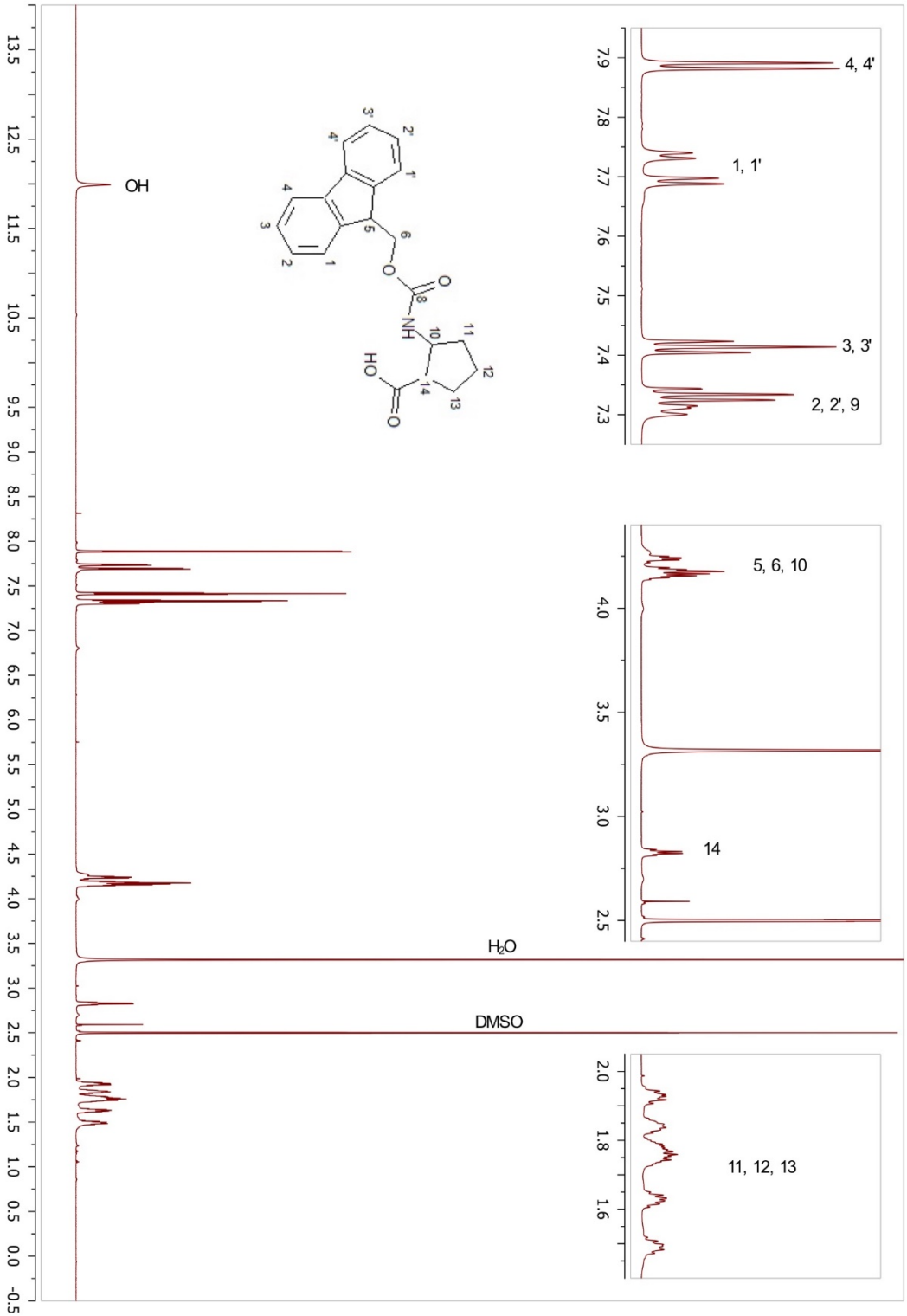

17 ***cis-2-(9-Fluorenylmethyloxycarbonyl)amino-cyclopentanecarboxylic acid (Fmoc-cispentacin)*** ^{13}***C-NMR***

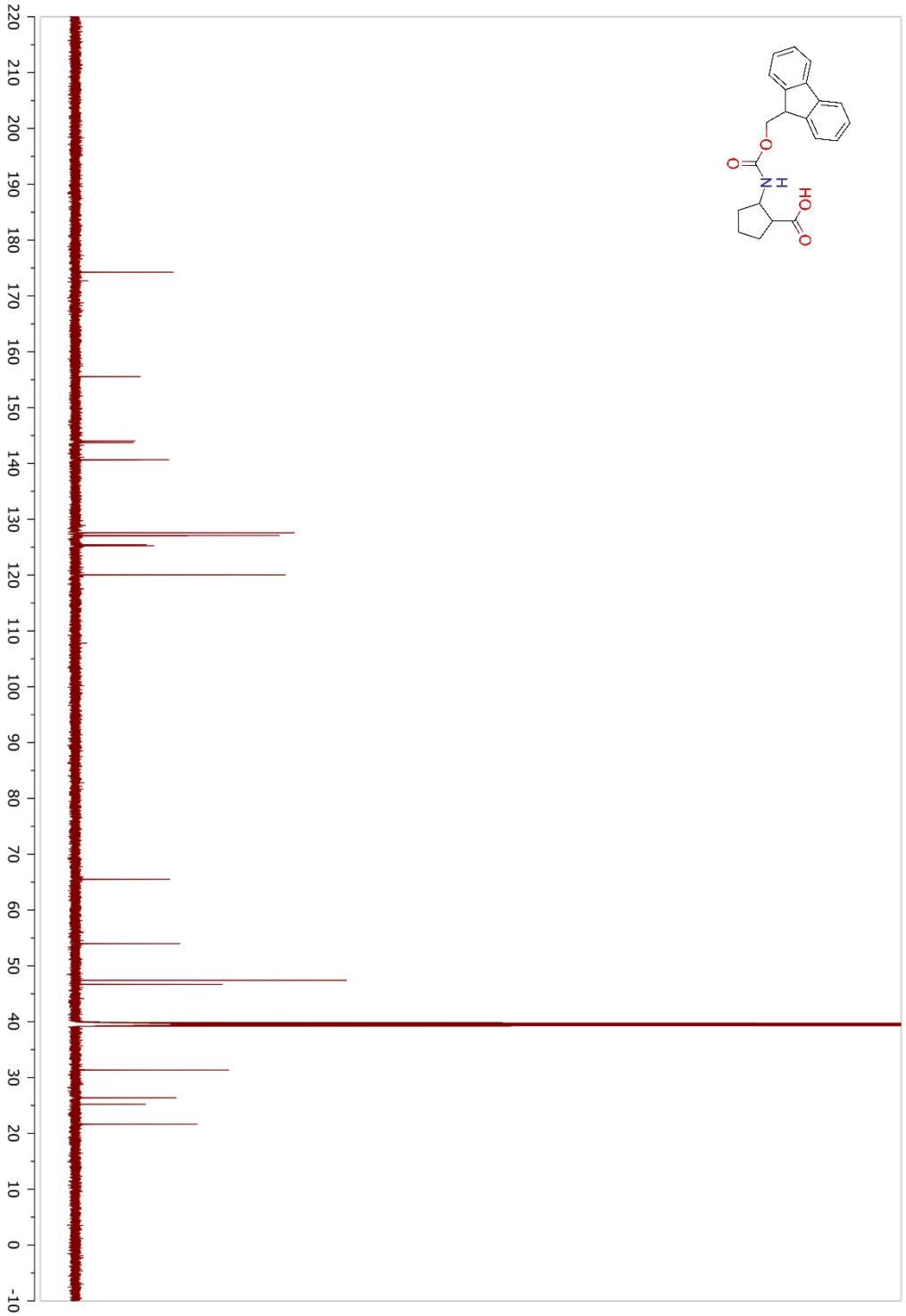

18 ***cis-2-(9-Fluorenylmethyloxycarbonyl)amino-cyclopentanecarboxylic acid (Fmoc-cispentacin) HSQC***

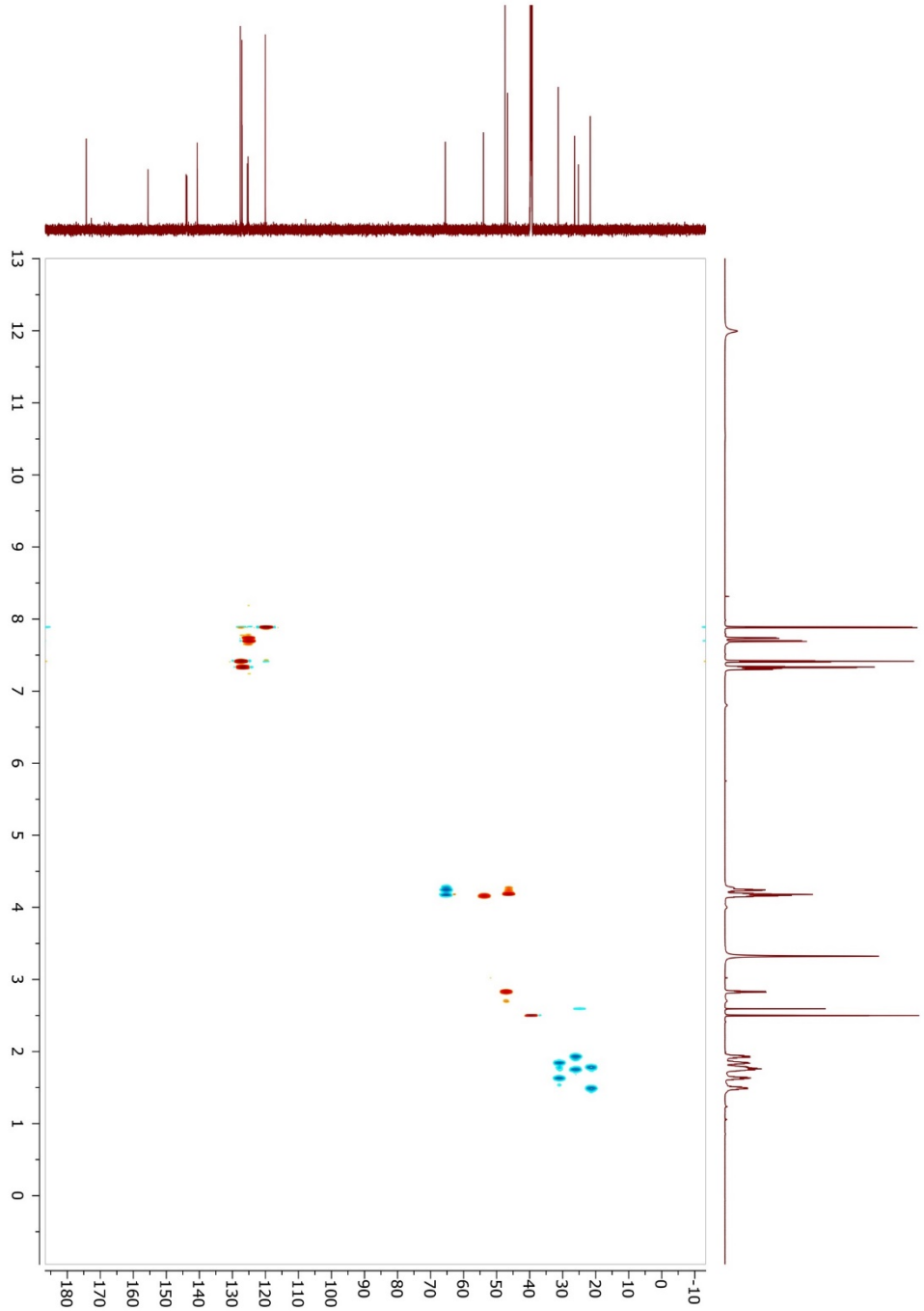

19 ***cis-2-(9-Fluorenylmethyloxycarbonyl)amino-cyclopentanecarboxylic acid (Fmoc-cispentacin) HMBC***